Christian Walchshofer

Analysis of the Dynamics at the Base of a Lifted Strongly Buoyant Jet Flame Using Direct Numerical Simulation

Monographic Series TU Graz

Computation in Engineering and Science

Monographic Series TU Graz

Computation in Engineering and Science Volume 12

Christian Walchshofer

Analysis of the Dynamics at the Base of a Lifted Strongly Buoyant Jet Flame Using Direct Numerical Simulation

---

This work is based on the dissertation *Analysis of the Dynamics at the Base of a Lifted Strongly Buoyant Jet Flame Using Direct Numerical Simulation*, presented by Christian Walchshofer at Graz University of Technology, Institute of Fluid Mechanics and Heat Transfer in July 2011.
Supervisor: H. Steiner (Graz University of Technology)
Reviewer: B.J. Boersma (Delft University of Technology)

Bibliographic information published by Die Deutsche Bibliothek.
Die Deutsche Bibliothek lists this publication in the Deutsche Nationalbibliografie; detailed bibliographic data are available at http://dnb.ddb.de.

Cover photo Vier-Spezies-Rechenmaschine
by courtesy of the Gottfried Wilhelm Leibniz Bibliothek –
Niedersächsische Landesbibliothek Hannover

Layout Wolfgang Karl, TU Graz / Universitätsbibliothek
Printed by TU Graz / Büroservice

Verlag der Technischen Universität Graz
www.ub.tugraz.at/Verlag
978-3-85125-185-2

Abstract

A major challenge in the development of modern combustion devices is to satisfy the often competing requirements of high efficiency, low pollutant emission, save and reliable operation. A profound knowledge of the underlying processes of combustion, especially on the flame stabilization, is crucial for future developments. In the present work a three-dimensional Direct Numerical Simulation (DNS) is performed to investigate the complex interactions between chemistry, flow and mixing conditions at the base of a lifted, turbulent, strongly buoyant, non-premixed methane-air jet flame. A nitrogen-diluted fuel feed is assumed to provide highly sensitive burning conditions, which are proven as convenient to clearly identify the most relevant processes for flame stabilization. Special attention is paid to particular effects which have been scarcely addressed in most previous studies, i.e., the effects of the flame on the incoming non-reacting flow, the effects of buoyancy-driven large-scale motion, and the importance of three-dimensional effects in the flame stabilization process. The generally disputed relevance of the scalar dissipation rate for the flame stabilization is investigated as well. In the present DNS, an existing jet code was extended to account for reacting flow by implementing the transport of multiple species and temperature, buoyancy force terms, as well as mixture- and temperature-dependent transfer coefficients. A robust outflow boundary condition for strongly buoyant jet flames was developed, ensuring stable simulations without significant losses in accuracy. A sufficient spatial resolution of the extremely thin reaction zone was ensured by applying a dynamically thickened flame approach. The results of the DNS show in general a good agreement with experimental data obtained from measurements with the same flow and stoichiometric conditions. Comparing the results of the jet flame against the results of a separately performed DNS of a non-reacting reference jet, it was shown that the increased viscosity and the volumetric dilatation in the hot product gases significantly reduce the turbulence intensity. High turbulence levels are retained only in the non-reacting core region around the flame base. Notable upstream effects of the flame on the non-reacting near field are manifested by a somewhat faster decay and spreading of the jet, which indicates that the lifted flame effectively impedes the oncoming jet flow. Notably increased velocity fluctuations were also observed in the radially outer region due to the action of buoyancy. An analysis of the DNS results on the most relevant mechanisms for the flame stabilization essentially confirmed the well established consensus that the stabilization is mainly determined by the premixed flame propagation. Additionally, the close interaction between buoyancy-induced acceleration, entrainment and reactive heat release was found to produce a further highly critical scenario for the stability of the flame. The buoyancy-driven large-scale motion involving the periodic formation, growth and lift-off of bulb-shaped low-density structures repeatedly leads to a strong temporal perturbation, where considerable azimuthal sections of the flame base are receding deeply downstream. The significant partial receding could be attributed to locally increased scalar dissipation rates leading to enhanced heat losses. It is finally shown that the three-dimensional nature of the

buoyancy-induced large-scale perturbation enables the partially blown-off flame to stabilize again from the non-receding, hence continuously reactive heat supplying, sections of the flame base.

Zusammenfassung

Die Entwicklung moderner Verbrennungsmaschinen ist häufig konfrontiert mit hohen, oft widersprüchlichen Anforderungen an Wirkungsgrad, Schadstoffausstoß und Betriebssicherheit. Ein tiefgreifendes Verständnis des Verbrennungsvorgangs, insbesondere der Flammenstabilisierung, ist deshalb unerlässlich. In der vorliegenden Arbeit wird das komplexe Wechselspiel zwischen den Strömungs-, Mischungs- und Reaktionsprozessen an der Basis einer abgehobenen, turbulenten, stark auftriebsbeeinflussten, nicht vorgemischten Methan-Luft-Freistrahlflamme mittels direkter numerischer Simulation (DNS) analysiert. Die Annahme einer mit Stickstoff verdünnten Treibstoffzufuhr bedingt eine leicht destabilisierbare Flamme, anhand derer die wesentlichen Stabilisierungsmechanismen detailliert darstellt werden können. Besonderes Augenmerk gilt bestimmten, in bisherigen Studien oft nur spärlich untersuchten, Effekten, wie der Stromaufwirkung der Flamme auf das inerte Nahfeld des Freistrahls, den großräumigen auftriebsbedingten Strömungsstrukturen, dem umstrittenen, häufig negierten Einfluss der Skalaren Dissipationsrate, sowie der Relevanz dreidimensionaler Störungen in der Flammenstabilisierung. Für die vorliegende DNS wurde ein bereits bestehendes Simulationsprogramm erweitert, um dem Transport der bei der Verbrennung relevanten Spezies und der Wirkung von Auftriebskräften Rechnung zu tragen. Zur Gewährleistung einer stabilen und akkuraten numerischen Lösung der durch Auftriebskräfte stark beeinflussten Freistrahlströmung wurden spezielle Austrittsrandbedingungen entwickelt. Die Annahme von dynamisch aufgedickten Reaktionszonen stellt eine ausreichende räumliche Auflösung der verschwindend dünnen chemisch reagierenden Flammenschichten sicher. Der Vergleich der Simulationsergebnisse mit experimentellen Daten einer Flamme mit identischen Strömungsbedingungen und Stöchiometrie zeigte generell gute Übereinstimmung. Die Gegenüberstellung der DNS-Resultate für die Freistrahlflamme mit den Simulationsergebnissen für einen inerten Referenzstrahl offenbart eine starke Dämpfung turbulenter Wirbel durch die Flamme, was durch die erhöhte Viskosität und die starke volumetrische Dilatation erklärt werden kann. Hohe Turbulenzgrade können lediglich in der nicht reagierenden Kernströmung im Zentrum der Flammenbasis nachgewiesen werden. Ein schnelleres Absinken der Zentrumsgeschwindigkeit sowie rascheres Aufweiten des Freistrahls stromauf der Flammenbasis lässt eine begrenzte Stauwirkung durch die abgehobene Flamme erkennen. Im radial äußeren Nahfeld des Freistrahls können überdies, verursacht durch Auftriebskräfte, deutlich erhöhte Fluktuationen der Geschwindigkeit festgestellt werden. Die Analyse der DNS-Daten hinsichtlich der wichtigsten Stabilisierungsmechanismen bestätigt generell die etablierte Theorie, wonach die Stabilisierung der Flamme an einer bestimmten Abhubhöhe hauptsächlich durch den Ausbreitungsmechanismus von Vormischflammen bestimmt wird. Die gegenwärtig untersuchte Flamme unterliegt zusätzlich einer stark destabilisierenden Störung, welche aus einem periodischen Wechselspiel der auftriebsinduzierten Beschleunigung, dem lateralen Ansaugen von Umgebungsgas, und der chemischen Wärmefreisetzung hervorgeht. Die daraus resultierenden großräumigen Strömungsmuster, welche mit der Bildung, dem

Anwachsen und Abheben großer birnenförmiger Strukturen von geringer Dichte einhergehen, verursachen zeitweise ein erhebliches Zurückweichen von beträchtlichen Teilen der Flammenfront. Die dabei beobachteten erhöhten Skalaren Dissipationsraten deuten auf eine Destabilisierung aufgrund lokal stark zunehmender Wärmeverluste hin. Überdies kann gezeigt werden, dass die dreidimensionale Natur der auftriebsbedingten großräumigen Störungen es der zu maßgeblichen Teilen abgeblasenen Flamme ermöglicht, durch die fortgesetzte Wärmefreisetzung in den nicht zurückgewichenen Sektoren der Flammenbasis ihre ursprüngliche stabile Form wiederherzustellen.

CONTENTS

Appendices

Nomenclature

Latin symbols

A	pre-exponential constant	reaction dependent
b	parameter	$[-]$
B	decay constant	$[-]$
c	parameter	$[1/m]$
C	parameter	$[-]$
c_p	specific heat at constant pressure	$[J/kg\,K]$
D	pipe diameter	$[m]$
e	internal specific energy	$[J/kg]$
$\mathbf{e}$	unit vector; direction denoted by subscript	$[-]$
E	efficiency of turbulent combustion	$[-]$
f	frequency	$\left[s^{-1}\right]$
$\mathbf{f}$	volumetric force vector	$\left[m/s^2\right]$
F	flame thickening factor	$[-]$
$\mathbf{g}$	gravitational acceleration vector	$\left[m/s^2\right]$
G	Gladstone-Dale constant	$\left[m^3/kg\right]$
h	specific enthalpy	$[J/kg]$
$[\mathrm{H}]$	hydrogen radical concentration	$\left[kg/m^3\right]$
$\mathbf{I}$	identity matrix	$[-]$
k	turbulent kinetic energy	$\left[m^2/s^2\right]$
l	length scale	$[m]$
L	length	$[m]$
m	mass	$[kg]$
$\dot{m}$	mass flux	$[kg/s]$
M	total number of reactions	$[-]$
$[\mathrm{M}]$	third body concentration	$\left[kg/m^3\right]$
n	refractive index	$[-]$
$\mathbf{n}$	normal unit vector at the boundary	$[-]$
N	total number	$[-]$
p	pressure	$[Pa]$
$\mathbf{q}$	heat flux	$\left[W/m^2\right]$
Q	heat released per *kmol* of fuel	$[J/kmol]$

r	radial coordinate	$[m]$
R	universal gas constant	$[J/kmol\,K]$
$\mathbf{R}$	Reynolds stress tensor	$[m^2/s^2]$
s	flame speed	$[m/s]$
S	surface	$[m^2]$
$\mathbf{S}$	strain rate tensor	$[s^{-1}]$
t	time	$[s]$
T	temperature	$[K]$
$\mathbf{u}$	velocity vector $[u\ v\ w]$	$[m/s]$
$\mathbf{u}'$	velocity fluctuation vector $[u'\ v'\ w']$	$[m/s]$
U	reference velocity	$[m/s]$
V	volume	$[m^3]$
$\mathbf{V}$	diffusive drift velocity vector	$[m/s]$
W	molecular weight	$[kg/kmol]$
$\mathbf{x}$	spherical coordinate vector	$[m]$ / [rad] / [rad]
Y	mass fraction	$[-]$
Z	mixture fraction	$[-]$

Greek symbols

α, β	parameters	$[-]$
γ	ratio of specific heats	$[-]$
Γ	boundary surface	$[m^2]$
Δ	grid spacing	$[m]$
ε	dissipation of turbulent kinetic energy	$[m^2/s^3]$
$\boldsymbol{\zeta}$	scalar flux vector	$[m/s]$
η	Kolmogorov length scale	$[m]$
θ	cross-stream coordinate	[rad]
κ	turbulent wavenumber	$[m^{-1}]$
λ	thermal conductivity	$[W/m\,K]$
Λ	correction parameter	$[-]$
μ	dynamic viscosity	$[Pa\,s]$
ν	stoichiometric coefficient	$[-]$
ξ	parameter	$[m]$
ρ	fluid density	$[kg/m^3]$
σ	hard sphere diameter	$[\mathring{A}]$
$\boldsymbol{\sigma}$	stress tensor	$[N/m^2]$
$\boldsymbol{\tau}$	viscous stress tensor	$[N/m^2]$
ϕ	equivalence ratio	$[-]$

φ	azimuthal coordinate	[rad]
χ	scalar dissipation rate	$\left[s^{-1}\right]$
ψ	arbitrary quantity	[ ]
$\dot{\omega}$	molar conversion rate; refers to a chemical reaction	$[kmol/kg\,s]$
$\Omega^{\mu}, \Omega^{\mathcal{D}}$	collision integrals for viscosity and diffusivity	$[-]$
$\dot{\Omega}$	mass conversion rate; refers to a species	$\left[s^{-1}\right]$
∇	vector of spatial derivatives	$\left[m^{-1}\right]$

Calligraphic symbols

$\mathcal{D}$	diffusivity	$\left[m^2/s\right]$
$\mathcal{F}$	discretized non-stiff terms in non-dimensionalized species and temperature transport equations	$[-]$
$\mathcal{G}$	discretized terms in non-dimensionalized momentum transport equation, excluding pressure	$[-]$
$\mathcal{H}$	enthalpy	$[J]$
$\mathcal{I}$	turbulence intensity	$[-]$
$\mathcal{L}$	integral length scale	$[m]$
$\mathcal{M}$	symbol for species	
$\dot{\mathcal{Q}}$	heat source term	$\left[J/m^3\,s\right]$
$\mathcal{R}$	discretized stiff term in non-dimensionalized species and temperature transport equations	$[-]$
$\mathcal{S}$	entropy	$[J/K]$
$\mathcal{V}$	volume of computational domain	$\left[m^3\right]$
$\mathcal{W}$	normalized vorticity	$[1/s]$

Subscripts

0	reference
1	denotes the fuel stream
2	denotes the oxidizer stream
a	activation
bc	boundary condition
bf	buoyant fluctuation
c	co-flow
D	diffusive
E	edge flame
eff	effective

f	forward
F	formation
fb	flame base
fl	flame
ft	flow-through
fuel	self speaking
g	gravity
J	iterator for reaction number
L	laminar
LFC	laminar flamelet concept
mom	momentum
nb	non-buoyant
op	operation
orif	jet orifice
out	outflow
oxi	oxidizer
q	quenching
P, Q	iterators for species
r	reverse
rad	radiative
react	reactive
sd	separation distance between counterflow nozzles
st	at stoichiometric conditions
stag	stagnation plane
T	turbulent
temp	temperature
th	thermal
tot	total
u	velocity
∞	ambient conditions
Z	mixture fraction

Superscripts

B	body
int	intermediate
n, $n+1$	time step iterators
t	thickened
T	transposed
$*$	predictor

Non-dimensional parameters

Ce_P	McMurtry number	$\dfrac{\Delta h^0_{f,P}}{c_{p,0}T_0}$
Da_P	Damköhler number	$\dot{\Omega}^*_{P,\max}$
Fr	Froude number	$\dfrac{U_0}{\sqrt{gL_0}}$
Le_P	Lewis number	$\dfrac{\lambda_0}{\rho c_{p,0}\mathcal{D}_{P,0}}$
Ma	Mach number	$\dfrac{U_0}{\sqrt{\gamma \dfrac{R}{W_0} T_0}}$
Pr	Prandtl number	$\dfrac{\mu_0 c_{p,0}}{\lambda_0}$
Re	Reynolds number	$\dfrac{\rho_0 U_0 L_0}{\mu_0}$
Sc_P	Schmidt number	$\dfrac{\mu_0}{\rho_0 \mathcal{D}_{P,0}}$

Acronyms

ACML	AMD core math library
ART	algebraic reconstruction technique
BC	boundary condition
BDF	backward differential formula
BLAS	basic linear algebra subprograms
CARS	coherent anti-Stokes Raman spectroscopy
CSRS	coherent Stokes Raman spectroscopy
CFD	computational fluid mechanics
CMC	conditional moment closure
CPU	central processing unit
CSP	computational singular perturbation
DNS	direct numerical simulation
DTF	dynamically thickened flame
EBU	eddy-break-up
FACR	Fourier analysis cyclic reduction

FFT	fast Fourier transform
FMAC	fused multiply-acumulate
HT	hypertransport
ILDM	intrinsically low-dimensional manifold
LDA	laser-Doppler anemometry
LES	large eddy simulation
LFC	laminar flamelet concept
LHS	left hand side
LIF	laser induced fluorescence
MKL	math kernel library
MPI	message passing interface
ODE	ordinary differential equation
OS	operating system
PDE	partial differential equation
PDF	probability density function
PIV	particle image velocimetry
RANS	Reynolds averaged Navier Stokes
RHS	right hand side
RMS	root mean square

LIST OF FIGURES

LIST OF TABLES

1 INTRODUCTION

1.1 General aspects

Combustion has been - and still is - a technical process of utmost importance. From early stages of human evolution onwards fire was controlled by mankind, mainly for the purposes of cooking and domestic heating. Today entire sectors of our economy are dependent on a stable supply of energy by means of combustion. Mobility on land and sea is provided using mainly internal combustion engines as a propulsion device. Gas turbines build the foundation for modern aviation, and are also used for the generation of electricity. Modern furnaces are used in the generation of domestic heat and hot water, as well as in various industrial thermal processing applications.

The predominance of combustion in the generation of thermal, electrical and mechanical energy is exemplarily underlined by studies of the International Energy Agency IEA (Priddle, 2008), see Fig. 1.1. According to this study, human energy demand is mainly satisfied using fossil fuels as a primary source. Fuel consumption has increased in the past, and is foreseen to further increase, especially due to the continuing economic growth of the world's emerging markets.

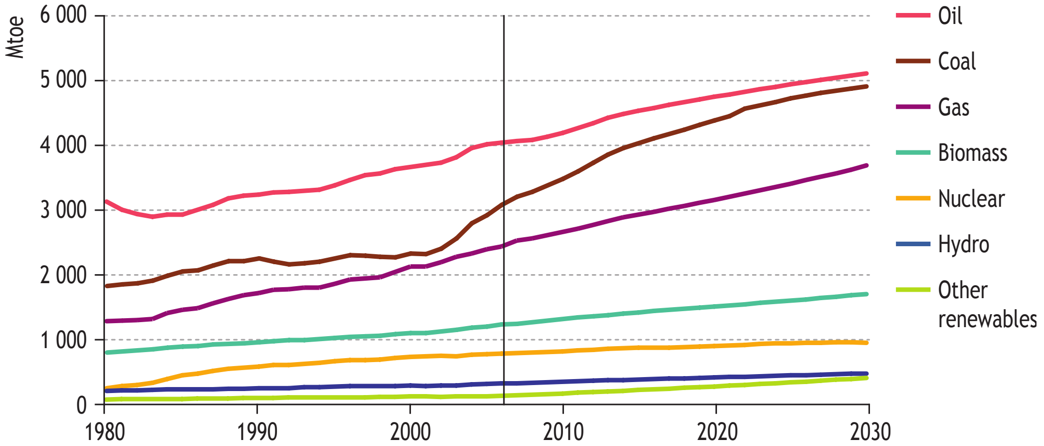

Figure 1.1: World primary energy demand by fuel type, measured in megatons of oil equivalent; history and forecast according to International Energy Agency (reference scenario, Priddle 2008)

The extensive usage of combustibles is not solely of advantage to modern society, but causes also severe problems. Supply safety is a critical issue. The mining process is often associated with pollution of the environment. Pollutants are also formed by the combustion process itself, causing damages and health hazards to flora as well as fauna. Combustion products, especially CO_2, are also discussed as being a major driver of global warming.

All the aforementioned circumstances make obvious that there is a need for further optimization of technical combustion processes. Efficiency factors have to be improved, and "clean" low-emission devices have to be developed. Using only trial and error procedures for this non-trivial task will not suffice, hence a more profound understanding of the underlying processes is crucial.

To achieve this understanding, empirical as well as theoretical research tools can be utilised. As for the empirical approach, research can be based on observations, measurements and visualizations. Various measurement principles have been applied to measure the underlying composition and flow field of a flame. Exemplarily, non-intrusive techniques like schlieren visualization, Laser-Doppler Anemometry (LDA), Particle Image Velocimetry (PIV), Laser Induced Fluorescence (LIF) and Coherent Stokes/Anti-Stokes Raman Spectroscopy (CSRS/CARS) should be noted in this context. For simple laminar flame configurations, these measurement techniques yield valuable and comprehensive results, as it has been exemplarily shown by Amantini *et al.* (2006) for a counterflow flame[*]. Also turbulent flames have been experimentally investigated into deep detail (see e.g. Muñiz & Mungal 1997, Kawanabe *et al.* 2000, Muñiz & Mungal 2001, Lyons *et al.* 2005, Barlow *et al.* 2005 and Köberl *et al.* 2010). However, for turbulent flow conditions it is difficult to resolve directly coherent structures and their interaction with chemical reactions. Statistical quantities are usually measured instead. For fully resolved information, data acquisition has to be simultaneous for velocities and concentrations, as well as continuous in time and space, i.e. in four dimensions. Most measurement techniques collect data as a function of time, but with reduced dimensionality in space. Schlieren visualizations e.g. represent a projection of density gradients into a two-dimensional plane; LDA is a pointwise measurement technique; PIV and LIF are essentially two-dimensional, although PIV can be extended to capture the out-of-plane component of the velocity. To obtain fully three-dimensional results, image reconstruction techniques like tomography are applied to measured projection data (see e.g. Heimel 2010). Nevertheless, the resolution of these results is still restricted due to a limited number of projections serving as an input[†]. Non-intrusive measurements are also limited for the measurement of flames that are sooting, e.g. in internal combustion engines. Due to a high optical thickness, the scattered laser light is usually too diffuse to obtain reasonably resolved measurements; in certain cases the laser might not even be able to adequately illuminate the measurement planes.

---

[*] A combination of PIV and LIF was used to capture flow field as well as concentrations.

[†] In principle high resolution four-dimensional data could be acquired using large arrays of synchronised high-speed cameras. In practice this approach is hardly doable as in technical devices the number of view directions is usually limited by engineering aspects. Additionally, such a setup would be exceptionally costly.

As an alternative to measurements, research might also be based on theoretical methods which are able to predict combustion phenomena by computations based on first principles. Certain reactive flows e.g. can be approximated by strongly simplified configurations, for which differential equations can be written that have analytical solutions. Clearly, this so called asymptotic analysis is restricted to very specific cases, but it is convenient in terms of hardware requirements and therefore widely used. The strength of analytical solutions is given by the fact, that parameters affecting the result can be identified directly in the solution itself. Solutions were derived for the structure and speed of laminar premixed flames, see e.g. the book of Poinsot & Veynante (2005). Also the structure of laminar diffusion flames was investigated, first by Liñán (1974), and later in more detail by Seshadri & Peters (1988). These results gave important insight into fundamental laminar flame configurations. Nevertheless, when using asymptotics, only limited information can be obtained w.r.t. turbulent flames. Asymptotic solutions of turbulent flow fields are scarce, and turbulent flame analysis is often based on embedding laminar flames in weakly perturbed flow fields. For flames in technical applications, with high turbulence levels, these solutions fail in providing a complete picture of all involved processes, hence more comprehensive methods have to be applied.

Numerical simulation can be considered as such a method. Extending the asymptotic approach, numerical simulation basically attempts to provide a most detailed mathematical description of a physical process. Solutions are obtained by discretization of the differential equations and subsequent numerical solution. Despite the complex mathematical formulation, the real world cannot be described to ultimate perfection. Numerical simulation still provides a very powerful research tool to investigate various phenomena in complex flows, e.g., the effect of gravity, which can be easily activated/deactivated in the formulation (Nichols *et al.*, 2007). By definition, numerical simulation offers the possibility to obtain fully three-dimensional information on the flow field, well resolved in time. Such detailed information is often not accessible in experiments.

Considering the fact, that the majority of technical combustion devices is operating under turbulent flow conditions, the present work is aiming at providing further insight into interactions between the flame and the underlying flow field. Based on the aforementioned considerations, numerical simulation is chosen as the main research tool for the present work. The following Sec. 1.2 shall briefly outline history and state of the art in Computational Fluid Mechanics (CFD), especially with respect to combustion. Sec. 1.3 will briefly discuss the topic of flame stabilization, which is a topic of high relevance in modern combustion research. Finally, Sec. 1.4 will outline the specific objectives for the present work.

1.2 Numerical simulation of reactive flow

When reviewing coarsely the history of CFD, a starting point can be found in the work of Richardson (1922). Long before the electronic computer was invented, Richardson already had visions of forecasting the weather by numerically solving differential equations. Clearly, at that time these ideas were just fantasies, and with a suggested "theatre" full of human computers the speed of computation was so slow that today it seems almost ironic that the word "forecast" was used. A next milestone was marked by the invention of digital/electrical computers during the second world war. In pace with the progress in available computational power for technical computations, numerical methods for fluid dynamics were developed intensively from the late 1960s on, especially in the United States at the Los Alamos (LANL) and Lawrence Livermore National Laboratories (LLNL). For a review thereof, see e.g. Johnson (1996).

When the first kinetic systems for describing chemistry became available, the development of early combustion codes began during the 1970s. The strongly nonlinear mathematical formulation of the reaction mechanisms and their numerical stiffness due to a large disparity of relevant time scales led to the development of automatic solvers for stiff Ordinary Differential Equations (ODEs)[‡]. In pace with the development of robust numerical schemes for solving the chemistry as well as the underlying flow field, early simulations of reactive flow problems could be performed, e.g. by Butler & O'Rourke (1977). Due to the comparatively limited computational power available at that time, the problems solved were still limited to simple configurations with a reduced spatial dimensionality.

The nature of turbulent fluctuating motion requires basically an unsteady, spatially three-dimensional simulation. In addition, turbulence is a multi-scale process, where kinetic energy is transferred in a cascade from big to small eddies. Thus, a comprehensive numerical description of turbulent flow has to capture the whole range of relevant scales which mostly leads to prohibitively high, since computationally unaffordable, resolution requirements. First direct computations of homogeneous turbulence in periodic boxes were performed by Orszag & Patterson (1972) using a spectral method. With a resolution of only 32 Fourier modes in each spatial direction, a Taylor microscale based Reynolds number of $\mathrm{Re}_\lambda = 35$ could be assumed. The scope of these numerical results is however limited, due to the assumption of low-intensity, isotropic turbulent motion, which in general does not apply to turbulent flow in real technical devices. Due to the lack of computational power, turbulence researchers had to investigate simpler problems governed by a mathematical formulation which requires a less costly numerical solution, or to get away with a less comprehensive averaged description of the flow. This strategy focused attention mainly on two concepts, which essentially involve mathematical formulations with a lower dimensionality: In the first approach, one investigated the early stages of instability

---

[‡] The GEAR method (Gear, 1969) and ODEPACK (Hindmarsh, 1983) should be referenced in this context.

leading to turbulence, which can be assessed using transient two-dimensional direct simulations. In the second approach, statistically averaged quantities of fully turbulent flow are simulated using moment methods such as the Reynolds Averaged Navier Stokes (RANS) formulation, where models are used to account for the effects of turbulence. Computing statistically stationary flows, the statistical mean quantities in time do not vary, and hence a full dimension can be omitted. Additionally, flow fields which exhibit a homogeneous direction allow for a further reduction of the spatial dimensionality requiring only two-dimensional simulations. Finally, in the context of RANS, a much coarser numerical resolution can be applied in comparison to model-free simulations, as the total dynamical effect of the unsteady turbulent fluctuations has to be provided by the turbulence model, so that the small-scale contributions need not to be resolved. Due to these benefits, the numerical costs could be kept within an acceptable range, so that the RANS approach has meanwhile become a well established concept especially for computing statistically steady-state, non-reacting turbulent flows.

For reacting turbulent flow, however, additional closure is required for the average reaction rates appearing in the formulation: Due to the highly nonlinear dependence of the reaction rates on temperature and species concentrations, the average reaction rates cannot be simply evaluated in terms of the scalar averages. Therefore, a combustion model has to be employed to close the formulation. Early combustion models relied on relatively restrictive assumptions. The Eddy-Break-Up (EBU) model proposed by Spalding (1971) for non-premixed combustion exemplarily assumes that the mean reaction rate is controlled by mixing, which is considered to be the rate determining factor due to infinitely fast chemistry. As an alternative approach, Pope (1985) suggested to solve for a transport equation of a velocity-composition joint Probability Density Function (PDF). In this formulation the reaction rate terms appear as closed expressions so that no closure model is required for these terms. However, the benefit of having closed chemical source terms is counteracted by the requirement to model the diffusive transport, and the increasingly high dimensionality problem when considering more complex chemistry dependent on more reactive scalars. A computationally less demanding method to model combustion was proposed in the early 1990s independently by Klimenko (1990) and Bilger (1993), the Conditional Moment Closure method (CMC). The CMC model is based on the primary assumption, that the fluctuations in the scalar quantities are linked for the most part to the fluctuations of only one, or just a few key parameters, such as the mixture fraction in the case of non-premixed combustion. The method computes the chemical source terms using conditional averages on these key parameters as scalar input quantities. The so obtained conditionally averaged source terms are significantly more accurate than their unconditional counterparts computed with unconditional mean scalar input quantities. Also the CMC model has its limitations. Modelling the reaction rate dependent on only one key quantity, important instationary effects like extinction cannot be captured. Proposals of using more than one conditioning quantity have been proven to be useful to capture extinction, but these extensions make the model more complex w.r.t. the mapping between the conditioning space and the physical space and they lead to excessively high computational costs.

The calibration of RANS models is often very case dependent, as they include by definition the modelling of the large-scale fluctuations, which may vary considerably from flow to flow. This conceptual limitation is not the case with the alternative method of Large Eddy Simulation (LES), which resolves directly the turbulent fluctuating large-scale structures, so that only the unresolved fluctuations on smaller time and length scales need to be modelled. These small-scale fluctuations tend to be more isotropic and are easier to model, which reduces the uncertainties introduced by the turbulence model. The improved accuracy in capturing the velocity fluctuations also translates into a better description of the instantaneous local mixing and thermal conditions, which provides highly valuable inputs into the modelling of the reactive source terms. Using LES, the predictions of the combustion models could be significantly improved, but the demand in computational resources also increased by an order of magnitude. LES requires by definition a spatially three-dimensional, unsteady simulation to capture the instationary three-dimensional large-scale structures of turbulence, and resolution has to be much finer in comparison to RANS as well.

In pace with the rapid development of supercomputers, and therefore advanced capabilities to resolve three-dimensional turbulent reacting flow directly, "model-free" simulations (Givi, 1989) have been gaining popularity since the 1990s. The term model-free essentially refers here to the concept of Direct Numerical Simulation (DNS) of turbulent flows, which implies that no turbulence model is employed[§], and therefore the turbulent flow structures should be ideally resolved down to the smallest (Kolmogorov) scales. Dealing with turbulent combustion, a still unfeasible computational effort excludes the same detailed and comprehensive level of the description for the chemistry, so that strongly reduced kinetic mechanisms are used. Since a reduced chemical mechanism involving only a few basic reactions essentially represents a simplified model of the full reactive process, the term "model-free" does certainly not apply in a strict sense to the numerical description used for the chemistry. First model-free computations were performed for generic flow configurations of mainly academic interest. Swaminathan *et al.* (1996), e.g., carried out a DNS of turbulent non-premixed combustion in a periodic box. Using a mesh consisting of 128 cells in each direction, extinction phenomena in isotropic turbulence could be investigated. The main assumptions in this study were the use of a reduced four-step mechanism for the chemistry, and constant density, thus neglecting the effect of volumetric dilatation. Carrying out a DNS of a turbulent reacting jet at a jet-exit Reynolds number of $\mathrm{Re} = 4000$, Boersma (1999) performed one of the first computations of a reacting, turbulent and three-dimensional configuration which comes close to experimentally realizable laboratory flames. The effect of volumetric dilatation was included in this study, and a one-step binary reaction mechanism was assumed for the chemistry. Another cutting-edge simulation was carried out by Mizobuchi *et al.* (2002) who performed a DNS of a lifted

---

[§] Although Givi (1989) considers LES as "model-free", this viewpoint is not adopted in this work.

hydrogen jet. They assumed a jet-exit Reynolds number of Re = 13600, and used more than 22 million grid points. They applied a very detailed hydrogen-air mechanism involving seventeen elementary reactions and nine species proposed by Westbrook (1982). In a follow-up work the simulation was repeated on a refined grid with 200 million gridpoints (Mizobuchi *et al.*, 2004). The study is also in the review by Westbrook *et al.* (2005). The most comprehensive and detailed "model-free" combustion simulations to date can be found in the works of Yoo *et al.* (2009) and Lu *et al.* (2010), where 940 million grid points have been used. A twenty-one-steps hydrogen-air reaction mechanism developed by Li *et al.* (2004) was applied.

Along with the model-free simulations significant progress in the modelling of turbulent combustion has been made as well. Simple models like the EBU are implemented in commercial CFD codes, and used in the everyday work of CFD engineers. The predictive capability of the combustion models could be continuously improved, especially when simulating the underlying turbulent flow with LES. The advancements can be seen from various computational studies, e.g. from the LES of a reacting turbulent jet flame by Steiner & Bushe (2001), or the LES of a Pratt & Whitney gas turbine combustor by Moin & Apte (2006).

All application examples given above for DNS, and also for the computationally less but still expensive LES, emphasize the important role of the increase in computational power. The capacities of the available hardware have been tremendously extended in the past, and this rapid development is expected to continue in the next future. Therefore, when considering the applications outlined above, it is foreseeable that DNS will become a more and more viable computational tool for basic research on turbulent reactive flows. With the possibility of doing large numerical simulations, the considered configurations have become close enough to laboratory flame conditions, which makes a comparison against experimental data possible for selected cases. Using the advantages of highly resolved numerical simulations in combination with validations against experiments opens new possibilities to investigate the turbulent reactive processes in much detail in the further research.

The review given here is not complete in a sense that computational research of combustion clearly includes many more applications than those addressed above. To give a better understanding of the present simulation capabilities and the specific challenges, it was intended to illustrate preferably the developments related to the topic of the present work.

1.3 Dynamics near the flame base and flame stabilization

Technical combustion devices are generally designed for a limited range of operation. In a perfect scenario, these devices should be steadily operated in this defined range, otherwise undesirable, often hazardous, conditions might arise. For example, the flame in a jet-engine combustor can be blown-off, or flash back from its stable burning position. In the case of gas-fuelled domestic hot water systems, an unnoticed flame extinction can lead to an accumulation of explosive gas mixtures in closed rooms. Flames have to be controlled and stabilized to ensure a reliable and save operation of the devices.

Non-premixed flames can be stabilized in different ways. Jet flames are usually distinguished into the two classes of nozzle-attached, and lifted jet flames. Unless stabilized by swirl or high-temperature coflow, nozzle attached flames appear only for low jet-exit velocities, so that the flow in general remains laminar. This configuration typically features a strong volumetric dilatation near the stoichiometric surface inside the initial shear layer, which attenuates the mixing of fuel and oxidizer, and hence leads to comparatively low conversion rates and extended flame-lengths. Due to these usually undesired features, nozzle attached jet flames are only of minor relevance for practical applications.

In contrast, lifted jet flames exhibit notably increased conversion rates due to mixing of fuel and oxidizer upstream of the flame. They also cause lower thermal loads on the nozzle, extending the material life time. Therefore, lifted flames are widely used in practical engineering applications, such as furnaces and engines. For an efficient and fast design process of these devices, it would be desirable to determine the lift-off heights of turbulent jet flames already a-priorily. Even more important, the burning conditions in these devices must be sufficiently controlled to achieve a well balanced operation characteristics. If this is not possible, undesired effects like strong flame oscillations, large-volume extinction or reignition, sudden blow-off and/or flashback might occur, which can damage or even destroy the whole system. The controlling parameters are usually determined by the dynamics at the flame base. For this reason, a profound knowledge about the behaviour of the flame base w.r.t. the incoming flow and mixing conditions is crucial.

Early measurements on the lift-off heights of jet flames were performed by Vanquickenborne & van Tiggelen (1966). They contended, based on their observations, that a fully premixed stoichiometric composition is found at the base of the lifted flame, and that the flame stabilizes at a downstream position, where the mean flow velocity is equal to some turbulent flame speed s_T. The relatively (to the laminar flame speed s_L) higher turbulent flame speed essentially reflects the increased flame surface area due to turbulent wrinkling. Kalghatgi (1981) contended in his experiments, that this turbulent flame speed is higher the higher the turbulence levels are, so that the flame can stably burn in regions with higher oncoming velocities. This hypothesis, which is essentially based on premixed flame propagation into a uniform stoichiometric mixture certainly conflicts with the mostly inhomogeneous flow and mixing conditions occurring in the vicinity of a lifted jet flame. A further eventual deficit may arise from the assumption that the increased flame propagation speed is mainly due to turbulence even under weakly turbulent flow conditions. As an alternative, Peters & Williams (1983) proposed that the lift-off is rather determined by the extinction of non-premixed diffusion flamelets. They argued that the scalar dissipation rate near the nozzle significantly exceeds the limit of extinction. In conclusion the flame can stably burn only further downstream, where the local scalar dissipation rate has fallen well below the extinction limit. This alternative explanation, which is derived from non-premixed flame analysis, could not be fully confirmed by experiments. The measured scalar dissipation rates, though two-dimensional, lie for the most part considerably below the extinction limit also in the region ahead of the flame base (Su *et al.*, 2006). Both hypotheses, the premixed as well as the non-premixed flame based, can evidently not exclusively explain the mechanisms of flame stabilization. The real physical explanation will be found somewhere in between.

Owing to the advancements in non-intrusive laser diagnostics, the stabilization mechanisms of lifted jet flames have been researched in more detail during the past two decades, e.g. by Muñiz & Mungal (1997), Won *et al.* (2002), Mansour (2003), Upatnieks *et al.* (2004), and Su *et al.* (2006). Various computational studies have been done on this subject as well, see, e.g., the work of Ruetsch *et al.* (1995), Nichols & Schmid (2008), and Lu *et al.* (2010).

In these works the dynamic and thermal conditions imposed at the inflow may vary considerably, so that the stabilization of the flames can also be governed by physically different mechanisms. This distinction applies especially to studies with rather artificial parameter settings. Lu *et al.* (2010) e.g. performed DNS of a high-speed hydrogen jet in a heated oxidizer coflow at 1100 $[K]$, which is well above the autoignition temperature of hydrogen. The mechanism which determines the lift-off height of the flame was found to be controlled by chemistry in terms of a time lag in autoignition. Won *et al.* (2002) experimentally investigated a highly buoyant, laminar jet flame at a low jet-exit Froude number of $\mathrm{Fr} \approx 2 \cdot 10^{-3}$ in both normal- and micro-gravity. For their parameter setting, they found that buoyancy was the single cause for the lift-off of the flame.

The experimentally measured laboratory jet flames of Muñiz & Mungal (1997), Mansour (2003), Upatnieks *et al.* (2004), and Su *et al.* (2006) consider more general parameter settings of naturally stabilized laboratory jet flames. In these studies the lift-off cannot be exclusively attributed to one single reason like in the work of Won *et al.* (2002), which is predominated by buoyancy. Muñiz & Mungal (1997) performed PIV measurements of the velocity field upstream of the flame base. The flame base was identified by the position, where the glycerol-water seeding evaporated, which presumably occurs at a temperature of 100 $[^\circ C]$. The measurements basically support the model of Vanquickenborne & van Tiggelen (1966). However, concerning the sensitivity of the (turbulent) flame propagation speed s_T to the turbulence level notable disagreement with the results of Kalghatgi (1981) was found. The turbulent flame propagation speed s_T appeared to be independent of the turbulence level. Consequently, Muñiz & Mungal (1997) argued that the flame propagates in an almost laminar mode. The fact that the local flow velocities in front of the flame base exceeds the laminar burning velocity s_L was rather attributed to the redirection of the flow approaching the leading edge of the flame, as shown by Ruetsch *et al.* (1995).

Mansour (2003) carried out lifted methane-air jet experiments, where the mixture fraction as well as the OH and $\mathrm{C_2H}_x$ radical concentrations were measured using Rayleigh scattering and LIF. His experimental observations confirmed the premixed flame propagation as the dominant stabilization mechanism, as originally suggested by Vanquickenborne & van Tiggelen (1966). At the same time, Mansour (2003) attributed only minor importance to extinction of non-premixed diffusion flamelets for the lift-off. Both the studies of Muñiz & Mungal (1997) and Mansour (2003) claim that triple flame structures could be observed in their data. The occurrence of this particular structure typical for lifted flames was experimentally attested first by Phillips (1965), and later numerically investigated in detail by Ruetsch *et al.* (1995). However, due to the limitations of the measurement techniques and comparatively weak raw signals it is mostly very difficult to clearly discern a separated reaction branch on the lean or rich side.

Upatnieks *et al.* (2004) performed cinema-PIV of a methane-air jet flame. The flame base was identified at the location, where the concentration of the ceramic seeding particles exhibited half the value of the cold inflow, which corresponds to the iso-contour of temperature at $T = 600\ [K]$. Similar to Muñiz & Mungal (1997), their results show that the flame propagation is only insignificantly affected by the local turbulence level. They further contend that the dilatational effects of the leading edge flame impedes the incoming eddies from penetrating into the reactive layers. Like Muñiz & Mungal (1997), they observe a redirection of the flow in the cross-stream direction ahead of the flame base, which creates a low-velocity zone upstream of the flame. They also provide an analytical description for the observed stagnation-point flow conditions based on a potential flow solution, where the leading edge of the flame is regarded as a point source of mass and momentum.

Very comprehensive measurements on lifted methane-air laboratory jet flames were carried out by Su *et al.* (2006), who measured both mixture fraction and velocities using LIF and PIV. The base of the flame was identified by the leading edge of the 100 $[°C]$ contour. Similar to the preceding studies, they found that the scalar dissipation rate, which governs the extinction of non-premixed diffusion flamelets, falls below the quenching limit considerably ahead of the lifted flame. Again, the flame appeared to stabilize at a position, where the local flow velocity is closely higher than the laminar flame speed s_L. Su *et al.* (2006) propose a simple model of flame stabilization, where the motion of the flame is essentially governed by the large-scale mixing structures which periodically pass the flame base. Thereby, as long as flammable mixtures are found, the flame preferentially stabilizes towards the radially outer region, where the streamwise velocity is lower.

In summary, the studies of the present survey commonly identify the premixed flame propagation as dominant stabilization mechanism. Despite the generally accepted theory, some uncertainties and/or open questions still remain. The present work attempts to highlight some of these issues. In particular, the focus is on the influence of the flame on the flow and mixing field upstream, the effect of buoyancy-induced large-scale motion, and the relevance and eventual impact of three-dimensional (out-of-the-plane) effects in the flame stabilization process. These issues have thus far not been satisfactorily addressed in most previous studies. This is partly due to a limited experimental access, partly due to the consideration of turbulent reacting flow regimes, where these issues can be a-priorily neglected. The present work is devoted to shed some light on these topics by performing numerical simulations of a strongly buoyant non-premixed reacting jet as well as a non-reacting reference jet.

1.4 Objectives & thesis outline

Based on a DNS of a strongly buoyant lifted reacting methane-air jet the present work attempts to investigate

- The effects of the flame on the near field of the jet ahead of the flame. The spreading and decaying behaviour of the fuel jet is here of particular interest. It shall be investigated, if the generally suggested full resemblance to the non-reacting case also applies without restrictions to the considered reacting turbulent jet with a comparatively low Reynolds number.
- The effects of the buoyancy-driven large-scale motion on the temporal evolution of the flow field. Being essentially generated by the reactive heat release the investigated large-scale structures are strongly coupled with the behaviour of the flame, so that a significant influence on the flame stabilization has to be expected as well.
- The dominant mechanisms for the stabilization of the flame at a certain lift-off height. The present study considers a methane/air jet, where the fuel feed is considerably diluted with nitrogen to make the flame highly sensitive to perturbations coming from upstream, as it could be seen from experiments carried out for reference. This setting shall provide sufficiently critical burning conditions, where the dominant effects for the flame stabilization can be very clearly identified.

The thesis is divided into seven main chapters. Following the introduction in Chp. 1, the mathematical description of reacting flow is presented in Chp. 2. The governing conservation equations, as well as those for the chemistry are given. The non-dimensionalization of the conservation equations as well as the physical behaviour of the transport coefficients are discussed.

Chp. 3 discusses the basic features of turbulent reacting flows. The statistical approach which is widely used for the description of (non-reacting) turbulence is explained first, and characteristic length and time scales for chemically inert turbulent flow are presented. Thereafter, definitions of important quantities for the description of reacting flow, like the mixture fraction, are given. Based on the parametrization of the flame different regimes of turbulent combustion are distinguished, which may be relevant for the presently considered lifted jet flame.

To estimate the resolution requirements for the three-dimensional computations, but also to derive valuable initialization data, numerical simulations of two simple, but canonical one-dimensional flame configurations are performed in Chp. 4. An unstrained, premixed plug-flow flame, and a strained counterflow diffusion flame are analyzed, to obtain the desired information for the premixed as well as for the non-premixed case, respectively.

Chp. 5 describes in detail the numerical methodology of the present DNS. The individual algorithms and solution concepts are illustrated, including the Dynamically Thickened Flame approach (DTF). The imposed Boundary Conditions (BCs) are described in detail as well.

The simulation results obtained for the considered reacting jet as well as for a non-reacting reference jet are presented and discussed in Chp. 6. To identify eventual upstream effects of the flame, mean and fluctuating quantities are compared against those of the non-reacting reference jet, and validated against experiments. Transient effects of buoyancy are investigated by analyzing qualitatively and quantitatively the large-scale behaviour of the reacting flow field. In a further subsection, the governing flame stabilization mechanism is determined from an analysis of the local flow and mixing conditions directly at the base of the lifted flame. A special focus is put on buoyancy-induced three-dimensional structures which might considerably affect the stabilization of the flame.

Conclusions will be given in Chp. 7.

Due to the comparatively expensive nature of DNS, this work had to meet extensive hardware requirements. Appendix A gives a brief overview of the hardware used, which was partly assembled in the course of the present work.

2 MATHEMATICAL FORMULATION

The present chapter serves to describe a mathematical formulation for reacting flow in gaseous phase, which can be later transferred into a numerical scheme. The governing equations are subdivided into the conservation equations for mass, momentum and material on the one hand, and the formulations for the chemical reaction mechanism on the other hand. Thermophysical properties appear in both of these groups, therefore methods for their estimation are also addressed in this chapter. Finally, it is briefly shown, how these equations can be transformed into a non-dimensional form, which facilitates the physical understanding of the individual relevant mechanisms by introducing characteristic parameters such as the well known Reynolds number.

Several assumptions are made when deriving the governing equations. They are summarised in the following list, and will be addressed in detail later in the respective parts of this section.

- Fick's law is considered to be valid for the diffusive mass transfer
- Equal diffusivities are assumed for all reactive scalars
- The Soret and Dufour effects are neglected
- Radiation is neglected
- The gas is considered to be incompressible (low Mach number flow)
- Perfect gas behaviour is assumed for all components

2.1 Conservation equations

Many physical phenomena are described based on the principle of the conservation of a certain quantity. For fluid flow, these conserved quantities are mass, momentum, species concentration, and energy.

2.1.1 Mass

In classical mechanics mass can neither be produced nor destroyed. Thus, the temporal change of of mass in a finite volume must be balanced by the net fluxes across the surface of the volume. In a mathematical formulation we write

$$\int_V \frac{\partial \rho}{\partial t} dV = -\int_S \rho\, \mathbf{u} \cdot \mathbf{n}\, dS\,, \tag{2.1}$$

where ρ represents the fluid density, $\mathbf{u}$ is the velocity vector and $\mathbf{n}$ the cell-normal unit vector. By applying Gauss' theorem, we can transform Eq. (2.1) to the differential form of the continuity equation

$$\frac{\partial \rho}{\partial t} + \boldsymbol{\nabla} \cdot (\rho\, \mathbf{u}) = 0\,, \tag{2.2}$$

where $\boldsymbol{\nabla}$ represents the vector of spatial derivatives.

2.1.2 Momentum

In analogy to mass conservation, the momentum conservation can be derived from a finite volume consideration. Applying Newton's second law to fluid motion, the temporal change of momentum within a volume, including the momentum fluxes across its surface must be balanced by external surface and body forces. This balance is written as

$$\int_V \frac{\partial \rho\, \mathbf{u}}{\partial t} dV + \int_S \rho\, \mathbf{u}\, \mathbf{u} \cdot \mathbf{n}\, dS = \int_S \boldsymbol{\sigma} \cdot \mathbf{n}\, dS + \int_V \rho\, \mathbf{f}^B dV\,, \tag{2.3}$$

where $\boldsymbol{\sigma}$ is the stress tensor, and $\mathbf{f}^B$ denote the body forces. Decomposing the surface forces into pressure and viscous friction, assuming gravitational forces as the only body forces, and applying Gauss' theorem again, we obtain the following differential form of the momentum equation

$$\frac{\partial \rho\, \mathbf{u}}{\partial t} + \boldsymbol{\nabla} \cdot (\rho\, \mathbf{u}\, \mathbf{u}) = -\boldsymbol{\nabla} p + \boldsymbol{\nabla}\, \boldsymbol{\tau} + \rho\, \mathbf{g}\,, \tag{2.4}$$

where p denotes the pressure, $\boldsymbol{\tau}$ is the viscous stress tensor and $\mathbf{g}$ is the gravitational acceleration vector. Assuming a Newtonian fluid and Stokes hypothesis, the viscous stress tensor $\boldsymbol{\tau}$ can be expressed as

$$\boldsymbol{\tau} = 2\mu \left(\mathbf{S} - \frac{1}{3} \mathbf{I} \boldsymbol{\nabla} \cdot \mathbf{u} \right)\,. \tag{2.5}$$

Here, μ denotes the dynamic viscosity, $\mathbf{S} = 1/2\left[\boldsymbol{\nabla}\mathbf{u} + (\boldsymbol{\nabla}\mathbf{u})^T\right]$ is the rate of strain tensor, and $\mathbf{I}$ is the identity matrix. Finally we get

$$\frac{\partial \rho\,\mathbf{u}}{\partial t} + \boldsymbol{\nabla}\cdot(\rho\,\mathbf{u}\,\mathbf{u}) = -\boldsymbol{\nabla}\,p + \boldsymbol{\nabla}\left[2\mu\left(\mathbf{S} - \frac{1}{3}\mathbf{I}\,\boldsymbol{\nabla}\cdot\mathbf{u}\right)\right] + \rho\,\mathbf{g}\,. \tag{2.6}$$

In accordance with standard literature, Eq. (2.2) combined with Eq. (2.6) will be henceforth referred to as the Navier-Stokes equations. For non-reactive constant density flows, the Navier-Stokes equations are already sufficient to solve for the primitive variables $\mathbf{u}$ and p.

2.1.3 Species

In reactive flows the spatial position of the reactive layers, as well as the reaction rate are strongly dependent on the local chemical composition (mixture) of the fluid. The composition is usually measured in terms of species concentrations, which are commonly expressed as fractions of molar, volumetric or mass quantities. In the present work, we choose mass fractions Y_P to represent the composition of the flow field. For any species P, the mass fraction $Y_P = m_P/m_{\text{tot}}$ is given as a ratio of the species mass relative to the total mass. By definition, these mass fractions add up to

$$\sum_P Y_P = \sum_P m_P/m_{\text{tot}} = 1\;. \tag{2.7}$$

Similar to the conservation of total mass m in Sec. 2.1.1*, a conservation equation can be derived for the mass fractions m_P of the species P. However, unlike the case for the total mass, two additional effects have to be considered: Firstly, species is not only advected by the underlying flow, it is also transported by diffusion. Hence, an additional diffusive drift velocity $\mathbf{V}_P$ has to be included in the formulation. Secondly, species mass fractions can be created and destroyed by chemical reactions, therefore a corresponding source term $\dot{\Omega}_P$ has to be added to the conservation equation. Accounting for these additional transport and source terms, the conservation of a species P for a finite volume reads

$$\int_V \frac{\partial \rho Y_P}{\partial t}\,dV = -\int_S \rho\,Y_P\,(\mathbf{u} + \mathbf{V}_P)\cdot\mathbf{n}\,dS + \int_V \dot{\Omega}_P\,dV\;. \tag{2.8}$$

Applying the divergence theorem once again, and reordering of the terms gives the differential form of the mass conservation equation

$$\frac{\partial \rho\,Y_P}{\partial t} + \boldsymbol{\nabla}\cdot(\rho\,\mathbf{u}Y_P) = -\boldsymbol{\nabla}\cdot(\rho\,\mathbf{V}_P Y_P) + \rho\,\dot{\Omega}_P\;. \tag{2.9}$$

---

*where the mass is represented by the density ρ.

As all mass fractions add up to unity, the continuity Eq. (2.2) must be recovered by summing Eq. (2.9) over all species $P^{\dagger}$. This consistency condition requires

$$\sum_P \dot{\Omega}_P = 0 \quad \text{and} \quad \sum_P \mathbf{V}_P Y_P = 0\,. \tag{2.10}$$

The first requirement is due to the fact, that the total mass cannot be changed by reactions. The second condition imposes a side condition on the modelling of the diffusion velocities $\mathbf{V}_P$ in Eq. (2.9). A rigorous determination of these velocities is a computationally arduous task even when neglecting the Soret effect‡. A fully detailed computation would require to solve linear systems of size N^2 at each instant of time at each point of the spatial domain, where N is the number of transported species (Poinsot & Veynante, 2005). Since this detailed approach is computationally too costly, especially for DNS, simpler models are often used. The simplification is mostly based on the assumption of a binary-type diffusion for all species, and Fick's law of diffusion

$$\mathbf{V}_P\, Y_P = -\mathcal{D}_P\, \boldsymbol{\nabla}\, Y_P \tag{2.11}$$

is used for all species (Kuo, 1986). This assumption is reviewed later in this work, when the thermal properties (Sec. 2.2) and the employed chemical mechanism (Sec. 2.3) are discussed. Substituting Eq. (2.11) into Eq. (2.9), the conservation equation for Y_P can be written as

$$\frac{\partial \rho\, Y_P}{\partial t} + \boldsymbol{\nabla}\cdot(\rho\,\mathbf{u} Y_P) = \boldsymbol{\nabla}\cdot(\rho \mathcal{D}_P\, \boldsymbol{\nabla}\, Y_P) + \rho\, \dot{\Omega}_P\,. \tag{2.12}$$

Note that the second condition in Eq. (2.10) holds only for uniform diffusion coefficients $\mathcal{D}_P$. If this is not the case, an additional correction velocity has to be added to the advective velocity $\mathbf{u}$, as shown in the book of Poinsot & Veynante (2005).

2.1.4 Energy

Dependent on the specification of the variable for the conserved energy, several different formulations for the conservation of energy can be derived. In a strict physical sense, only the total energy defined as a sum of chemical, mechanical and thermal ("internal") energy is conserved. However, in fluid mechanics it is common to introduce a balance equation for the sum of internal ($\rho\, e$) plus mechanical energy ($\rho\, \|\mathbf{u}\|^2 / 2$), written as

$$\frac{\partial \left(\rho\, e + \frac{1}{2}\rho\, \|\mathbf{u}\|^2\right)}{\partial t} + \boldsymbol{\nabla}\cdot\left(\rho\,\mathbf{u}\, e + \frac{1}{2}\rho\mathbf{u}\, \|\mathbf{u}\|^2\right) = \boldsymbol{\nabla}\cdot(\boldsymbol{\sigma}\cdot\mathbf{u}) - \boldsymbol{\nabla}\cdot\mathbf{q} + \rho\,\mathbf{u}\cdot\mathbf{f}^B + \dot{\mathcal{Q}} \tag{2.13}$$

---

†This is easily shown by comparing the terms on the LHS of both equations.

‡Diffusion of mass due to temperature gradients.

Here, the terms represent from left to right: the temporal and the advective change in energy, the work done by mechanical surface forces, the heat flux, the work done by volumetric body forces, and a heat source term $\dot{Q}$. Clearly, similar to the aforementioned cases, Eq. (2.13) can be derived from a finite volume, see e.g. the book of Kuo (1986). Taking the scalar product of the momentum equation with $\mathbf{u}$, and subtracting the result from Eq. (2.13), we obtain a transport equation for the internal specific energy only

$$\frac{\partial \rho\, e}{\partial t} + \boldsymbol{\nabla} \cdot \rho\, \mathbf{u}\, e = \boldsymbol{\sigma} : \boldsymbol{\nabla} \mathbf{u} - \boldsymbol{\nabla} \cdot \mathbf{q} + \dot{Q}\,. \tag{2.14}$$

The surface stress tensor $\boldsymbol{\sigma}$ can be decomposed into pressure p and viscous stress $\boldsymbol{\tau}$

$$\boldsymbol{\sigma} = \boldsymbol{\tau} - p\,\mathbf{I}\,, \tag{2.15}$$

where the pressure is defined as one third of the first invariant of $\boldsymbol{\sigma}$. Using this decomposition and the relation between energy and enthalpy $h = e + p/\rho$ Eq. (2.14) can be recast into a transport equation for enthalpy

$$\frac{\partial \rho\, h}{\partial t} + \boldsymbol{\nabla} \cdot \rho\, \mathbf{u} h = \frac{\partial p}{\partial t} + \mathbf{u} \cdot \boldsymbol{\nabla} p + \boldsymbol{\tau} : \boldsymbol{\nabla} \mathbf{u} - \boldsymbol{\nabla} \cdot \mathbf{q} + \dot{Q}\,. \tag{2.16}$$

Finally, introducing the relation between enthalpy and temperature $\partial h = c_p \partial T$, where c_p denotes the specific heat at constant pressure, the conservation equation can be rewritten in a differential equation for the temperature, which is convenient for CFD implementations:

$$c_p \left(\frac{\partial \rho\, T}{\partial t} + \boldsymbol{\nabla} \cdot \rho\, \mathbf{u} T \right) = \frac{\partial p}{\partial t} + \mathbf{u} \cdot \boldsymbol{\nabla} p + \boldsymbol{\tau} : \boldsymbol{\nabla} \mathbf{u} - \boldsymbol{\nabla} \cdot \mathbf{q} + \dot{Q}\,. \tag{2.17}$$

The first three terms on the RHS, representing the work of the pressure forces and viscous dissipation of mechanical energy, can be neglected here due to the assumption of low Mach number flow. The heat flux can be expressed using

$$\mathbf{q} = -\lambda \boldsymbol{\nabla} T + \rho \sum_{P} h_P Y_P \mathbf{V}_P\,. \tag{2.18}$$

The first term represents Fourier's law, where λ denotes the thermal conductivity. The second term represents the transport of enthalpy h caused by concentration gradients (Dufour effect). As this contribution can be usually considered negligible, it is neglected throughout the further work.

The heat source term $\dot{Q} = \dot{Q}_{\text{rad}} + \dot{Q}_{\text{react}}$ accounts for two processes: Heat transfer due to radiation, and heat release by chemical reactions. For the former, two types of radiation can be distinguished. Solid body radiation, which can be described by the laws of Planck and Boltzmann, occurs e.g. in the presence of soot particles. In the present work, which considers only soot-free cases of gas phase combustion, this type of radiation is neglected. The second type of radiation, the gas radiation is by far weaker than its solid counterpart due to the discrete emission spectra of radiating gases. For methane, which is a simple structured fuel, the number of emitting bands is comparably limited. This circumstance also holds true for most of its decomposition products. In the present case, where air is used as oxidizer[§], radiating intermediate and product species are additionally highly diluted, hence gas emission is also neglected. For the reactive heat release term $\dot{\mathcal{Q}}_{\mathrm{react}}$, an expression can be given as a linear combination of the species conversion rates $\dot{\Omega}_P$

$$\dot{\mathcal{Q}}_{\mathrm{react}} = \rho \sum_P \Delta h^0_{F,P}\, \dot{\Omega}_P \, . \tag{2.19}$$

Here, $\Delta h^0_{F,P}$ denotes the specific enthalpy of formation of a species P at standard conditions (101.3 [kPa], 298.15 [K]).

Using the low Mach number assumption, together with the relations for the heat flux (Eq. 2.18) and the heat source term (Eq. 2.19), Eq. (2.17) can be finally expressed as

$$\frac{\partial \rho T}{\partial t} + \nabla \cdot (\rho \mathbf{u} T) = \frac{1}{c_p} \nabla \cdot (\lambda \nabla T) + \frac{\rho}{c_p} \sum_P \Delta h^0_{F,P}\, \dot{\Omega}_P \, . \tag{2.20}$$

2.2 Thermophysical properties & transfer coefficients

The solution of the considered conservation equations requires the determination of thermophysical properties and transfer coefficients. In particular, the specific heat c_p and the transfer coefficients μ, λ and $\mathcal{D}_P$, which are used to model the diffusive fluxes of momentum, thermal energy and mass fractions, respectively, have to be prescribed. The density ρ is obtained from the thermal equation of state.

2.2.1 Density

The thermal equation of state generally reads $\rho = f(p, T)$. Considering an ideal gas, the ideal gas law

$$p \frac{1}{\rho} = \frac{RT}{W} \tag{2.21}$$

can be used. Here, $R = 8314\ [J/kmol\, K]$ is the universal gas constant, and W is the molecular weight in $[kg/kmol]$. The assumption of ideal gas is justified for the combustion of methane, especially when ambient air is used as oxidizer. Water vapour, which is basically most likely to show real gas behaviour, is only produced at high temperatures. Additionally, due to the high fraction of inert nitrogen contained in air, the partial pressure of the water vapour remains comparatively small.

[§] Air consists mainly (76% by mass) of the non-radiating nitrogen N_2, which is also conserved (inert) in the combustion process.

The molecular weight of a multi-component mixture is given as $W^{-1} = \sum_P Y_P/W_P$. Using this relation Eq. (2.21) can be rewritten to give the density as

$$\rho = \frac{p}{RT \sum_P \frac{Y_P}{W_P}} \,. \tag{2.22}$$

2.2.2 Specific heat

Whenever heat is added to a system, the temperature is changed depending on the conditions under which the heat has been added. For constant pressure systems, which are relevant in the present case, this circumstance can be expressed in terms of the change in enthalpy, written as

$$dh = c_p \, dT \;, \tag{2.23}$$

where c_p represents the specific heat coefficient for constant pressure. Generally, c_p is a nonlinear function of the temperature. For the most gases, these functions are similar in that there exist two regions, where c_p is only a slow function of temperature, with a strong increase in between, as can be seen from Fig. 2.1.

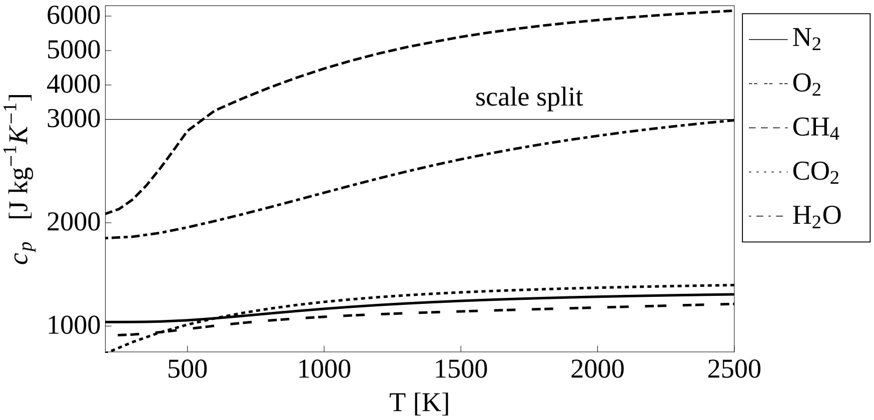

Figure 2.1: Specific heat of selected species as a function of temperature.

To prescribe values for the specific heat c_p various proposals have been given in literature. Values can be measured experimentally, or computed with the help of statistical thermodynamics. For a fit to experimental data, NASA polynomials can be used, which provide c_p values using two polynomials of fourth order (Burcat, 1984). Data fitting representations using more than 2 polynomials have been provided as well, see e.g. Rohsenow *et al.* (1998). Rather than using such polynomial fits, the present work determines the c_p values by a linear interpolation of the comprehensive data given in the JANAF thermochemical tables (Chase, 1998).

For mixtures, the specific heat can be simply obtained from a linear combination weighted with the mass fractions

$$c_p = \sum_P c_{p,P} Y_P \, . \tag{2.24}$$

2.2.3 Viscosity

The computation of the shear stresses according to Eq. (2.5) requires the prescription of the dynamic viscosity μ. The viscosity μ can be either measured, or computed based on the kinetic gas theory, which yields for an ideal gas

$$\mu = 2.6693 \cdot 10^{-6} \frac{\sqrt{WT}}{\sigma^2 \Omega^\mu (T)} \, . \tag{2.25}$$

Here σ is the assumed hard-sphere diameter in [Å], which is an empirical quantity, and $\Omega^\mu (T)$ is the collision integral for viscosity. Values for σ, as well as models for the collision integral can be found, e.g., in the book of Poling *et al.* (2001). As seen from Eq. (2.25), the dynamic viscosity is independent of pressure, but approximately proportional to the square root of temperature[¶]. This dependence is exemplarily illustrated in Fig. 2.2 a, where the viscosity is plotted vs. the temperature for selected species of relevance to the present work.

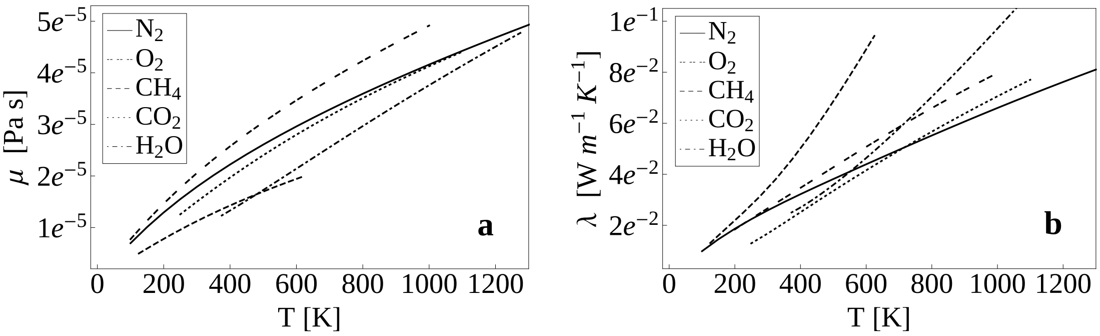

Figure 2.2: **a** Viscosity and **b** thermal conductivity of selected species as a function of temperature. Data taken from the NIST Chemistry WebBook.

For mixtures of gases, the viscosity does in general not depend linearly on the mass fractions of the components (Poling *et al.*, 2001, Chp. 9). The book of Warnatz *et al.* (2001) therefore proposes to use a simple, empirical mixing law, written as

$$\mu(Y_P, T) = \frac{1}{2} \left[W \sum_P \frac{Y_P \, \mu_P(T)}{W_P} + \left(W \sum_P \frac{Y_P}{W_P \, \mu_P(T)} \right)^{-1} \right] , \tag{2.26}$$

which is very convenient for a numerical evaluation.

[¶] Approximately because the collision integral is a function of temperature, too.

2.2.4 Thermal conductivity

Similarly to the viscosity for the viscous flux of momentum, the thermal conductivity λ needs to be prescribed to compute the heat fluxes according to Fourier's law (Eq. 2.18). Again, the thermal conductivity λ can be either measured or computed, e.g., using the modified Eucken correlation

$$\lambda = \mu \left(c_p - \frac{R}{W} \right) \left(1.32 + \frac{1.77}{W c_p / R - 1} \right) . \tag{2.27}$$

It can be clearly seen from this correlation, that the thermal conductivity is roughly proportional to the dynamic viscosity. However, due to the temperature dependence of the specific heat c_p occurring in Eq. (2.27) as well, the conductivity does not scale with the square root of temperature, so that λ increases faster with T than the viscosity μ.

In previous DNS of reactive flows, conductivity has been prescribed using various models. These range from assuming a constant conductivity in the simplest case, over the assumption of a exponential dependence on temperature in the form $\lambda = \lambda_0 \cdot (T/T_0)^{\alpha}$, to complex kinetic formulations. In the present work, the conductivity of pure gases is obtained from a linear interpolation of the tabulated data given in the NIST Chemistry WebBook. The thermal conductivity for selected species is exemplarily illustrated in Fig. 2.2 b.

For mixtures, Warnatz *et al.* (2001) suggest an analogous law to Eq. (2.26) written as

$$\lambda(Y_P, T) = \frac{1}{2} \left[W \sum_P \frac{Y_P \, \lambda_P(T)}{W_P} + \left(W \sum_P \frac{Y_P}{W_P \, \lambda_P(T)} \right)^{-1} \right] . \tag{2.28}$$

2.2.5 Diffusivity

The diffusion coefficients are essential inputs to determine the diffusive mass flux of a species P into the rest of the mixture. Detailed models for these fluxes usually require the specification of binary diffusion coefficients $\mathcal{D}_{P,Q}$. As given in the book of Poling *et al.* (2001), these binary diffusion coefficients can be expressed using

$$\mathcal{D}_{P,Q} = \frac{2.66 \cdot 10^{-7} \, T^{3/2}}{p \, W_{P,Q}^{1/2} \, \sigma_{P,Q}^2 \, \Omega^{\mathcal{D}}(T)} , \tag{2.29}$$

where $W_{P,Q} = 2 \left[W_P^{-1} + W_Q^{-1} \right]^{-1}$, $\sigma_{P,Q} = 1/2 \, (\sigma_P + \sigma_Q)$ is the characteristic Lennard-Jones length in [Å], and $\Omega^{\mathcal{D}}(T)$ is the collision integral for diffusion. Eq. (2.29) shows, that the diffusion is proportional to the temperature to the power of 1.5, and inversely proportional to the pressure p.

The numerical evaluation of the net diffusive fluxes can be a relatively expensive procedure, if it is based on binary diffusion between all considered species. Therefore, the procedure based on binary diffusion was circumvented in many DNS of combustion. Rather than considering a complex binary diffusive exchange between the individual species, the simplified approach assumes only one diffusion coefficient $\mathcal{D}_P$, which is used in Fick's law (Eq. 2.11) to give the diffusive flux of species P into the mixture. The value of $\mathcal{D}_P$ is usually estimated introducing the Lewis number, which is defined as a ratio of the thermal to the molecular diffusivities as

$$Le_P = \frac{\lambda}{\rho c_p \mathcal{D}_P} = \frac{\mathcal{D}_{\text{th}}}{\mathcal{D}_P} \, . \tag{2.30}$$

For many species this quantity is close to unity, varying only negligibly across the flame front. Hence, constant values can be assumed (see Tab. 2.1). For reasons of simplicity, but also to satisfy the zero total net flux condition given in Eq. (2.10), a unity Lewis number is assumed for all considered species throughout this thesis[‖].

Species	N_2	O_2	CH_4	CO_2	H_2O	CO	H_2	H
Value	1.00	1.11	0.97	1.39	0.83	1.1	0.3	0.18

Table 2.1: Simplified transport model Lewis numbers (Smooke & Giovangigli, 1991*a*)

2.3 Chemical reaction mechanisms

The chemical source terms occurring on the RHS of the transport equations of species and energy, Eq. (2.12) and Eq. (2.20), respectively, require correlations for the species (mass) conversion rates $\dot{\Omega}_P$. For this purpose, a model for the chemistry has to be introduced, which is commonly referred to as reaction mechanism. When considering, e.g., methane-air combustion, the simplest model for the chemistry would be the assumption of a single-step irreversible forward reaction

$$CH_4 + 2\,O_2 \rightarrow CO_2 + 2\,H_2O \, . \tag{2.31}$$

The scope of such a strongly simplified mechanism is certainly limited, as combustion of fuels is usually a multi-step process involving various elementary reactions, where numerous intermediate species are formed and consumed.

[‖] This assumption will be reviewed in the discussion of the reduced chemistry in Sec. 2.3.2.

2.3.1 Detailed kinetic mechanisms

Detailed ("full") mechanisms basically provide the most accurate and comprehensive mathematical description of the considered reactive system. Formally, a system of $J = 1, M$ elementary forward and reverse reactions can be generally written as (Poinsot & Veynante, 2005)

$$\sum_P \nu'_{P,J} \mathcal{M}_P \rightleftharpoons \sum_P \nu''_{P,J} \mathcal{M}_P \,, \tag{2.32}$$

where $\nu'_{P,J}$ and $\nu''_{P,J}$ denote the molar stoichiometric coefficients for species P occurring as reactants and products, respectively, in the forward reactions, and vice-versa in the reverse reactions, and $\mathcal{M}_P$ is the chemical symbol of the species P. The stoichiometric "matrices" $\nu_{P,J}$ are usually sparse, as uni-, bi- and tri-molecular reactions are the most likely ones to occur. For a given chemical system, the net rate of a single elementary reaction J can be written as

$$\dot{\omega}_J = K_{f,J} \prod_P \left(\frac{\rho Y_P}{W_P} \right)^{\nu'_{P,J}} - K_{r,J} \prod_P \left(\frac{\rho Y_P}{W_P} \right)^{\nu''_{P,J}} \,, \tag{2.33}$$

where $K_{f,J}$ and $K_{r,J}$ are the so called specific reaction-rate constants for forward and reverse reactions, respectively. The specific forward reaction rate constant can be be expressed using the Arrhenius law

$$K_{f,J} = A_{f,J} T^{\beta_J} \exp\left(-\frac{T_{a,J}}{T} \right) \,. \tag{2.34}$$

The pre-exponential constant $A_{f,J}$, the temperature exponent β_J and the activation temperature $T_{a,J}$ are empirical quantities. Their estimation is complex and still a challenge to experts in the field of chemical kinetics.

The specific reverse rate constants can be expressed analogously to Eq. (2.34), but are generally computed from the forward rates using the equilibrium constants, hence they can be expressed as

$$K_{r,J} = \frac{K_{f,J}}{\left(\frac{p}{RT}\right)^{\sum\limits_P \left(\nu''_{P,J} - \nu'_{P,J}\right)} \exp\left(-\frac{\Delta\mathcal{H}_J^0 - \Delta\mathcal{S}_J^0 T}{RT} \right)} \,. \tag{2.35}$$

The net reaction rate of each species P is obtained as the sum over all elementary reactions weighted with the stoichiometric coefficients, written as

$$\dot{\Omega}_P = W_P \sum_J \left(\nu''_{P,J} - \nu'_{P,J} \right) \dot{\omega}_J \,. \tag{2.36}$$

Detailed mechanisms involve a high number of elementary reactions, depending on the fuel which is burnt. A full mechanism for hydrogen combustion ($2\,H_2 + O_2 \rightarrow 2\,H_2O$) e.g. may consist of 37 reactions (Warnatz *et al.*, 2001). Mechanisms for more complex fuels exhibit a hierarchical structure which contains subsets of mechanisms, where smaller components of the initially broken fuel molecules are reacted. When dealing with fuel-rich flames, additional recombination reactions can occur, hence additional reactions of fuels of higher molecular complexity have to be accounted for. As such, combustion represents a highly multi-step process, which implies, that for an already relatively simple methane-air flame, 325 elementary reactions have to be considered in a detailed mechanism (GRI-Mech 3.0). For liquid fuels, full mechanisms generally involve thousands of reactions.

The complex nature of the chemistry is also a major stumbling block for DNS of combustion. Even when considering combustion of the relatively simple methane, an application of full mechanisms is prohibitively expensive in terms of numerical cost. Using, e.g., GRI-Mech 3.0, the chemical system would have to account for 53 reacting species. For each of these, an individual transport equation (Eq. 2.12) would have to be solved for. Thus, as compared to the five conservation equations to be solved for inert flow (continuity, momentum into three spatial directions, and energy), the computational costs associated with the chemistry would exceed the costs for the solution of the flow field by an order of magnitude[**]. Moreover, the Arrhenius-type mathematical expression for the reaction rates (Eq. 2.34) yields differential equations which are stiff with respect to time integration, hence additional complications arise. Finally, the simple fact of the occurrence of exponential functions increases the computational costs. On modern computers, the exponential function is not implemented directly in the hardware, and hence cannot be evaluated within one clock cycle. Instead, it is rewritten by the compiler in terms of multiple hardware-implemented Fused Multiply-Accumulate operations (FMAC) $a \leftarrow a + b \cdot c$, which results in an evaluation speed which is an order of magnitude slower than the speed of a simple multiplication.

For all these reasons, the DNS studies performed to date were restrained from using full mechanisms[††].

2.3.2 Skeletal and reduced mechanisms

Due to the prohibitively high computational costs brought about by detailed mechanisms, DNS in general applied the computationally cheaper alternative of reduced kinetic mechanisms. Starting from the full mechanisms, so called skeletal mechanisms can be obtained by eliminating species and reactions which are comparably insignificant to the global structure of a flame. To identify the negligible contributions, simple test cases with reduced spatial dimensionality are computed using the full chemistry first. In a subsequent post-processing step, the reaction branches are analyzed to determine those which are only insignificantly contributing to the conversion of species (see Fig. 2.3). For this

---

[**] It should be noted that the DNS of non-reacting flow is already limited by the high computational costs.

[††] Illustrations of current capabilities have been given in Sec. 1.2.

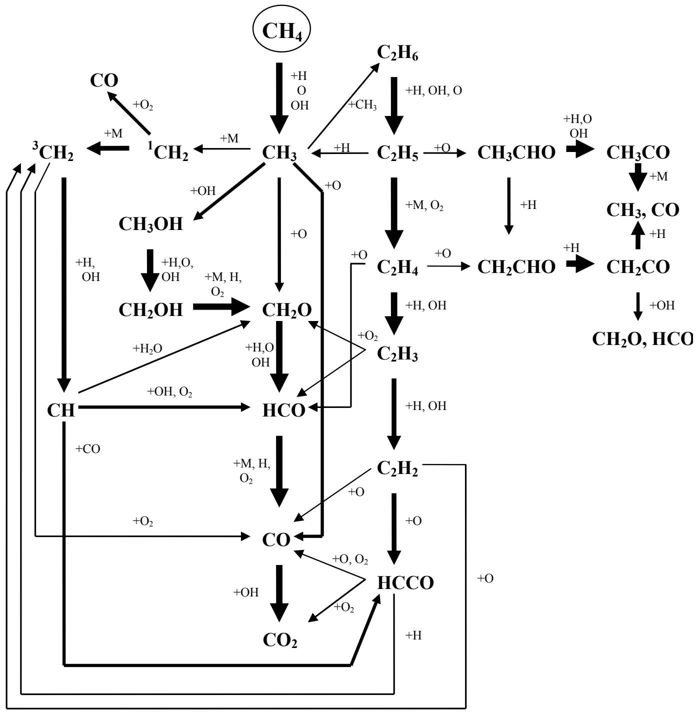

Figure 2.3: Analysis of reaction branches for a stoichiometric methane-air flame at 25 [°C] and ambient pressure. The arrow thickness is representative of the share in decomposing a certain species. Only branches with a share $> 5\%$ are shown. Image taken from Zeuch (2003).

post-processing steps, special techniques for sensitivity analysis (Warnatz *et al.*, 2001) or Computational Singular Perturbation (CSP, Lam & Goussis 1994) have been developed.

Depending on the size of the underlying full mechanism and the required level of accuracy, skeletal mechanisms account only for a limited number of the original reactions. For hydrocarbon flames, skeletal mechanisms consisting of about 50 reactions are sufficient to reproduce the laminar flame speed for variable stoichiometry and pressure. Even smaller mechanisms can be derived when dealing with more specific flame configurations, e.g. lean methane-air flames. The mechanism presented by Smooke & Giovangigli (1991*a*) involves, e.g., 25 reactions and 16 species.

Considering DNS, the computational costs of skeletal mechanisms are still too high and further rigorous reductions are needed. So called "reduced" mechanisms can be derived based on physical reasoning, by applying partial equilibrium and steady-state assumptions. Alternatively, mathematical concepts such as the method of Intrinsically Low-Dimensional Manifolds (ILDM), or again CSP can be used for this task. The so obtained reduced mechanisms usually involve up to twenty reactions. Clearly, as a consequence of the rigorous reduction, these mechanisms are incapable of reproducing certain specific features of flames. Marked changes in the thermodynamic pressure can for instance lead to inaccurate results, and phenomena such as auto-ignition or detonations may not be represented at all. However, using these reduced mechanisms, DNS of reactive flows is possible at least on middle to large scale computing systems. The methods for reduction of reacting systems, and the unfavourable consequences inferred thereby are still under research of experts of chemistry. A more detailed review of this subject, which is beyond the scope of this work, can be found in the work of Law *et al.* (2003). The reduced mechanism, which is used in the present work, follows essentially a proposal of Williams (1991). It involves the two elementary reactions

$$\mathrm{CH_4 + O_2 \rightarrow INT + PRO} \qquad \text{(Reaction I)} \qquad (2.37)$$

$$\mathrm{INT + O_2 \rightarrow 2\,PRO} \qquad \text{(Reaction II)}\,, \qquad (2.38)$$

carrying the four reactive species CH_4, O_2, INT, and PRO. INT and PRO denote intermediate and product species, which are defined as a combination of two species, written as

$$\mathrm{INT} = \frac{2}{3}\mathrm{CO} + \frac{4}{3}\mathrm{H_2}\,, \qquad \mathrm{PRO} = \frac{1}{3}\mathrm{CO_2} + \frac{2}{3}\mathrm{H_2O}\,, \qquad (2.39)$$

respectively. The two elementary reaction rates are given as

$$\dot{\omega}_I = 1.57 \cdot 10^{14}\ \exp\left(-\frac{9624}{T}\right)\ Y_{\mathrm{CH_4}}\ [\mathrm{H}]\ , \qquad (2.40)$$

$$\dot{\omega}_{II} = 3.00 \cdot 10^{17}\ T^{-0.8}\ Y_{\mathrm{O_2}}\ [\mathrm{H}]\ [\mathrm{M}] \qquad (2.41)$$

in units of $[kmol/kg \cdot s]$. [M] denotes the third body concentration. Using the collision efficiencies given by Warnatz (1984), it is written as

$$[\mathrm{M}] = \frac{\rho}{1000}\,(0.014 + 0.392\ Y_{\mathrm{CH_4}} - 0.002\ Y_{\mathrm{O_2}} + 0.072\ Y_{\mathrm{INT}} + 1.67\ Y_{\mathrm{PRO}})\ . \qquad (2.42)$$

[H] is the hydrogen radical concentration which is modelled based on a partial equilibrium assumption

$$[\mathrm{H}] = \frac{0.136\,\rho}{1000}\exp\left(\frac{3045}{T} - 22.1\frac{Y_{\mathrm{CH_4}}}{Y_{\mathrm{O_2}}}\right)\left\{1 - \exp\left[-\left(\frac{T}{1000}\right)^5\right]\right\}\frac{\sqrt{Y_{\mathrm{INT}}^3 Y_{\mathrm{O_2}}}}{Y_{\mathrm{PRO}}}\ . \qquad (2.43)$$

Using this partial equilibrium relation, no transport equation needs to be solved for the fast diffusing hydrogen radical as indicated by its low Lewis number. In view of this aspect, the assumption of unity Lewis number for all transported species appears to be less critical.

The elementary reaction rates given in Eqs. (2.40) and (2.41) can be transformed into mass conversion rates for the individual species by applying Eq. (2.36). Using the stoichiometric coefficients as shown in Eqs. (2.37) and (2.38), they are written as

$$\begin{aligned} \dot{\Omega}_{CH_4} &= -W_{CH_4}\ \dot{\omega}_I, & \dot{\Omega}_{O_2} &= -W_{O_2}\,(\dot{\omega}_I + \dot{\omega}_{II})\,, \\ \dot{\Omega}_{INT} &= \ \ W_{INT}\,(\dot{\omega}_I - \dot{\omega}_{II})\,, & \dot{\Omega}_{PRO} &= \ \ W_{PRO}\,(\dot{\omega}_I + 2\,\dot{\omega}_{II})\,, \end{aligned} \qquad (2.44)$$

in units of $\left[s^{-1}\right]$.

According to Eq. (2.19), the reactive heat source term $\dot{Q}_{\text{react}}$ can be expressed in terms of the species conversion rates $\dot{\Omega}_P$. However, as the present four species conversion rates linearly depend on the two elementary reaction rates, Eq. (2.19) can be rewritten more compactly as

$$\dot{Q}_{\text{react}} = \rho \left(Q_I \, \dot{\omega}_I + Q_{II} \, \dot{\omega}_{II} \right) . \tag{2.45}$$

In this relation, $\dot{Q}_{\text{react}}$ has a dimension of $[J/m^3 s]$, and $Q_I = 2.91205 \cdot 10^8$ and $Q_{II} = 5.11098 \cdot 10^8$ are the amounts of heat released per converted *kmol* of fuel in $[J/kmol]$. For the present two-step mechanism, the representation of $\dot{Q}_{\text{react}}$ in Eq. (2.45) involves less mathematical operations in contrast to Eq. (2.19), and causes therefore less numerical costs.

2.4 Non-dimensional representation

To obtain a more general mathematical description of the considered problem, the conservation equations derived in Sec. 2.1 are recast into a non-dimensional form. The dimensionless parameters obtained hereby allow for the assessment of the individual terms in regard to their physical meaning and relevance. This will facilitate later the reasoning for the computational setup, as well as the interpretation of the results.

Using the reference quantities L_0, U_0, ΔT_0, ρ_0, $c_{p,0}$, μ_0, λ_0, $\mathcal{D}_{P,0}$, W_0 and R, the non-dimensional variables for the presently considered problem can be written as

$$x_i^* = \frac{x_i}{L_0}, \quad \mathbf{u}^* = \frac{\mathbf{u}}{U_0}, \quad t^* = \frac{t\,U_0}{L_0}, \quad T^* = \frac{T}{T_0}, \quad p^* = \frac{p\,W_0}{\rho_0\,R\,T_0}, \quad \boldsymbol{\nabla}^* = L_0 \boldsymbol{\nabla} \tag{2.46}$$

$$\rho^* = \frac{\rho}{\rho_0}, \quad c_p^* = \frac{c_p}{c_{p,0}}, \quad \mu^* = \frac{\mu}{\mu_0}, \quad \lambda^* = \frac{\lambda}{\lambda_0}, \quad \mathcal{D}^* = \frac{\mathcal{D}}{\mathcal{D}_0} \quad \text{and} \quad \dot{\Omega}_P^* = \frac{\dot{\Omega}_P\,L_0}{U_0} .$$

It is noted that no non-dimensionalization is required for Y_P, which is already non-dimensional by definition. The introduction of these variables into the equations of continuity (Eq. 2.2), momentum (Eq. 2.4), species (Eq. 2.12) and energy (Eq. 2.20) leads to the following non-dimensional conservation equations:

$$\frac{\partial \rho^*}{\partial t^*} + \boldsymbol{\nabla}^* \cdot (\rho^* \mathbf{u}^*) \quad = 0\,, \tag{2.47}$$

$$\frac{\partial \rho^* \mathbf{u}^*}{\partial t^*} + \boldsymbol{\nabla}^* \cdot (\rho^* \mathbf{u}^* \mathbf{u}^*) = -\frac{1}{\gamma \mathrm{Ma}^2} \boldsymbol{\nabla}^* p^* + \frac{1}{\mathrm{Re}} \boldsymbol{\nabla}^* \left[2\mu^* \left(\mathbf{S}^* - \frac{1}{3} \mathbf{I} \boldsymbol{\nabla}^* \cdot \mathbf{u}^* \right) \right] + \frac{\rho^*}{\mathrm{Fr}^2} \mathbf{e}_g\,, \tag{2.48}$$

$$\frac{\partial \rho^* Y_P^*}{\partial t^*} + \boldsymbol{\nabla}^* \cdot (\rho^* \mathbf{u}^* Y_P^*) = \frac{1}{\mathrm{Re\,Sc}} \boldsymbol{\nabla}^* \cdot \left(\rho^* \mathcal{D}^* \boldsymbol{\nabla}^* Y_P^* \right) + \rho^* \dot{\Omega}_P^*\,, \tag{2.49}$$

$$\frac{\partial \rho^* T^*}{\partial t^*} + \boldsymbol{\nabla}^* \cdot (\rho^* \mathbf{u}^* T^*) = \frac{1}{\mathrm{Re\,Pr}} \frac{1}{c_p^*} \boldsymbol{\nabla}^* \cdot \left(\lambda^* \boldsymbol{\nabla}^* T^* \right) + \frac{\rho^*}{c_p^*} \sum_P \mathrm{Ce}_P \dot{\Omega}_P^*\,. \tag{2.50}$$

Here, γ denotes the ratio of specific heats and $\mathbf{e}_g$ is a unit vector into the direction of gravity. The dimensionless parameters occurring in these equations are the following:

- The Mach number, which is a ratio of the characteristic speed of the flow field to the speed of sound

  $$\mathrm{Ma} = \frac{U_0}{\sqrt{\gamma \frac{R}{W_0} T_0}}\,. \tag{2.51}$$

  The number basically measures the compressibility of the flow field. In the limit of Ma → 0, which is assumed in this work, the flow field becomes incompressible, which implies that pressure variations propagate at an infinitely fast velocity. The assumption of incompressible flow associated with a low Mach number has a consequence for the numerical solution procedure for the instantaneous pressure field, as will be shown later.

- The well known Reynolds number

  $$\mathrm{Re} = \frac{\rho_0 U_0 L_0}{\mu_0}\,, \tag{2.52}$$

  which can be understood as a ratio of inertial and viscous forces. Re is of primary importance for the determination of the stability of a flow w.r.t. a transition to turbulence.

- The Froude number, defined as

  $$\mathrm{Fr} = \frac{U_0}{\sqrt{g L_0}}\,, \tag{2.53}$$

  describes the ratio of inertial to buoyancy forces‡‡.

---

‡‡Attention should be paid when comparing with other literature, where Fr is also given as the square of Eq. (2.53), or the Richardson number Ri $= \mathrm{Fr}^{-2}$ is used.

- The Schmidt and Prandtl numbers are defined as the ratios of momentum ($\mathcal{D}_{\text{mom}}$), species ($\mathcal{D}_P$) and thermal ($\mathcal{D}_{\text{th}}$) diffusivities written as

$$\text{Sc}_P = \frac{\mathcal{D}_{\text{mom}}}{\mathcal{D}_P} = \frac{\mu_0}{\rho_0\,\mathcal{D}_{P,0}} \quad \text{and} \quad \text{Pr} = \frac{\mathcal{D}_{\text{mom}}}{\mathcal{D}_{\text{th}}} = \frac{\mu_0\,c_{p,0}}{\lambda_0}\,, \tag{2.54}$$

respectively. Together with the already given Lewis number, these three quantities form a triad ($\text{Le}_P = \text{Sc}_P\,/\,\text{Pr}$) relating the diffusive transport properties of the considered fluid.

- The Damköhler number is a ratio of the flow to the chemical timescales

$$\text{Da} = \frac{\Delta t_{\text{flow}}}{\Delta t_{\text{chem}}}\,. \tag{2.55}$$

For reactive systems, a Damköhler number may be given for each elementary reaction. Among the various definitions given in literature, the definition of Da using the maximum of the non-dimensional reaction rate $\text{Da}_P = \dot{\Omega}^*_{P,\max}$ appears as a very senseful choice.

- The reactive heat release is represented by the Damköhler number in combination with a quantity referred to as McMurtry number (Nichols, 2005)

$$\text{Ce}_\text{P} = \frac{\Delta h^0_{F,P}}{c_{p,0}\,T_0}\,. \tag{2.56}$$

It should be noted that, in literature, Da and Ce are often lumped together to appear as a single coefficient in front of the reactive source term in the equation of energy.

3 TURBULENT REACTING FLOW

Before applying the derived mathematical formulation to any specific test case, the present section aims at illustrating the basic concepts for the description of turbulent reacting flow. For this purpose, different concepts for the description of turbulent motion are discussed first. Then, specific methods for the description of turbulent flames are given.

3.1 Turbulence

Depending on the magnitude of a characteristic Reynolds number, most flows occurring in nature or technical applications are turbulent. Especially for the present case of jet flows, turbulence is triggered by the very strong Kelvin-Helmholtz instability, so that the transition from laminar to turbulent flow occurs at comparatively low Reynolds numbers. A precise definition of turbulence is hard to find. Instead, scientists usually resort to the specification of characteristic features of turbulent flow. According to Tennekes & Lumley (1972) these essentially comprise irregularity, large Reynolds numbers, three-dimensional velocity fluctuations, dissipation, and the fact that turbulence is a property of flows instead of fluids.

3.1.1 Statistical description

Assuming the turbulent motion basically as a random process suggests the use of statistical methods to describe the essential features of the flow. The statistical description of the turbulent flow in terms of first-order moments is based on the Reynolds decomposition, which decomposes all turbulent fluctuating quantities ψ into a mean $\langle\psi\rangle$ plus a fluctuating component ψ'

$$\psi = \langle\psi\rangle + \psi' \ , \quad \text{where} \quad \langle\psi\rangle = \frac{1}{N}\sum_{n=1}^{N}\psi_n, \quad N \to \infty \ , \tag{3.1}$$

is the ensemble average over N samples, and $\langle\psi'\rangle = 0$ by definition. In the case of statistically stationary flow the ensemble average $\langle\psi\rangle$ becomes invariant w.r.t. time, as it is the case for jet flow. Considering statistically stationary flow, the ensemble average can be replaced by temporal averages

$$\psi = \overline{\psi} + \psi', \quad \text{with} \quad \overline{\psi}(\mathbf{x}) = \frac{1}{\Delta t} \int_0^{\Delta t} \psi(\mathbf{x},t)\, dt \;, \tag{3.2}$$

where again $\overline{\psi'} = 0$ by definition. Based on the Reynolds decomposition Eq. (3.2), the turbulent flow field can be described by solving the time averaged equations of motion for the temporal averages $\overline{\psi}$, which requires closure models for the higher order terms appearing as the so called Reynolds stress tensor

$$R_{ij} = \overline{u'_i u'_j} \tag{3.3}$$

in the averaged formulation. For isotropic turbulence, the diagonal elements of R_{ij} representing the magnitude of the velocity fluctuations are the same in all spatial directions, so that they can be quantified by one scalar quantity, the turbulent kinetic energy $k = \overline{u_i{}' u_i{}'}/2$, or the turbulence intensity $\mathcal{I} = \sqrt{2/3\, k}/U_0$, where U_0 is a reference velocity.

For non-isotropic turbulence, as it is typically found in near wall regions, turbulence intensities are different in the three spatial directions. Dynamically, the diagonal elements of R_{ij} represent normal stresses, and the off-diagonal elements of the Reynolds stress tensor $\overline{u'_i u'_j}$, $i \neq j$, represent shear stresses, all associated with the turbulent motion.

When scalar transport is considered, closure for the turbulent scalar fluxes $\zeta_{i,k} = \overline{u'_i Y'_k}$ has to be provided as well to solve the transport equations for the averaged scalar $\overline{Y_k}$.

3.1.2 Length scales

The Reynolds stress tensor given in Eq. (3.3) basically measures the auto- and cross-correlations of the fluctuating velocity components at one single point. Such correlations can be given for different locations in space as $\overline{\psi_i(\mathbf{x})\, \psi_j(\mathbf{x} + \xi \mathbf{e}_k)}$ as well. As such, they are useful to identify and to measure the size of coherent structures in a turbulent flow field. When normalising the above correlation for velocities, and integrating from an origin position $\mathbf{x}$ into the direction $\mathbf{e}_k$, an integral length scale can be obtained as

$$\mathcal{L}_{i,j}^{\mathbf{e}_k} = \int_0^{\infty} \frac{\overline{u_i(\mathbf{x})\; u_j(\mathbf{x} + \xi \mathbf{e}_k)}}{\operatorname{std}(u_i(\mathbf{x}))\; \operatorname{std}\left(u_j(\mathbf{x} + \xi \mathbf{e}_k)\right)} d\xi \;. \tag{3.4}$$

For isotropic turbulence, this length scale is equal for all directions $\mathbf{e}_k$ and velocity components i and j, so that it can be expressed using a single scalar $l_t \approx \mathcal{L}_{i,j}^{\mathbf{e}_k}$. The magnitude of this integral length scale l_t represents the average size of the large energy containing

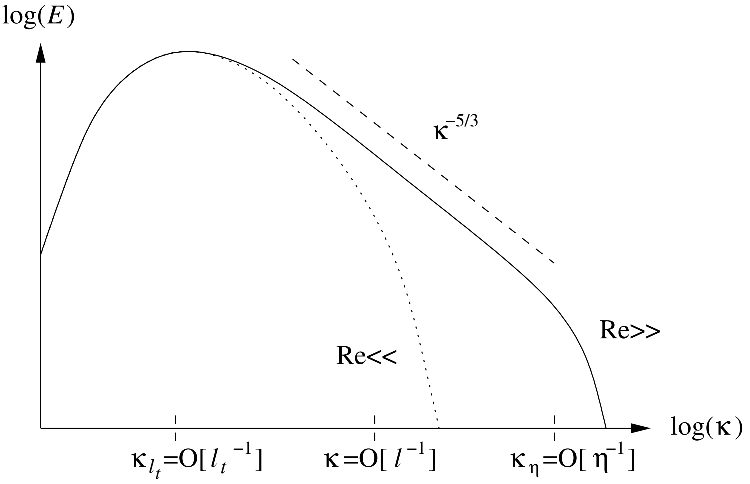

Figure 3.1: Spectrum of turbulent kinetic energy density $E(\kappa)$.

eddies, and it is typically of the same order as a characteristic geometric length of the flow. For pipe flows, e.g., this geometric length would be the pipe diameter.

A major part of the turbulent kinetic energy k is contained within the largest eddies of a flow. The turbulent transfer of momentum is generally assumed as a cascading process, where bigger eddies successively transfer kinetic energy to the smaller ones. The kinetic energy cascading down from the large eddies to the smallest ones becomes finally dissipated by viscous dissipation. This cascading process can be illustrated in terms of the spectral density of the turbulent kinetic energy $E(\kappa)$, where

$$k = \int_0^\infty E(\kappa)\, d\kappa \,, \tag{3.5}$$

and κ is the turbulent wave number. A typical profile of the energy density $E(\kappa)$ is plotted in Fig. 3.1. There exists a maximum of $E(\kappa)$ approximately at a wave number corresponding to the integral length scale $\kappa_{l_t} \sim {l_t}^{-1}$, which is followed by an almost linear decrease until $E(\kappa)$ vanishes for high wave numbers κ. The wave number κ_η at the lower limit of the region, where the viscous dissipation of the turbulent eddies becomes dominant, determines the size of the smallest turbulent eddies, the Kolmogorov length scale $\eta \sim \kappa_\eta^{-1}$. According to Kolmogorov's hypothesis on the turbulence cascading process, energy is produced at the large, flow configuration dependent scales, corresponding approximately to l_t. Subsequently, in the so called inertial range, energy is transferred from the larger to the smaller eddies with negligible viscous losses at a constant rate. Following the cascading theory, the rate of this basically inviscid energy transfer must be equal to the total dissipation rate at the high wave number end of the spectrum. Thus, the dissipation rate ε, which can be estimated as

$$\varepsilon = \frac{u_t^2}{l_t/u_t} = \frac{u_t^3}{l_t} = \frac{u^3}{l} = \frac{u_\eta^3}{\eta} , \tag{3.6}$$

where $u_t \approx \sqrt{k}$ and l_t denote the velocity fluctuation and the size of an eddy at the integral scale, essentially determines the turbulent transfer of energy in the inertial range. In Fig. 3.1, the inertial range is indicated by the straight dashed line. In this region, Kolmogorov correlated the spectral density as $E(\kappa) \propto \kappa^{-5/3}$, based on a dimensional analysis. Beyond the inertial range, where eddies become of the size of the Kolmogorov length, the action of viscous forces becomes relevant. Accordingly, a Reynolds number expressed in terms of the length and velocity scale of a Kolmogorov eddy

$$\mathrm{Re}_\eta = \frac{u_\eta \eta}{\mu/\rho} = \frac{\varepsilon^{1/3}\eta^{4/3}}{\mu/\rho} \tag{3.7}$$

becomes unity, and eddies much smaller in size than η cannot exist, as they are dissipated by viscous forces. Following from $\mathrm{Re}_\eta = 1$, the Kolmogorov length scale η can be written as

$$\eta = \left(\frac{\mu^3}{\rho^3 \varepsilon}\right)^{\frac{1}{4}} . \tag{3.8}$$

Relating Eq. (3.7) to an equivalent Reynolds number specified at the integral scale, the size ratio of the largest to the smallest turbulent eddies can be estimated as

$$\frac{l_t}{\eta} = \mathrm{Re}_{l_t}^{3/4} . \tag{3.9}$$

As seen from this relation, the separation of scales leading to an extended inertial range requires a sufficiently high (integral) Reynolds number, so that Kolmogorov's theory can be applied. For low Reynolds numbers viscous dissipation becomes relevant already at low wave numbers, and practically no inertial range with negligible viscous forces exists, as it is required by Kolmogorov's theory. Aside from the condition of sufficiently high Reynolds numbers, Kolmogorov's theory is also based on the assumption of homogeneous isotropic turbulence for wave numbers in the inertial range and beyond. In shear flow configurations, this is not the case, as mechanisms like the Kelvin-Helmholtz instability produce large vortices with a distinct orientation in space. However, this limitation affects mainly the large-scale motion, because the turbulent eddies tend to become more and more isotropic as they get smaller.

It is consistent with the well established theory of Kolmogorov on the turbulent energy cascade, to regard turbulence not only as a pure stochastic random process. Turbulent flow essentially features randomness and structure. The latter can be used for turbulence modelling, as in the case, e.g., of LES, where the dynamical effect of the smaller eddies, which tend to exhibit isotropic behaviour, is modelled, while the large eddies are resolved.

For the DNS of turbulent flows, the length scale ratio Eq. (3.9) is a critical quantity. Due to the fact that no turbulence model is used in a DNS, turbulent eddies must be resolved down to the Kolmogorov scales η. This criterion determines the required numerical resolution to be provided by the computational mesh. A further practical difficulty arises from the fact, that the Kolmogorov length scale can basically not be computed in advance, but is computed a posteriori from Eq. (3.8) with $\varepsilon = 2\frac{\mu}{\rho}\,[\mathbf{S}:\mathbf{S}]$ obtained from the numerical results. Hence, the mesh has theoretically to be adapted until the resolution requirement imposed by the smallest relevant scale η is satisfied. Such repeatedly performed simulations on refined mesh are often prohibited by computational costs.

3.2 Flame structure

3.2.1 Classification of flames

A classification of flames and flame regimes is necessary for the development of models describing the structure of a flame, but also for the setup and design of numerical as well as laboratory flames. A very basic classification relies in general on two criteria: the level of reactant premixing, and the state of the underlying flow field w.r.t. turbulence.

The first criterion distinguishes flames dependent on the mixedness of the reactants before the combustion process starts. In premixed flames, fuel and oxidizer are perfectly mixed prior to ignition. The combustion process of such flames is controlled by thermodiffusive preheating of the unburnt reactants ahead of the flame, which is sustained by a the strong heat release in a successive oxidation layer. In non-premixed flames, fuel and oxidizer are supplied separately from both sides of the reactive layer, and hence the reactants have to get mixed down to the molecular level before they can react. Since the mixing process on the molecular level is controlled by the diffusion of mass, such flames are commonly termed “diffusion flames”. Flames which do not clearly fall into these two basic categories are the so called partially premixed flames. These flames are often met in lifted reacting jets, but they are found also in other technical devices such as internal combustion engines with direct, fuel stratified injection.

The flow regime criterion divides flames into the two classes of laminar and turbulent reacting flows, and the distinction between both cases is rather obvious. Transitions between both regimes may occur, e.g., in the case of flame induced turbulence, or when laminarization occurs. Theoretical descriptions for the transitional regime are however scarce, because this regime is in general very hard to parameterize. Therefore, this regime is excluded from the scope of many textbooks.

Laminar flame configurations typically occur in candles, lighters and domestic furnaces. Aside from these applications, they appear rather seldom in technical devices. Nevertheless, laminar flames represent a fundamental building block for the description of the structure of the reaction zones embedded in a turbulent flow field. As such, they allow for a qualitative as well as quantitative analysis of some fundamental phenomena occurring in the reaction layer, which makes them an important reference case. For this reason, the basic properties of premixed as well as non-premixed laminar flames are briefly discussed in the next two subsections. Based on the description of laminar flames, in combination with turbulent length and time scales already presented in Sec. 3.1, turbulent flame regimes are identified in a further subsection for premixed, as well as non-premixed flames. For the latter case, a well established approach, the so called laminar flamelet concept is discussed as well.

3.2.2 Laminar premixed combustion

The basic nature of a premixed flame is essentially determined by the composition of the premixed gas w.r.t. stoichiometric conditions, the thermodynamic state, the chemical kinetic mechanism and the diffusive transfer of heat and mass. The first is commonly quantified by the equivalence ratio

$$\phi = \frac{Y_{\text{fuel}}}{Y_{\text{oxi}}} \bigg/ \left(\frac{Y_{\text{fuel}}}{Y_{\text{oxi}}}\right)_{\text{st}}, \tag{3.10}$$

which is defined by relating the given fuel to oxidizer ratio in the premixed feed to the stoichiometric conditions. For an equivalence ratio of unity, fuel and oxidizer can be fully converted into combustion products. For $\phi < 1$, the oxidizer is an excess quantity, so that it is not completely consumed in the combustion process, and the flame is called “lean”. For $\phi > 1$, there is an excess of fuel, and the flame is referred to as “rich”.

It has been already outlined, that premixed flames are basically controlled by an interaction between preheating of the reactants and successive heat release. As a consequence, the propagation of a premixed flame is dependent on all parameters, which are able to influence this thermal balance. These parameters are related to the heat release, the thermal conductivity and the mass diffusivities, but also to the fresh gas temperature, which defines the preheating necessary to achieve the activation temperature, to the stoichiometry in terms of ϕ, which determines the effectively followed reaction branches, to the heat capacity of the mixture of reactants, products and inert components, and to the heat losses induced by flame stretch and curvature*.

For the analysis of premixed flames, comprehensive measurements of all relevant parameters are often not possible. Instead, it is commonly accepted, to describe the kinetic behaviour of the flame by one single characteristic quantity, the laminar flame speed s_L. This quantity, which represents the speed of the laminar flame propagation relative to the

---

*... and pressure, which controls the diffusive mobility of radicals. As the present work is focused on atmospheric combustion, this issue is not discussed further.

fresh gases, is characteristic for each specific chemical system. For most hydrocarbon flames, the flame speeds s_L measured at room temperature and atmospheric pressure are in the range of 0.4 $[m/s]$. Based on the flame speed s_L further characteristic scales can be derived, such as the length scale

$$l_{\text{fl}} = \mathcal{D}_{\text{th}}/s_L \, , \tag{3.11}$$

which represents a measure for the thickness of premixed laminar flames. Substitution of a typical flame speed of 0.4 $[m/s]$ and a thermal diffusivity of $\mathcal{D}_{\text{th}} = 2 \cdot 10^{-5}$ $\left[m^2/s\right]$ valid for cold air, yields a length scale of $l_{\text{fl}} = 50\,[\mu m]$.

3.2.3 Laminar non-premixed combustion

In non-premixed flames, fuel and oxidizer have to get mixed down to a molecular level before they can react. Non-premixed combustion is therefore mainly controlled by the instantaneous local mixing state of the reactants. The mixing state is described by the so called mixture fraction

$$Z = \frac{m_1}{m_1 + m_2} = \frac{m_1}{m_{\text{tot}}} \, , \tag{3.12}$$

where m_1 and m_2 denote the masses which originate from the fuel and oxidizer feed streams, respectively. This mixture fraction is related to the local equivalence ratio by

$$Z = \frac{\phi}{\phi + \left(\frac{m_2}{m_1}\right)_{st}} \, , \quad \text{or} \quad \phi = \frac{Z}{1-Z}\left(\frac{m_2}{m_1}\right)_{\text{st}} \, . \tag{3.13}$$

By definition, the mixture fraction varies between $Z = 0$, in the pure oxidizer stream, and $Z = 1$, in the pure fuel stream. The reaction zone is located closely around the stoichiometric mixing conditions $Z = Z_{\text{st}}$.

As seen from Eq. (3.12) the mixture fraction is defined as the local fraction of mass which originated from the fuel feed. While mass fractions of reactive species can be converted into other species in the reactive process, this is not the case for the mixture fraction, as mass which was issued from one source cannot be converted into mass which issued from another source. Therefore, Z is conserved even through flame fronts, and no source term appears in the conservation equation written for this passive scalar as

$$\frac{\partial \rho Z}{\partial t} + \nabla \cdot (\rho \mathbf{u} Z) = \nabla \cdot (\rho \mathcal{D}_Z \nabla Z) \, , \tag{3.14}$$

where $\mathcal{D}_Z$ is usually assumed to be equal to the thermal diffusivity $\mathcal{D}_{\text{th}}$. This implies, that the mixing in flames can be basically described independently of a specific chemistry.

For a specific reaction mechanism, several definitions of Z depending on the number of transported scalars might be given†. These definitions can be derived from a linear combination of the species and energy transport equations, and thus depend on the boundary conditions of the respective fuel and oxidizer feed streams. For a detailed description thereof, see the book of Poinsot & Veynante (2005). For the kinetic mechanism used in the present work (Sec. 2.3.2), the mixture fraction is given as

$$Z = \frac{Y_{\mathrm{CH_4}} - \frac{2\,W_{\mathrm{CH_4}}}{W_{\mathrm{O_2}}}\left(Y_{\mathrm{O_2}} - Y_{\mathrm{O_2},2}\right) - \frac{W_{\mathrm{CH_4}}}{W_{\mathrm{P}}} Y_{\mathrm{PRO}}}{Y_{\mathrm{CH_4},1} + \frac{2\,W_{\mathrm{CH_4}}}{W_{\mathrm{O_2}}}\left(Y_{\mathrm{O_2},2} - Y_{\mathrm{O_2},1}\right)}\,, \tag{3.15}$$

where the subscripts 1 and 2 refer to the boundary values at the fuel and oxidizer inlets, respectively.

The kinetic behaviour of non-premixed flames is mainly controlled by diffusive mixing. This process is commonly described using the scalar dissipation rate at the stoichiometric condition

$$\chi_{\mathrm{st}} = 2\,\mathcal{D}_{Z,\mathrm{st}}\left(\nabla Z\right)^2_{\mathrm{st}}\,, \tag{3.16}$$

which basically measures the mixing rate dependent on the mixture fraction gradient and the diffusivity. χ_{st} has the dimension $\left[s^{-1}\right]$ and is therefore interpreted as the inverse of a time scale t_D for diffusive mixing. For low values of the scalar dissipation rate the mixing speed is slow, hence, the reactive processes are slow as well, due to a shortage in reactants. For high values of χ_{st}, the opposite is the case. There exists, however, an upper limit for χ_{st}, where the consumption of the reactive species in the reaction zone hardly balances the supply of reactants from the mixing process. When the scalar dissipation rate is increased beyond this limit, the heat produced by the flame does not compensate the conductive cooling losses to the fuel and the oxidizer side, and the flame extinguishes. This so called "quenching" limit, denoted by $\chi_{\mathrm{st},q}$, can be considered as analogous to the process which determines the laminar flame speed for premixed flames. In the premixed case, the flame propagates at a speed, where the heat release of the reaction is just high enough to preheat the incoming mixture sufficiently for ignition.

For non-premixed flames, the flame thickness can be estimated by introducing a diffusive length scale defined as $l_D = \sqrt{\mathcal{D}_{Z,\mathrm{st}}/\chi_{\mathrm{st}}}$. Since χ_{st} is a strongly varying, local property of the turbulent flow field, the length scale l_D is not a universal characteristic quantity, as it is the case for the thickness of premixed flames defined by Eq. (3.11). Only in the quenching limit of $\chi_{\mathrm{st},q}$, which is characteristic for every chemical system, the expression

$$l_{D,q} = \sqrt{\mathcal{D}_{Z,\mathrm{st}}/\chi_{\mathrm{st},q}} \tag{3.17}$$

[†] This is due to the fact, that for every single kind of atom (e.g. C, H, O, N) a source-free conservation equation can be given.

yields a universal characteristic length scale representing a minimum possible diffusive length of the considered non-premixed flame. Assuming for the diffusivity the thermal diffusivity of cold air, $\mathcal{D}_{Z,\mathrm{st}} = 2 \cdot 10^{-5}\ \left[m^2/s\right]$, and $\chi_{\mathrm{st},q} = 10\ \left[s^{-1}\right]$, which is the typical order of magnitude of the scalar dissipation rate at quenching in methane-air flames, a length scale of $l_{D,q} = 2\,[mm]$ is obtained. It should be emphasized, that this length scale represents the thickness of the mixing layer between fuel and oxidizer; the reactive layer itself which is located inside the mixing layer, is usually much thinner.

3.2.4 Turbulent flames

When the underlying flow is turbulent, the effect of the turbulent motion on the flame is generally described making again a distinction between premixed and non-premixed flames. For the premixed case, the main impact of the turbulence is an increase in flame speed, for which, as a first approximation, the relation

$$\frac{s_T}{s_L} = 1 + \frac{\sqrt{k}}{s_L} \tag{3.18}$$

was found in experimental works (see Poinsot & Veynante 2005). This relation is only approximately valid for low levels of turbulence. For higher turbulence levels, the turbulent flame speed s_T is overpredicted by Eq. (3.18). The flame finally may extinguish when a certain turbulence level is reached. Similar to the quenching of non-premixed laminar flames, the extinction here is caused by exceeding heat losses of the flame, which are due to the intensified turbulent mixing.

Turbulent premixed combustion occurs in different regimes. According to Peters (2000), the different regimes can be demarcated in a nomogram dependent on the ratio of turbulent velocity fluctuations to the laminar flame speed $\sqrt{k}/s_L$, and the ratio of the turbulent length scale to the laminar flame thickness l_t/l_{fl}, as shown in Fig. 3.2. In this nomogram, several regimes can be distinguished based on different non-dimensional parameters. The laminar flame regime can be delineated by a unity Reynolds number defined as

$$\mathrm{Re} = \frac{\sqrt{k}l_t}{s_L l_{\mathrm{fl}}}\,, \tag{3.19}$$

appearing in the lower left corner of Fig. 3.2. The Karlovitz number is introduced as a ratio of the characteristic time scales of a laminar flame and a Kolmogorov eddy as

$$\mathrm{Ka} = \frac{t_{\mathrm{fl}}}{t_\eta} = \frac{l_{\mathrm{fl}}^2}{\eta^2}\,. \tag{3.20}$$

If $\mathrm{Ka} < 1$, the smallest eddies occurring in the flow are bigger than the flame thickness, hence they cannot penetrate into the flame. Therefore, the inner structure of the flame

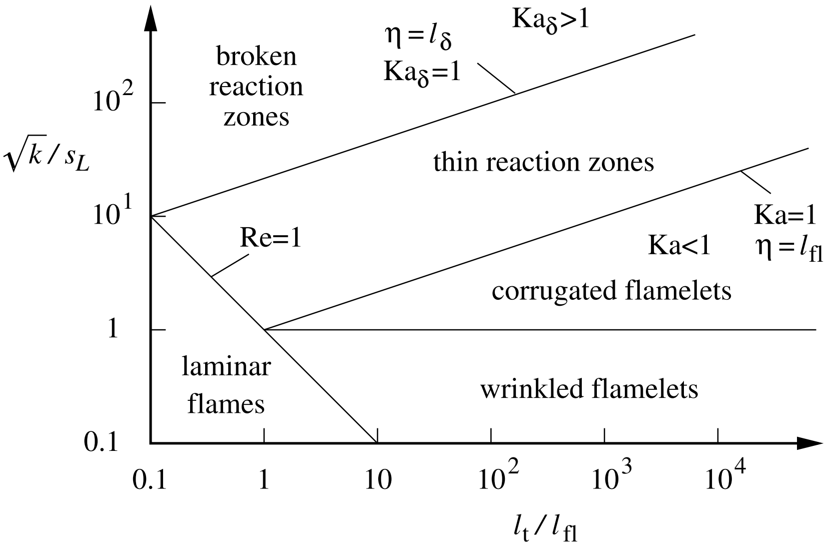

Figure 3.2: Regimes in premixed turbulent combustion. Replotted following Peters (2000).

remains unchanged by all eddies, and the flame is only convected by the turbulent motion. This regime is referred to as the so called "flamelet" regime.

According to Peters (2000), a premixed flame usually consists of a preheating, an inner, and an oxidation layer, where the inner layer is "responsible for keeping the reaction processes alive". Due to this distinction of several sub-layers, the premixed flame thickness given by the length scale l_{fl} appears to be inadequate to represent the inner layer, which is usually ten times thinner. Using this estimate, a Karlovitz number can be defined which corresponds to the thickness l_δ of this inner layer, written as

$$\mathrm{Ka}_\delta = \frac{l_\delta^2}{\eta^2} \approx \frac{(l_{fl}/10)^2}{\eta^2} = \mathrm{Ka}\,/100\,. \qquad (3.21)$$

If $\mathrm{Ka}_\delta < 1$, the smallest eddies may be smaller than the overall flame thickness, and can therefore penetrate into the preheating layer. Nevertheless, these eddies are not considered to be small enough to enter the inner layer, hence this layer remains unaffected. The corresponding regime in Fig. 3.2 is called the "thin reaction zone" regime, and is located between the lines of $\mathrm{Ka} = 1$ and $\mathrm{Ka}_\delta = 1$. Finally, if $\mathrm{Ka}_\delta > 1$, the smallest eddies occurring in the flow are small enough to enter the inner layer. Accordingly, the time scales associated with these small eddies are smaller than a typical time scale of the chemical reactions as well. As a consequence, the turbulent mixing process is faster than the reactive process, and is therefore unaffected by the latter. Depending on the author, this regime is either referred to as the the regime of the well stirred reactor, the regime of broken reaction zones, or the thickened flame regime.

Turbulent motion affects also non-premixed flames, and a regime diagram can also be derived for these flames. However, it should be noted that, in contrast to premixed combustion, the demarcation of different combustion regimes in non-premixed flames can differ considerably between the individual authors, as they rely on different parameters to characterize the turbulence and the flame structure. In the present work, we follow an approach given by Poinsot & Veynante (2005), where turbulent diffusion flames are classified based on the values of the integral Reynolds number Re_{l_t} and the Damköhler number Da, as seen from Fig. 3.3. The authors argue that the diffusive time and length scales, $t_D = \chi_{\mathrm{st}}^{-1}$ and l_D, respectively, are determined by the Kolmogorov scales, so that $t_D = t_\eta$ and $l_D = \eta$. This assumption implies, that a Reynolds number written in terms of the diffusive time and length scales is equal to the Reynolds number based on the Kolmogorov scales

$$\mathrm{Re}_D = \frac{l_D^2 \chi_{\mathrm{st}}}{\mathcal{D}_Z} = \frac{u_\eta \eta}{\mu/\rho} = \mathrm{Re}_\eta \tag{3.22}$$

for unity Schmidt number $\mathcal{D}_Z \rho/\mu = 1$. Eq. (3.22) makes evident that the Reynolds number based on the diffusive scales becomes unity for Kolmogorov eddies, where $\mathrm{Re}_\eta = 1$.

Introducing a local Damköhler number

$$\mathrm{Da}_D = \frac{t_D}{t_{\mathrm{chem}}} = \frac{1}{\chi_{\mathrm{st}}\, t_{\mathrm{chem}}} = \frac{t_\eta}{t_{\mathrm{chem}}} \,, \tag{3.23}$$

which is defined as the ratio of the diffusive to the chemical time scale, different flame regimes can be distinguished. Following Kolmogorov's theory, this local Damköhler number can be related to an integral Reynolds number and the global Damköhler number by

$$\mathrm{Da}_D = \frac{t_\eta}{t_{\mathrm{chem}}} = \frac{t_\eta}{t_{l_t}} \frac{t_{l_t}}{t_{\mathrm{chem}}} = \mathrm{Re}_{l_t}^{-1/2}\, \mathrm{Da} \,, \tag{3.24}$$

hence the demarcation lines associated with a certain threshold value of Da_D exhibit a slope of $1/2$ in the double logarithmic scaling used in Fig. 3.3.

In the limit of very high values of $\mathrm{Da}_D > \mathrm{Da}_{D,\mathrm{LFC}}$, the chemistry is fast, and the flame is thin. This implies, that even the smallest Kolmogorov eddies cannot enter the reactive layers, and hence the flame structure is not affected by the turbulent motion, but is just convected as a whole and burns like a laminar flame. This regime is called the laminar flamelet regime, and is seen in the upper part of Fig. 3.3. For values of Da_D lower than a certain threshold $\mathrm{Da}_{D,\mathrm{LFC}}$, the time scales of t_D and t_{chem} attain values of the same magnitude, and unsteady effects come into play. Finally, for the lowest values of $\mathrm{Da}_D < \mathrm{Da}_{D,q}$, the mixing time is shorter than the characteristic time for the chemistry, and extinction occurs. The left part of Fig. 3.3 is occupied by the region of laminar flames, which is associated with an integral Reynolds number smaller than unity. In contrast to Poinsot & Veynante (2005), it is explicitly mentioned here that also laminar flames can be quenched, and hence the extinction region should reach into the laminar flow region, as denoted by the dashed line in Fig. 3.3.

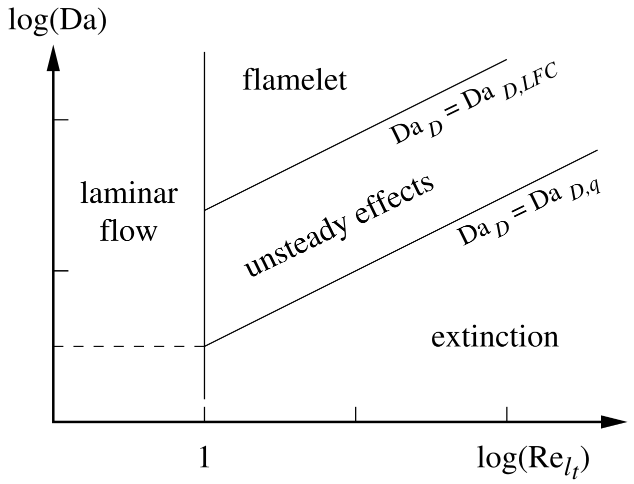

Figure 3.3: Regimes in non-premixed turbulent combustion. Replotted following Poinsot & Veynante (2005).

One major simplification has been assumed in the classification of combustion regimes, for the premixed as well as for the non-premixed case: In both cases, the turbulent flame regimes are classified assuming a one-way coupling between the turbulent motion and the flames, so that the flames do not feed back on the turbulent flow field, and Kolmogorov's theory on turbulent, non-reacting, flow can be still applied. In reality, the flow field can be severely affected by chemical reactions, which makes the extension of Kolmogorov's theory to reacting flows questionable. Nonetheless, it has become generally accepted in combustion literature to ignore the feedback of the flame on the flow in the classification of the different flame regions.

In the present work, where a lifted methane-air jet flame is investigated, two distinct flame zones are expected: As schematically shown in Fig. 3.4 a, a turbulent leading edge flame stabilizes at a certain lift-off height above the nozzle, facing the oncoming partially premixed reactants. As such, the leading edge flame basically belongs to a burning regime between the asymptotic limits of premixed and non-premixed combustion. As shown in the photograph in Fig. 3.4 b, the leading edge flame is indicated by an increased luminosity at the flame base. Downstream of this leading edge flame, a trailing diffusion flame is burning between the rich and the lean side. It has been outlined in the introduction Sec. 1.3, that the flame stabilization process associated with the propagation of the partially premixed turbulent leading edge flame is crucial for the operation conditions of technical combustion devices. Propagating into an inhomogeneous mixture of fuel and oxidizer, turbulent leading-edge flames can be neither assigned to any specific regime in the combustion nomogram of fully premixed combustion (Fig. 3.2), nor to any regime in the nomogram of fully non-premixed combustion (Fig. 3.3). This ambiguity clearly limits the scope of early works which assigned the turbulent leading edge flame either to fully

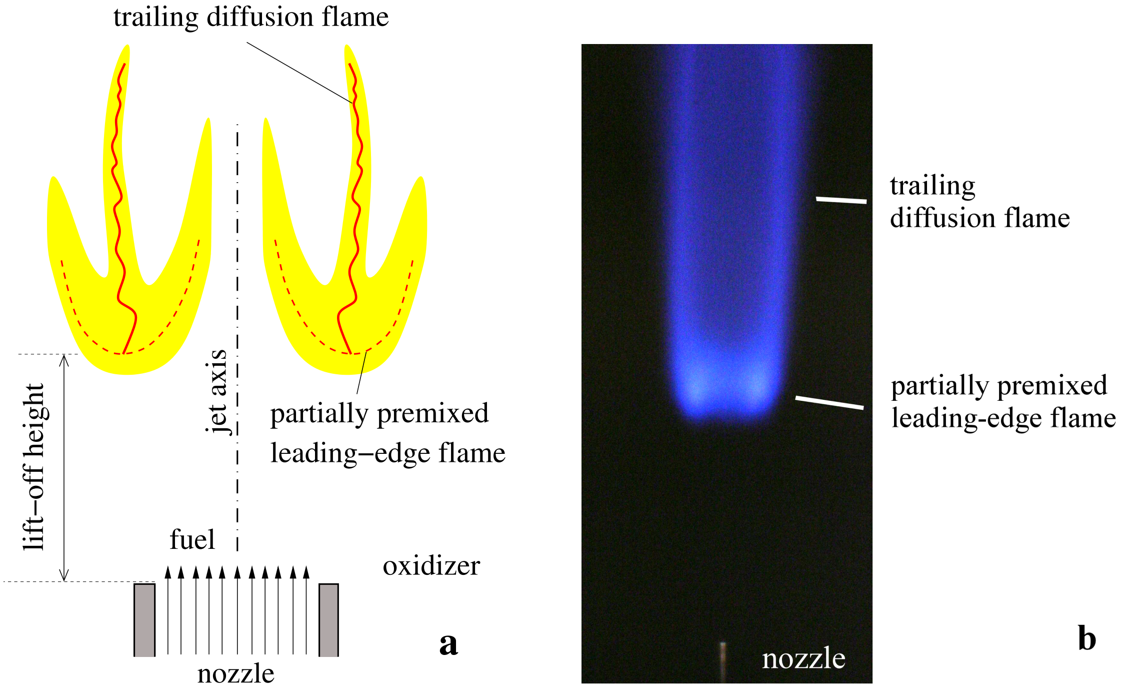

Figure 3.4: **a** Schematical illustration and **b** photograph of a turbulent, lifted methane-air jet. Photograph provided by Köberl *et al.* (2010).

premixed (Vanquickenborne & van Tiggelen, 1966), or to fully non-premixed combustion (Peters & Williams, 1983). Some theoretical computational studies on leading edge flames were performed by Ruetsch *et al.* (1995), Ruetsch & Ferziger (1996), Poinsot *et al.* (1996), Domingo & Vervisch (1996) and Nichols & Schmid (2008) for two-dimensional cases of stratified mixtures. These studies, which were mainly focused on laminar, or weakly turbulent flow, identified the so called "triple flame" structure, which was indicated first by Phillips (1965). As sketched in Fig. 3.5, a triple flame basically consists of a leading flame edge, to which three flame branches are attached: A branch, which is burning on the fuel-rich side $Z > Z_{\mathrm{st}}$, a branch, which is burning on the fuel-lean side $Z < Z_{\mathrm{st}}$, and a trailing diffusion flame burning at stoichiometric conditions $Z = Z_{\mathrm{st}}$. The formation of this bow-shaped triple flame structure can be certainly expected and explained on the principles of premixed flame propagation, where the flame speed decreases with increasing deviation from the stoichiometric conditions towards the lean or rich side. In the computational studies mentioned above these particular structure could be realized and investigated for rather academic burning conditions, assuming a two-dimensional laminar or weakly turbulent flow, and fairly high stoichiometric mixture fractions Z_{st}[‡]. For closer to real life conditions with comparatively small stoichiometric mixture fractions and three-dimensional turbulent flow, only one or two flame branches might exist (see the review of Chung 2007).

[‡] Nichols & Schmid (2008): $Z_{\mathrm{st}} = 0.33$; Ruetsch *et al.* (1995): $Z_{\mathrm{st}} = 0.5$.

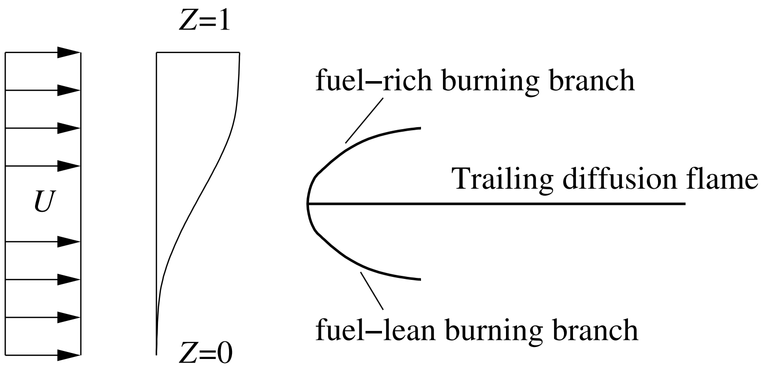

Figure 3.5: Schematical sketch of a triple flame.

In contrast to the leading edge flame the trailing diffusion flame can be classified in the regime diagram for non-premixed combustion (Fig. 3.3). Clearly, this flame will not belong to the extinction region in Fig. 3.3, which would conflict with the existence of the preceding leading edge flame. It is possible, that local extinction occurs at some points in the trailing diffusion flame, so that unsteady effects play a significant role. However, these events are not to be expected, as they would require a high local scalar dissipation rate, which is very unlikely to appear in this regions. The high viscosity and the low density, which are due to the high temperatures, usually lead to a relaminarization and a dampening especially of the small scale vortical motion. Therefore, the trailing diffusion flame in the present case rather corresponds to the laminar flamelet regime in Fig. 3.3. The one-dimensional solution of the flame structures in the laminar flamelet regime has become a well established concept for the modelling of non-premixed combustion. A laminar flamelet solution will be also used in the present work to initialize the reacting flow field. The Laminar Flamelet Concept (LFC) is briefly described in the next section.

3.2.5 Laminar flamelet concept

The diffusive thicknesses of both the premixed, as well as the non-premixed flames (l_{fl}, l_D) assume generally comparatively low values of the order of a millimeter and less (Eqs. 3.11, 3.17). Thus, compared to the typical dimensions of turbulent flow structures, the “thickness” of such flames can be substantially smaller than the size of the smallest Kolmogorov-eddies contained in a flow. This is generally the case for sufficiently low Karlovitz numbers (Eq. 3.20), which are, basically, equivalent to sufficiently high Damköhler numbers (i.e. “fast” chemistry). For such conditions falling into the flamelet regimes in the turbulent combustion nomograms (Figs. 3.2, 3.3), the reactive layers form comparatively thin laminar sheets, which are embedded in the underlying turbulent flow field. Such two-dimensional sheets, which are exemplarily illustrated in Fig. 3.6 for the non-premixed case, can be only wrinkled or corrugated by the three-dimensional turbulent motion. Since the comparatively large turbulent eddies do not penetrate into the reactive layer to perturb the reactive processes, the flame can be considered as laminar. Strong gradients of the flow quantities are expected in the direction normal to the flame, while the gradients in the tangential direction can be usually neglected. Accordingly, the so called Laminar Flamelet Concept (LFC) derives a description of flames burning in the flamelet regimes, where the convective/diffusive transport in the direction tangential to the flame surface are neglected, so that the flame structure can be described only dependent on the distance normal to the flame.

To derive the flamelet equations for non-premixed combustion, we start from a one-dimensional formulation of the conservation equation for an arbitrary species P obtained from Eq. (2.12), written as

$$\frac{\partial \rho Y_P}{\partial t} + \frac{\partial \rho u Y_P}{\partial x} = \frac{\partial}{\partial x}\left(\rho \mathcal{D}_P \frac{\partial Y_P}{\partial x}\right) + \rho\, \dot{\Omega}_P \,, \tag{3.25}$$

where x is the coordinate in the direction normal to the flame. Extracting the continuity equation (Eq. 2.2), Eq. (3.25) can be transformed into the so called non-conservative formulation, written as

$$\rho\left(\frac{\partial Y_P}{\partial t} + u\frac{\partial Y_P}{\partial x}\right) = \frac{\partial}{\partial x}\left(\rho \mathcal{D}_P \frac{\partial Y_P}{\partial x}\right) + \rho\, \dot{\Omega}_P \ . \tag{3.26}$$

The non-premixed flame, which is burning in the proximity of $Z = Z_{\mathrm{st}}$, separates the unburnt fuel ($Z = 1$) and oxidizer ($Z = 0$) streams, see Fig. 3.6. Due to diffusive mixing Z varies monotonously between these two limits. The mixture fraction Z is therefore bijective with x, and may serve as an independent transform variable for Eq. (3.26), so that $Y_P = f(x,t)$ can be expressed as $Y_P = f(Z,t)$. Introducing this change of variables a trans-

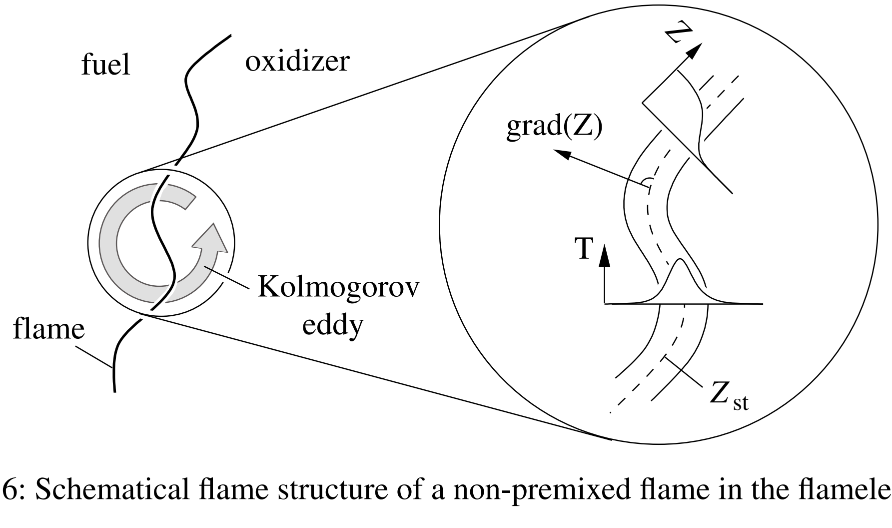

Figure 3.6: Schematical flame structure of a non-premixed flame in the flamelet regime.

port equation can be written in mixture fraction space as

$$\rho \frac{\partial Y_P}{\partial t} + \frac{\partial Y_P}{\partial Z}\left[\rho \frac{\partial Z}{\partial t} + \rho u \frac{\partial Z}{\partial x} - \frac{\partial}{\partial x}\left(\rho \mathcal{D}_P \frac{\partial Z}{\partial x}\right)\right] = \rho \mathcal{D}_P \left(\frac{\partial Z}{\partial x}\right)^2 \frac{\partial^2 Y_P}{\partial Z^2} + \rho\, \dot{\Omega}_P \ . \tag{3.27}$$

Assuming equal diffusivities for species, $\mathcal{D}_P$, and mixture fraction, $\mathcal{D}_Z$, the term written in square brackets on the LHS vanishes due to Eq. (3.14). Furthermore, the first term on the RHS may be rewritten introducing the scalar dissipation rate χ (Eq. 3.16). Dividing Eq. (3.27) by the density ρ, finally yields the unsteady laminar flamelet equation for species mass fractions

$$\frac{\partial Y_P}{\partial t} = \frac{1}{2}\,\chi\, \frac{\partial^2 Y_P}{\partial Z^2} + \dot{\Omega}_P \ . \tag{3.28}$$

Analogously to Eqs. (3.25 - 3.28), a flamelet equation can be derived for the temperature as well, which reads

$$\frac{\partial T}{\partial t} = \frac{1}{2}\,\chi\, \frac{\partial^2 T}{\partial Z^2} + \frac{1}{c_p}\sum_P \Delta h^0_{F,P}\, \dot{\Omega}_P \ . \tag{3.29}$$

As seen from the flamelet Eqs. (3.28, 3.29), the structure of non-premixed flames depends only on the two important key quantities, the mixture fraction Z, and the scalar dissipation rate χ, which basically incorporates the effects of the flow field. The reaction rate terms $\dot{\Omega}_P$ adopt non-zero values only in the vicinity of the stoichiometric mixture Z_{st}, where the mixing conditions are within the burning limits. As a consequence, only the scalar dissipation rate in the region around the stoichiometric surface is important for the solution of Eqs. (3.28) and (3.29), and the flame structure can be determined as $Y_P = Y_P\left(Z, \chi_{\mathrm{st}}\right)$ and $T = T\left(Z, \chi_{\mathrm{st}}\right)$. Based on this parameterization, solutions for non-premixed flames can be computed in a two-step process: In a first step, the flow field is solved, and, in a subsequent step, the obtained information in terms of Z and χ_{st} is used as an input for the solution of the flame structures embedded in the flow field. This method has become a well established combustion model for non-premixed turbulent flames.

For steadily burning flames, i.e. in the absence of transient effects like extinction or ignition, the transient terms on the LHS are neglected. The structure of diffusion flames is then obtained from the steady flamelet equations, written as

$$-\frac{1}{2}\,\chi\, \frac{\partial^2 Y_P}{\partial Z^2} = \dot{\Omega}_P \ , \quad \text{and} \quad -\frac{1}{2}\,\chi\, \frac{\partial^2 T}{\partial Z^2} = \frac{1}{c_p}\sum_P \Delta h^0_{F,P}\, \dot{\Omega}_P \tag{3.30}$$

These steady-state equations simply indicate that mixing is balanced by reaction. They cover two limiting cases for the flame structure. In the first case, when reactions are negligibly slow, the RHS of Eq. (3.30) vanishes. In such a non-reacting, pure mixing case, the profiles of species mass fractions Y_P and temperature T are linear functions of the mixture fraction, whose slopes are determined by the corresponding boundary values at $Z = \{0, 1\}$. This limiting case is illustrated in Fig. 3.7, where the physically possible regions for the

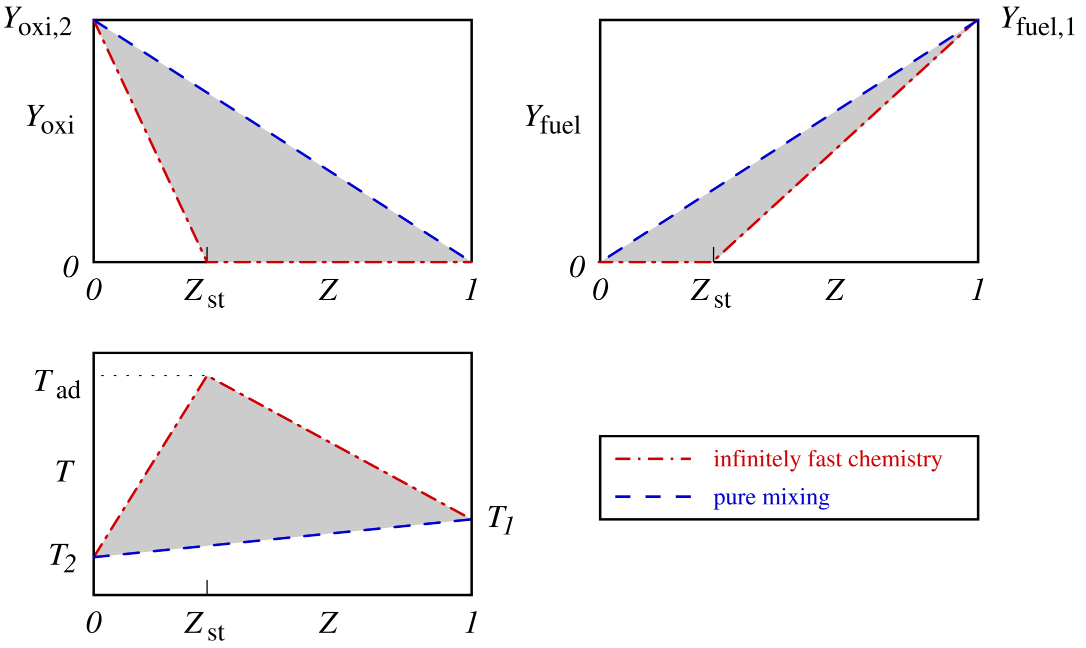

Figure 3.7: Possible regions of flames structures in mixture fraction (Z) space. The non-reacting limit is denoted by the "pure mixing" line, the Burke-Schumann flame structure is denoted by the "infinitely fast chemistry" lines.

flame structures of the oxidizer and fuel mass fractions, and the temperature are shown in the mixture fraction domain. The case of inert mixing is indicated as the "pure mixing" line.

In the second limiting case, the chemistry is assumed as irreversible and infinitely fast. In this case, generally termed "mixed = burned", all reactions occur infinitely fast at the stoichiometric point, so that fuel and oxidizer are immediately consumed to zero, $Y_{\mathrm{fuel,st}} = 0$, $Y_{\mathrm{oxi,st}} = 0$. All heat is released instantly at one spatial location, and there is no time for conductive losses. As a consequence, the temperature at Z_{st} is equal to the adiabatic flame temperature $T_{\mathrm{st}} = T_{\mathrm{ad}}$. According to Eq. (3.30), the curvature of Y_P and T becomes infinite at Z_{st}, which results in a sharp kink in the corresponding profiles. On either side of the stoichiometric point, $Z = Z_{\mathrm{st}}$, the fuel and the oxidizer mass fractions, as well as the temperature are piecewise linear functions of Z. This particular case, which is in literature mostly referred to as Burke-Schumann limit, is shown as well in Fig. 3.7, where the corresponding lines are labelled as "infinitely fast chemistry".

For real diffusion flames all states which can be realized must lie between the two limits limits discussed above. In Fig. 3.7, these states are denoted by the grey shaded areas. The exact profile of a steadily burning laminar flamelet solution in the mixture fraction space is determined by the scalar dissipation rate χ_{st}, where, for the irreversible case, $\chi_{\mathrm{st}} \to 0$ corresponds to the asymptotic limit of infinitely fast chemistry, and $\chi_{\mathrm{st}} > \chi_{\mathrm{st,q}}$ corresponds to the pure mixing case after flame extinction. For high activation temperatures, which are usually only a few hundred Kelvin below the adiabatic flame temperature, and scalar dissipation rates below the quenching limit $\chi_{\mathrm{st}} < \chi_{\mathrm{st,q}}$, all burning flame states lie close to the lines associated with infinitely fast chemistry. Once, quenching occurs, the profiles in Z-space move quickly towards the corresponding pure mixing lines. Thus, the relevance of local extinction/ignition phenomena can be demonstrated by plotting experimentally or computationally obtained scalars in Z-space.

4 ONE-DIMENSIONAL FLAME ANALYSIS

4.1 Objectives

In the laminar regime, there exist a few canonical flame configurations which allow for a one-dimensional computation and analysis of the flame structure. In the present study, one-dimensional flames were computed and analyzed for the following reasons:

- Three-dimensional DNS of turbulent reactive flow is a non-trivial task. Due to a high computational demand, in combination with a limited computational power, the discretization in the spatial as well as in the temporal domain is a critical issue. This severe restriction has to be accounted for, when a three-dimensional DNS is set up to avoid a consideration of parameter settings which cannot be resolved numerically with the available resources. To do so, the resolution requirements dictated by the flow and chemistry should be known already a priorily. The resolution requirements for the relevant turbulent flow structures are determined by the size of the Kolmogorov scale, which basically can be obtained only a posteriori[*]. The resolution requirements for the flame structures are usually more stringent, and they are essentially determined by the size of a minimum flame thickness. The estimates given in Sec. 3.2 for the (minimum) diffusive length scales l_{fl} and $l_{D,q}$ are fairly crude, as they represent rather global, or, integral quantities. For multi-step, finite-rate chemistry the inner structure of a flame constituted by the reactive layers may exhibit sub-scales considerably different from these global scales. A one-dimensional flame analysis provides therefore a numerically inexpensive way to obtain very reliable estimates for the expected flame sizes, and consequently, for the resolution requirements.

- When choosing a specific reduced reaction mechanism, it must be ensured that this mechanism reproduces accurately certain characteristics of the considered chemical system, like the laminar flame speed s_L, and is therefore capable do deliver realistic results. Again, one-dimensional computations represent a useful approach to evaluate a given reaction mechanism, and to compute the characteristic values of interest in a most efficient way.

- The initialization of a DNS of a three-dimensional reacting flow field can be a tedious task. Imposing “hot spots” in the flow domain to trigger locally ignition is

---

[*] Since lifted flame front tends to relaminarize the incoming flow due to a strong increase in the kinematic viscosity, save estimates for the smallest flow structures can be obtained from a non-reacting precursor DNS of a reference case.

computationally not very efficient. After such a local ignition the computation has to be run for a very long time until a statistically steady state of the reacting flow field is reached. Alternatively, if results for simpler one-dimensional flames are already at hand, they can be efficiently mapped into the three-dimensional flow fields using the already discussed laminar flamelet concept. This alternative approach for flame initialization produces a flow field which is much closer to the final statistically converged state.

4.2 Considered flame configurations

For the one-dimensional flame analysis, two canonical flame configurations were chosen. These are:

1. A premixed, unstrained, steady and planar laminar plug flow flame. In this case, illustrated in Fig. 4.1, a premixed mixture of fuel and oxidizer enter a pipe at the laminar flame speed s_L. Due to this upstream condition the flame resides at a fixed streamwise position in the pipe, where it separates the burnt from the unburnt gases. This generic configuration is used for a detailed analysis of laminar premixed flame structure, as well as the computation of the laminar flame speed s_L. Clearly, such an ideal configuration is hardly to realize in experiments. Due to the existence of wall boundary layers, the flame front does not remain planar near the wall. Additionally, the basic impossibility of perfectly uniform upstream flow-conditions, as well as the real heat loss conditions, generally lead to a pre- or receding of the flame, if the measurements are not perfectly tuned. For this reasons, usually mildly strained flames are measured in cones or combustion bombs. However, using a specially adapted experimental design the measured cases can be closely matched to the ideal reference case, and therefore a rich database can be found for experimental values of the (unstrained) flame speed to compare with.

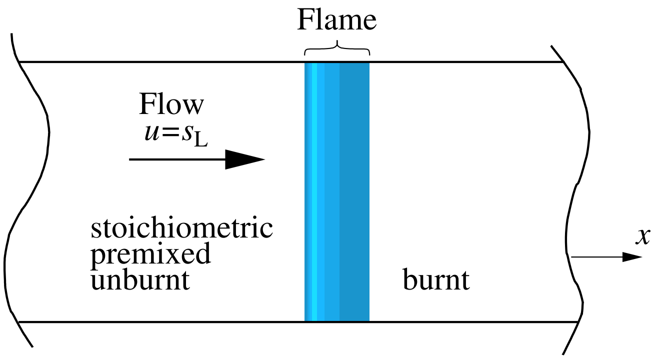

Figure 4.1: Plug flow flame.

2. A non-premixed, strained, axisymmetric steady laminar counterflow flame. In this case, fuel and oxidizer are supplied to the flame separately from two sides through an opposed jet flow configuration as illustrated in Fig. 4.2. A one-dimensional description of this case is possible along the axis of the opposed jets, where all cross-stream derivatives vanish except that of the cross streamwise velocity. Two distinct points along this axis can be found: The point of stagnation x_{stag}, where the flow velocity $u = 0$, and the point of stoichiometric mixing x_{st}, which corresponds to the position of the flame. When computing for counterflow flames, not only the structure of a steadily burning non-premixed flame can be studied, but also the extinction characteristics dependent on the strain rate a_q, or the scalar dissipation rate χ_q at quenching conditions. A limited amount of experimental data exists also for these quenching parameters, which will be later reviewed when discussing the computational results.

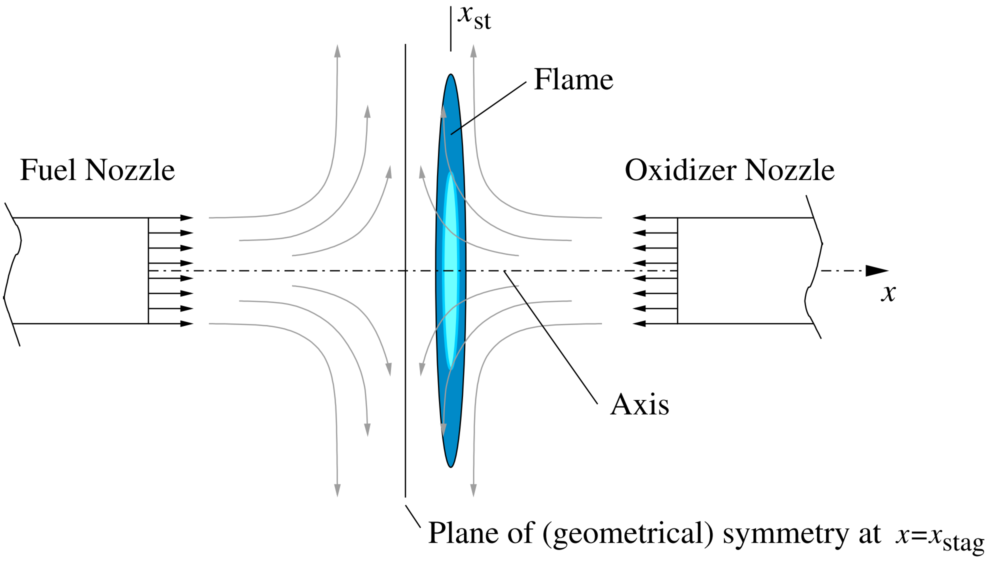

Figure 4.2: Counterflow flame.

4.3 Numerical solution procedure

The numerical solution procedure discussed in the following is almost identical for both the plug flow and the counterflow cases. In principle, the reacting flow field of the two cases is governed by the fully three-dimensional set of equations given in Chp. 2. However, when restricting oneself to a purely one-dimensional study, some peculiarities arise in the solution for the flow velocity normal to the flame u. For the stationary plug flow case, the solution for the flow velocity u is obtained straightforwardly through the continuity equation, and is written as

$$u = u_1 \frac{\rho_1}{\rho} \ , \tag{4.1}$$

where the subscript 1 refers to the fuel inlet.

For the counterflow configuration, the velocity field on the axis of symmetry cannot be obtained directly from the one-dimensional versions of the mass and momentum conservation equations (Eq. 2.2 and 2.6) without further assumptions. In the present work, the derivation for the velocity field follows an approach given in the book of Poinsot & Veynante (2005), where the flow field between the nozzles is assumed as an inviscid stagnation point flow. In the constant-density case the velocity field of this flow is given by

$$\frac{\partial u}{\partial x} = -\frac{\partial v}{\partial y} = -a \tag{4.2}$$

essentially dependent on a given strain rate a. To incorporate the dilatational effects of a flame, the Eulerian formulation given in Eq. (4.2) is rewritten in Lagrangian coordinates (Fig. 4.3), using the so called Howarth-Dorodnitzyn transformation

$$X = \frac{1}{\rho_0} \int_{x_0}^{x} \rho\left(\tilde{x}\right) d\tilde{x} \ , \tag{4.3}$$

where the subscript 0 corresponds to a reference point, which is assumed to be the stagnation point $x_0 = x_{\text{stag}}$. Based on the transformations

$$\begin{aligned} x\,,\,y \quad &\longrightarrow \quad X\,,\,Y \\ u\,,\,v \quad &\longrightarrow \quad \rho u\,,\,\rho v \\ u = -ax \quad &\longrightarrow \quad \rho u = -\rho_0 a X\ , \end{aligned} \tag{4.4}$$

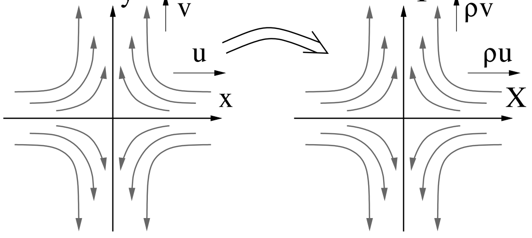

Eulerian space Lagrangian space

Figure 4.3: Schematical illustration of the mapping from Eulerian to Lagrangian frame of reference.

the velocity u can be obtained as

$$u = -a\,\frac{\rho_0}{\rho}\,X = -\frac{a}{\rho}\int_{x_0}^{x} \rho\,(\tilde{x})\,d\tilde{x}\,. \tag{4.5}$$

Using the solutions for the velocity variation of the plug flow and the counterflow configurations obtained from Eqs. (4.1) and (4.5), respectively, the flame structure is computed from the transport equations for the species mass fractions Y_P and the temperature T (refer Sec. 2.1, Eqs. 2.12 and 2.20).

In a one-dimensional non-conservative form, they can be written as

$$\rho\left(\frac{\partial Y_P}{\partial t} + u\frac{\partial Y_P}{\partial x}\right) = \frac{\partial}{\partial x}\left(\frac{\lambda}{c_p}\frac{\partial Y_P}{\partial x}\right) + \rho\dot{\Omega}_P\,, \tag{4.6}$$

$$\rho\left(\frac{\partial T}{\partial t} + u\frac{\partial T}{\partial x}\right) = \frac{1}{c_p}\frac{\partial}{\partial x}\left(\lambda\frac{\partial T}{\partial x}\right) + \frac{\rho}{c_p}\sum_P \Delta h^0_{F,P}\,\dot{\Omega}_P\,. \tag{4.7}$$

The appearance of the thermal conductivity in the species transport Eq. (4.6) results from the unity Lewis number assumption already discussed in Chp. 2.

In the present work, Eqs. (4.6) and (4.7) are numerically solved using a finite-difference formulation. As the presently employed discretization scheme is basically equal for both temperature and species mass transport, the scheme is exemplarily outlined for the species mass transport only. The finite-difference formulation of Eq. (4.6) at grid point x_i reads

$$\begin{aligned}
&\frac{\partial Y_{P,i}}{\partial t} + u_i\frac{Y_{P,i+1} - Y_{P,i-1}}{2\,\Delta x_i} = \dot{\Omega}_{P,i} \\
&+\frac{1}{2\,\Delta x_i\,\rho_i}\left[\underbrace{\left(\frac{\lambda_{i+1}}{c_{p,i+1}} + \frac{\lambda_i}{c_{p,i}}\right)}_{\mathrm{dd}_{i+\frac{1}{2}}}\frac{Y_{P,i+1} - Y_{P,i}}{\Delta x_{i+\frac{1}{2}}} - \underbrace{\left(\frac{\lambda_i}{c_{p,i}} + \frac{\lambda_{i-1}}{c_{p,i-1}}\right)}_{\mathrm{dd}_{i-\frac{1}{2}}}\frac{Y_{P,i} - Y_{P,i-1}}{\Delta x_{i-\frac{1}{2}}}\right]\,,
\end{aligned} \tag{4.8}$$

where the arithmetic mean transport coefficients of the neighbouring points are lumped into a variable dd, which is used in the further formulation. For stability reason, the integration in time applies a semi-implicit scheme for the temporal discretization of the diffusive transport term. The stability restrictions associated with the advective term are less stringent, so that it is discretized explicitly. The chemical source term is discretized explicitly as well, in order to avoid a nonlinear formulation which has to be solved iteratively. The temporally and spatially discretized scheme, which is presently solved, reads

$$\begin{aligned}
&\frac{Y^{n+1}_{P,i}}{\Delta t} + \frac{\beta}{2\,\Delta x_i\,\rho_i}\left[-Y^{n+1}_{P,i-1}\cdot\mathrm{dd}_{i-\frac{1}{2}} + Y^{n+1}_{P,i}\left(\mathrm{dd}_{i-\frac{1}{2}} + \mathrm{dd}_{i+\frac{1}{2}}\right) - Y^{n+1}_{P,i+1}\cdot\mathrm{dd}_{i+\frac{1}{2}}\right] \\
&= \frac{Y^n_{P,i}}{\Delta t} + u_i\frac{Y^n_{P,i-1} - Y^n_{P,i+1}}{2\,\Delta x_i} + \dot{\Omega}_{P,i} \\
&+\frac{1-\beta}{2\,\Delta x_i\,\rho_i}\left[-Y^n_{P,i-1}\cdot\mathrm{dd}_{i-\frac{1}{2}} + Y^n_{P,i}\left(\mathrm{dd}_{i-\frac{1}{2}} + \mathrm{dd}_{i+\frac{1}{2}}\right) - Y^n_{P,i+1}\cdot\mathrm{dd}_{i+\frac{1}{2}}\right]\,.
\end{aligned} \tag{4.9}$$

Therein, the parameter β can be set between $\beta = 0$ and $\beta = 1$, implying a fully explicit/implicit treatment of the diffusion term. For the implicit case with $\beta \neq 0$, a tridiagonal linear system of equations has to be solved for $Y_{P,i}^{n+1}$, which is done directly using a Thomas algorithm. For the present study, an implicitness factor of $\beta = 0.5$ was chosen.

4.4 Results

A code was written in C++ for the discretized system of equations outlined in the previous section using the two-step chemistry given in Chp. 2. The results will be illustrated in the following.

4.4.1 Premixed plug flow flame

As a most fundamental test, a stoichiometrically premixed methane-air flame ($\phi = 1$) was computed for the plug flow configuration. The air was assumed as a binary oxygen-nitrogen mixture containing 20.94% oxygen by volume. In this case the stoichiometric mixture is composed of the following mass fractions of methane, oxygen and nitrogen:

$$Y_{\mathrm{CH}_4} = 0.055, \quad Y_{\mathrm{O}_2} = 0.219, \quad Y_{\mathrm{N}_2} = 0.726\,. \tag{4.10}$$

Prescribing this mixture at the inflow boundary of the plug flow reactor, together with an inflow temperature of $T_1 = 300\,[K]$, yielded a laminar flame speed of $s_L = 0.396\,[m/s]$, which is well in accordance with experimentally measured values (Gu *et al.* 2000, Law *et al.* 2003). The same applies for the maximum (adiabatic) flame temperature, which was computed to be $T_{\mathrm{ad}} \approx T_{\max} = 2315\,[K]$ (see Smooke & Giovangigli 1991*b*).

A second test case of premixed combustion was computed, where the reactive mixture is diluted with some additional nitrogen, so that the stoichiometric composition is written as

$$Y_{\mathrm{CH}_4} = 0.052, \quad Y_{\mathrm{O}_2} = 0.208 \quad \text{and} \quad Y_{\mathrm{N}_2} = 0.74\,. \tag{4.11}$$

This particular mixture will be of relevance later in the three-dimensional computations. Using this mixture, a significantly lower flame speed of $s_L = 0.308\,[m/s]$ was obtained, which can be explained by the additional inert mass which needs to be preheated by the flame. This additional thermal resistance also leads to a somewhat lower (adiabatic) flame temperature of $T_{\mathrm{ad}} \approx T_{\max} = 2289\,[K]$

The structure of the diluted premixed flame can be seen in Fig. 4.4, where the quantities of major interest are illustrated. In this figure, the inflow is located on the left side at $x = 0$, and the outflow is located on the right side. The profile for the temperature T is shown in Fig. 4.4 a, where an approximate thermal thickness of the flame can be estimated as

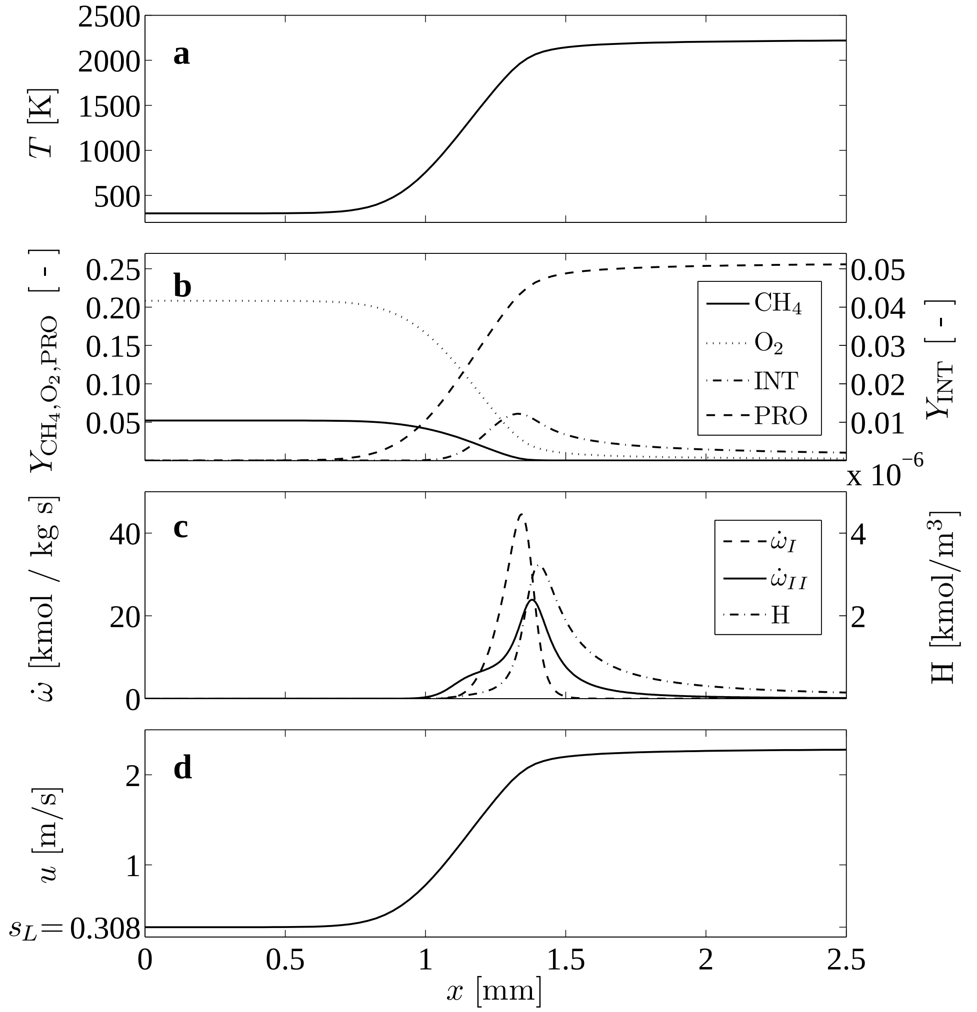

Figure 4.4: Flame structure of a nitrogen-diluted, premixed methane-air flame: **a** temperature, **b** species mass fractions, **c** reaction rates and hydrogen radical concentration, and **d** velocity.

0.5 mm. This quantity is a factor of 10 bigger than the estimate given by Eq. (3.11) for a thermal flame thickness l_{fl}, which was computed using the thermal diffusivity of cold air[†].

The curves for the species mass fractions are shown in Fig. 4.4 b. It can be seen, that the profile of the product (composed of CO_2 and H_2O) mass fraction basically follows the trend of the temperature profile, which is due to the fact that most reactive heat is released when the product species is formed. For the intermediate species (composed of

---

[†] Using values of air at the adiabatic flame temperature, and the lower flame speed of 0.3 $[m/s]$ yields a flame thickness of 1.6 $[mm]$, which matches the real situation somewhat better, but nevertheless only crudely.

CO and H_2) rather low mass fractions are observed. The profile extends notably far into the hot region. This observation can be explained by the negative temperature exponent of the reaction rate for the intermediate species consuming reaction $\dot{\omega}_{II}$ (Eq. 2.41), which attenuates the reaction at high temperatures. This reasoning is also supported by Fig. 4.4 c, where the reaction rates and the hydrogen radical concentration are plotted. The tendency of $\dot{\omega}_{II}$ to react the intermediate species preferably on the low temperature side of the flame is manifested by the bump in the profile protruding into the cold zone, which is adjacent to the layer, where the intermediate species are produced by $\dot{\omega}_{I}$.

The profiles for the reaction rates have in common that they increase rapidly to peak values inside very thin layers, which is most challenging for the numerical resolution. According to literature, the humps in the $\dot{\omega}$ profiles should be resolved using at least 10 gridpoints to compute the value of the laminar flame speed within acceptable error bounds. For the present case, where the widths of the peaks in the profiles have an extension of approximately $0.1\,[mm]$, this resolution criterion would require a maximum grid spacing of $\Delta x \approx 10\,[\mu m]$.

The velocity is plotted in Fig. 4.4 d. Clearly visible is the effect of volumetric dilatation, which leads to a significant acceleration of the flow downstream of the flame.

4.4.2 Non-premixed counterflow flame

For the counterflow configuration, again two test cases are considered. In the first case, the fuel stream consists of pure methane, and the opposed oxidizer stream is pure air, so that the stoichiometric mixture fraction is $Z_{\mathrm{st}} = 0.055$. For the temperature of both the fuel and oxidizer streams a value of $T_1 = T_2 = 300\,[K]$ was assumed again.

The reliability of the one-dimensional description and, more importantly, the employed kinetic mechanism is commonly assessed by comparing the computationally predicted flame quenching against experimental data. While the scalar dissipation rate at quenching $\chi_{\mathrm{st},q}$ is provided by the computational results, the experimental measurement of this quantity is very difficult and therefore rare. Therefore, the present comparison is rather based on the (global) strain rate at quenching a_q, which is defined in Eq. (4.4), and is strongly related to $\chi_{\mathrm{st},q}$. Since experimental measurements of the strain rate are still very tedious, many experimental works (e.g. Lee *et al.* 2006) resort to express the (global) strain rate using the simple formula

$$a = \frac{2}{L_{\mathrm{sd}}} \left(U_{\mathrm{oxi}} + U_{\mathrm{fuel}} \sqrt{\frac{\rho_{\mathrm{fuel}}}{\rho_{\mathrm{oxi}}}} \right) , \tag{4.12}$$

where L_{sd} denotes the spatial distance between the fuel and oxidizer nozzles. This correlation is essentially based on an analytical solution obtained by Seshadri & Williams (1978) in the limit of inviscid flow. Based on the rate of strain, experimentally measured, or, obtained from Eq. (4.12), the scalar dissipation rate at quenching can be estimated using a formula due to Peters (1997), written as

$$\chi_{\mathrm{st},q} = \frac{a_q}{\pi} \exp\left\{-2\left[\mathrm{erfc}^{-1}\left(2Z_{\mathrm{st}}\right)\right]^2\right\} . \tag{4.13}$$

For the pure methane-air counterflow flame, the presently computed values for a_q and χ_q are compared against those obtained by previous computational and experimental studies. The values for both quantities are given in Tab. 4.1, and good agreement is found for the presently obtained values. The maximum flame temperature at quenching is computed to be $T_{\mathrm{max},q} = 1856\,[K]$, which is almost $100\,[K]$ higher than experimentally measured values. This discrepancy is attributed to the strongly reduced two-step mechanism, which is is employed in the present work. It was also observed in the computational study of Smooke & Giovangigli (1991*b*), who obtained considerably higher values for $T_{\mathrm{max},q}$ when employing a reduced mechanism, as compared to a more detailed skeletal mechanism.

Analogously to the considered premixed cases, a second, non-premixed test case was computed, where the fuel stream was diluted with nitrogen, so that it consists of $Y_{\mathrm{CH}_4,1} = 0.498$ and $Y_{\mathrm{N}_2,1} = 0.502$. The stoichiometric mixture for this case ($Z_{\mathrm{st}} = 0.104$) corresponds to the state of the unburnt premixed gas in the nitrogen-diluted premixed case (Sec. 4.4.1). The diluted non-premixed flame configuration shows again, that the dilution with nitrogen increases the chemically inert mass, whose heat-up requires a larger portion of the reactive heat produced by the flame. This effectively reduces the speed of the chemical reactions, and extinction is observed at lower strain values as compared to the pure methane case. The quenching values which are obtained for this flame are $\chi_{\mathrm{st},q} = 22\left[s^{-1}\right]$ and $a_q = 335.5\left[s^{-1}\right]$, respectively, and they agree well with the experimentally obtained results of $a_q = 374.9\left[s^{-1}\right]$ obtained by Lee *et al.* (2006). Similar to the pure methane case, the maximum flame temperature at quenching conditions $T_{\mathrm{max},q} = 1819\,[K]$ is overpredicted again by approximately $100\,[K]$ in comparison with the experiments.

Source	a_q	$\chi_{\mathrm{st},q}$	type
present study	534	12.4	computation
Tsuji & Yamaoka (1969)	640	15.8	experiment
Puri & Seshadri (1986)	540	13.3	experiment
Chelliah *et al.* (1993)	≈ 550	≈ 18	computation
Du & Axelbaum (1996)	750	18.3	experiment
Peters (1997)	550	13.6	computation

Table 4.1: Strain and scalar dissipation rates for non-premixed pure methane-air counterflow flames as obtained by different authors. For experimental works, the strain rates are expressed according to Eq. (4.12), and the values of the scalar dissipation rates are estimated according to Eq. (4.13).

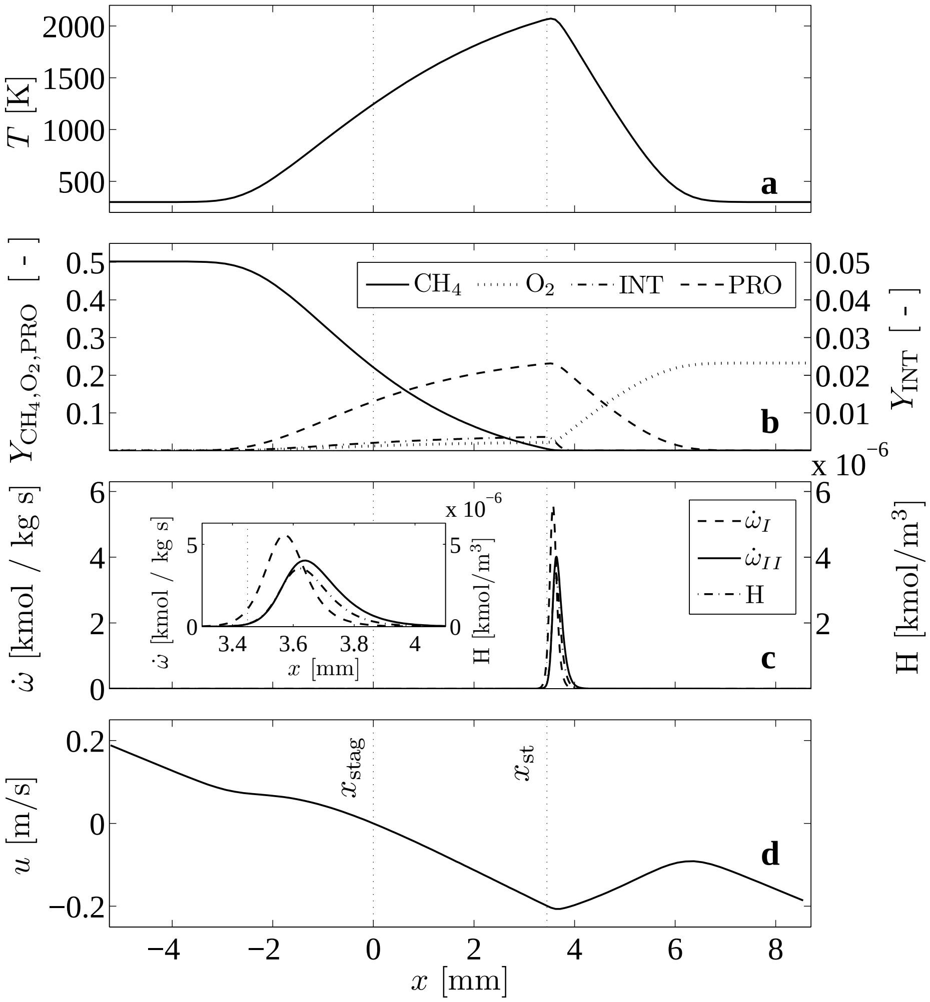

Figure 4.5: Flame structure of a diluted methane-air counterflow flame ($Z_{st} = 0.104$) at a strain rate of $a = 50\ \left[s^{-1}\right]$: **a** temperature, **b** species mass fractions, **c** reaction rates and hydrogen radical concentration, and **d** velocity.

The structure of this nitrogen-diluted methane-air counterflow flame can be seen in Fig. 4.5, for a burning state sufficiently far from quenching at $a = 50\ \left[s^{-1}\right]$. In the shown results, the fuel nozzle is located on the left hand side, and the oxidizer nozzle is located on the right hand side. The location of the point of stagnation, where $u = 0$, is denoted in all subfigures by a thin dotted vertical line at $x_{stag} = 0$. The location of the stoichiometric mixture is also marked by a thin dotted vertical line, and it is indicated by x_{st}.

The temperature of the flame is shown in Fig. 4.5 a. It can be seen, that non-premixed flames can exhibit (thermal) flame thicknesses of substantially increased size when compared to the premixed case. For the shown flame, the thermal thickness turns out to be approximately 8 $[mm]$.

The profiles for the species mass fractions are plotted in Fig. 4.5 b. Similar to the premixed case, it can be observed that the curve for the product mass fraction matches well with temperature. For the curve of oxygen, non-zero values are observed on the fuel-rich side $x < x_{\text{st}}$. This behaviour is also seen in experiments, and is evidently predicted by the employed two-step reaction mechanism[‡]. As a consequence of the oxygen leakage through the reaction zone, also non-zero values for the intermediate species are observed on the rich side.

The reaction rate terms $\dot{\omega}$, together with the hydrogen radical concentration H, are illustrated in Fig. 4.5 c. It can be clearly seen, especially in the zoomed insert, that the reaction which corresponds to fuel breakup $\dot{\omega}_I$ is located closer to the fuel-rich side, whereas the second reaction $\dot{\omega}_{II}$ is shifted towards to the oxidizer side. Nonetheless, the major part of both profiles appears on the lean side, where $Z < Z_{\text{st}}$. Consistent with the findings in the premixed case, it can be conjectured that the observed behaviour is linked to the negative temperature exponent of the main oxidation reaction $\dot{\omega}_{II}$ (Eq. 2.41), which would bias the peak in the $\dot{\omega}_{II}$ profile to the colder, lean side of the mixture. This behaviour would consequently also bias the fuel breakup reaction $\dot{\omega}_I$ somewhat to the lean side, where it is able to benefit from the heat released by the other reaction $\dot{\omega}_{II}$.

In contrast to the premixed case, it is obvious for the non-premixed case that the thickness of the reactive layers is much smaller than the thermal thickness of the flame. In the present case, the $\dot{\omega}$ "humps" exhibit a spatial extension of approximately 0.2 $[mm]$, which is only negligibly larger than in the premixed case. This observation has a severe impact on the resolution requirements for large-scale computations: Similar to the premixed case, the $\dot{\omega}$ humps in the non-premixed case should be resolved using at least 10 gridpoints. Having to resolve the flame structures also close to extinction, where the reaction rate profiles are roughly only half as thin as those shown in Fig. 4.5, the required resolution needs to be of the same magnitude as in the premixed case ($\Delta x = 10\,[\mu m]$) discussed above.

Fig. 4.5 d shows the velocity profiles. The effect of the flame on the flow field described in Eq. (4.5) is clearly visible, especially on the oxidizer side, where the dilatation decelerates the oncoming flow, so that the velocity does not decrease monotonously to the negative inflow velocity prescribed at the oxidizer inflow boundary. In an Eulerian frame of reference, the position of the reactive layers remains steadily at a fixed location in space. However, as can be seen from the profiles depicted in Fig. 4.5, the reactive layers are not located at the stagnation point x_{stag}, but near the position of the stoichiometric mixture x_{st}, where the velocity is non-zero. This implies, that in the specific case of a counterflow diffusion flame, the flame is propagating at a certain velocity, which is generally not the case for all diffusion flame configurations, e.g. in the mixing layer of diffusive jet flames.

[‡] A single-step mechanism would not be able to produce this phenomenon.

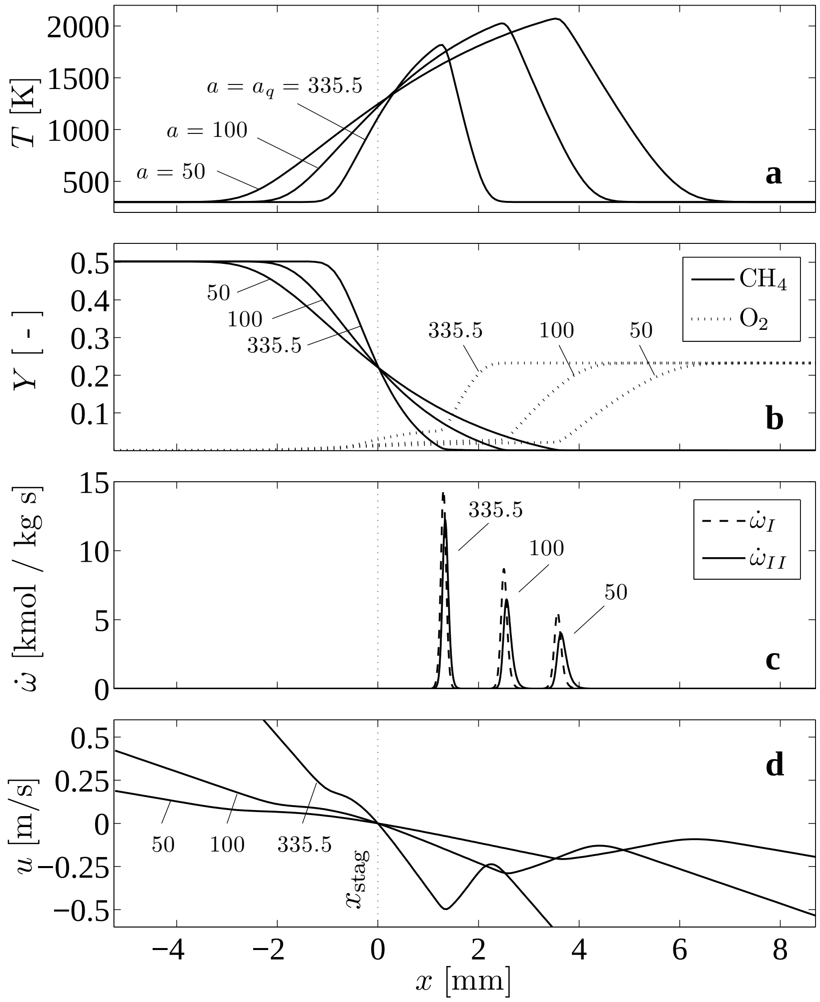

Figure 4.6: Quenching process of a diluted methane-air counterflow flame ($Z_{st} = 0.104$), captured at three different strain rates $a = 50,\ 100,\ 335.5\ \left[s^{-1}\right]$: **a** temperature, **b** species mass fractions, **c** reaction rates and **d** velocity.

The extinction behaviour is studied in more detail in Fig. 4.6. The shown curves are obtained for three increasing strain rates, where the strain rate a_q represents the maximum value associated with a steadily burning flame. For $a > a_q$ flame quenching occurs. As a primary effect of increased strain, it becomes evident that the flame becomes more compressed by the increased momentum of the opposed feed streams reducing the thickness of the flame. For infinitely fast chemistry, the increased supply of fresh reactants associated with the higher strain rates would inevitably result in higher conversion rates. This tendency is also observed for the presently considered finite rate chemistry, as can be seen from Fig. 4.6 c. The increased heat release due to the intensified reactive processes leads also to a stronger volumetric dilatation, which further impedes the oncoming flow, as indicated by the more pronounced local maxima in the velocity curves on the oxidizer side in Fig. 4.6 d. On the other hand, the temperature curves in Fig. 4.6 a show, that the increased reactive heat release does not fully compensate the also increased diffusive heat losses towards both sides with the incoming reactants, so that the maximum flame temperature is decreasing with increasing strain rate. This observation is also consistent with the fact that greater portions of oxygen leak through the reaction zone, as shown in Fig. 4.6 b.

It has become common practice in the analysis of non-premixed flames to illustrate the quenching behaviour of a particular flame by plotting the maximum flame temperature over the inverse of the applied strain rate. The corresponding curves are shown in Fig. 4.7 for both considered stoichiometric mixing conditions (pure and diluted methane feed). The shown curves basically represent the stably burning upper branch of the so called “s-shaped curve”, which essentially illustrates the dependence of the maximum flame temperature on the characteristic mixing time represented by $a^{-1}[s]$ until the limit of extinction. It is obvious, that with decreasing mixing time scales, i.e. with enhanced mixing, the maximum temperature decreases due to the limited supply of reactive heat released at a finite rate. At a certain point, when flame quenching occurs (a_q^{-1}), the curves exhibit vertical slopes as indicated by the dashed lines in Fig. 4.7. At this point, any further increase in the strain rate a reduces the temperature below the activation temperature, so that the flame extincts. It can be clearly seen from Fig. 4.7, that the pure methane flame ($Z_{\mathrm{st}} = 0.055$) is more robust w.r.t. extinction, i.e. quenching occurs at smaller mixing time scales a^{-1} or larger strain rates a when compared with the nitrogen diluted flame ($Z_{\mathrm{st}} = 0.104$). This behaviour

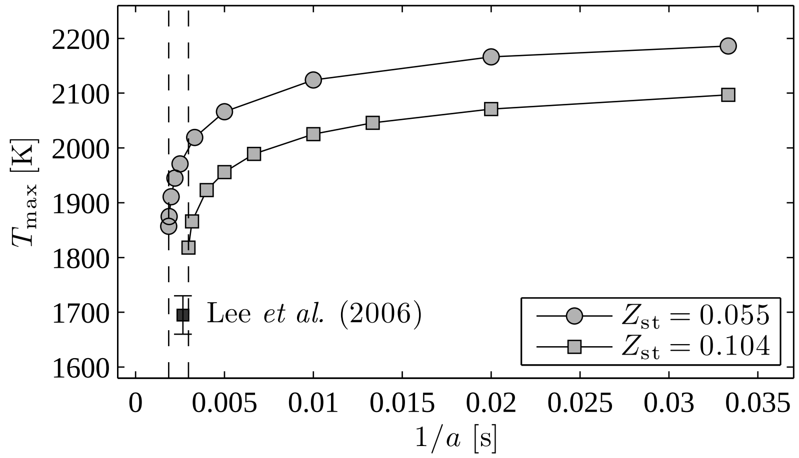

Figure 4.7: Stably burning branches of the s-shaped curves for a pure ($Z_{\mathrm{st}} = 0.055$) and a diluted ($Z_{\mathrm{st}} = 0.104$) methane-air flame. For both mixtures, the vertical dashed lines denote the characteristic mixing time at quenching as indicated by the simulations. For the nitrogen-diluted case, the quenching value measured by Lee *et al.* (2006) is indicated by the candlestick.

can be attributed to the presence of a higher fraction of inert mass which is heated in the diluted case. Accordingly, at equal strain rates, the maximum flame temperature is notably higher for the pure methane case. A further interesting detail which is shown by the s-shaped curves is the lower quenching temperature for the diluted case, a tendency which is consistent with the experiments of Lee *et al.* (2006) and Du & Axelbaum (1996).

The solutions of the one-dimensional counterflow flame analysis prove very useful later, when large-scale three-dimensional simulations need to be initialized, and the results of the three-dimensional simulations are interpreted. For this purpose, the one-dimensional solutions for the flame structure are mapped from the spatial coordinate x into the mixture fraction space Z. The profiles for the flame structure in this Z-space are exemplarily illustrated in Fig. 4.8, for the diluted methane-air case ($Z_{\mathrm{st}} = 0.104$) near the quenching limit ($a \approx a_q$). On the first sight, the profiles appear very similar to the flame structure in the Burke-Schumann limit (Fig. 3.7). However, in contrast to the Burke-Schumann solution, it is clearly visible from Fig. 4.8 a, that the maximum flame temperature remains substantially below the adiabatic flame temperature of $T_{\mathrm{ad}} \approx 2289\,[K]$. Furthermore, the effect of finite rate chemistry is also visible from the finite curvature in the temperature profile at $Z = Z_{\mathrm{st}}$. For the shown state close to extinction, where the mixing processes are fast, a typical time scale of the reactions is large when compared to a typical time scale of the flow. It can be seen from the steady flamelet Eqs. (3.30), that a low reaction rate in combination with intense mixing, i.e. high scalar dissipation rates χ_{st}, must lead to low values of the curvature in the temperature profile in mixture fraction space. Finite rate chemistry effects appear also in Fig. 4.8 b, where again finite curvature, and additionally a leakage of oxidizer through the reactive zone are observed. Fig. 4.8 c finally illustrates the reaction rate profiles in Z-space. It can be clearly seen, that chemical reactions occur only in a very limited window of mixture fraction Z. However, as a consequence of the low values for the curvature of the species- and temperature profiles, the extension of non-vanishing reaction rate profiles $\dot{\omega}$ in Z-space is comparably wide for this state close to extinction. For chemistry which is fast when compared to the flow phenomena. i.e. in the case of high Damköhler numbers, or when the strain rate is low, the solution converges towards the limit of Burke and Schumann, where the $\dot{\omega}$-profiles become increasingly narrow, until they become a Dirac-delta function located at Z_{st} (not shown here). For the presently considered finite-rate chemistry the flame cannot exist at strain rates higher than the value referring to the conditions shown in Fig. 4.8. Thus, the here depicted reaction rate profiles being close to extinction represent the widest profiles which are possible in Z-space.

In the present chapter, solutions have been obtained for the flame structure of canonical premixed as well as non-premixed flames. These solutions serve well for the estimation of the resolution requirements of succeeding three-dimensional computations, as well as for their initialization. Additionally, the results of the three-dimensional jet flame can be later compared against data from the one-dimensional, canonical reference configurations.

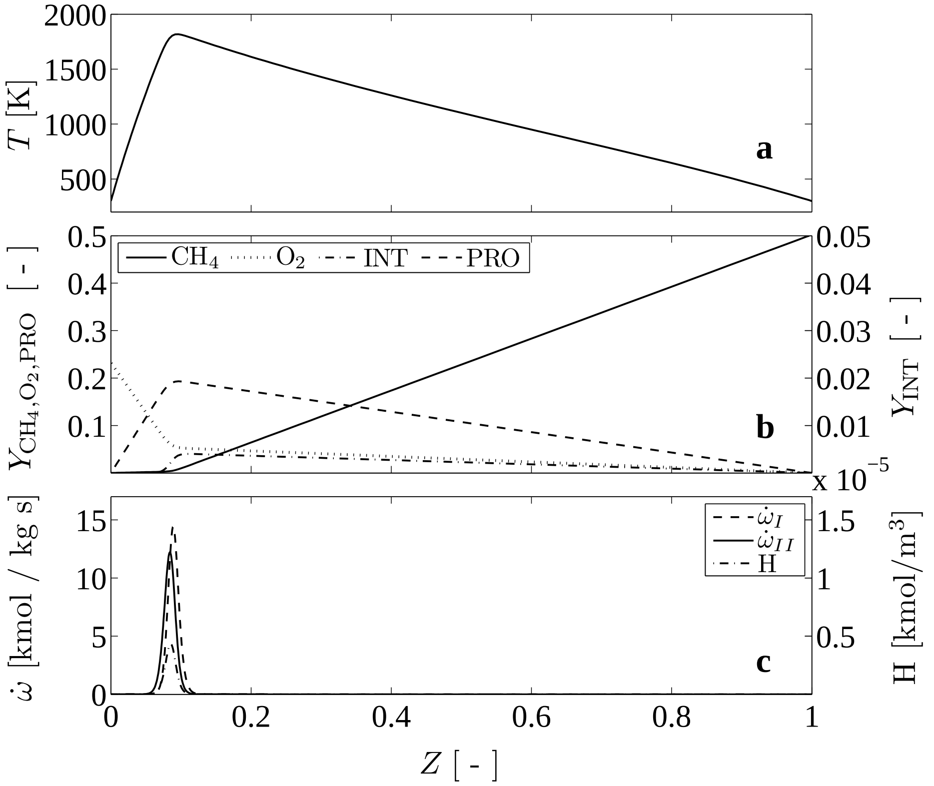

Figure 4.8: Flame structure of a diluted methane-air counterflow flame ($Z_{\mathrm{st}} = 0.104$) near extinction in mixture fraction (Z) space: **a** temperature, **b** species mass fractions, and **c** reaction rates and hydrogen radical concentration.

5 DIRECT NUMERICAL SIMULATION METHODOLOGY

The present section describes the numerical approach which is used to solve directly the governing set of equations. This particularly includes the discretization in time and space, the applied solution scheme, as well as the boundary and initial conditions imposed on the simulation.

5.1 Numerical solution procedure

A numerical code, originally written by Boersma *et al.* (1998), was used as a flow solver tool for the present computations. The initial version of this base code is written in Fortran and parallelized with MPI. It solves for the conservative version of the three-dimensional Navier-Stokes equations in the low Mach number limit, and for the transport of a conserved, non-reacting scalar. The corresponding partial differential equations are written in spherical coordinates in non-dimensional form, and they are discretized in space applying a second order accurate finite volume method on a staggered grid.

The so determined structured mesh topology based on a spherical coordinate system leads to a cone-shaped computational domain, which matches well the geometry of the considered jet flow configurations. A schematical illustration the computational domain, together with the individual boundaries Γ is given in Fig. 5.1. The indices of the discretized spherical coordinates r, θ, φ are denoted by i, j and k, respectively. At the bottom boundary surface, denoted by Γ_i, a jet is injected into the domain so that a statistically axisymmetric mixing layer emerges downstream which finally leaves the domain at the "upper" outflow boundary Γ_o at $r_{\max}$. As already noted above, the specific choice of a cone-shaped computational domain accounts inherently for the broadening of the jet with increasing distance from the orifice, which always ensures a sufficient distance between the jets outer region of the mixing layer and the lateral boundary Γ_t. Thus, the turbulent eddying motion of the jet basically never reaches the lateral boundary, which would trigger numerical instabilities. The chosen grid topology for the computation of cylindrical jet flow evidently combines very well numerical robustness as well as computational efficiency. On the other hand, using a spherical coordinate system introduces the centerline boundary Γ_c, which represents a mathematical singularity at the axis associated with $\theta = 0$. The treatment of numerical difficulties for this singularity will be discussed later along with the other boundary conditions in Sec. 5.2.

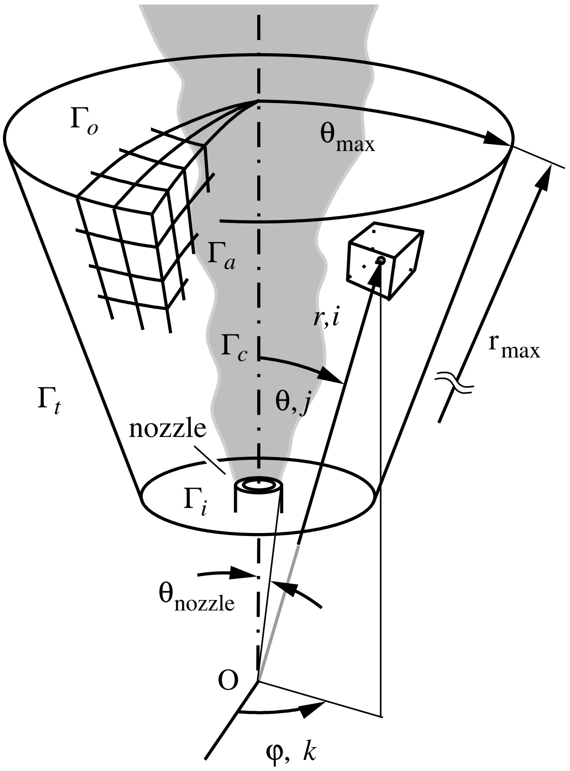

Figure 5.1: Schematical view of the computational domain.

As for the discretization in time, the initial version of the code applied a fractional step predictor-corrector method, which is essentially equivalent to the “non-stiff” projection scheme proposed by Najm *et al.* (1998).

Considering a lifted, reacting methane-air jet at low Reynolds numbers, the code had to be extended in the first place to the numerical solution of the full set of equations written for chemically reacting flow in Chp. 2. This includes essentially the following three major points:

- The temperature and the composition of the mixture are needed as inputs into the considered reaction mechanism. To provide these quantities, transport equations (including the corresponding chemical source terms) were implemented for the energy and each component of the assumed reactive system (CH_4, O_2, INT, PRO).
- Thermophysical properties and transfer coefficients may vary considerably trough flame fronts. To account for this essentially strong dependence on the temperature, look-up tables for the quantities c_p, λ, μ were implemented to retrieve the species related data from selected reference libraries[*] (see Chp. 2). In the code, these single

---

[*] In interpolated form. . .

species related data are further transferred to mixture related data applying appropriate mixing laws.

- Owing to the relatively low inertial forces associated with low jet-exit Reynolds numbers, strong effects of buoyancy are expected in the present flow configuration (Muñiz & Mungal, 2001). Therefore, a buoyancy term has been added to the momentum transport equations.

At a first glance, the numerical implementation of these three main modifications into the code might appear to be rather straightforward, which in fact holds true for the second point (thermophysical properties and transfer coefficients). As for the first task, the stiffness of the reactive source terms appearing in the transport equations requires a special numerical treatment concerning the integration in time. Moreover, the buoyancy term was implemented by rewriting the formulation of the momentum transport in Eq. (2.6). Both modifications will be discussed in more detail in the following Secs. 5.1.3 and 5.1.4, respectively.

5.1.1 Integration in time: Predictor-corrector scheme

Various techniques are available for the numerical integration in time. Most commonly either Adams or Runge-Kutta methods are used, which can be constructed for different orders of accuracy, in explicit as well as in implicit form. Aside from accuracy and computational costs, stability plays an important role for the choice of a specific scheme. The simulation of reactive flow in the limit of low mach numbers is particularly challenged by comparatively large temporal fluctuations of the density in the flame zone. Since these fluctuations would inevitably lead to unstable simulations when using fully explicit schemes, special, semi-implicit, predictor-corrector schemes have been developed to handle this difficulty, see e.g. Najm & Wyckoff (1997), Boersma (1998). In the present work we apply a particular scheme which is very similar to the "stiff" predictor-corrector projection scheme introduced by Najm *et al.* (1998), and shall be outlined in the following.

Predictor-step

At the beginning of this step, predictions for the species mass fractions and the temperature, Y^* and T^*, respectively, are computed explicitly using

$$\frac{Y^* - Y^n}{\Delta t} = \frac{3}{2}\mathcal{F}_Y^n - \frac{1}{2}\mathcal{F}_Y^{n-1} + \mathcal{R}_Y \, , \tag{5.1}$$

$$\frac{T^* - T^n}{\Delta t} = \frac{3}{2}\mathcal{F}_T^n - \frac{1}{2}\mathcal{F}_T^{n-1} + \mathcal{R}_T \, . \tag{5.2}$$

The first two terms on the RHS represent the non-stiff part $\mathcal{F}$, which is integrated here using a second-order accurate Adams-Bashforth scheme. The last terms represent the stiff part $\mathcal{R}$, which is integrated here using an appropriate stiff solver[†]. For the considered variable-density flow, the non-stiff part $\mathcal{F}$ consists of an advective, a dilatational and a diffusive component

$$\mathcal{F}_Y = [\mathrm{adv}_Y + \mathrm{dil}_Y + \mathrm{diff}_Y], \qquad \mathcal{F}_T = [\mathrm{adv}_T + \mathrm{dil}_T + \mathrm{diff}_T], \tag{5.3}$$

where the individual terms stand for spatially discretized representations of the corresponding mathematical definition in continuous space, so that one may write

$$\mathrm{adv}_Y \mathrel{\widehat{=}} -\boldsymbol{\nabla}\cdot(\mathbf{u}Y), \qquad \mathrm{dil}_Y \mathrel{\widehat{=}} Y\,\boldsymbol{\nabla}\cdot\mathbf{u}, \qquad \mathrm{diff}_Y \mathrel{\widehat{=}} \frac{1}{\rho\mathrm{ReSc}}\boldsymbol{\nabla}\cdot(\rho\mathcal{D}\boldsymbol{\nabla}Y), \tag{5.4}$$

$$\mathrm{adv}_T \mathrel{\widehat{=}} -\boldsymbol{\nabla}\cdot(\mathbf{u}T), \qquad \mathrm{dil}_T \mathrel{\widehat{=}} T\,\boldsymbol{\nabla}\cdot\mathbf{u}, \qquad \mathrm{diff}_T \mathrel{\widehat{=}} \frac{1}{\rho c_p\mathrm{RePr}}\boldsymbol{\nabla}\cdot(\lambda\,\boldsymbol{\nabla}Y). \tag{5.5}$$

The stiff part corresponds directly to the reactive source terms, so that

$$\mathcal{R}_Y \mathrel{\widehat{=}} \dot{\Omega}_P, \qquad \mathcal{R}_T \mathrel{\widehat{=}} \frac{1}{c_p}\sum_P \Delta\mathrm{Ce}_P\,\dot{\Omega}_P. \tag{5.6}$$

The integration of the scalar transport equations using Eqs. (5.1) and (5.2) is followed by the integration of the momentum transport equation using a fractional step method. In the first fractional step, an intermediate mass flux field $\widehat{\rho\mathbf{u}}$ is determined applying an explicit second-order accurate Adams-Bashforth integration

$$\frac{\widehat{\rho\mathbf{u}} - (\rho\mathbf{u})^n}{\Delta t} = \frac{3}{2}\mathcal{G}^n - \frac{1}{2}\mathcal{G}^{n-1} \tag{5.7}$$

of the advective, the diffusive and the buoyant terms only, such that

$$\mathcal{G} = [\mathbf{adv_u} + \mathbf{diff_u} + \mathbf{buoy_u}], \tag{5.8}$$

omitting the pressure term. The individual terms on the RHS of Eq. 5.8 symbolize the spatially discretized representation of the flux and force terms in the momentum transport equations, given by

$$\mathbf{adv_u} \mathrel{\widehat{=}} -\boldsymbol{\nabla}\cdot(\rho\,\mathbf{u}\,\mathbf{u}), \quad \mathbf{diff_u} \mathrel{\widehat{=}} \boldsymbol{\nabla}\cdot\left[2\mu\left(\mathbf{S} - \frac{1}{3}\mathbf{I}\boldsymbol{\nabla}\cdot\mathbf{u}\right)\right] \quad \text{and} \quad \mathbf{buoy_u} \mathrel{\widehat{=}} \rho\,\mathbf{g}. \tag{5.9}$$

The intermediate flux field $\widehat{\rho\mathbf{u}}$ obtained from Eq. (5.7) does in general not fulfil the continuity equation. To enforce the conservation of mass in the predicted flux field $(\rho\mathbf{u})^*$

[†] The discussion of the stiff solver is deferred to Sec. 5.1.3.

we rewrite the discretized representation of the full momentum equation (including the pressure term)

$$\frac{(\rho \mathbf{u})^* - (\rho \mathbf{u})^n}{\Delta t} = \frac{3}{2}\mathcal{G}^n + \frac{1}{2}\mathcal{G}^{n-1} - \nabla p^{\mathrm{int},*} \, , \tag{5.10}$$

and subtract Eq. (5.7), which yields

$$\frac{(\rho \mathbf{u})^* - \widehat{\rho \mathbf{u}}}{\Delta t} = -\nabla p^{\mathrm{int},*}. \tag{5.11}$$

Taking the divergence of Eq. (5.11) yields a Poisson equation written as

$$\Delta p^{\mathrm{int},*} = \frac{1}{\Delta t}\left[\nabla \cdot \widehat{\rho \mathbf{u}} - \nabla \cdot (\rho \mathbf{u})^*\right] \, , \tag{5.12}$$

which has to be solved for the pressure field $p^{\mathrm{int},*}$. The conservation of mass is enforced for the predicted mass flux field $(\rho \mathbf{u})^*$ by expressing the second divergence term on the RHS of Eq. 5.12 in terms of the continuity equation

$$\left(\frac{\partial \rho}{\partial t}\right)^* + \nabla \cdot (\rho \mathbf{u})^* = 0 \, , \tag{5.13}$$

so that Eq. 5.12 becomes

$$\Delta p^{\mathrm{int},*} = \frac{1}{\Delta t}\left[\nabla \cdot \widehat{\rho \mathbf{u}} + \left(\frac{\partial \rho}{\partial t}\right)^*\right] \, , \tag{5.14}$$

Therein, the density transient can be approximated second order accurately using a backwards Taylor expansion

$$\left(\frac{\partial \rho}{\partial t}\right)^* \approx \frac{3\rho^* - 4\rho^n + \rho^{n-1}}{2\Delta t} \, . \tag{5.15}$$

The resulting linear system Eq. 5.14 can be finally solved for the pressure $p^{\mathrm{int},*}$. In the so called pressure-correction step the obtained solution for the pressure is substituted into Eq. (5.11), to give a flux field $(\rho \mathbf{u})^*$, which satisfies continuity. It is evident that the accuracy of the solution for the pressure field depends on the numerical approximation for the density transient term occurring in Eq. (5.14). As a possible alternative to the direct Taylor expansion of the density shown in Eq. (5.15), the temporal density gradient can be obtained from the equation of state. A convenient form for numerical implementation of this alternative approach can be derived by applying the differentiation w.r.t. time to the logarithm of the thermal equation of state Eq. (2.22), which yields

$$\left(\frac{\partial \rho}{\partial t}\right) = -\frac{\rho}{T}\frac{\partial T}{\partial t} - \rho W \sum_P \frac{1}{W_P}\frac{\partial Y_P}{\partial t}. \tag{5.16}$$

This formulation evidently shifts the problem to the estimation of the time derivatives of the species mass fractions and temperature, which can be approximated again by Taylor expansions analogously to Eq. (5.15). Both alternative formulations were tested in the present code, using Taylor expansions for transient terms on the RHS of Eq. (5.16). A comparison of the predictions of Eq. (5.15) and Eq. (5.16) showed notable differences for $\partial\rho/\partial t$ only in the vicinity of flame fronts. Quantitatively, these differences appear to be negligibly small, as can be seen from Fig. 5.2. The shown contours display the relative difference between the results of both formulations obtained for an instantaneous reactive flow field. Due to the lower computational costs, the direct approximation of $\partial\rho/\partial t$ given by Eq. (5.15) was therefore further used in the code.

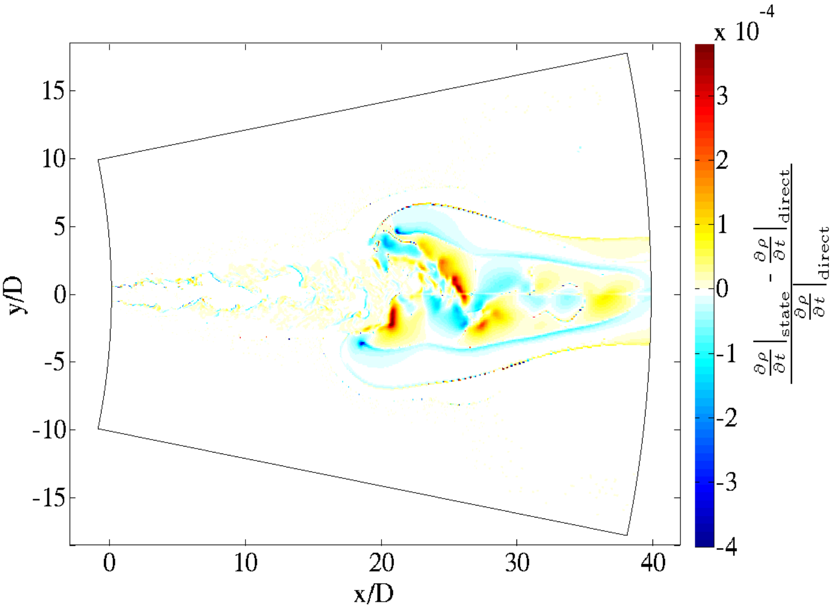

Figure 5.2: Instantaneous contours of the relative difference of the density gradients predicted by Eq. (5.15) “$\left.\frac{\partial\rho}{\partial t}\right|_{\mathrm{direct}}$” and Eq. (5.16) “$\left.\frac{\partial\rho}{\partial t}\right|_{\mathrm{state}}$” displayed on a meridional cut through the computational domain.

At the end of the predictor step, the predicted velocity is computed. The velocity is then obtained by dividing the predicted mass flux by the predicted density, written as

$$\mathbf{u}^* = \frac{(\rho\mathbf{u})^*}{\rho^*}, \tag{5.17}$$

where ρ^* is obtained from the equation of state $\rho^* = \rho\left(Y^*, T^*\right)$.

Corrector-step

The procedure of the corrector step basically repeats all of the individual sub-steps of the predictor step, except that the temporal integrations of the non-stiff parts is carried out using the semi-implicit Adams-Moulton method instead of the explicit Adams-Bashforth scheme. Accordingly, the corrected species mass fraction and temperature fields are computed from

$$\frac{Y^{n+1}-Y^{n}}{\Delta t}=\frac{1}{2}\mathcal{F}_Y^{n}+\frac{1}{2}\mathcal{F}_Y^{*}+\mathcal{R}_Y, \tag{5.18}$$

$$\frac{T^{n+1}-T^{n}}{\Delta t}=\frac{1}{2}\mathcal{F}_T^{n}+\frac{1}{2}\mathcal{F}_T^{*}+\mathcal{R}_T, \tag{5.19}$$

where the stiff terms $\mathcal{R}$ are left unchanged, so that the corresponding values can be taken from the predictor-step. The non-stiff terms denoted by $\mathcal{F}^*$ are obtained by evaluating their advective, diffusive and dilatational components shown in Eqs. (5.3) to (5.5) with the solution of the predictor-step $\mathcal{F}^* = \mathcal{F}\left(\rho^*, u^*, Y^*, T^*\right)$. Analogously to the scalar transport, the equation of momentum is also integrated using a semi-implicit Adams-Moulton scheme, written as

$$\frac{\widetilde{\rho\mathbf{u}}-(\rho\mathbf{u})^{n}}{\Delta t}=\frac{1}{2}\mathcal{G}^{n}+\frac{1}{2}\mathcal{G}^{*}, \tag{5.20}$$

with $\mathcal{G}^* = \mathcal{G}\left(\rho^*, u^*, Y^*, T^*\right)$. The obtained intermediate flux field $\widetilde{\rho\mathbf{u}}$ is then further corrected to $(\rho\mathbf{u})^{n+1}$ in a pressure correction step

$$\frac{(\rho\mathbf{u})^{n+1}-\widetilde{\rho\mathbf{u}}}{\Delta t}=-\boldsymbol{\nabla} p^{\mathrm{int},n+1}, \tag{5.21}$$

which enforces the conservation of mass. The pressure field $p^{\mathrm{int},n+1}$ is obtained here again from a Poisson equation written as

$$\Delta p^{\mathrm{int},n+1}=\frac{1}{\Delta t}\left[\boldsymbol{\nabla}\cdot\widetilde{\rho\mathbf{u}}+\left(\frac{\partial\rho}{\partial t}\right)^{n+1}\right], \tag{5.22}$$

with

$$\left(\frac{\partial\rho}{\partial t}\right)^{n+1}\approx\frac{3\rho^{n+1}-4\rho^{n}+\rho^{n-1}}{2\Delta t}. \tag{5.23}$$

The density on the new time level is computed from the equation of state $\rho^{n+1} = \rho\left(Y^{n+1}, T^{n+1}\right)$. The new density field is also used to extract the new velocity field from the mass fluxes according to $\mathbf{u}^{n+1} = (\rho\mathbf{u})^{n+1}/\rho^{n+1}$.

5.1.2 Pressure solver

One of the computationally most demanding parts of the temporal integration procedure outlined above is the solution of the Poisson equation for the pressure. In the presently used predictor-corrector scheme a Poisson equation has even to be solved twice per time step (Eqs. 5.14, 5.22). In principle, various techniques can be applied for solving such a linear system of equations. There exist several direct and iterative solution concepts. In practice however, the number of applicable solvers is strongly limited due to the huge matrix system that arises from the millions of computational cells commonly used when performing DNS. The Fourier Analysis Cyclic Reduction scheme (FACR, for details see Swarztrauber & Sweet 1996, Gander & Golub 1997) has been proven useful for this task in many previous studies, and is also used in the present code.

For a brief summary, the FACR algorithm as used in the present case can be described as follows: In a first step, the periodicity of the computational domain in azimuthal direction φ is exploited, refer to Fig. 5.1. A Fourier analysis is employed in this homogeneous direction to decouple the system, so that k_{max} independent, two-dimensional Poisson equations are obtained, where k_{max} denotes the number of cells in direction of φ. For this transformation from the physical space into wave space, Fast Fourier Transforms (FFTs) are used. In a next step, a cyclic reduction is applied to the decoupled two-dimensional systems in the streamwise direction r, which yields a successive series of one-dimensional Poisson equations. The remaining tri-diagonal systems can then be solved using the simple but efficient Thomas algorithm. Finally, as a last step, the solutions need to be transformed back into the spatial domain, which can be achieved efficiently by inverse FFTs.

The three major advantages of FACR can be seen already from this brief description:

- The Fourier analysis performed in the first step decouples the problem into a number of independent linear systems, which reduces the dimensionality of the problem, and is in favour of an efficient parallelization of the code.
- The cyclic reduction produces a series of basically one-dimensional Poisson equations, which have very low storage requirements. Due to the limited amount of memory, this circumstance is crucial. Additionally, the low memory requirements result in strongly limited number of memory accesses, which in turn reduces memory latency and bandwidth problems and therefore results in a high numerical performance.
- All employed algorithms (Fourier analysis, cyclic reduction, Thomas algorithm) are direct, hence the FACR is also a direct solver. This implies also that the conditioning of the matrix is not as crucial as with iterative solvers, and that the obtained solutions are exact to roundoff error.

For the implementation of the solver into the code, various public domain packages are available. In the present code, FISHPACK handles the solution process of the two-dimensional Poisson equations, and VFFTPACK provides the FFTs[‡].

[‡] For improved efficiency on a given hardware, VFFTPACK could also be replaced by vendor specific products such as the AMD Core Math Library (ACML) or the Intel Math Kernel Library (MKL). For reasons of generality, this concept has not been further followed.

5.1.3 Time integration of chemical source terms

A second computationally demanding task, which is related to the temporal integration scheme, is the time-integration of the stiff chemical source terms $\dot{\Omega}_P$ and $\dot{\mathcal{Q}}_{\mathrm{react}}$. Depending on the chemistry and the instantaneous conditions of the underlying flow field, the reactive terms might vary on time scales considerably shorter than those of the underlying flow. Clearly, combustion always occurs in reactive-diffusive systems, where both effects act on comparable timescales. The discrepancy of these timescales to the comparatively larger advective flow timescales is accounted for applying a time step splitting concept. This concept is based on the assumption of frozen flow conditions, where the chemical source terms ($\mathcal{R}$) are integrated separately using an appropriate stiff ODE-solver within every flow time step.

In the present work, the stiff ODE solver LSODA is used, which is part of the Netlib-library ODEPACK (Hindmarsh, 1983). The solver performs the integration from one time step n to the next $n+1$ using smaller substeps, which are chosen according to an error-estimator. Stiffness is automatically detected in the course of the integration. In the non-stiff case, the solver applies a combination of Adams-Bashforth and Adams-Moulton formulas, similar to the predictor-corrector scheme outlined before. Solutions are iteratively obtained applying multiple corrector steps until convergence is reached. If stiffness is detected, the more suitable Backward Differential Formulas (BDFs) are used. BDFs approximate the RHS of ODEs by interpolation polynomials according to

$$y^{n+1} = \sum_{i=0}^{q-1} \alpha_i \, y^{n-i} + h \beta_1 \left. \frac{\partial y}{\partial t} \right|^{n+1} , \tag{5.24}$$

where α_i and β_1 are interpolation coefficients, q determines the degree of the interpolation polynomial, and h is the step size. LSODA solves the implicit Eq. (5.24) again iteratively, using modified Newton iterations with approximated Jacobians.

The temporal integration of the stiff reactive source terms consumes considerable numerical resources. In the present case, the reactive source terms are therefore evaluated only in regions, where significantly non-zero values can be expected, i.e. within a generously chosen ignition window $Z_{\mathrm{ign,min}} < Z < Z_{\mathrm{ign,max}}$, determined by the mixture fraction Z. Applying such a criterion, roughly one fifth of the total wall time consumed by the code is spent on the LSODA part. More detailed results obtained in several benchmark tests on this subject are shown in Appendix A.

5.1.4 Buoyancy

The effect of buoyancy is basically due to the action of gravitational force in the conservation of momentum. Affecting the momentum balance, it essentially also influences the instantaneous pressure field obtained from the solution of the Poisson equation. For sake of numerical stability the magnitude of eventual buoyancy induced disturbances of the pressure field can be effectively reduced by decomposing the pressure into a dynamic and a hydrostatic part, which reads

$$p = p_{\mathrm{dyn}} + \frac{\rho_\infty}{\mathrm{Fr}^2}\,\mathbf{e}_g \cdot \mathbf{x}\,. \tag{5.25}$$

Here, ρ_∞ denotes the ambient density, Fr the Froude number, $\mathbf{e}_g$ is the unit vector in the direction of gravitation and $\mathbf{x}$ represents the coordinate vector. Introducing Eq. (5.25) into the momentum transport Eq. (2.6) yields

$$\frac{\partial \rho\,\mathbf{u}}{\partial t} + \boldsymbol{\nabla}\cdot(\rho\,\mathbf{u}\,\mathbf{u}) = -\boldsymbol{\nabla}\,p_{\mathrm{dyn}} + \frac{2}{\mathrm{Re}}\boldsymbol{\nabla}\cdot\left[\mu\left(\mathbf{S} - \frac{1}{3}\mathbf{I}\boldsymbol{\nabla}\cdot\mathbf{u}\right)\right] + \frac{\rho-\rho_\infty}{\mathrm{Fr}^2}\,\mathbf{e}_g\,, \tag{5.26}$$

where the buoyancy-induced source term vanishes for the major part of the computational domain, as $\rho \approx \rho_\infty$.

5.1.5 Thickened flame approach

In a strict sense, DNS attempts to resolve all time- and length scales, including those which are solely relevant for the chemistry. For the case of a diluted flame, the mesh width, which is required to resolve the inner structure of a laminar premixed flame has been shown to be of the order of 10 [μm] (see Sec. 4.4.1). Exemplarily speaking, if a lab-scale flame of dimension $5\times5\times10$ [cm] shall be computed on a uniform mesh which provides such a fine discretization, a mesh consisting of 250 billion cells would be required. This numerical demand is prohibitively high, even for the most modern supercomputers. Clearly, the total number of cells can be reduced by using structured or even unstructured adaptive meshes, where grid points are clustered in the regions of interest, while the grid is coarsened in the other regions[§]. A high spatial adaptivity provided by strongly clustered unstructured grids generally excludes the use of direct solvers for the solution of the Poisson equation. Indirect, iterative solvers, which have to be used instead, are known mostly less accurate and, more importantly, markedly slower than the direct solvers. Therefore, a significant reduction of the grid size achieved with a highest possible spatial adaptivity does often not pay off, as it does not effectively reduce the required total computation time.

An insufficient spatial resolution of the flame may have multiple consequences. Mathematical errors may reach unacceptable values, which result, e.g., in systematical overpredictions of the flame speed (Al-Khateeb *et al.*, 2010), but also in considerable mispredictions for the involved species mass fractions, and may even lead to numerical instabilities. For these reasons, additional methods have to be considered.

[§] In the present code structured clustering is possible only in the r and θ directions. In φ direction, structured clustering is prohibited by the employed FACR pressure solver.

A concept to relax the chemical resolution requirements in finite rate chemistry computations is represented by the thickened flame approach, which was introduced first by Butler & O'Rourke (1977). In their approach, the authors showed that a laminar flame can be spatially thickened by a factor F, while the speed of the unthickened flame is retained. This is achieved by multiplying the diffusive terms in the species and energy transport equations by F, and dividing the reactive source terms by the same factor. It is straightforward to show, that this method corresponds to a linear coordinate stretching of the transport equations, written as

$$\mathbf{x} = F\,\mathbf{x}^{\mathrm{ref}}\,. \tag{5.27}$$

For this reason, the spatial structure of the thickened canonical one-dimensional flames discussed before must be fully affine to the unthickened case. The fact that the laminar flame speed, and hence also the conversion rate of a planar, premixed flame are not changed by the flame thickening can be easily demonstrated by applying the concept to the scaling law for s_L (Eq. 3.11), which yields

$$s_L = \frac{\mathcal{D}_{\mathrm{th}}|_{\mathrm{thick}}}{l_{\mathrm{fl}}|_{\mathrm{thick}}} = \frac{(F \cdot \mathcal{D}_{\mathrm{th}})}{(F \cdot l_{\mathrm{fl}})} = \frac{\mathcal{D}_{\mathrm{th}}}{l_{\mathrm{fl}}}\,, \tag{5.28}$$

where the parameter F evidently cancels. The one-dimensional non-premixed case does not exhibit a characteristic "flame speed"; however, the conversion rate is also retained for this case. Nevertheless, it is worth to mention that the rate controlling parameter χ formally changes it's value proportional to F^{-1}.

The introduction of an artificially increased diffusivity has some undesirable effects in more complex flow fields. In the case of a lifted jet flame, the turbulent inert mixing occurring upstream of the flame base would be unacceptably enhanced due to the increased diffusive transport. To avoid this drawback, Legier *et al.* (2000) proposed an extension to the original model, which is termed Dynamically Thickened Flame (DTF) model. In this concept, the thickening factor F is modified dependent on the local reaction rate, written as

$$F = 1 + (F_{\max} - 1)\tanh\left(\dot{\omega}/\dot{\omega}_{\mathrm{ref}}\right)\,, \tag{5.29}$$

so that the thickening vanishes in regions remote from the flame. As such the DTF model ensures that the increased diffusivity used for flame thickening remains restricted to the reactive regions.

When using the thickened flame model in the context of LES of turbulent flames, the interaction of the unresolved subgrid-scale motion with the chemistry would effectively increase the total conversion rate and the flame speed. To account for this increase of the effective flame speed, which scales in the laminar regime with $s_L \propto \sqrt{\mathcal{D}\dot{\omega}}$, the diffusive and the reactive terms are generally premultiplied with an efficiency factor E (Colin *et al.* 2000, Charlette *et al.* 2002), so that a transport equation for an arbitrary reactive scalar

Eq. (2.12) is rewritten as

$$\frac{\partial \rho Y_P}{\partial t} + \nabla \cdot (\rho \mathbf{u} Y_P) = \nabla \cdot (\rho E F \mathcal{D}_P \nabla Y_P) + \frac{E}{F} \rho \dot{\Omega}_P \,. \tag{5.30}$$

The efficiency factor E is thereby mostly modelled dependent on the ratio of the grid size to the flame thickness, Δ/l_{fl}, and the ratio of the unresolved turbulent velocity scale to the laminar flame speed u'_Δ/s_L. The flame thickening approach used in the present DNS introduces an efficiency factor E as well. This factor is however rather based on the specific mixing conditions near the base of the lifted jet flame than on the effect of unresolved velocity fluctuations typically met in LES. The reasoning behind the presently used efficiency factor shall be outlined in the following.

In the present case of DNS of a lifted jet flame, the numerically obtained lift-off height depends strongly on the dynamics of the partially premixed leading edge flame. Therefore, it is a prerequisite that the propagation speed of such a leading edge flame is retained by the employed DTF approach. Strictly speaking, the DTF model can meet the constraint of an unchanged laminar flame speed of a thickened flame only in the case of a laminar premixed flame. The extension of the DTF model to the partially premixed case needs a further modification of the formulation due to the effective change in the mixing conditions. Being in between the premixed and non-premixed case, the kinetics of a partially premixed edge flame is controlled by both the rate parameters of the premixed (s_L) and the non-premixed regimes (χ, see Ruetsch *et al.* 1995[¶]). Applying the DTF model in multi-dimensional reactive flow simulations changes the value of the scalar dissipation rate χ upstream of the flame base. The local values obtained in the simulations do, however, in general not match the theoretically required value $\chi \cdot F^{-1}$ associated with the coordinate transformation Eq. (5.27) noted above. This mismatch would result in a wrong prediction for the propagation speed of the considered edge flame, so that an efficiency factor E is introduced for correction. The specific mixing situation which fully requires such a correction for the DTF model is exemplarily illustrated in Fig. 5.3 showing the mixture fraction (Z) contour lines approaching the flame. The scalar dissipation rate is defined according to Eq. (3.16) dependent on the mixture fraction gradient ∇Z, so that densely aligned Z contours correspond to high values of χ and vice versa. In the non-thickened, upstream part, the closely aligned Z contours indicate a comparatively high oncoming scalar dissipation rate χ. Downstream, in the transitional layer between the non-thickened and the thickened regions, the flame thickening parameter F is ramped up according to Eq. (5.29), and the Z contours should ideally expand corresponding to the transformation Eq. (5.27). An ideal Z contour is exemplarily shown as dashed line in Fig. 5.3. For such ideal mixing conditions, a correct unchanged propagation speed of the laminar edge flame would be obtained. When using the DTF model in the simulation, however, the mapping Eq. (5.27) is achieved indirectly based on an increased molecular diffusivity. The broadening of the Z contours

---

[¶] In this study, the effect of χ is represented by the mixture fraction gradient

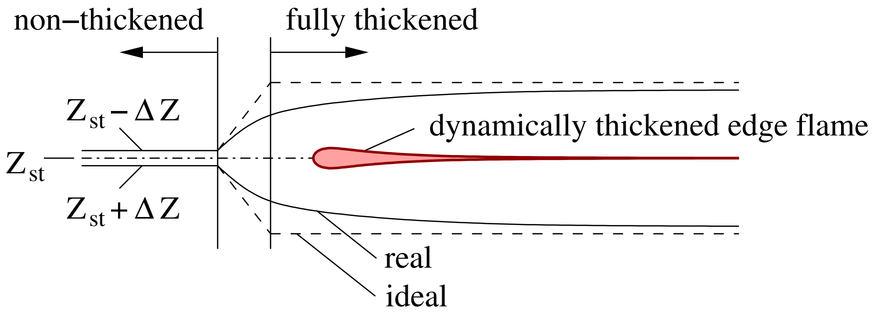

Figure 5.3: Schematic view of mixture fraction contour lines for a dynamically thickened laminar edge flame; solid lines indicated as “real” represent typical simulation results, dashed lines indicated as “ideal” represent contours satisfying the transformation Eq. (5.27).

resulting from the continuously increased diffusivity lags behind the ideal case. As a consequence, the scalar dissipation rate χ in the vicinity of the edge flame remains higher than in the ideal case, which leads to higher heat losses to the ambient region and consequently to lower propagation speeds of the edge flame. The introduction of an efficiency factor E, which is is premultiplied with the diffusive and the reaction term in Eq. (5.30), helps to compensate for these increased heat losses, so that a correct flame propagation speed can be retained with the DTF model used in the present DNS. The efficiency factor E is thereby prescribed as constant in the region close to the leading edge of the flame, further downstream it is ramped down smoothly to reach unity near the outflow boundary. Certainly, the increase in the reaction rates caused by $E > 1$ must lead to a somewhat higher heat release as will be seen also later, when the numerical results are compared with experiment. Nevertheless, the presently used approach provides a reliable way to describe the dynamics of a stably lifted jet flame at a correctly predicted lift-off height.

5.2 Boundary conditions

The prescription of Boundary Conditions (BCs) for highly transient flow simulations is a topic of high relevance. Applying sophisticated, highly accurate discretization schemes can become useless, when the accuracy of a simulation is spoiled by inappropriate BCs. In the present case of a jet flow, BCs also need to be prescribed at open boundaries, which basically model the flow field outside of the considered computational domain. This is especially for transient flows a non-trivial task.

For the presently considered computational domain, the individual boundary surfaces Γ have already been sketched in Fig. 5.1. The boundaries Γ_i, Γ_t and Γ_o correspond to the physical inflow, tangential and outflow boundaries, respectively. Γ_a and Γ_c correspond to the azimuthal and centerline boundaries, which basically represent mathematical boundaries associated with the spherical coordinate system. BCs are needed for the three velocity components, the species mass fractions, temperature and the pressure, respectively. The individual BCs are discussed in the following, except for the azimuthal boundary Γ_a, where periodic BCs apply by definition.

5.2.1 Inflow

As seen from Fig. 5.4, the prescription for the inflow boundary Γ_i distinguishes three individual zones: An inner part, where the cylindrical pipe inflow is prescribed, an outer part, which is prescribed as a free-slip wall, and a thin region in between, corresponding to the lip of the pipe, where no-slip conditions are imposed.

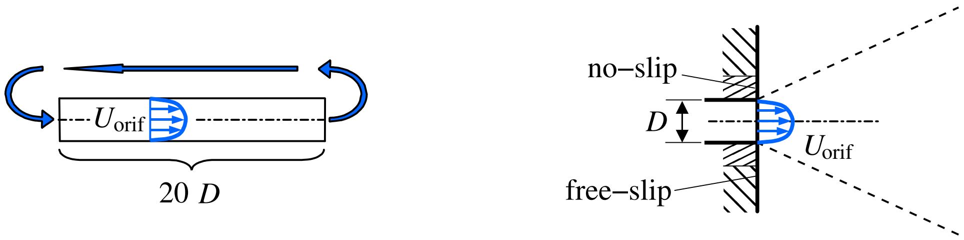

Figure 5.4: Inflow boundary conditions.

For the prescription of realistic inflow BCs at the inner part, a separate DNS of periodic pipe flow was carried out. To surely capture the largest coherent structures in the streamwise direction, but also to provide enough data to avoid any inflow-generated periodicity in the jet flow downstream, the length of the simulated pipe was chosen to be $x/D = 20$. A statistically developed turbulent pipe flow solution is provided to the jet code via an auxiliary file. An instantaneous velocity field of the pipe-solution obtained on a cross-sectional plane is then imposed as an instantaneous inflow condition at the nozzle.

In the experiment which shall be used for validation, the nozzle is fixed in a disk-shaped plane wall. Since the top of the nozzle slightly exceeds the surrounding wall[‖], no-slip conditions are applied on the co-annular surface of the top of the nozzle, while frictional effects of the receding wall in the radially outer region are neglected, so that non-slip conditions are imposed there.

For the species mass fractions Y_P and the temperature T, constant values are prescribed inside the nozzle assuming perfect mixing of methane and its diluent. In the region outside of the nozzle zero heat and species mass transfer is assumed in the wall-normal direction, so that a von-Neumann type zero gradient BC $\partial/\partial\mathbf{n} = 0$ is applied.

[‖] Approx. 1 [mm].

A von-Neumann type zero gradient BC $\partial p_{\text{dyn}}/\partial \mathbf{n} = 0$ is also imposed for the pressure on the whole inflow surface Γ_i. The prescription of the BC for the pressure follows immediately from the Dirichlet type prescription of the normal velocity component at this boundary.

5.2.2 Lateral boundary

Basically two main requirements have to be met here: The lateral BCs should be consistent with a reliable description of entrainment, and they should allow for a computationally feasible lateral extension of the domain without generating numerical instabilities which may significantly perturb the solution in the core region. Boersma *et al.* (1998) has shown that free-slip BCs are not appropriate, as this basically assumes Γ_t as a frictionless, but impermeable wall surface inhibiting the entrainment of mass from the surroundings. There are basically two alternative approaches available, which can handle the entrainment process in an acceptable way. The so-called traction-free BC $\boldsymbol{\sigma} \cdot \mathbf{n} = 0$, assuming zero stress at Γ_t, and the von Neumann BC, assuming zero gradients for the velocity components at Γ_t. The latter type is used in the present simulations.

For species Y_P and temperature T, Dirichlet BCs are used prescribing the corresponding values of the fresh ambient air.

For the pressure, a Dirichlet BC has to be prescribed somewhere in the computational domain, as the Poisson Eq. (5.14), or Eq. (5.22), would otherwise yield non-unique solutions. In the present computational setup such a Dirichlet BC is assumed at Γ_t by imposing $p_{\text{dyn}} = 0$. The prescription of a zero dynamic pressure basically assumes an undisturbed, purely hydrostatic pressure field laterally outside.

5.2.3 Outflow

Special care has to be taken for the specification of the outflow boundary condition. The comparatively low jet-exit velocities, which are due to the low Reynolds numbers required for DNS, usually lead to strong effects of buoyancy in variable-density flows. Strongly buoyant jets with off-source heating can develop large vortical structures leading to extended regions with reversed flow, even in a statistically steady-state. If these structures reach the outflow boundary, large perturbations can arise which finally lead to unphysical behaviour and numerical instability.

Many standard BCs for open boundaries fail in such situations. The traction-free BC as well as the von Neumann BC have to be discarded, as they are only stable for low normal velocity components at the boundary. The widely used convective outflow BC, written as

$$\frac{\partial \mathbf{u}}{\partial t} + \overline{U}_{\text{out}} \frac{\partial \mathbf{u}}{\partial n} = 0, \tag{5.31}$$

basically assumes a predominantly outwards directed motion represented by an average advection velocity $\overline{U}_{\text{out}}$, which is not always the case. For the present case of a strongly buoyant jet, first tests showed that BCs of the type Eq. (5.31) are prone to instability. As a first workaround, the outflow boundary could be moved further downstream, to a position, where the intensity of the reversed flow and of the vortical motion have typically decreased substantially. Unfortunately, this is not a practical solution for DNS. Additional millions of gridpoints would have to be introduced, leading to a prohibitively high computational cost.

Several sophisticated methods have been derived to prevent outflow instabilities without a need for drastically increased domain sizes. Nevertheless, the implementation of these commonly termed "absorbing" BCs is often troublesome. Most of these BCs are developed for compressible flow, and hence not applicable in the low Mach number regime (see e.g. Grinstein 1994, Frolov *et al.* 2001), or they involve complex mathematical algorithms, which leads again to an unacceptable increase of the computational costs. Within the frame of the present work, a robust boundary treatment was developed for transient reactive jet flow computations, which ensures stable simulations even in the presence of some limited backflow. The details of this concept and its first application to a DNS of a reacting jet assuming purely mixing controlled infinite-rate chemistry can be found in Walchshofer *et al.* (2011). The basic ideas and the application of this specially developed BC to the presently considered finite-rate chemistry shall be outlined in the following.

The dynamic part of the developed outflow BC follows, to some extent, an approach of Fournier *et al.* (2008), who proposed as well an improved convective outflow BC for use in low Mach number flow. They argued, that contaminations of the flow field at the outlet are caused by pressure-overcorrection of the intermediate flow field $\widehat{\rho \mathbf{u}}$. They suggested to reduce the quantitative level of this pressure-overcorrection at the boundary by using a more accurate boundary layer type formulation than the purely convective formulation of Eq. (5.31). Following this argumentation of Fournier *et al.* (2008), this is achieved in the present approach by addition of a viscous shear stress term in the cross-stream direction to the convective outflow BC, so that it reads for the streamwise component u

$$\frac{\partial \rho u}{\partial t} + \overline{U}_{\text{out}} \frac{\partial \rho u}{\partial r} = \frac{1}{\text{Re}} \frac{1}{r^2 \sin\theta} \frac{\partial}{\partial \theta} \left(\mu \sin\theta \frac{\partial u}{\partial \theta} \right) . \tag{5.32}$$

The prescribed convective outflow velocity $\overline{U}_{\text{out}}$ is assumed to vary as a Gaussian function of the cross-stream coordinate, as this shape approximates very well the typical velocity profiles found in jet flows. For the cross-stream velocity components, von Neumann BCs are applied, respectively.

Using the extended BC Eq. (5.32) instead of Eq. (5.31) led to improvements w.r.t. stability. Nevertheless, some unphysical pressure perturbations could still be observed, which in the long run may jeopardize a stable simulation. To dampen these spurious perturbations, an additional viscous-sponge type buffer layer is introduced. This is effectively done by adding an artificial (boundary) viscosity μ_{bc} to the molecular one, so that the total viscosity is written as

$$\mu = \mu_{\mathrm{m}} + \mu_{\mathrm{bc}}. \tag{5.33}$$

Similar to Liu & Liu (1994), the added viscosity is increased within the narrow viscous-sponge layer towards the outflow. However, in contrast to Liu & Liu (1994), the added viscosity μ_{bc} is computed in the present work dependent on the local flow conditions using a Smagorinsky (1963) type eddy-viscosity model

$$\mu_{\mathrm{bc}} = \rho (C\,\Delta x_{\mathrm{eff}})^2 \|\mathbf{S}\| \,, \tag{5.34}$$

where Δx_{eff} denotes the mesh size and C is the model constant. The increase in viscosity towards the outflow is realised by a parabolic ramping of the Smagorinsky constant towards the boundary, where it assumes a value of $C|_{\Gamma_o} = 0.2$. This improved viscous-sponge layer based concept was proven as an efficient, robust, but still accurate approach. As illustrated by Walchshofer *et al.* (2011), the model effectively limits an uncontrollable growth of boundary perturbations, the increase of the total viscosity remains on average very small, and no notable upstream effects are observed, as well.

The concept for the dynamic BCs as described so far fully corresponds to the one outlined in (Walchshofer *et al.*, 2011). To increase the stability for the present finite rate case, an additional parabolizing effect was achieved by clipping the outflow values predicted by Eq. (5.32) to a positive value $u|_{\Gamma_O} \geq 0$, enforcing outwards directed motion. Not only, but mainly for this reason, the simulation results in close proximity to the outflow have to be considered to be not fully reliable.

For the pressure, a von-Neumann BC $\partial p_{\mathrm{dyn}}/\partial \mathbf{n} = 0$ is imposed at the outflow boundary.

Special care has to be taken also for the thermal and species BCs. Using here either a Dirichlet BC, or a von Neumann BC has certain advantages and disadvantages. A Dirichlet BC basically imposes a certain “frozen” state immediately downstream of the outflow boundary. In some sense, this anchors the solution near the boundary to presumed thermal conditions, which can be beneficial for a controlled, long term stable simulation. On the other hand, an eventual mismatch between the imposed boundary values and the instantaneous thermal conditions inside represents a potential source of instability triggered by strong fluctuations in the local density. In contrast, the von Neumann type zero-gradient BC basically inhibits by definition the occurrence of such a stability problem. The von Neumann BC has however the drawback that it may lead to an accumulation of individual species at the boundary, which can further lead to a broadening of the reactive mixing layer at the outflow. To exploit the advantages of both types of BCs, a combination of a Dirichlet and a von-Neumann BC, commonly known as Robin BC

$$\begin{aligned}\frac{\partial Y_P}{\partial \mathbf{n}} &= c\left(Y_{P,\text{target}} - Y_P\right) ,\\ \frac{\partial T}{\partial \mathbf{n}} &= c\left(T_{\text{target}} - T\right) ,\end{aligned} \tag{5.35}$$

is applied for the species mass fractions as well as the temperature. Depending on a blending parameter c, the Robin BC biases the solution smoothly towards a target function $Y_{P,\text{target}}$ and T_{target}. The value of the parameter $c = 0.12$ is determined based on the variation of the density w.r.t. the mixture fraction Z (for details see Walchshofer *et al.* 2011). $Y_{P,\text{target}}$ is chosen to be zero for all reactive species** to enforce an outwards directed transport. The target function for the temperature is prescribed using a beta-shaped profile dependent on the cross-stream coordinate θ, which is written as

$$T_{\text{target}} = \beta(\theta)\frac{\displaystyle\int T\, d\Gamma_o}{\displaystyle\int \beta(\theta)\, d\Gamma_o} \quad \text{with} \quad \beta(\theta) = \left[1 - \left(\frac{\theta}{\theta_{\max}}\right)^2\right]^b . \tag{5.36}$$

In this formula, the parameter b determines the width of the temperature target-profile, which should, for stability reasons, match closely with the conditions in the oncoming flow. Analogously to the procedure proposed by Walchshofer *et al.* (2011), the presently used value of $b = 8$ was derived from the typical rate of spread of turbulent jets.

5.2.4 Centerline

Mathematically, the centerline boundary Γ_c is a singularity, which is associated with the spherical coordinate system used for the mathematical formulation. In the present work, a staggered grid is used, where the velocities are defined at the cell faces, while all scalar quantities are defined at the cell centers. As illustrated in Fig. 5.5, the presently applied staggered grid discretization handles the mathematical problem at the centerline by locating the finite volumes always at off-center positions, so that they basically exclude the centerline singularity. It becomes evident that for the momentum balance in the streamwise and the azimuthal direction the area of inner face perpendicular to the θ-direction is zero (see Fig. 5.5 a and c), hence the momentum transfer across this face must be zero, and the centerline singularity is irrelevant. This is however not the case for the momentum balance in the cross-stream direction, where the momentum flux across the innermost cell face has to be specified depending on the ambiguous velocity conditions on the singular centerline. The here required velocity components at the centerline singularity are obtained from an interpolation between the values of the considered control volume and the

---

[**] CH_4, O_2, INT, and PRO. Note that, by Eq. (2.7), this implies $Y_{N_2,\text{target}} = 1$.

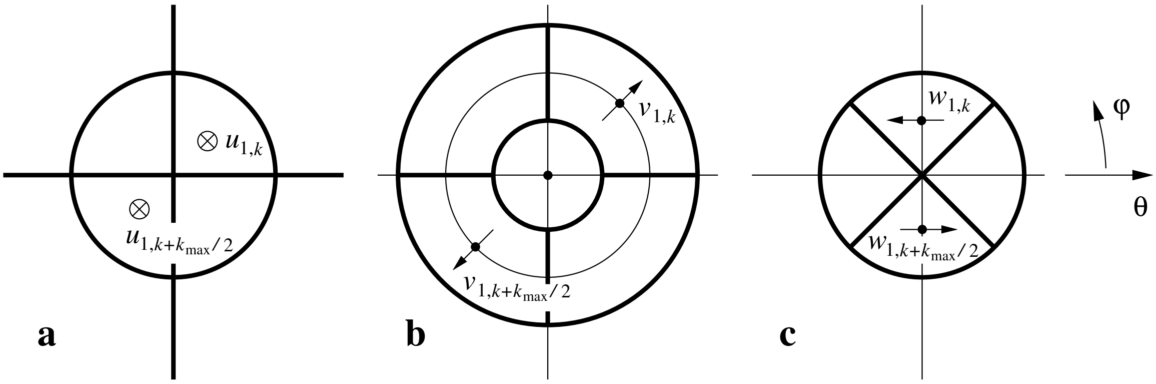

Figure 5.5: Schematical illustration of the positions of the staggered finite volumes in a vicinity of the centerline. Bold dots denote the positions of the centers of the volumes. The indices j,k correspond to the coordinate directions θ and φ. **a** cells for the streamwise momentum balance; **b** cells for the cross-streamwise momentum balance; **c** cells for the azimuthal momentum balance.

values of the opposite volume w.r.t. the azimuthal direction ϕ, associated with the indices k and $k+k_{\max}/2$, respectively.

All scalar variables, which are defined at the cell centers, are coincident with the position of u in the axial projection shown in Fig. 5.5 a. Since a higher-order scheme is used for the advective scalar fluxes, boundary conditions in the cross-stream direction have to be specified. The required boundary values are obtained using the values on the opposite side of the centerline associated with the azimuthal index $k = k+k_{\max}/2$. For the pressure p_{dyn}, a von Neumann BC $\partial p_{\text{dyn}}/\partial \theta = 0$ is applied.

5.3 Initialization of the DNS

As already outlined briefly in Sec. 4.1, the initialization of three-dimensional reactive DNS represents a non-trivial task. It is evident that the analysis of the results of unsteady simulations like DNS cannot be started unless a statistically converged flow field is achieved. In the case of reactive DNS, a considerable amount of computational time has to be spent to reach this point. To accelerate the process, an initial solution should be imposed which is already fairly close to the final, statistically steady flow field.

A fundamental issue in this context is the ignition of the flame. To start the chemical reactions, hot spots can be introduced into the computational domain. However, if badly placed in the domain the initial flame emerging from the hot spots can be blown off, or it can take a long computational time until the flame reaches its final dynamically stable position.

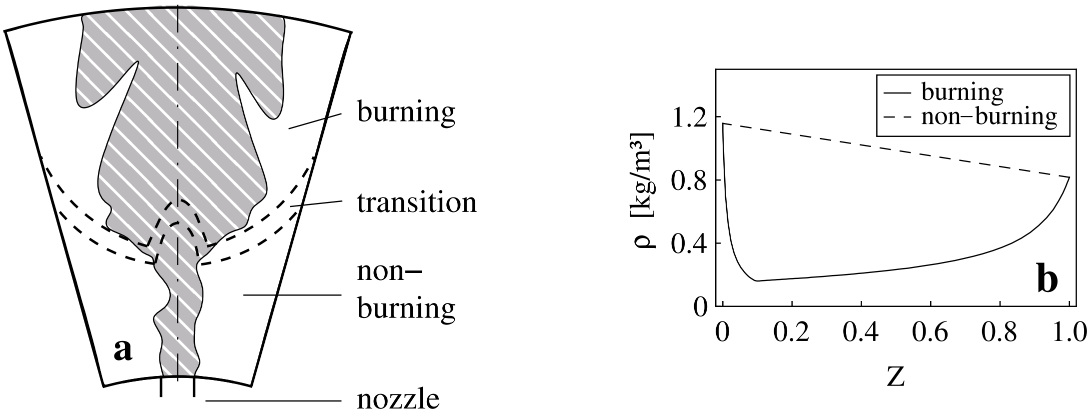

Figure 5.6: Laminar flamelet solution. **a** Prescription of lift-off height illustrated on a meridional cut through the computational domain; **b** density profiles for the burning and the non-burning case.

The present work applies an alternative approach, where the initial solution is computed from a separate, numerically less demanding DNS. For this purpose a code version has been developed which incorporates the hydrodynamic effects of a flame, by applying a comparatively simple flame model based on a uniform[††], steady-state laminar flamelet solution. As described in Sec. 3.2.5, the laminar flamelet solution provides the species mass fractions Y_P and temperature T, and hence also the hydrodynamically important quantities density ρ and viscosity μ as functions of the mixture fraction Z. In the DNS used for initialization a uniform laminar flamelet solution is imposed, which was obtained from a one-dimensional simulation of a counterflow flame for the same stoichiometric conditions and a strain rate $a = 30\ [s^{-1}]$ (Chp. 4). The evolution of the mixture fraction field in the physical space is obtained by solving for a mixture fraction transport equation (Eq. 3.14, recast in non-dimensionalized form), which had to be implemented in the code.

The assumption of a uniform flamelet solution is a strongly simplified model for the flame structure in that the effect of the variability of χ_{st} is neglected. Although the imposed steady-state laminar flamelet solution basically corresponds to a finite rate case ($\chi_{\mathrm{st}} > 0$), the assumption of a uniform burning flame structure for the whole computational domain is equivalent to assuming infinitely fast chemistry. In the case of a non-premixed free jet, where stoichiometric mixing conditions are met right from the orifice, this implies that the flame would instantly anchor at the pipe exit. In the present DNS a lift-off is enforced, as the burning flamelet solution is prescribed only in a “burning” region, which is located downstream of the nozzle (see Fig. 5.6 a). Upstream of this position, a “non-burning” inert mixing solution is prescribed, which is also parametrized in terms of the mixture fraction Z. The density profiles of both the mixing and the flamelet solutions are exemplarily

---

[††] $\chi_{\mathrm{st}} = const. < \chi_{\mathrm{st},q}$.

illustrated in Fig. 5.6 b. In a transitional region, located in between, a smooth ramping from the non-burning to the burning flamelet is used, based on Hermitian polynomials.

The DNS of the reacting jet based on the simple uniform flamelet model was initialized itself from a cylindrical column consisting of pure fuel, which is moving along the centerline with the speed of the inflowing jet. Certain stages following the initialization can be seen from the density contours shown in Fig. 5.7. Obviously, large, buoyancy driven structures are produced already by the here employed simple flamelet approach. The bulb-like shape and the size of these structures are already fairly consistent with those observed in the finite rate simulations.

The artificial anchoring of the flame base at a fixed streamwise position associated with the prescription of the lift-off height can be clearly seen from all time instants after the initialization.

A quantitative insight into the multi-scale nature of the considered problem is given in Fig. 5.7 as well. The contour plots suggest that the cold jet region upstream of the flame base appears to be statistically converged already after $t = 50$, which is a little bit higher than one flow-through time based on the bulk jet exit velocity, defined as

$$\Delta t_{\mathrm{ft}} = \frac{L_x}{U_{\mathrm{orif}}} = 40 \, . \tag{5.37}$$

In contrast, the first large, bulb-shaped, buoyant structure does not leave the domain before $t = 350$. This aspect makes evident that in the considered reacting jet flow substantially more computational time is needed for approaching a statistically converged flow field as well as for the acquisition of data for statistical analysis thereafter as compared to typical non-reacting jet configurations.

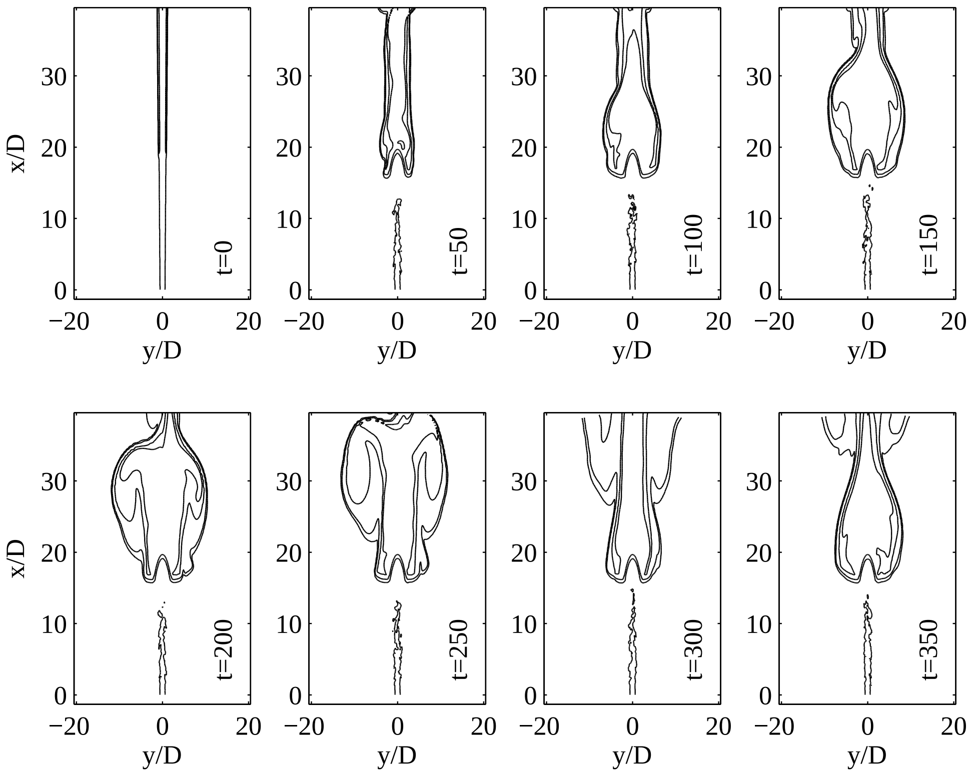

Figure 5.7: Density contours at different stages after initialization. From outwards to inwards, the three plotted contours correspond to $\rho = 1.2, 0.7, 0.2$, respectively.

6 SIMULATION RESULTS

6.1 Considered configuration

In the present work, chemistry-turbulence interactions shall be investigated for the case of a lifted jet flame. For an evaluation of the numerical results, the computed flame should ideally have an experimental counterpart.

Unfortunately, most of the technically relevant, real flame conditions cannot be computed by means of DNS. Computational power is limited, and so is the achievable resolution in time and space. Therefore, before setting up an experimental reference case, the accessible parameter range for the DNS must be marked out. This can be done by order of magnitude reasoning, see e.g. Poinsot & Veynante (2005). To capture the whole range of eddies within a turbulent flow, the motion on all turbulent scales has to be resolved. On the one hand, the computational domain must extend at least over one integral length scale l_t, to capture the biggest eddies. On the other hand, in order to capture also the smallest eddies, this domain has to be discretized with computational cells of the size of a Kolmogorov eddy η. Consequently, the required total number of cells in each spatial direction is proportional to the ratio l_t/η, which scales with $\mathrm{Re}_{l_t}^{3/4}$ (Eq. 3.9). This implies for a three-dimensional DNS a total number of cells $N \sim \mathrm{Re}_{l_t}^{9/4}$. Thus, an exemplary mesh with $N = 2 \cdot 10^8$ would be restricted to flow fields with an integral Reynolds number up to $\mathrm{Re}_{l_t} = 5000$ to provide sufficient spatial resolution.

In the case of reacting flow, additional resolution requirements have to be satisfied. As a commonly accepted rule of thumb flame fronts should be numerically resolved by approximately $N_{\mathrm{react}} = 10 \div 20$ cells. This requirement puts a restriction on the possible Damköhler number, which is basically defined as a ratio of flow to chemical timescale, but can also be represented by the ratio of the Kolmogorov length to the flame thickness η/l_{fl}.

The turbulent flame regime accessible for DNS is illustrated in Fig. 6.1. The declined straight line exemplarily shows the upper limit of the accessible region for a case with $N = 2 \cdot 10^8$ computational cells, which has become amenable to some modern supercomputers. Even for such large computational resources, it is obvious that a high Damköhler number can only be reached in combination with relatively low Reynolds number. Although the parameter range of industrial combustors is clearly outside of the domain accessible for DNS, at least some part of the domain of experimentally realized laboratory jet flames combining low Reynolds and Damköhler numbers, can be considered.

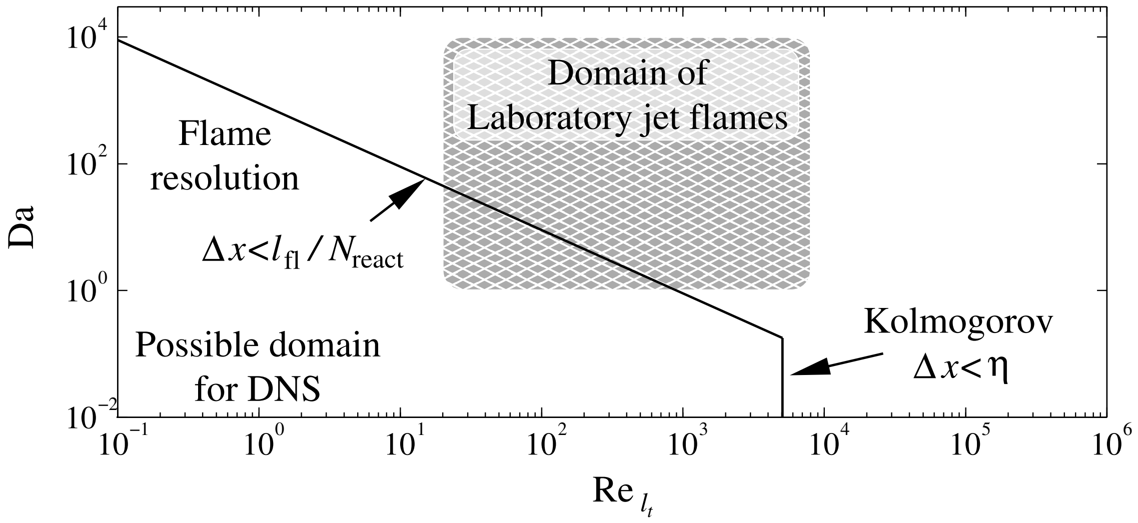

Figure 6.1: Accessible regime for the DNS of reactive flows, $N = 2 \cdot 10^8$ cells . Sketch plotted following Vervisch & Poinsot (1998).

For the present work, the implications of the preceding rationale are the following: On the one hand, in order to be able to investigate chemistry-turbulence interactions, a sufficiently large jet-exit Reynolds number should be chosen, which provides enough instability to produce a fully developed turbulent jet-flow not too far downstream of the orifice. On the other hand, the value of the Reynolds number must be small enough to be computationally amenable for DNS. These two restrictions basically suggest to employ a fully developed turbulent pipe flow as inflow condition, with a pipe Reynolds number somewhat above the critical value of 2300. For such a case, the flow is already turbulent right from the orifice position.

To meet the resolution requirements imposed by the chemical reactions, a low Damköhler number should be realized*, which provides comparatively thick reaction zones. This can be achieved by diluting the fuel stream with chemically inert nitrogen, which inhibits to some extent the fast reactions. Besides the benefit of a spatially resolvable flame, the addition of nitrogen has a second advantage: By increasing the fraction of nitrogen in the fuel stream, the chemical reactions in the lifted jet flame downstream can be attenuated to a point, where the flame is finally blown out. Choosing a state close to this blow-out limit should guarantee a flame which is considerably affected by turbulent motions. Thus, an appropriate dilution with nitrogen can provide highly sensitive flame conditions close to the blow-out limit, which is of particular interest when investigating the influence of the flow field on the flame stabilization.

The DNS of the present work considers a methane-air jet flame configuration, which was experimentally investigated by Köberl *et al.* (2010) and Heimel (2010) at the Institute for

---

*i.e. “slow” chemistry.

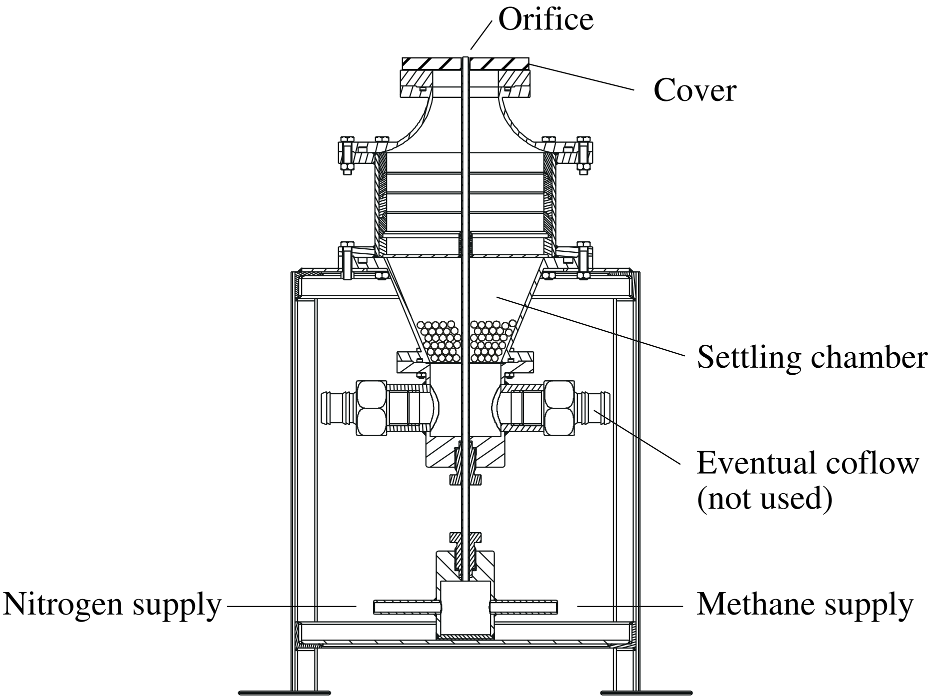

Figure 6.2: Meridional cross-section of the burner used in the present study. Image courtesy of Köberl *et al.* (2010) and Kawanabe *et al.* (2000).

Parameter	Symbol	Value (dimensional)	Unit	Value (dimensionless)
Pipe diameter	D	$4^{\square}$	$[mm]$	1
Bulk jet exit velocity	U_{orif}	$11.3^{\square}$	$[m/s]$	1
Methane mass fraction in fuel	$Y_{\mathrm{CH_4},1}$			0.5
Nitrogen mass fraction in fuel	$Y_{\mathrm{N_2},1}$			0.5
Stoich. mixture fraction	Z			0.104
Laminar flame speed	s_L	$0.308^{\Diamond}$	$[m/s]$	0.027
Fuel temperature	T_1	$25^{\square}$	$[°C]$	1
Adiabatic flame temperature ($\phi = 1$)	T_{ad}	$2016^{\Diamond}$	$[°C]$	7.63
Ambient temperature	T_{∞}	$25^{\square}$	$[°C]$	1
Fuel density	ρ_1	$0.82^{\Diamond}$	$[kg/m^3]$	1
Adiabatic density ($\phi = 1$)	ρ_{ad}	$0.15^{\Diamond}$	$[kg/m^3]$	0.18
Ambient density	ρ_{∞}	$1.16^{\Diamond}$	$[kg/m^3]$	1.41
Jet exit Reynolds number	Re_1			2750
Jet exit Froude number	Fr_1			57

Table 6.1: Parameter setting of the lifted, diluted methane-air jet flame. Dimensional values correspond either to experiment ($^{\square}$) or to the 1D computational results Sec. 4.4 ($^{\Diamond}$).

Thermal Turbomachinery and Machine Dynamics at Graz University of Technology. A burner design from Kawanabe *et al.* (2000) was adopted (see Fig. 6.2), where the inlet pipe has a fixed inner diameter of 4 $[mm]$. Differently to previous studies with this burner, no co-flow was used in the present case. In order to obtain controlled and reproducible experiments, the co-flow orifice of the burner was covered with a circular plate. The parameter setting which applies to the experiments as well as the present computations is given in Tab. 6.1. It has to be noted, that the stoichiometry which was imposed here corresponds to the one-dimensional flame computations for the diluted premixed and diluted non-premixed cases, whose results were given in Sec. 4.4. It is also noted to the present setup, that any further dilution of the fuel stream with nitrogen led to a blown out flame, which implies that the considered lifted flame is burning in a very fragile state.

Two different DNS cases were set up for the present study: A computation of a reacting jet with the inflow parameters given in Tab. 6.1, and a corresponding non-reacting, inert jet with the same inflow parameters. The latter is used for an evaluation of the jet flow simulation against analytical results and data from literature. It also serves as a non-reacting reference case for a comparison against the reacting case.

6.2 Inert Jet

6.2.1 Computational Setup

The DNS of the non-reacting, inert reference case was computed on a mesh consisting of $768 \times 230 \times 128^{\dagger}$ cells in the streamwise, lateral, and azimuthal directions, respectively, which implies a total number of gridpoints $N = 22.6$ Mio. The axial length of the domain is 40 pipe-orifice diameters D. Due to the conically shaped domain, the domain extends in the lateral direction between $y/D = \pm 10$ at the orifice and $y/D = \pm 18$ at the outflow boundary. In the chemically inert case only one scalar conservation equation for the mixture fraction Z is solved, which provides the variable gas properties of the local methane-nitrogen-air mixture using basically a non-burning, only mixing, flamelet solution, i.e. $\rho = \rho(Z)$, $\mu = \mu(Z)$.

The simulation was started from a moving column of the methane-nitrogen mixture, surrounded by ambient air. A comparatively coarse mesh was used for the first time after initialization, to save computational time until the solution has converged to a statistically steady flow field. The initial coarse mesh was successively refined two times before the finest resolution ($768 \times 230 \times 128$) was reached. After the solution had converged to a statistically steady state, statistical data were taken during the non-dimensional timespan

---

[†] N_r, N_θ, N_φ, see Fig. 5.1.

$1160 < t < 1580$. This time span for the statistical analysis corresponds to three flow-through times based on the streamwise average of the centerline velocity and the axial extension of the domain obtained as

$$\Delta t_{\mathrm{ft}} = \int_{L_x} \frac{1}{u_c}\, dx = 140\,. \tag{6.1}$$

In contrast to the definition used in Eq. (5.37), the expression above is used here to reflect more accurately the average advective velocity into the streamwise direction.

6.2.2 Resolution of the flow field

The exact requirements for a fully resolved DNS are disputed in literature. They depend on the discretization scheme, but also on the nature of the flow field. Moin & Mahesh (1998) state that, for a valid DNS, most of the dissipative scales must be captured, but the Kolmogorov scale needs not to be resolved exactly. According to their reasoning, this should be generally the case, if the order-of-magnitude of the grid spacing is $\mathcal{O}(\eta)$. For the present inert jet, the quality of the resolution of the turbulent scales is illustrated in Fig. 6.3 showing contours of the ratio of the effective grid spacing

$$\Delta x_{\mathrm{eff}} = \sqrt[3]{\Delta r \cdot r\Delta\theta \cdot r\sin\theta\Delta\varphi}\,, \tag{6.2}$$

to the Kolmogorov length scale η. Maximum ratios up to 3.5 can be seen in the near field of the orifice ($x/D = 0$) in Fig. 6.3. This appears to be acceptable in view of the

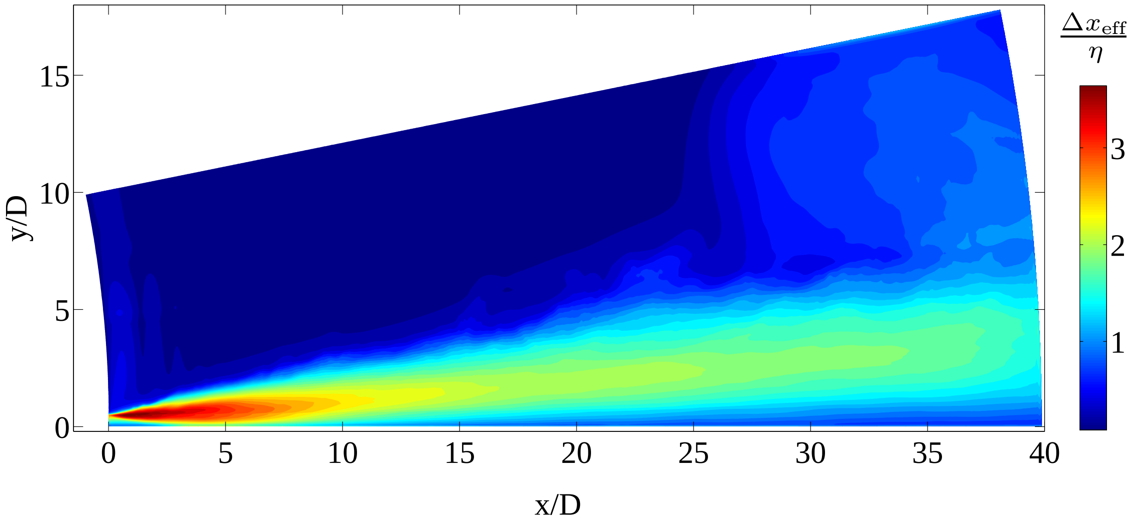

Figure 6.3: Contours of the ratio of effective grid spacing Δx_{eff} to the Kolmogorov length scale η; inert jet.

fact that the very steep velocity gradients near the nozzle would require an excessively large number of additional gridpoints to further reduce the ratio $\Delta x_{\text{eff}}/\eta$ close to unity. Moreover, Kolmogorov's theory basically applies to fully developed isotropic turbulence, which is not the case in the neighbourhood of the pipe orifice.

Summing up, it can be stated that the presently used computational mesh provided reasonable resolution in most parts of the turbulent flow field, where a ratio $\Delta x_{\text{eff}}/\eta < 2$ is generally observed, which is comparable with the values obtained in previous works (Moin & Mahesh, 1998).

6.2.3 Structure of the flow field

The qualitative structure of the turbulent jet flow field is exemplarily illustrated in Fig. 6.4 showing instantaneous contours of the azimuthal component of the normalized vorticity

$$\mathcal{W} = (\boldsymbol{\nabla} \times \mathbf{u}) \frac{U_{\text{orif}}}{\overline{u}_c} \frac{\overline{y_{.5,u}}}{D} , \tag{6.3}$$

on a meridional plane. In the vicinity of the orifice at $x/D = 0$, the vorticity field is notably influenced by the vortical structures injected with the turbulent pipe inflow. Small scale vortical structures can be seen in the shear layer at $y/D = \pm 0.5$, but the strength of vortices in the core region remains comparatively low. This core region breaks down at a position $x/D \approx 7$, where the cylindrically symmetric shear layer reaches the jet axis. Downstream of this position, a typical free-jet flow is developed. In this far-field, the jet spreads continuously with increasing distance from the orifice. Comparatively large and strong turbulent eddies are formed. At a certain off-axis position y/D, the vorticity drops to negligibly small values, which marks the instantaneous position of the so called

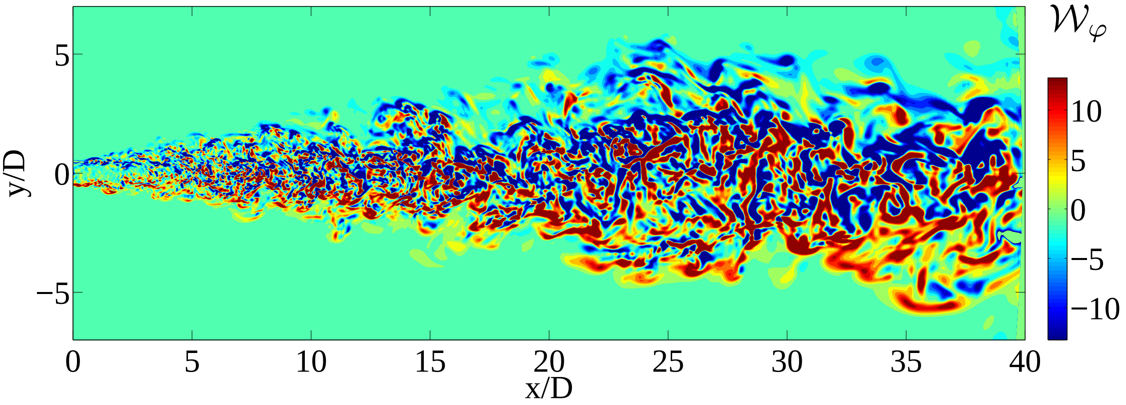

Figure 6.4: Instantaneous contours of the normalized azimuthal vorticity $\mathcal{W}_\varphi$ for the inert jet. The colorbar is clipped at $\mathcal{W}_\varphi = \pm 13.25$.

turbulent/non-turbulent interface representing the boundary surface between the rotational fully turbulent inner region and the irrotational ambient region associated with $\mathcal{W}_\varphi \approx 0$.

For a quantitative assessment, the computational results can be compared against experiments from various sources. A large amount of experimental data is available in literature, see e.g. Wygnanski & Fiedler (1969), Chen & Rodi (1980), Papanicolaou & List (1988), Panchapakesan & Lumley (1993), Richards & Pitts (1993), Amielh *et al.* (1996), Westerweel *et al.* (2002), and Xu & Antonia (2002). Due to the different experimental conditions applied in these measurements, the data must be transformed into (ideally) universal, hence comparable, representations. This is generally done based on the theory that constant-density, non-buoyant free jet flows become self-similar in the far-field (Yarin, 2007). In the present case of an inert nitrogen-diluted methane jet discharging into air, the density is clearly not constant. Nevertheless, Chen & Rodi (1980) argue that the density difference becomes sufficiently small with increasing distance from the orifice, so that the assumption of self-similarity can be upheld modifying the momentum of the inflow with the density ratio between the jet and the ambient fluid. The self-similarity assumption, which is based on the conservation of the momentum injected at the nozzle inflow, can be also jeopardized by the effect of buoyancy particularly in the case of low jet-exit Reynolds numbers. Inertial forces are strongest in the vicinity of the jet orifice, but decay with increasing axial distance. As a consequence, buoyant forces can become relevant downstream from some position $(x/D)|_{\mathrm{nb}}$. Based on a comprehensive review of existing experimental data, Chen & Rodi (1980) derived a correlation for the axial limit of the non-buoyant region, written as

$$\left.\frac{x}{D}\right|_{\mathrm{nb}} = \frac{1}{2}\,\mathrm{Fr}\sqrt{\frac{\rho_1}{\rho_\infty - \rho_1}}\,\sqrt[4]{\frac{\rho_1}{\rho_\infty}}\,. \tag{6.4}$$

Evaluating this correlation for the presently considered inert jet case gives $x/D|_{\mathrm{nb}} = 40.2$, which is just downstream of the outflow boundary of the computational domain. Hence, concluding from this estimate for $x/D|_{\mathrm{nb}}$, no notable effects of buoyancy are expected to appear in the computational results for this inert jet case, and the solutions should generally exhibit self-similar behaviour.

Mean values

The spreading of the jet is commonly measured in terms of the streamwise evolution of the half-width of the velocity ($\overline{y_{.5,u}}/D$) and the mixture fraction profiles ($\overline{y_{.5,Z}}/D$), which denote the radial position of local half-maximum. The self-similarity of the solution for round jets is subject to the constraint that the half-width of the jet axially increases at a constant rate of spread $\dot{\overline{y_{.5}}} = d\left(\overline{y_{.5}}\right)/dx$. Both the half-widths of the velocity and the mixture fraction are plotted in Fig. 6.5 a. Apart from a slight bending, the profiles of the velocity and the mixture fraction half-widths essentially show a linear streamwise variation downstream of $x/D \approx 7$, pointing at self-similar behaviour. The rates of spread obtained for the region $20 < x/D < 40$ are compared against experimental data of non-buoyant jets in Tab. 6.2. The numerically obtained spread rates are in general below the experimentally obtained values. As a possible reason of this deviation, it is supposed that some weak, though notable effects of buoyancy might be already present in the considered low Reynolds number jet.

For self-similar round jets, the linear increase of the half-width, together with the assumption of conserved total momentum, translates into a linear streamwise increase of the inverse of the centerline velocity according to

$$\frac{U_{\text{orif}}}{\overline{u}_c} = \frac{1}{\Lambda B_u} \left(\frac{x}{D} - \frac{x_0}{D} \right), \tag{6.5}$$

where U_{orif} is the bulk jet exit velocity, B_u is a decay constant, and x_0/D refers to the position of the virtual orifice. The parameter Λ accounts for the effect of the inflow velocity profile, which is presently estimated as $\Lambda \approx U_{\text{orif}}/\overline{u}_{c,\text{orif}}$ dependent on the average centerline velocity at the orifice $\overline{u}_{c,\text{orif}}$ following Amielh *et al.* (1996). For jets issuing from a contraction nozzle, this modification is irrelevant as $U_{\text{orif}}/\overline{u}_{c,\text{orif}} \approx 1$, while it is required for jets with turbulent pipe inflow conditions. A streamwise variation equivalent to Eq. (6.5) with a decay constant B_Z is found for the average centerline mixture fraction $\overline{Z}_c$, when introducing a constant species mass flow. The centerline decays of the velocity,

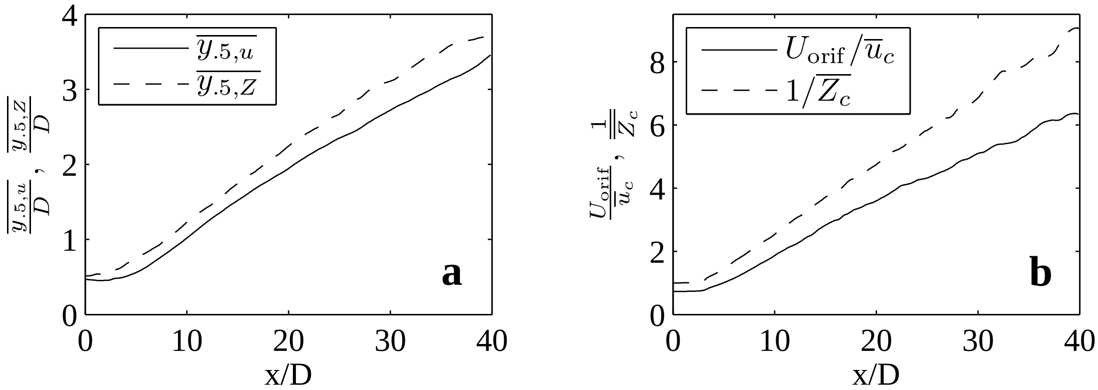

Figure 6.5: Spreading and axial decay behaviour of the inert jet: **a** spread rate of the jet half-width $\overline{y_{.5}}$ for velocity u and mixture fraction Z, **b** decay of the mean centerline velocity $\overline{u}_c$ and the mixture fraction $\overline{Z}$.

Study	$\frac{\rho_1}{\rho_\infty}$	Re	Orifice	$\overline{\dot{y}_{.5,u}}$	$\overline{\dot{y}_{.5,Z}}$	$B_{u,\Delta\rho 0}$	B_Z	$\left.\frac{\sqrt{\overline{u'^2}}}{\overline{u}_c}\right\|_{\max}$	$\left.\frac{\sqrt{\overline{u'^2}}}{\overline{u}_c}\right\|_{c}$	$\left.\frac{\overline{u'v'}}{\overline{u}_c^2}\right\|_{\max}$	$\left.\frac{\sqrt{\overline{Z'^2}}}{\overline{Z}_c}\right\|_{\max}$
Present DNS	0.71	2750	pipe	0.072	0.080	6.2	4.7	0.25	0.22	0.019	0.25
Wygnanski & Fiedler (1969)	1.00	100000	c.n.	0.086	n.a.	5.4	n.a.	0.29	0.29	0.018	n.a.
Chen & Rodi (1980)	1.00	univ.	univ.	0.086	0.110	6.2	5.0	0.28	0.28	0.018	0.21-0.26
Papanicolaou & List (1988)	1.00	600-11000	c.n.	0.087	0.116	6.7	6.4	0.25	0.25	n.a.	0.25
Panchapakesan & Lumley (1993)	1.00	11000	c.n.	0.096	n.a	6.1	n.a.	0.25	0.24	0.019	n.a.
Richards & Pitts (1993)	0.55	25000	pipe	n.a.	0.115	n.a.	4.0	n.a.	n.a.	n.a.	0.27
Amielh *et al.* (1996)	0.14	7000	pipe	0.083	n.a.	9.1	n.a.	0.26	0.24	0.019	n.a.
	1.00	21000	pipe	0.062	n.a.	9.1	n.a.	0.22	0.20	0.014	n.a.
Westerweel *et al.* (2002)	1.00	2000	pipe	0.097	0.125	n.a.	n.a.	0.26	0.24	0.019	0.3
Xu & Antonia (2002)	1.00	86000	pipe	0.086	n.a.	6.5	n.a.	0.25	0.24	0.015	n.a.

Table 6.2: List of selected key quantities obtained for the inert jet and corresponding experimental data from literature. The numerically obtained rates of spread $\overline{\dot{y}_{.5}}$ and decay constants B of the present study, are evaluated in the region $20 < x/D < 40$. The abbreviations indicate: c.n.: contraction nozzle; n.a.: no values available; univ.: universal, i.e., authors claim general applicability without restrictions on Reynolds number and nozzle geometry.

normalized by the jet-exit bulk velocity, and the mixture fraction, normalized by the constant jet-exit value of unity, are presented in Fig. 6.5 b showing the streamwise variation of the corresponding inverse expressions. In consistence with the self-similarity based Eq. (6.5), the plotted profiles should vary almost linearly with x. Again, a slight bending can be observed in the decay curve for the centerline velocity. A quantitative comparison of the obtained centerline decay parameters against experimental data from literature can be found again in Tab. 6.2. For variable-density jets, the centerline velocity decay is usually compared against a density corrected velocity decay constant $B_{u,\Delta\rho 0} = B_u\sqrt{\rho_\infty/\rho_1}$, which accounts for the change of the inertia of the inflowing jet associated with the density difference to the ambient medium (see Chen & Rodi 1980). The numerically obtained decay constants $B_{u,\Delta\rho 0}$ and B_Z evaluated for the range $20 < x/D < 40$ show good agreement with experiments.

The radial variation of the axial velocity is plotted in self-similar coordinates in Fig. 6.6 a. Since the numerical solution essentially features self-similar behaviour, the individual normalized representations obtained within $10 < x/D < 40$ practically collapse into one self-similar average profile with a deviation range $\Delta\overline{u}/\overline{u}_c \approx \pm 0.04$. In Fig. 6.6 a the normalized profile obtained at $x/D = 20$ (solid line) is compared against the analytical self-similar solution for laminar jet flow, which, under the assumption of a constant turbulent viscosity μ_t, can also be applied to the turbulent case (Yarin, 2007). Good agreement is found in the neighbourhood of the jet axis $y/\overline{y_{.5,u}} < 1$, however, notable discrepancies appear for the radially outer region $y/\overline{y_{.5,u}} > 1$, where the numerically obtained profile is always lower. The same behaviour was observed in previous numerical studies, e.g. by Boersma *et al.* (1998), but also in the experimental work of Wygnanski & Fiedler (1969). It is somewhat surprising that a simple Gaussian fit denoted by the symbols in Fig. 6.6 a agrees notably

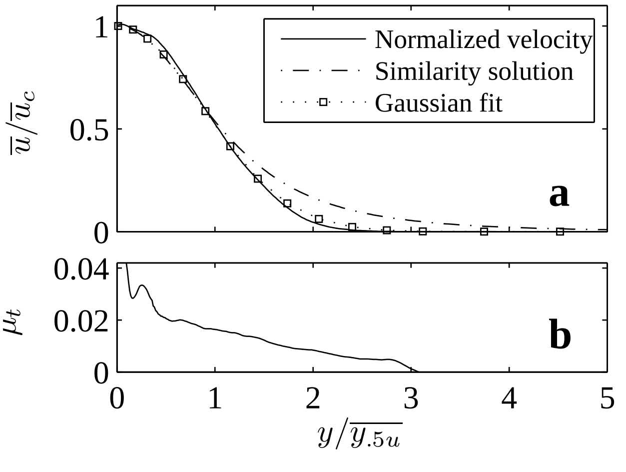

Figure 6.6: Radial profiles in self-similar coordinates for the inert jet: **a** mean normalized axial velocity $\overline{u}/\overline{u}_c$ at $x/D = 20$, **b** turbulent viscosity μ_t obtained from Eq. (6.6).

better with the numerical result, although this empirical fit has no physical background unlike the analytical self-similar solution. This observation is also supported by the experimental studies of Chen & Rodi (1980), Papanicolaou & List (1988), Amielh *et al.* (1996), Westerweel *et al.* (2002), and Xu & Antonia (2002), who compare their measured data against Gaussians instead of the self-similar analytical solution.

An explanation for this observed discrepancy can be found by scrutinizing the assumption of a constant turbulent viscosity μ_t. The radial variation of this quantity which can be recomputed from the present DNS results by

$$\mu_t = -\frac{\overline{\rho}\,\overline{u'v'}}{\partial \overline{u}/\partial y}\,, \tag{6.6}$$

is plotted in Fig. 6.6 b. In contrast to the assumption of a constant line, the turbulent viscosity radially decreases. This implies that the turbulent transfer of axial momentum is effectively reduced resulting in lower axial velocities in the radial outer region as compared to the analytical self-similar solution, where the turbulent transfer of momentum is computed using an invariant turbulent viscosity $\mu_t = \text{const.}$

It has to be noted, that alternative self-similar, but non-analytical velocity profiles have been found, e.g. Tollmien's solution, which give reasonable agreement (see Wygnanski & Fiedler 1969).

Turbulence quantities

The self-similar behaviour is also reflected by the turbulent second-order statistics. This is exemplarily illustrated in Fig. 6.7 a and b, where the radial variation of the streamwise

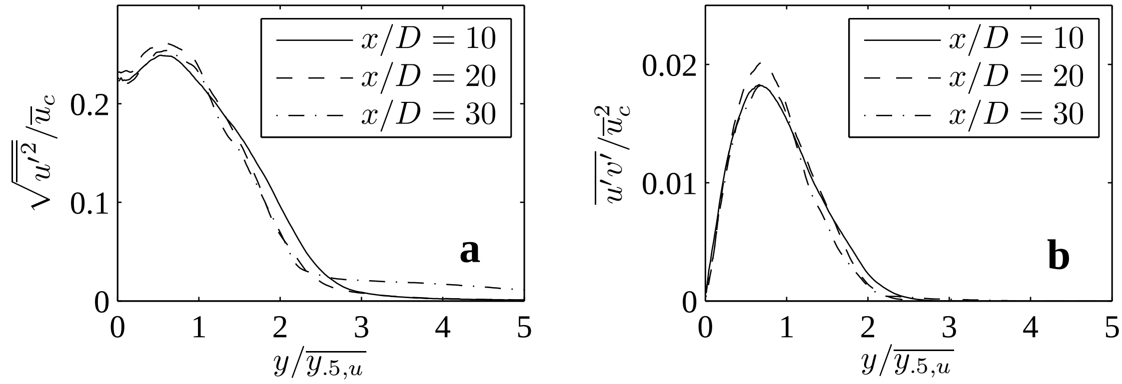

Figure 6.7: Radial variation of turbulent second-order quantities in self-similar coordinates for the inert jet at $x/D = 10, 20, 30$: **a** streamwise turbulence level $\left(\overline{u'^2}\right)^{1/2}/\overline{u}_c$, **b** normalized turbulent shear stress $\overline{u'v'}/\overline{u}_c^2$.

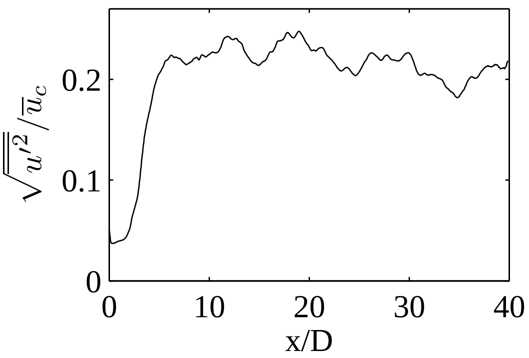

Figure 6.8: Axial evolution of the streamwise turbulence intensity $\left(\overline{u'^2}\right)^{1/2}/\overline{u}_c$; inert jet.

turbulence level $\left(\overline{u'^2}\right)^{1/2}/\overline{u}_c$ and turbulent shear stress $\overline{u'v'}/\overline{u}_c^2$ are plotted in self-similar coordinates. The shown profiles collapse almost perfectly for all three axial positions. A maximum value of $\left(\left(\overline{u'^2}\right)^{1/2}/\overline{u}_c\right)_{\max} = 0.25$ is exhibited in the shear layer, which is in good agreement with the experimental values listed in Tab. 6.2. At the jet axis, the turbulent shear stress is zero, due to the axial symmetry. The observed maximum value of $\left(\overline{u'v'}/\overline{u}_c^2\right)_{\max} = 0.019$ belongs to the upper range of the corresponding experimental values reported in literature on constant-density jets. This particular feature can be attributed to the jet-to-ambient density ratio of the present jet following a study of Amielh *et al.* (1996). They illustrated with their experiments that the turbulent shear stress is very sensitive to density variations, so that for jets lighter than the ambient medium, higher turbulent shear stresses are expected.

The axial variation of the turbulent fluctuations for the streamwise velocity can be seen from Fig. 6.8. A relatively low turbulence level for the streamwise velocity is observed near the orifice, which basically corresponds to the centerline turbulence level of the incoming turbulent pipe flow. When the initial shear layer reaches the center, the turbulence level abruptly increases to a constant plateau-value of $\left(\overline{u'^2}\right)^{1/2}/\overline{u}_c = 0.22$. Again, a good agreement with experiments is seen also for this value (Tab. 6.2). The observed transition to a nearly constant plateau-like turbulence level indicates that the turbulent jet flow approaches the self-similar regime, which is associated with $\left(\overline{u'^2}\right)^{1/2}/\overline{u}_c = \text{const.}$

The self-similar behaviour in the far-field is also reflected in the scalar field, as seen from the radial variation of the normalized mixture fraction fluctuations $\left(\overline{Z'^2}\right)^{1/2}/\overline{Z}_c$ in Fig. 6.9. Similar to the velocity fluctuations, individual profiles obtained at different streamwise positions almost collapse into one curve. A good agreement with the corresponding experimental data listed in Tab. 6.2 is observed as well.

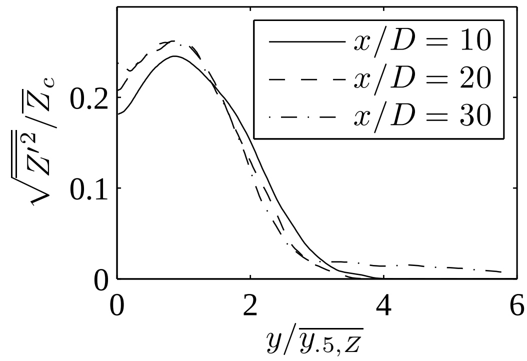

Figure 6.9: Radial variation of the normalized mixture fraction fluctuations $\left(\overline{Z'^2}\right)^{1/2}/\overline{Z}_c$ at $x/D = 10, 20, 30$; inert jet.

6.3 Reacting Jet

6.3.1 Computational Setup

For the reacting case, significantly higher computational costs arise in comparison to the inert case. To mitigate this exceeding demand on computational power, the reacting jet case was set up using a somewhat coarsened mesh in the regions away from the flame base comprising $512 \times 150 \times 128$ cells, which corresponds to a total number of grid cells $N = 9.8$ Mio. The cells were clustered in the axial direction in the vicinity of the expected flame base, to increase the local resolution near the the partially premixed flame base. Like in the inert case, the domain extends over 40 orifice-pipe diameters D in the axial direction. The extension in the lateral direction varies between 20 D at the orifice, and 36 D at the outflow boundary. The reactive layers were dynamically thickened based on the Eqs. (5.29) and (5.30) using the parameters $F_{\text{max}} = 4.34$ and $\dot{\omega}_{2,\text{ref}} = 0.02$. The maximum efficiency factor in the region around the flame base was chosen $E = 1.85$. The layer at the outflow boundary, where the viscosity is increased according to Eq. (5.34), extends five diameters upstream from the boundary.

Similar to the inert case, the simulation was started on a coarse mesh, using a moving column of nitrogen-diluted methane as initial condition. The flame was initialized by incorporating a uniform burning flamelet solution as described in Sec. 5.3. After the non-dimensional computation time $t = 640$, the mesh was refined to attain the final resolution. From $t = 770$ onwards, the uniform flamelet model is dropped, and the simulation is continued using the two-step finite-rate chemistry described in Sec. 2.3.2. The following presented instantaneous and statistical data were obtained within the timespan $1000 < t < 1950$. This timespan used for analysis corresponds to 7.6 flow-through times, defining the flow through time based on the average centerline velocity in the computational domain analogously to Eq. (6.1) as

$$\Delta t_{\mathrm{ft}} = \int\limits_{L_x} \frac{1}{\overline{u}_c}\, dx = 125\ . \tag{6.7}$$

6.3.2 Resolution of the flow field

The spatial resolution of the small scale turbulent motion is illustrated in Fig. 6.10 showing instantaneous contours of the ratio of the effective grid spacing Δx_{eff} to the Kolmogorov length scale η. Reasonable values are observed for the entire domain of the simulation. In comparison to the inert case shown in Fig. 6.3, somewhat larger ratios of up to $\Delta x_{\mathrm{eff}}/\eta = 5.4$ can be seen in the initial shear layer close to the orifice. This can be explained by the larger values for Δx_{eff} in this region, where a somewhat coarser resolution is used in the reactive case. Nevertheless, the maximum values observed are still within the acceptable range suggested by Moin & Mahesh (1998). In the refined mesh region near the flame base, which is located around $x/D \approx 16$, the resolution parameter $\Delta x_{\mathrm{eff}}/\eta$ assumes approximately the same local values as in the inert case. Downstream of $x/D \approx 20$, the ratio $\Delta x_{\mathrm{eff}}/\eta$ drops down to values of unity and below in the reacting case. This strong decrease points already at a strong dynamic effect of the flame, which evidently leads to a significant increase of the Kolmogorov length scale η, as the effective grid spacing Δx_{eff} does not significantly change in this region.

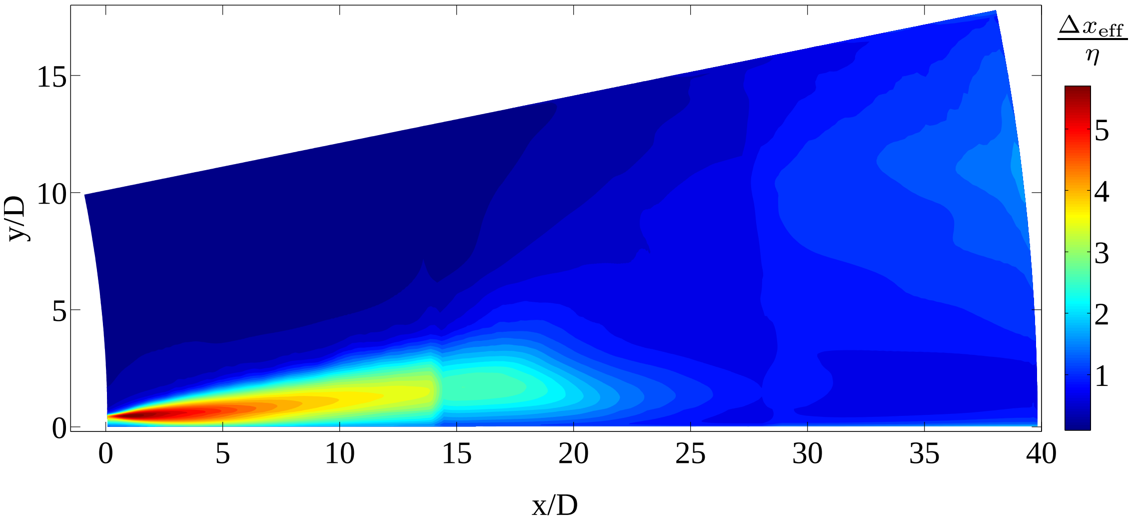

Figure 6.10: Contours of the ratio of effective grid spacing Δx_{eff} to the Kolmogorov length scale η; reacting jet.

6.3.3 Structure of the flow field

A first qualitative picture of the impact of the flame on the underlying turbulent flow field is given in Fig. 6.11 showing a snapshot of the normalized instantaneous azimuthal vorticity contours on a meridional plane. Clear differences can be observed between the the near field next to the orifice, where the flow is not yet reacting, and the far-field region occupied by the flame downstream of $x/D > 20$. In the non-burning near field, the vorticity contours are very similar to the inert case, as expected. First differences appear at a position closely upstream of the reactive layer (marked by bold solid lines), where the vortical zone extends somewhat farther into the cross-stream direction. Downstream of the flame base, the vorticity decreases considerably. Predominantly small scale vortical structures still persist in the core region around the flame base, where they can be observed up to a downstream position of $x/D \approx 30$. Except for the cold core region, which protrudes into the flame base, the vortical motion is evidently attenuated significantly by the reactive layer. The reactive layer appears thereby in the shape of a distorted cylinder as seen from Fig. 6.11.

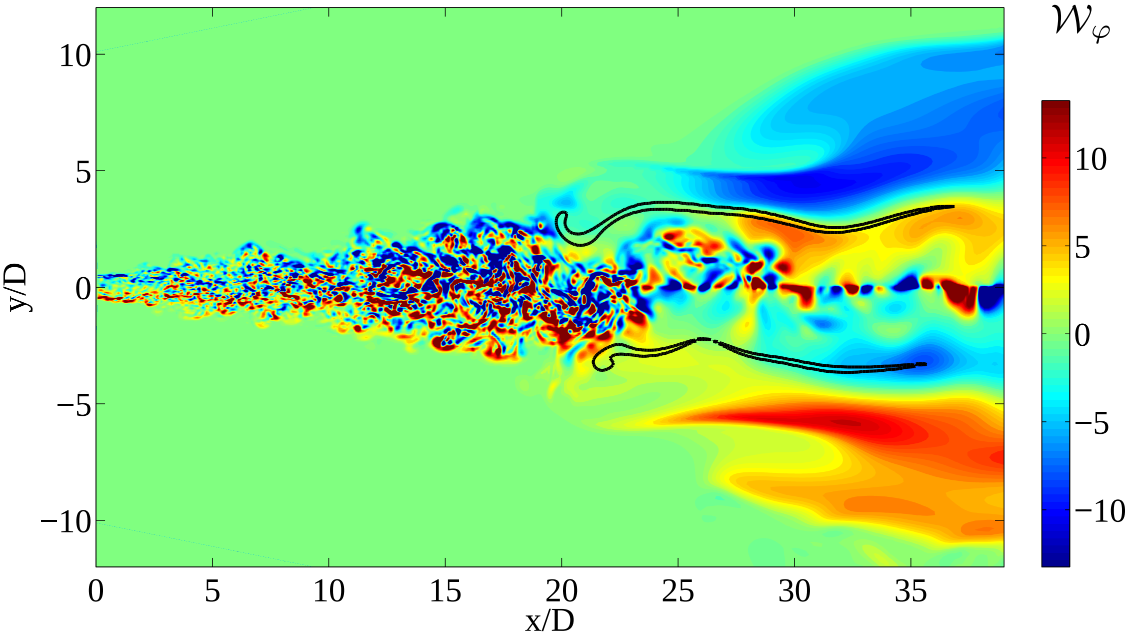

Figure 6.11: Instantaneous contours of the normalized azimuthal vorticity $\mathcal{W}_\varphi$ (Eq. 6.3) for the reacting jet. The colorbar is clipped at $\mathcal{W}_\varphi = \pm 13.25$. The bold solid lines denote the reaction iso-contour of $\dot{\omega}_I = 0.01$.

Mean values

A comprehensive qualitative insight into the structure of the averaged velocity and scalar fields is given by the contours of selected flow and scalar quantities shown in Figs. 6.12 a-f. The mean density $\overline{\rho}$ is illustrated in Fig. 6.12 a. In the inert near field of the jet, intense turbulent mixing with the (heavier) ambient air leads to a notable streamwise increase of the density. As a consequence, the density of the mixture immediately upstream of the flame approaches almost the density level of the ambient air. The heat release of the flame leads to a strong increase in temperature, and hence a marked drop in density. This induces strong dilatational effects, which, in turn, lead to a significant lateral expansion of the region, where the density is lower than the ambient density. The dark-blue regions, where the average density reaches almost the adiabatic value of $\rho_{\text{ad}} = 0.18$ corresponding to the adiabatic flame temperature $T_{\text{ad}} = 7.63$ (refer to Tab. 6.1), basically mark out the average position of the reactive layer. The region near the centerline downstream of the flame base exhibits a comparatively high density, indicating non-burning low temperature flow conditions. This non-burning core region can be attributed to the oncoming portion of cold mixture beyond the rich burning limit which penetrates into the flame base, and effectively keeps the reaction zones away from the center.

The average velocity field is illustrated in Figs. 6.12 b and c showing contours of the axial and cross-stream components, $\overline{u}$ and $\overline{v}$, respectively. For the axial component $\overline{u}$, a fast decay is observed in the non-reacting near field, which is typical for inert jets. In the flame region, the already discussed dilatational effects lead to a considerable spreading of the contours of $\overline{u}$. In the broadened jet region the streamwise velocity assumes an almost constant value near the center. Further downstream toward the outflow a slight increase is observed indicating an acceleration due to buoyancy.

For the cross-stream velocity $\overline{v}$, slender patches with a positive, radially outwards directed motion are observed in the initial shear layer near the orifice, which typically occurs here for continuity reason due to the strong deceleration of the streamwise velocity component. Radially outside of the initial shear layer, indicated by the blue regions, an inwards directed motion is observed due to the entrainment of ambient fluid. Downstream of the flame base, a large drop-shaped region with an intense outwards directed motion appears indicating again the strong dilatational effect caused by the heat release. It is also interesting to note that this region associated with strong volumetric dilatation extends over a confined streamwise distance ($\sim 8\,D$). This implies, the major part of the chemical reactions, and hence, of the heat release, occur in a region close to the flame base.

The structure of the reactive scalar field can be seen from Figs. 6.12 d and e showing exemplarily the average species mass concentrations of oxygen ($\overline{Y}_{\text{O}_2}$) and methane ($\overline{Y}_{\text{CH}_4}$), respectively. Strong mixing of oxygen into the non-reacting fuel stream can be seen again in the near field of the jet (Fig. 6.12 d). The blue regions in the flame zone illustrate the reactive consumption of oxygen. Evidently, the contours are similar to those of the density,

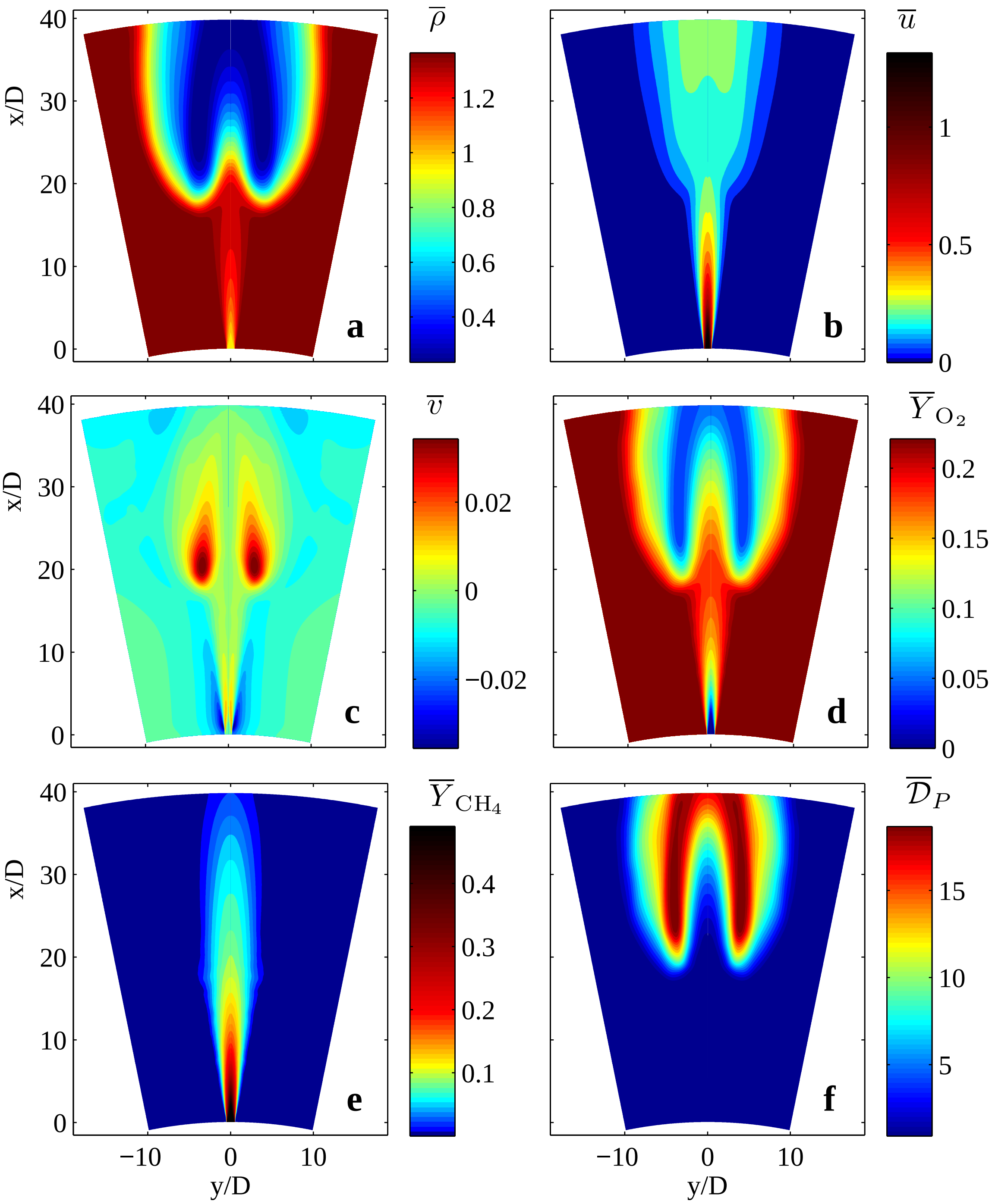

Figure 6.12: Mean values of velocities and scalar quantities in the reacting jet: **a** density $\overline{\rho}$, **b** streamwise velocity $\overline{u}$, **c** cross-stream velocity $\overline{v}$, **d** oxygen concentration $\overline{Y}_{\mathrm{O_2}}$, **e** methane concentration $\overline{Y}_{\mathrm{CH_4}}$, **f** mass diffusivity $\overline{\mathcal{D}}_P$.

as the regions with low oxygen concentrations generally exhibit in turn high concentrations of hot product species associated with low densities. Similar to the density field, the regions of lowest oxygen concentration mark out the average position of the reactive layer. The non-burning, cold core region at the flame base becomes evident again, as seen from the cone-shaped zone with unburnt, oxygen rich mixture protruding into the lifted flame.

The contours of the methane concentration $\overline{Y}_{\mathrm{CH}_4}$ displayed in Fig. 6.12 e show the typical mixing-induced decay along the centerline upstream of the flame. In the flame zone, the region with non-zero methane concentration is apparently confined by the reactive layer, which indicates that there is no notable leakage of methane through the flame front.

Exemplarily for the physical transfer coefficients, the distribution of the molar mass diffusivity $\overline{D}_P$ is shown in Fig. 6.12 f. Large values are seen especially in the regions of the reactive layers. Assuming constant Schmidt and Lewis numbers, the presented picture is equivalently valid for the kinematic viscosity and the thermal diffusivity. The equivalently strong increase in the diffusive transfer coefficients is mainly due to an increase in temperature caused by the reactive heat release. The increased kinematic viscosity leads to a significantly higher dissipation of turbulent eddies in the flame region, where the local Reynolds number is markedly reduced. This relaminarization effect of the flame was already illustrated in the instantaneous vorticity field shown in Fig. 6.11.

The spreading behaviour and centerline decay of the reacting jet are shown in Fig. 6.13. The corresponding results of the inert case are plotted as well for comparison. In the near field of the jet, upstream of $x/D = 16$, the half-width profiles for both the velocity and the mixture fraction increase somewhat faster for the reacting case (Fig. 6.13 a), indicating a slightly enhanced decay. This observation was initially attributed to the different spatial

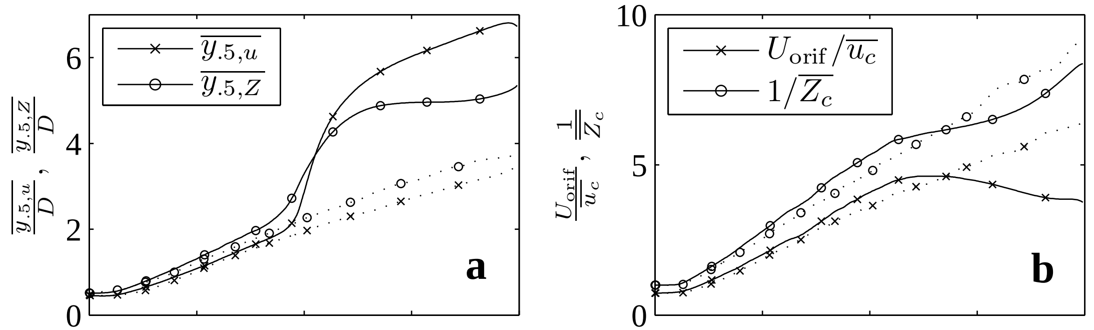

Figure 6.13: Spreading and axial decay characteristics of the reacting jet. — Reacting jet, ··· inert jet.
a spread rate of the jet half-width $\overline{y_{.5}}$ for velocity u and mixture fraction Z,
b decay of the mean centerline velocity $\overline{u}_c$ and the mixture fraction $\overline{Z}$.

resolutions employed in the setup of the inert and reacting cases. To verify this possible explanation, a separate DNS was carried out for the inert case using exactly the same (coarser) mesh as for the reacting case. The same tendency was observed when comparing the results computed on the same meshes. Therefore, the shown difference in the spread rate cannot be attributed to spatial resolution issues. They point rather at a small, though notable, upstream effect. Downstream of $x/D = 16$, consistent with the dilatational effects observed in Fig. 6.12, both half-widths increase markedly. The spreading is more pronounced for the half-width of the streamwise velocity field, so that it exceeds the mixture fraction half-width downstream from $x/D = 20$. This observation can be attributed to the action of the buoyancy forces, which represent a source of momentum in the shear layer, enhancing the entrainment. In contrast, no buoyancy-induced source term appears in the scalar transport equation resulting in the observed smaller half-width $\overline{y_{.5,Z}}$.

In the decay curves for the centerline streamwise velocity and mixture fraction shown in Fig. 6.13 b small upstream effects of the flame are observed again in the near field $x/D < 16$. Consistently with the comparatively broader half-widths, the centerline quantities decay somewhat faster in the reacting case, so that the inverse values of streamwise velocity and mixture fraction assume higher values as seen from Fig. 6.13 b. The impeding effect of the flame on the axial motion upstream becomes especially evident in the region immediately ahead of the average position of the reactive layer, at $x/D = 20$. More pronounced effects of the flame on the flow field are observed downstream of $x/D = 20$. Due to buoyancy forces, the streamwise velocity decay comes to an end, and is followed by a notable acceleration. This buoyancy-driven acceleration counteracts the decay of the mixture fraction. Since a demixing is basically impossible, the inverse centerline mixture fraction maintains a monotonically increasing profile throughout the domain.

The radial variation of the mean normalized axial velocity in self-similar coordinates is plotted in Fig. 6.14 at three axial positions. The three profiles evidently do not collapse, showing that there is no self-similar solution for the reacting jet. At $x/D = 10$, where

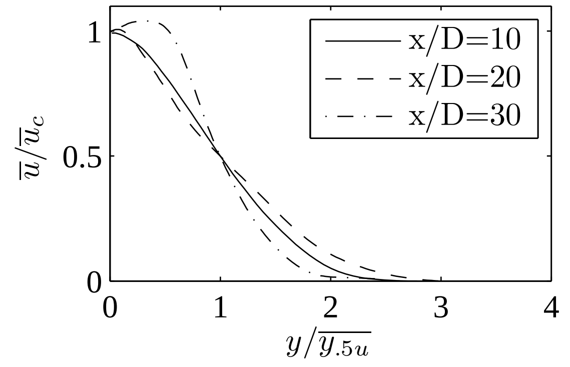

Figure 6.14: Radial variation of the mean normalized axial velocity at the positions $x/D = 10, 20, 30$; reacting jet.

no reactions occur, the solution resembles essentially the profile obtained for the inert jet shown in Fig. 6.6. Near the flame base, which is expected at $x/D \approx 20$, first differences are seen on both sides of $y/\overline{y_{.5,u}} \approx 1$, which denotes here approximately the position of the reactive layer. In the radially outer region ($y/\overline{y_{.5,u}} > 1$) a buoyancy-induced acceleration can be observed, while this is not the case in the core region ($y/\overline{y_{.5,u}} < 1$) leading to a somewhat lower profile as compared to the self-similar type profile at $x/D = 10$. The third shown curve refers to a position well inside the flame region at $x/D = 30$. A pronounced departure from the typically bell-shaped profile can be seen, as the maximum of the curve does not occur at the centerline, but at an off-axis position. The new maximum indicates that the reactive layer, and hence the buoyancy-induced momentum source have moved towards the center. The enhanced entrainment associated with the increased acceleration of the core flow also leads to the observed steepening of the velocity profile.

Buoyancy effects were already addressed several times in the discussion of the salient features shown in the last three figures (Figs. 6.12 - 6.14). It is conceivable that strong effects of buoyancy must be expected due to the large density variations occurring in the flame region as compared to the inert jet case, where the buoyancy forces remain practically irrelevant. It appears also a significant effect on the entrainment of ambient gas. The strong influence of the buoyant forces on the entrainment process can be well illustrated in terms of the integral flow rate along the centerline axis of the jet, which is written as

$$\dot{m} = \int_{\varphi=0}^{2\pi} \int_{\theta=0}^{\theta_{\max}} \overline{\rho u}\, r^2 \sin\theta \, d\theta \, d\varphi \, . \tag{6.8}$$

For the inert jet, where the buoyancy effect is negligible, similarity analysis requires an integral mass flow varying proportional to x/D (Ricou & Spalding, 1961). As seen from Fig. 6.15 showing the integral mass flow rates $\dot{m}$ for both cases, the inert case is in perfect agreement with the similarity theory. For the reacting jet, however, self-similar behaviour

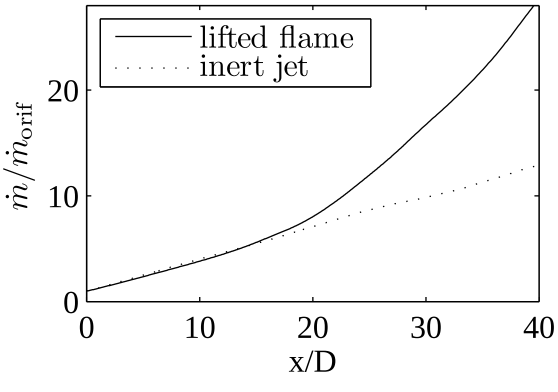

Figure 6.15: Comparison of the normalized integral mass flow rate $\dot{m}$ along the centerline for the inert and the reacting jet.

is only observed up to an axial position of $x/D = 16$. Downstream of this position, a marked increase in the integral mass flow rate is found as compared to the inert jet, pointing at an enhanced entrainment of the ambient gas due to the buoyancy-driven acceleration of the streamwise velocity.

The presently considered lifted jet flame configuration was experimentally investigated by Köberl *et al.* (2010) for a pure methane fuel feed. The particular case with a nitrogen-diluted fuel feed, which is considered in the present DNS, was investigated on the same facility by Heimel (2010). The focus of these works was put on optical measurements of the mean density and density fluctuations based on schlieren images and laser interferometry. The density data obtained in these measurements shall be used for a comparison against the present DNS results.

Fig. 6.16 shows a comparison between the measured and the computed mean density fields. The experimental values were obtained by differential interferometry (shearography), which basically provides line-of-sight integral values. These integral values served as an input for a tomographic reconstruction[‡], so that the experimental values shown in Fig. 6.16 basically represent averages in time and the azimuthal direction φ. The shown values of the simulation are consistently obtained by averaging the instantaneous densities in time and the azimuthal direction φ. As seen from the density contours shown in Fig. 6.16 a, a fairly good agreement between experiment and simulation is observed for the shape of the low-density region. A good agreement is seen also for the lift-off height, which is predicted slightly longer by the simulation than the experimentally measured height.

The variation of the mean density in the cross-stream direction is shown in Fig. 6.16 b, c, d at the selected streamwise positions $x/D = 20, 25, 30$. The variations agree qualitatively well showing essentially the same tendencies, but two quantitative differences are seen: The profiles for the computed mean density appear to extend farther into the lateral region, and they assume lower values at the two further downstream positions. Possible explanations for these deviations can be found in the measurements as well as the simulation. The differential interferometry technique basically measures differences in the optical path length caused by modulations of the refractive index n, which depends on the density as

$$n - 1 = G \cdot \rho \ , \tag{6.9}$$

where $G(Y_P)$ is the composition dependent Gladstone-Dale “constant”. Thus, for a precise interferometric measurement of the density, a simultaneous measurement of both the composition Y_P, and the refractive index n would be necessary. For the present nitrogen-diluted flame no measurements of the local composition were available so that the Gladstone-Dale constant G was estimated based on experiments with pure methane fuel (Köberl *et al.*,

---

[‡] The Algebraic Reconstruction Technique (ART) was used.

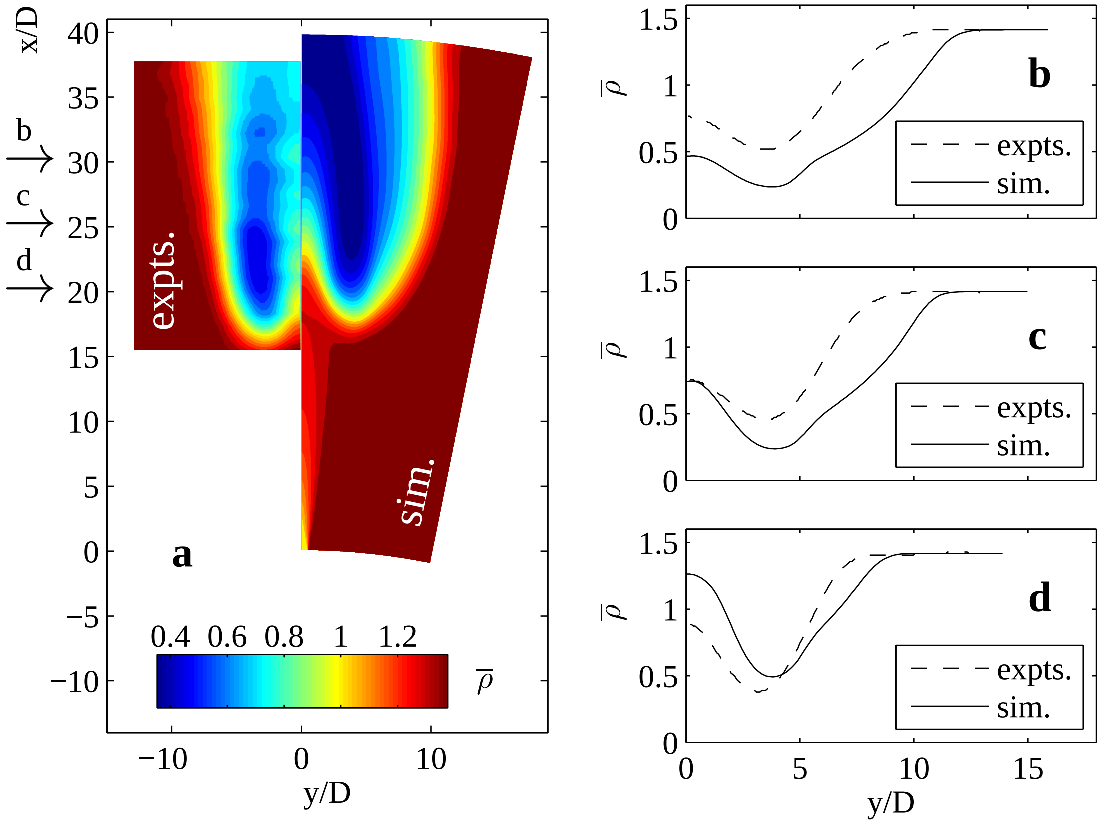

Figure 6.16: Computed mean density compared against experimental interferometry data obtained by Köberl *et al.* (2010) and Heimel (2010). **a** Contours for the experimental (left) and computational data (right). **b**, **c** and **d** show radial density profiles at $x/D = 20, 25, 30$, respectively.

2010). This uncertainty in the determination of the local value of G might explain to some extent the higher densities measured in the experiments.

Aside from this possible uncertainty in the measurements, the numerical treatment of the flame particularly applied in the present DNS has to be considered as a further important reason for the disagreement observed in Fig. 6.16. As already described in Sec. 5.1.5 the Dynamically Thickened Flame concept (DTF) is used to provide a spatially resolvable flame structure on the employed mesh. Since the DTF concept is essentially derived for steady planar flames, its application to a multi-dimensional lifted jet flame has to compensate the strong (gradient-driven) heat losses on the lateral sides of the leading edge flame. In order to retain the correct propagation speed of the leading flame edge, an "efficiency factor" E is therefore introduced, which effectively increases the heat release at the flame base. It was already noted in Sec. 5.1.5, that this enhanced heat release will also increase the heat transfer into the lateral direction along the leading edge flame, which explains the observed wider radial density profiles in Fig. 6.16 b, c, d. Using the DTF concept together with the efficiency factor E evidently reproduces very well the real flame propagation speed as seen from the predicted lift-off height. On the other hand, the increased heat release associated with the reaction rates enhanced with E appears to widen the flame zone. It also explains the absolutely lower densities observed in the simulated data.

Turbulence quantities

For the presently considered flame as specified by the parameter setting in Tab. 6.1, special care has to be taken in the determination of the turbulent fluctuations. A simple averaging of the instantaneous solutions would yield unrealistically high turbulence intensities $\left(\overline{u'^2}\right)^{1/2}/\overline{u}_c$ of up to 0.45 in the flame region. Further analysis can show, that these high fluctuations are not caused by the turbulent fluctuations, but rather by long-wavelength oscillations of the whole flow field, which are illustrated in Fig. 6.17.

Fig. 6.17 a plots the temporal evolution of the total mass $\int_{\mathcal{V}} \rho\, dV$ contained in the computational domain. Large sine-like oscillations with amplitudes of approximately 8 % of the average value can be seen, suggesting that the action of the buoyancy forces leads to a periodic entrainment behaviour. The length of the individual periods is $\Delta t_{\mathrm{bf}} = 350$, which is considerably larger than one flow-trough time based on the average centerline velocity ($\Delta t_{\mathrm{ft}} = 125$) as defined in Eq. (6.7). Since this periodic length exceeds by far the largest turbulent time scales, which are in the present non-dimensionalization of order unity, the observed large-scale oscillations are clearly not related to turbulence.

It is conceivable that the large variations of the total mass caused by the action of the gravitational forces must also translate into large variations of the streamwise momentum. The temporal variation of the total streamwise momentum of the domain $\int_{\mathcal{V}} \rho u\, dV$ is shown in Fig. 6.17 b. The shape of this curve is not sine-like, as it is considerably skewed towards the right hand side. The large-scale oscillations have the same period $\Delta t_{\mathrm{bf}} = 350$ as those of the total mass, so that they must not be interpreted as turbulent fluctuations, which act on significantly smaller timescales.

With the help of Figs. 6.17 a, b the transient effect of buoyancy can be described in some more detail. It can be seen, that the position of the maximum total momentum follows with a certain lag in time the occurrence of the minimum total mass, which is equivalent to a maximum in the buoyancy forces. This lag of $\Delta t = 130$ is caused by the inertia of the entrained ambient mass, and it corresponds roughly to a third of the full period. In turn, the maximum in momentum appears only shortly before the maximum in total mass, where the buoyancy forces reach a minimum. As soon as the accelerating effect of buoyancy

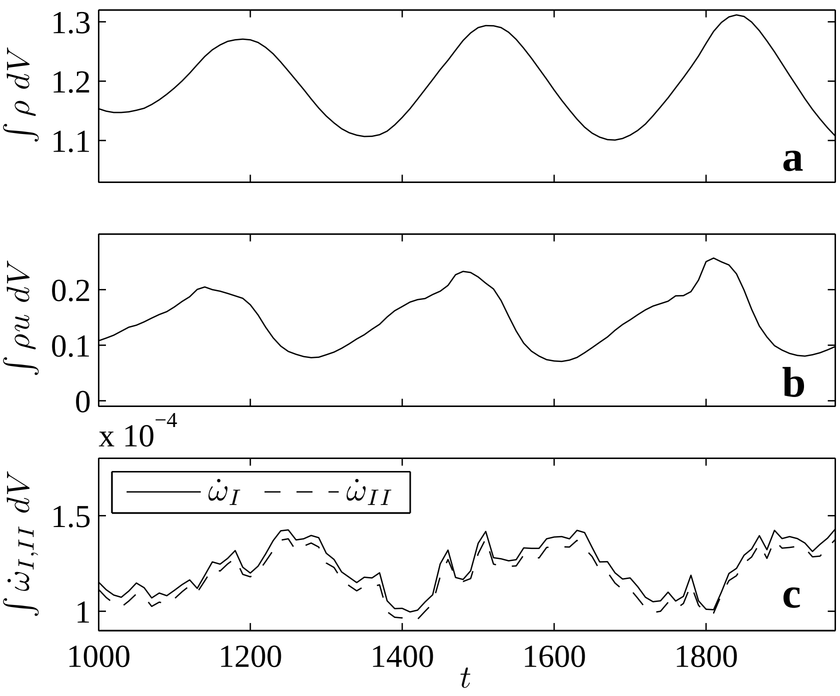

Figure 6.17: Temporal evolution of domain integral values for the reacting jet: **a** total mass $\int_{\mathcal{V}} \rho \, dV$, **b** total momentum $\int_{\mathcal{V}} \rho u \, dV$, **c** total rates $\int_{\mathcal{V}} \dot{\omega}_{I,II} \, dV$ of both elementary reactions.

becomes minimum (the entrainment has reduced the density difference to the ambient fluid), the magnitude of the momentum flux decreases rapidly resulting in the observed skewed profile. A lag of $\Delta t = 90$ (roughly a quarter of the full period) is found between the maximum in the total mass and the minimum in the total momentum.

Fig. 6.17 c illustrates, that the volume integrals of the two elementary reaction rates ($\int_{\mathcal{V}} \dot{\omega}_{I,II} \, dV$) are strongly affected by the long-wavelength oscillations. Since the chemical reactions basically act on much smaller timescales than buoyancy, the shown curves are notably corrugated. Nevertheless, a lowest frequency mode with the period $\Delta t_{\mathrm{bf}} = 350$ can be distinguished. The maxima in the reaction rates always precede the minima in the total mass: The highest reaction rates associated with the highest rates of heat release evidently lead to a fast decrease in the density. The resulting dynamical effect of volumetric dilatation pushes considerable amounts of fluid out of the computational domain, which reduces further the total mass. Vice versa, the lowest reaction rates are accompanied by an increase in the total mass.

It is noted, that a similar interaction between reaction, buoyancy and convection was already found by Won *et al.* (2002) for the case of a laminar, extremely buoyant flame with a Froude number $\mathrm{Fr} \approx 2 \cdot 10^{-3}$. In their study, the lift-off of the flame was shown to be solely caused by buoyancy, which does not apply to the present turbulent case with a much higher Froude number $\mathrm{Fr} = 57$.

The observed buoyancy-induced large-scale oscillations make evident, that the instantaneous results produced by the DNS must be appropriately post-processed (buoyancy-corrected) before turbulence statistics can be extracted. For this correction, it would be basically desirable to subtract only the lowest-frequency mode (period $\Delta t = \Delta t_{\mathrm{bf}}$, frequency $f = 1/\Delta t_{\mathrm{bf}}$) from the raw data to obtain a corrected signal. This would correspond to a sharp "mode-block" filter in Fourier space. Working in a Fourier space, with signals decomposed into sines and cosines, this treatment would be however not fully adequate to the actual physics of the problem. As seen from the skewed signal in Fig. 6.17 b, the lowest-order mode of the oscillation will most probably not correspond to a sine function, so that it would not be accurately captured by just one single mode. On the other hand, no alternative filtering procedures could be found which are better suited to the present problem[§]. Therefore, in order to capture at least some part of the skewness in the signal, the present data were corrected by applying a band block filter for all frequencies $f < 1.\dot{3}/\Delta t_{\mathrm{bf}}$ instead of a sharp "mode-block" filter for one single frequency.

The effect of the presently applied, here termed "buoyancy-correction" technique, is exemplarily illustrated in Fig. 6.18 for the streamwise velocity u. The shown curves refer to instantaneous velocity data obtained for the inert and the reacting case at a position $x/D = 35.2$, $y/D = 0.8$. At this particular position close to the jet axis and the outflow boundary, pronounced effects of buoyancy are expected for the reacting jet, but none for the inert jet. The applied buoyancy-correction should therefore ideally affect only the former case. In Fig. 6.18 a, the unfiltered (raw) turbulent velocity signal is plotted together with the filtered signal[¶] for the inert jet. The filtered signal assumes an almost constant value, as expected. Consequently, the buoyancy-corrected signal for the non-reacting case in Fig. 6.18 b is almost identical with the unfiltered, raw signal. The raw and filtered velocity signals for the reacting jet are plotted in Fig. 6.18 c. The oscillating nature of the turbulent flow can already be clearly seen from the unfiltered signal. It is also evident, that the filtered signal captures the buoyancy contribution reasonably well. The corresponding buoyancy-corrected signal for the reacting case is plotted in Fig. 6.18 d, where the buoyancy-induced oscillation appears to be effectively removed. All remaining fluctuations can be attributed to turbulent eddies, so that the smaller RMS values obtained from the buoyancy-corrected signal represent the real turbulent fluctuations.

The global effect of the buoyancy-correction is exemplarily shown for the streamwise tur-

---

[§] Wavelet filters were alternatively tested, which, in contrast to the Fourier methods, have a local support and a different basis. The different basis proved to be useful to some extent. Nevertheless, the local support showed tendencies to filter also turbulent eddies from the signal. The use of wavelet filters was therefore discarded for the present case.

[¶] The content in Fourier space with $f < 1.\dot{3}/t_{\mathrm{bf}}$.

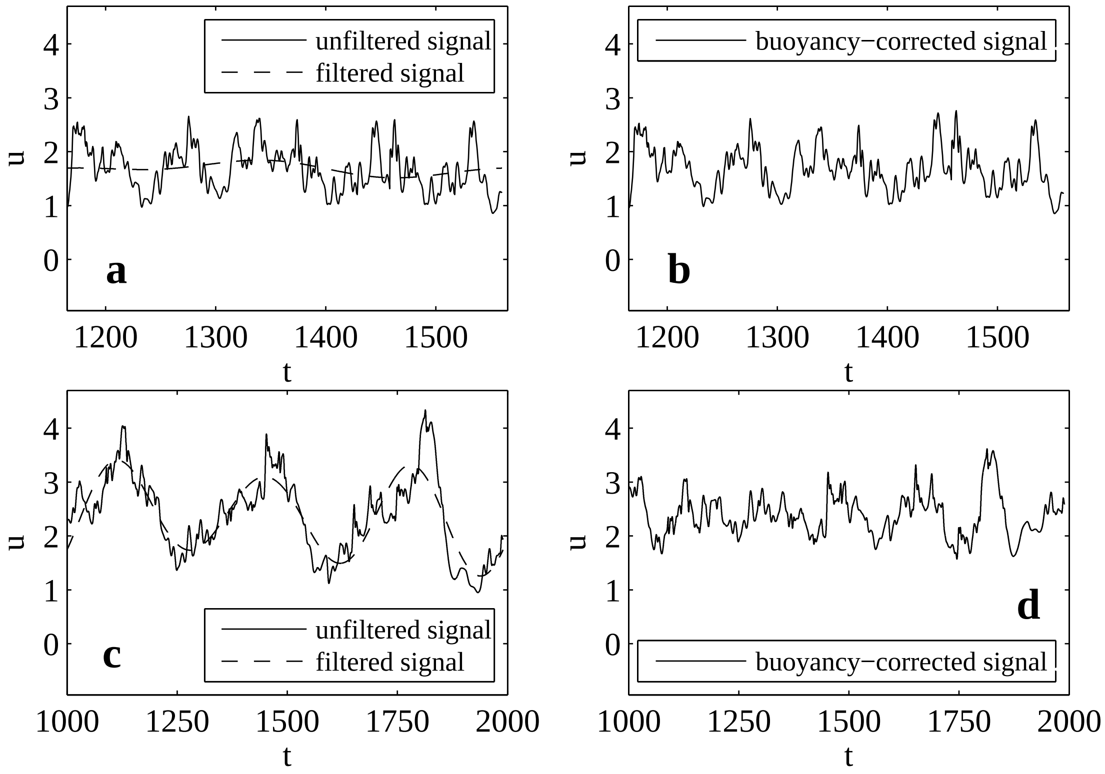

Figure 6.18: Long term evolution of the instantaneous streamwise velocity at $x/D = 35.2$, $y/D = 0.8$. **a** Inert jet; unfiltered and low-pass frequency-filtered signal, **b** inert jet; buoyancy-corrected signal, **c** reacting jet; unfiltered and low-pass frequency-filtered signal, **d** reacting jet; buoyancy-corrected signal.

bulence intensity $\left(\overline{u'^2}\right)^{1/2}/\overline{u}_c$ in Fig. 6.19. For comparison reasons the results for the inert jet are plotted as well. The left half-plane of each jet-domain corresponds to the unfiltered field, while the right half-plane corresponds to the buoyancy-corrected field. It can be clearly seen for the inert jet, that the value of the streamwise turbulence intensity is only marginally changed by the buoyancy-correction throughout the domain. For the reacting jet however, the buoyancy-correction exerts the desired effect in the flame zone, where buoyancy-induced large-scale fluctuations in the raw data are effectively reduced.

The radial profiles for the buoyancy-corrected streamwise turbulence intensities $\left(\overline{u'^2}\right)^{1/2}/\overline{u}_c$ of the reacting jet are plotted in Fig. 6.20 a. The shown profiles refer to the three axial positions $x/D = 10, 20, 30$, which correspond to regions reasonably upstream of the flame base, directly at the flame base, and well inside of the flame zone, respectively. As already seen for the streamwise velocity, the curves do not collapse indicating non-self-similarity. The profiles at $x/D = 10$, are essentially the same as those shown for the inert jet in Fig. 6.7 a. At the flame base, at $x/D = 20$, a somewhat decreased streamwise turbulence intensity is

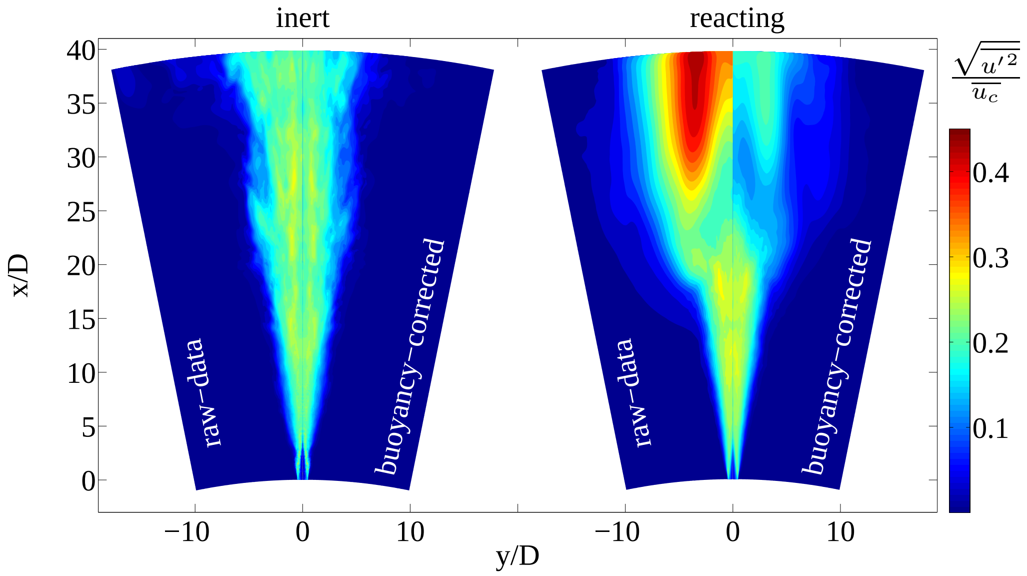

Figure 6.19: Effect of the buoyancy correction on both the inert and the reacting jet, illustrated in terms of the streamwise turbulence level $\left(\overline{u'^2}\right)^{1/2}/\overline{u}_c$. Left: inert jet; right: reacting jet. The left half-planes show raw data; the right half-planes show the buoyancy-corrected fields, respectively.

observed. This appears most pronouncedly at $y/\overline{y_{.05,u}} \approx 1$, where the reactive layer is located. Inside the flame zone at $x/D = 30$, a significantly lower turbulence intensity is seen, pointing at relaminarization effects caused by the strong temperature dependent increase in the kinematic viscosity.

The same tendencies observed for the streamwise turbulence intensity are also found for the normalized turbulent shear stress plotted in Fig. 6.20 b. The profiles do not collapse. At $x/D = 10$, the profile is basically the same as those of the inert case shown in Fig. 6.7 b. In comparison to the streamwise turbulence intensity an even stronger axial decay can be seen for the values of the normalized turbulent shear stress. Again, the lower turbulent shear stress appears most pronouncedly in the zone of the reactive layer ($x/D = 20$, $y/\overline{y_{.05,u}} \approx 1$).

The axial evolution of the buoyancy-corrected streamwise turbulence intensity is plotted in Fig. 6.21. Similar to the inert case, a plateau is observed upstream of the flame, for $7 < x/D < 20$. For $x/D > 20$ the streamwise turbulence intensity assumes considerably lower values caused by the relaminarization effects. For the last ten diameters of the computational domain, a slight increase in turbulence is seen again. This suggests, that the flow approaches the regime of a buoyant plume, which reaches similar turbulence levels like the inert jet (Papanicolaou & List, 1988).

Finally, to evaluate the mixing characteristics of the turbulent reacting jet, the buoyancy-

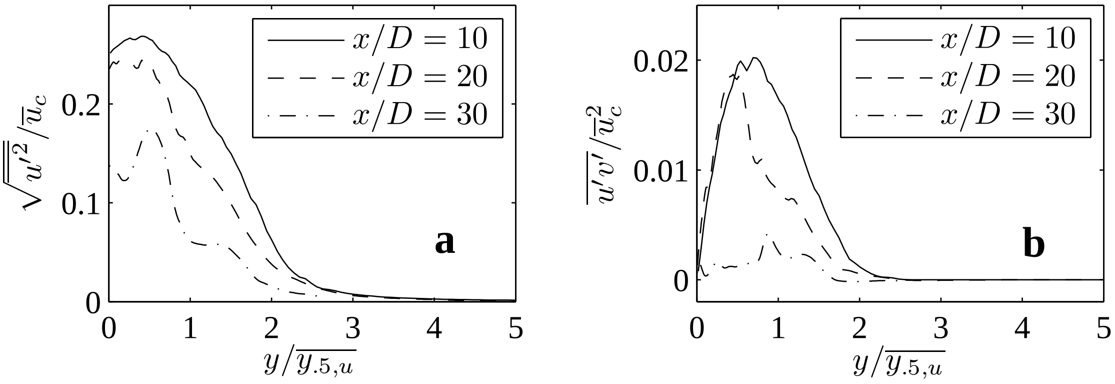

Figure 6.20: Buoyancy-corrected profiles for the turbulence quantities of the reacting jet, plotted at $x/D = 10, 20, 30$: **a** streamwise turbulence level $\left(\overline{u'^2}\right)^{1/2}/\overline{u}_c$, **b** normalized turbulent shear stress $\overline{u'v'}/\overline{u}_c^2$. According to the average reaction rate $\dot{\omega}_I$, the flame base at $x/D = 20$ is located between $0.85 < y/\overline{y_{.05,u}} < 1.2$.

corrected radial variations of the normalized mixture fraction fluctuations $\left(\overline{Z'^2}\right)^{1/2}/\overline{Z}_c$ are plotted in Fig. 6.22. The shown curves exhibit the same tendencies as those of the streamwise turbulence intensities (Fig. 6.20 a). The findings made for the turbulent transfer of momentum do evidently apply here also to the turbulent scalar transport.

In the following paragraphs, a comparison with experiments will be carried out for the turbulence quantities. Like for the mean values in Fig. 6.16, data for the density fluctuations are available from the differential interferometry measurements of Köberl *et al.* (2010) and Heimel (2010). In these experimental measurements a series of 800 differential-interferometric snapshots were taken, from which the RMS value was computed. Thereafter, the line-of-sight integral measurements were transferred into an axi-symmetric data representation using tomographic reconstruction techniques.

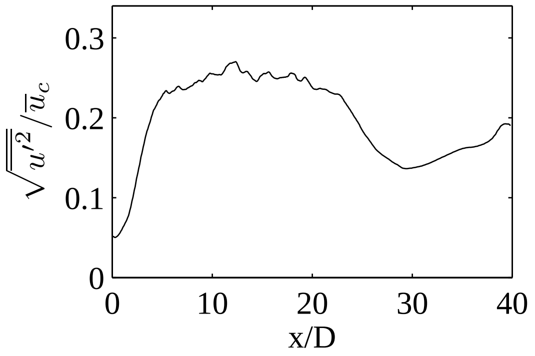

Figure 6.21: Axial evolution of the buoyancy-corrected streamwise turbulence intensity $\left(\overline{u'^2}\right)^{1/2}/\overline{u}_c$; reacting jet.

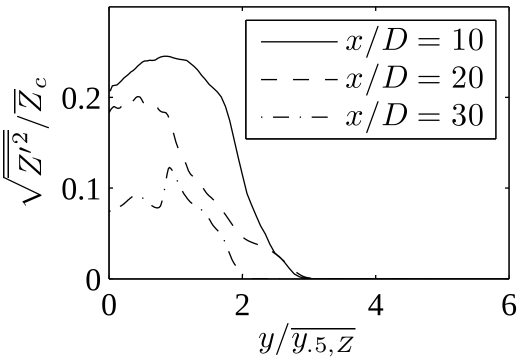

Figure 6.22: Radial profiles of the normalized buoyancy-corrected mixture fraction fluctuations $\left(\overline{Z'^2}\right)^{1/2}/\overline{Z}_c$, plotted at $x/D = 10,20,30$. According to the average reaction rate $\dot{\omega}_I$, the flame base at $x/D = 20$ is located between $0.8 < y/\overline{y_{.05,Z}} < 1.1$; reacting jet.

A comparison of the density fluctuations computed in the present work against the experimental interferometry data obtained by Köberl *et al.* (2010) and Heimel (2010) is shown in Fig. 6.23. Before comparing experimental and simulation data at hand, some more details have to be addressed: Firstly, in contrast to the computational results shown afore, the presently compared data are *not* in a buoyancy-corrected form, as the measured data are not filtered for any buoyant fluctuations. Secondly, for calibration reason the differential interferometry is not fully capable of capturing the high-frequency parts of the signal. As a consequence, to allow for a meaningful comparison, the RMS value computed from the computational results contains only fluctuations with a period larger than $\Delta t > 141$[‖]. Thirdly, it has been already mentioned that the presently used differential-interferometry data are produced by line-of-sight integral measurements. It can be therefore assumed, that the absolute level of fluctuations typically obtained from such integral measurements is somewhat underestimated.

The radial profiles of the density fluctuations illustrated in Fig. 6.23 exhibit considerable differences for the levels of the fluctuations. Near the base of the lifted flame at $x/D = 20$ (Fig. 6.23 d) the disagreement is less pronounced, but at the further downstream positions $x/D = 25,30$ (Fig. 6.23 b, c) the computed density fluctuations are more than a factor of two higher than the experimentally measured fluctuations. Explanations for the observed deviations may be sought again in both measurements and simulation. As already noted above, the density-fluctuations in the experiments might be somewhat underestimated due to the line-of-sight integral measurements, where fluctuations can cancel each other to some extent along the line of integration. On the other hand, the DNS results for the mean

---

[‖] A density power spectrum was computed from the computational data. The RMS values depicted in Fig. 6.23 were obtained by integration of the power spectrum up to a frequency of $f = 1/141$, which corresponds to a frequency of 20 Hz.

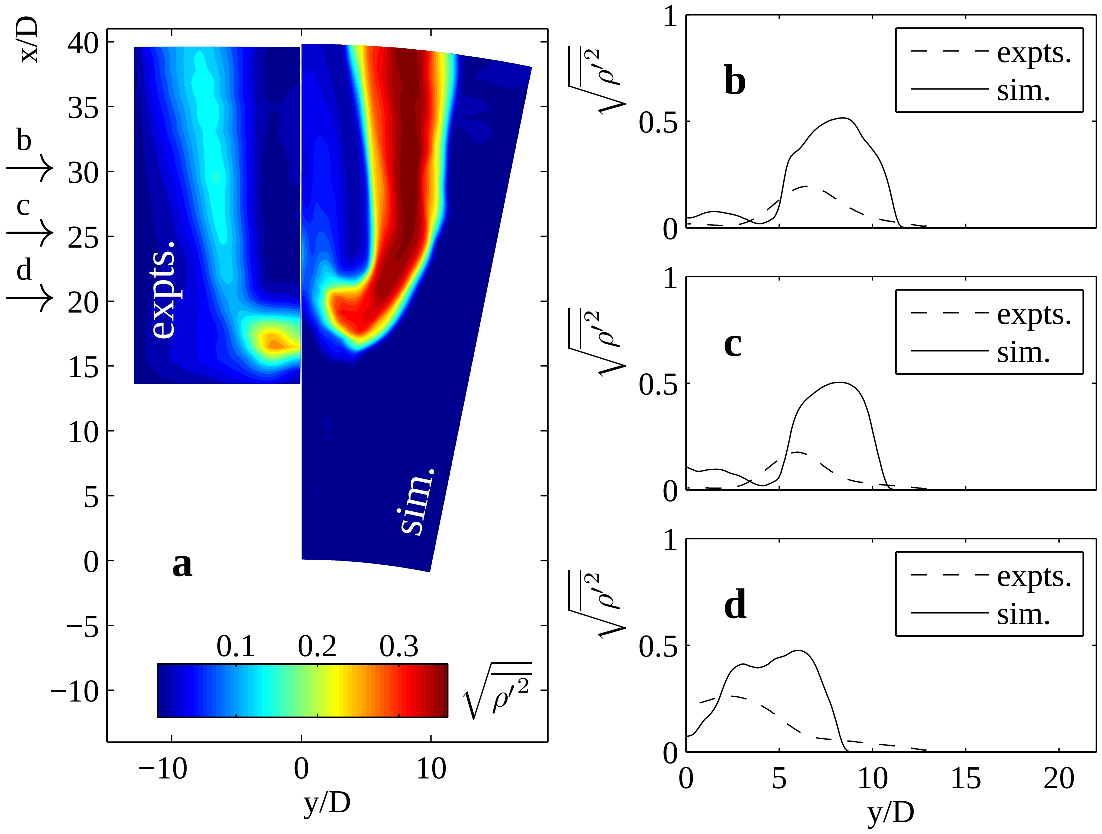

Figure 6.23: Comparison of the density fluctuations computed in the present work against the experimental interferometry data obtained by Köberl *et al.* (2010) and Heimel (2010). For the computed fluctuations, only fluctuations with a period $\Delta t < 875$ are considered ($\widehat{=}$20 Hz, see text). **a** Contours for the experimental (left) and computational data (right). **b**, **c** and **d** illustrate selected radial density profiles at $x/D = 20, 25, 30$, respectively.

density shown in Fig. 6.16 did already exhibit in general a larger bandwidth between minimum and maximum values in comparison to the experiments. This discrepancy, which was essentially attributed to effects of the DTF model, may also explain the overpredictions of the density fluctuations. It has to be noted, that the RMS value represents basically the second moment of the underlying probability distribution. As seen from the density probability distribution in Fig. 6.24, strong intermittency is found in the DNS results, pointing at an alternating existence of either completely cold, high density fluid, or hot fluid with very low densities. As seen from the almost double-delta shape of the probability distribution in Fig. 6.24, the maximum RMS values obtained for the DNS data will expectedly lie in the range of half the span between the hot and cold densities. In contrast to the

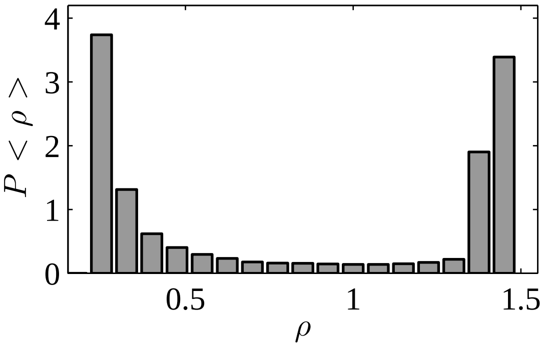

Figure 6.24: Probability distribution of the density ρ at $x/D = 25$, $y/D = 8.5$.

computational results, the comparatively low relative RMS values observed in the experiments indicate considerably less intermittency suggesting rather a single-peak shape of the probability distribution. It remains questionable, if this very low intermittency observed in the experimental data is realistic, or, if the intermittency cannot be fully resolved by the interferometric measurements. The occurrence of a considerable level of intermittency is, however, qualitatively indicated by the schlieren visualizations, which will be presented at the end of the next section.

Despite the large differences in the density fluctuation levels good agreement is found for the shape of the contours associated with increased density fluctuations, as seen from Fig. 6.23 a. In consistence with the wider mean density profiles illustrated in Fig. 6.16, the maximum fluctuation values of the DNS are found at a somewhat further radial distance from the jet-axis.

Transient effects of buoyancy

The high relevance of the buoyancy effects for the present flame has already been demonstrated several times in the preceding analysis of the mean values and the turbulence quantities. Thereby, the strong transient effect of buoyancy became evident in the large oscillations of the flow quantities occurring over comparatively long time periods, see, e.g., Fig. 6.17. Due to the great importance of this transient effect for the evolution of the entire flow field, including the dynamical effect on the flame stabilization, this issue deserves a more detailed discussion.

The time dependent distribution of buoyancy forces in the flow field can be demonstrated most conveniently by displaying a time-series of instantaneous iso-surfaces of density at $\rho = 1.3$. Fig. 6.25 a illustrates the temporal evolution of one buoyancy-induced total oscillation recorded with six successive snapshots. The shown iso-surfaces of density are associated with a relatively high density $\rho = 1.3^*$, which basically sets the outer limits of the region with lower density, i.e. with relevant buoyancy forces. To give some insights into the underlying velocity field, the contours are coloured by the value of the local streamwise velocity u. Additionally, a dark-grey shaded contour is introduced showing the reactive layer associated with $\dot{\omega}_I = 0.004$. This layer also indicates the zone of the lowest density. For explanation purposes of the observed phenomena, the temporal evolution of the integral values for the total mass, momentum, and reaction shown in Fig. 6.17 is replotted for the timespan under consideration in Fig. 6.25 b.

At all instances of time shown in Fig. 6.25 a strongly corrugated density contours are visible in the inert near field of the jet indicating the small isothermal drop in density in the turbulent mixing layer between the methane-nitrogen jet and the somewhat heavier ambient air. Large bulb-like structures can be seen in the reacting far-field of the jet, which are comparatively slowly convected into the streamwise direction. The generation of such a low-density bulb is initiated, once the preceding bulb has separated from the base of the flame. At the beginning of the shown period ($t = 1440$) a comparatively narrow low-density region protrudes from the bottom of the big bulb structure which has already been generated in the preceding period. It contains the base of the reactive layer at its lower end, which propagates relative to the incoming flow. At this moment of separation, the integral momentum $\int\limits_{\mathcal{V}} \rho u \, dV$ exhibits a relatively large value, which indicates the presence of a large amount of high-density ambient fluid which was entrained at the end of the preceding period.

At the second snapshot $t = 1510$, the bulb which was generated in the preceding period has almost left the computational domain. A high level of the integral momentum can still be seen at this moment. This high momentum is caused by the fluid located close to the outflow boundary, which is advected downstream with the outgoing bulb structure. Directly at the flame base, negative streamwise velocities u are indicated by the black coloured density contour. The reverse motion can be attributed to the effect of dilatation, which pushes hot fluid upstream, and also leads to a generally low streamwise velocity in the vicinity of the flame base.

From $t = 1510$ to $t = 1650$ (second to fourth snapshot), a new low-density bulb is generated. It grows continuously, fed by the heat release of the reaction of the incoming partially-premixed flow, and successive dilatation. During this phase, the density contour at the flame base moves also notably upstream. Considering the integral quantities in Fig. 6.25 b, this phase is associated with high reaction rates, and a strong decrease in the total mass, while the level of the total streamwise momentum remains comparatively low. The latter is explained by the fact, that the fluid entrained by the preceding bulb has just left the domain, and the buoyancy forces which are building up anew have not yet been translated into advective motion.

---

[*] The density of the ambient air is $\rho = 1.41$, refer to Tab. 6.1.

The build-up of buoyancy forces is accompanied by an interesting observation: Large zones of reversed flow can be seen at the radially outer rims of the bulb surface at $t = 1580, 1650, 1720$ (black). Buoyancy forces are by definition the strongest for the lowest densities, i.e., in the reactive layer. As a consequence the fluid near the reactive layer, which is basically located closely around the central core of the flow field, becomes accelerated most effectively by the buoyancy forces. For reasons of continuity, the stronger streamwise advection in the core of the flow is compensated by a reverse motion in the laterally outer region, as observed in the contours. With increasing time, also the low density zones in the lateral regions experience buoyant acceleration, so that the flow reversal becomes less pronounced (seen from the grayish-white contours at the last two snapshots $t = 1720$ and 1790).

After $t = 1650$, the total streamwise momentum has been notably increased again. As it is clearly seen from the density contours, the bulb has already lifted a bit at $t = 1720$. At this instance of time, the beginning of the separation of the bulb from the annular shaped region near the flame base is already visible. Due to the strong streamwise momentum, the flame base is receding downstream, which is also indicated by the blue coloured density contours at the base. Finally, as seen from the contours at $t = 1790$, the bulb separates, and a new oscillation cycle starts

Interesting features of the reactive processes are unveiled by a closer look at the contours of the reactive layer. For the snapshots which correspond to the strongest decrease in density, $t = 1580$, and 1650 (bulb build-up), a bulky laterally widened surface of the flame can be seen. The total volume occupied by the flame is evidently very large during this phase, as it is also indicated by the high values of the volumetric integral reaction rates shown in Fig. 6.25 b for that time. On the other hand, at the stage of bulb separation and lift-off, i.e. at $t = 1790$, the shape of the reactive layer appears as a rather slender cylinder. The comparatively small flame surface in this phase is reflected by the comparatively small value of the integral reaction rate in Fig. 6.25 b.

The illustrations in Fig. 6.25 miss out two important aspects: Firstly, no information is given on the ambient flow, which will be undoubtedly affected by the large bulb-like structures observed in the density contours. Secondly, it did not become evident how the buoyancy-induced instability develops, which leads to a periodic formation and separation of bulb-like structures from the flame base. Both aspects shall be highlighted based on the temporal evolution of (three-dimensional) streamlines shown in Fig. 6.26. In reference to the density fields discussed above, the surface of the buoyancy-relevant low-density bulb is also indicated as a temperature iso-surface $T = 1.1$[†]. Due to the effect of volumetric dilatation, the streamlines which penetrate into the low-density bulb are likely

---

[†] For the flame zone, the $T = 1.1$ iso-surface corresponds well to the one for $\rho = 1.3$, which was plotted in Fig. 6.25. The iso-surface of temperature is used here for a better visibility of the streamlines in the isothermal near field of the jet, where no iso-surface appears.

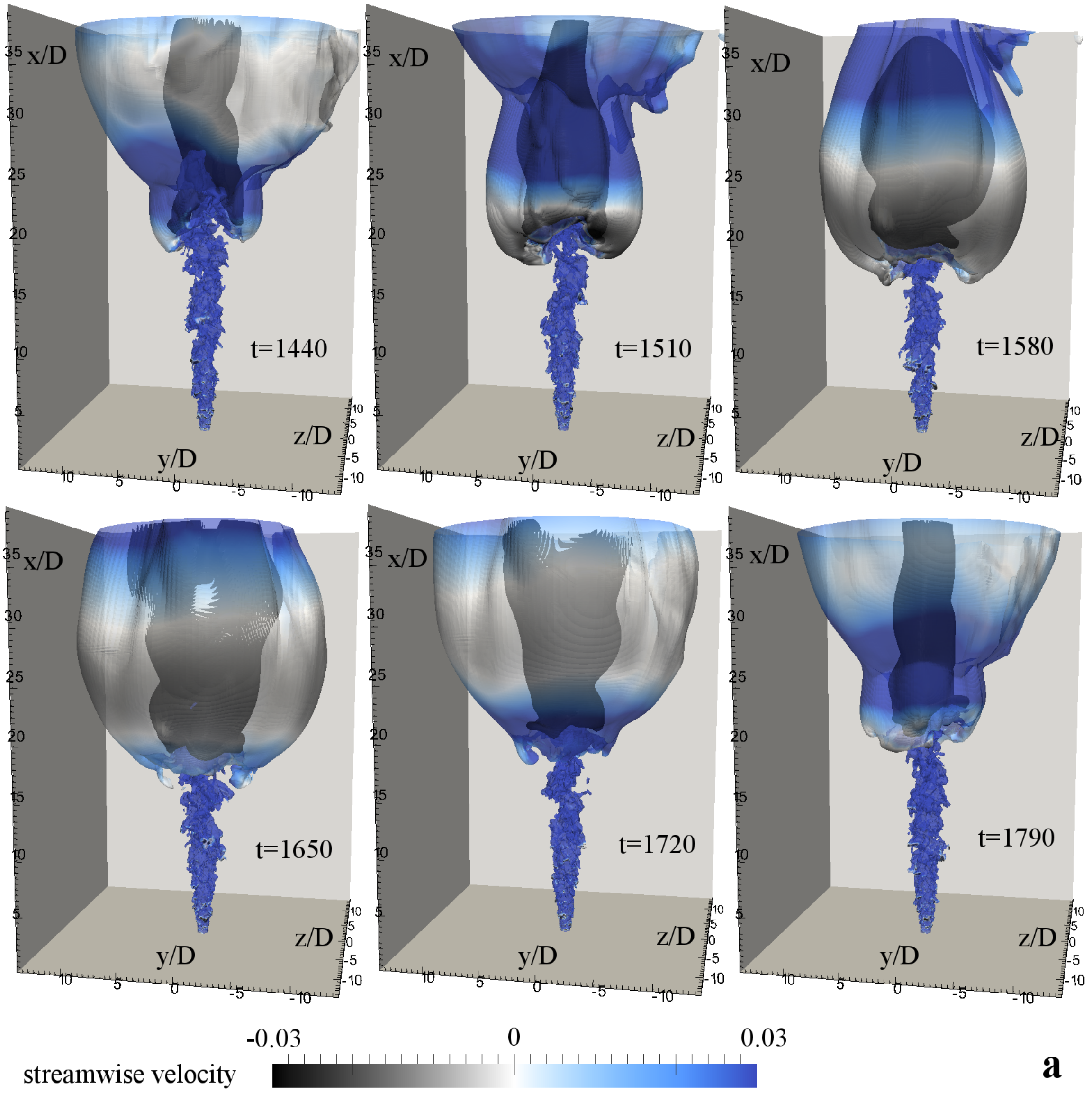

Figure 6.25: **a** Instantaneous iso-surfaces of density at $\rho = 1.3$, illustrating exemplarily the period of one full buoyancy-induced oscillation $1440 < t < 1790$. The iso-surfaces are coloured by the instantaneous streamwise velocity u. The inner dark-grey iso-surface refers to the instantaneous reactive layer, where $\dot{\omega}_I = 0.004$. **b** Temporal evolution of the total mass, momentum, and reaction rates replotted analogously to Fig. 6.17 for the timespan under consideration. The six dashed lines denote the instances of time at which the density iso-surfaces are shown in **a**.

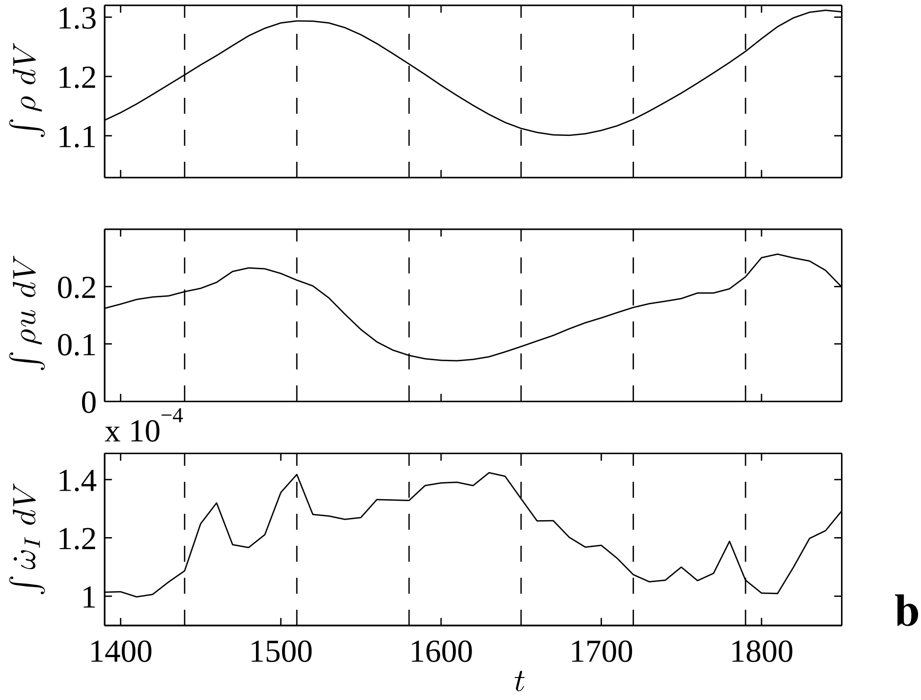

Fig. 6.25. (continued): caption: see facing page.

to come out again further downstream. For clarity, only ingoing branches of the streamlines are shown, so that the regions void of streamlines indicate reverse or radially outwards directed motion, or stagnant zones.

When the bulb separates from the base and lifts off, at $t = 1440$, ambient fluid is entrained across the entire lateral boundary, as it is indicated by the nearly uniform distribution of streamlines entering the domain at the lateral boundary. As the low-density bulb grows in size at $t = 1510$, a strong displacement of fluid becomes visible by the occurrence of large regions void of streamlines. Across large parts of the lateral boundary, fluid is evidently rather pushed out of the computational domain, than entrained. The absence of streamlines in the jet near field upstream of the flame, also points at notable upstream effects caused by the flame during this phase. In the region close to the outflow boundary, an increased entrainment caused by the outgoing bulb is indicated by the dense streamlines[‡], which are notably inclined into the streamwise direction. The behaviour observed at $t = 1510$ is basically seen as well at $t = 1580$, except that the outgoing bulb has already left the domain.

The effect of the buoyancy-driven increase of the streamwise momentum, which induces the lift of the bulb and reinforces the entrainment of ambient fluid can be seen at $t = 1650$. The inert near field as well as the region around the flame base are occupied by streamlines again indicating unimpeded entrainment. Later on at $t = 1720$, unimpeded entrainment is found along the whole lateral boundary.

The underlying mechanism for the buoyancy-induced periodic instability is evidently constituted by the periodic formation of a big low-density bulb-like region due to the reactive heat release, and the successive onset of strong buoyant forces leading to a significant streamwise acceleration, which in term enhances the entrainment triggering the separation and lift-off of the bulb from the flame base. The entrained fluid has to be heated again by the flame so that a new low-density bulb can be generated to start the next cycle. The buoyancy-driven entrainment is seen most pronouncedly in the region, where the bulb separates from the flame, as seen in Fig. 6.26 from the very dense streamlines in this zone at $t = 1440$, or $t = 1790$.

At the later three stages, where the flame is notably receding, divergent streamlines are seen upstream of the flame base, indicating stagnation-like regions. Basically, the flame burns most stably in stagnant mixtures close to stoichiometry. The formation of such comparatively large stagnation zones, as particularly seen at $t = 1790$, essentially helps to stabilize the flame also during the most critical stage, where the underlying flow field is strongly accelerated by the buoyancy.

The transient effects of buoyancy manifested in the evolution of the low-density bulb-like region can be also seen in the experimental results. Bulb-like structures were already observed in seeding visualizations of a methane flame with a similar parameter setting (Muñiz

---

[‡] For reasons of continuity, the accumulation of streamlines corresponds to an acceleration of the flow.

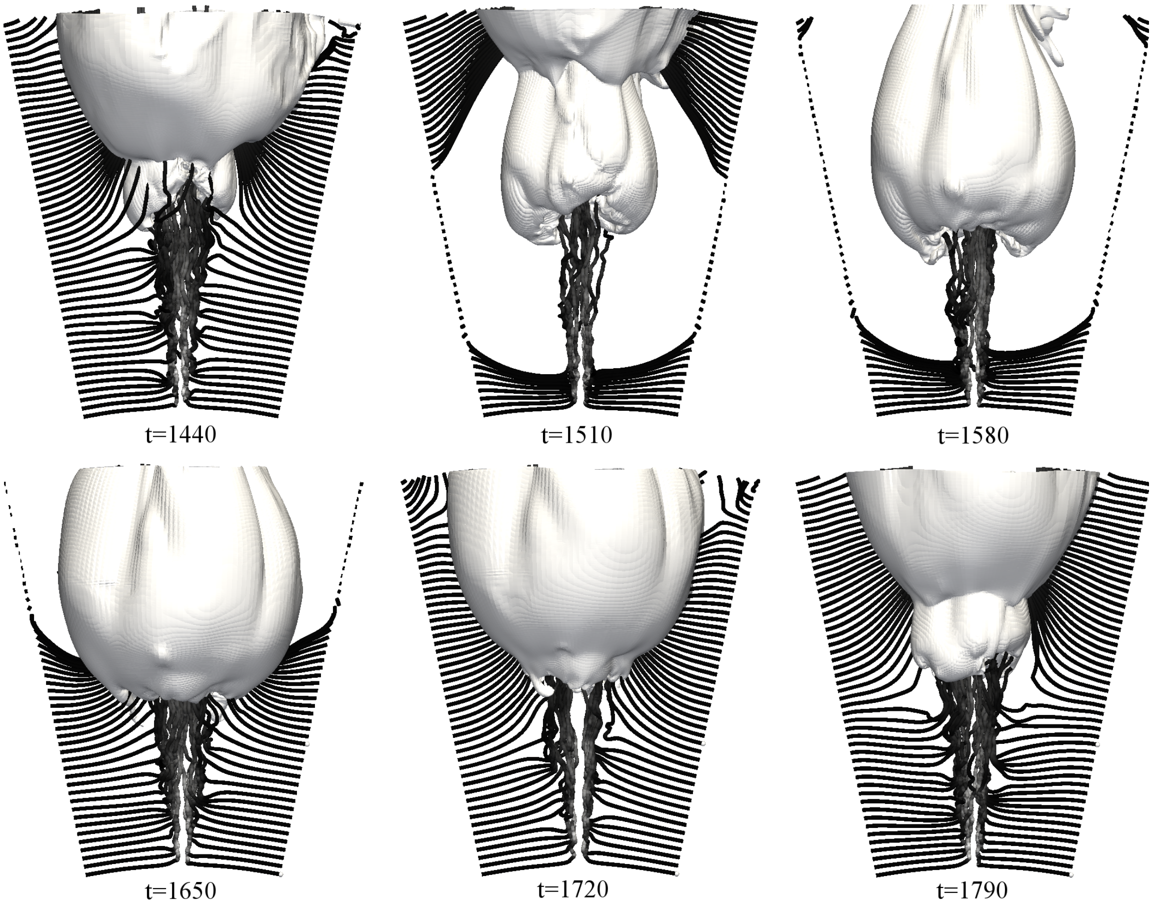

Figure 6.26: Three-dimensional view of the instantaneous temperature iso-surfaces at $T = 1.1$, and three-dimensional streamlines originating from the lateral boundary, illustrated exemplarily for the period of one full oscillation $1440 < t < 1790$.

& Mungal, 1997)[§]. However, these buoyancy-driven large-scale effects were not explicitly addressed in this study. Schlieren visualizations are provided in the measurements by Köberl *et al.* 2010 and Heimel 2010. Fig. 6.27 depicts a time series of six schlieren images, which cover one buoyancy-driven oscillation pulsation. For these visualizations, a spot-like schlieren target was used, so that density gradients perpendicular to the line of sight appear as bright regions. If density gradients exceed a certain upper limit, the refracted light cannot enter the lens of the camera anymore, so that the corresponding higher gradients are indicated by the black regions. Although the shapes of the experimental bulbs appear somewhat more corrugated, a generally good agreement with the DNS results is found for the shapes of the bulbs (refer to Figs. 6.25 and 6.26). Using high-speed camera schlieren visualizations the frequency of the oscillations could be determined as

---

[§] Even though the flame was confined, and co-flow was used.

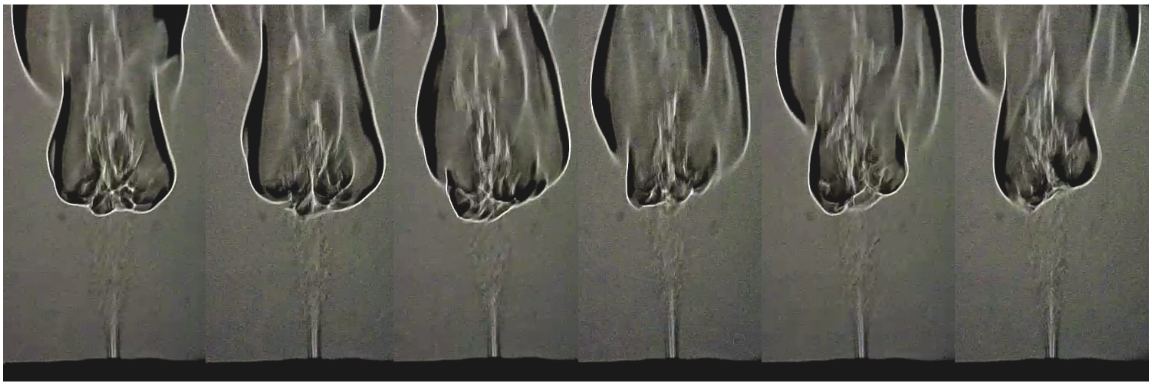

Figure 6.27: Temporal evolution of one low-density bulb from experimental schlieren visualizations (Köberl *et al.* 2010, Heimel 2010).

well. The experimentally observed frequency $f \approx 11.6$ Hz[¶] is somewhat higher than the computationally obtained frequency of $f = 8.5$ Hz.

In the following experimentally obtained schlieren visualizations are compared against schlieren visualizations which are post-processed from the DNS data using the scientific visualization software ParaView (www.paraview.org). As seen from Fig. 6.28, good agreement is found between experiment and simulation. In both half-planes, the buoyancy-induced separation of one low density bulb can be seen. The dark zones at the lateral boundaries of the bulbs indicate strong density gradients into the cross-stream direction, indicating a considerably sharp interface between cold and hot fluid. The strongly intermittent behaviour associated with the deformations of the sharp density-interface, which are due to the motion of the low-density bulb-like structures, confirms the comparatively higher values for $\left(\overline{\rho'^2}\right)^{1/2}$ observed in the DNS results in Fig. 6.24.

Aside of the occurrence of low-density bulbs, also other features of the flame observed in the schlieren images are in good agreement. Both experimental and computational visualization exhibit a cold core of unburnt fluid which penetrates deeply into the flame. Also the density variation in the inert, non-reacting near field of the jet is reproduced fairly well. The vortical structures near the nozzle appear somewhat more accentuated in the computational results though. The rather diffused structures observed here in the experiments are due to the finite exposure time of the camera smearing high-frequency contributions.

[¶] For comparison reason, dimensional quantities are used here.

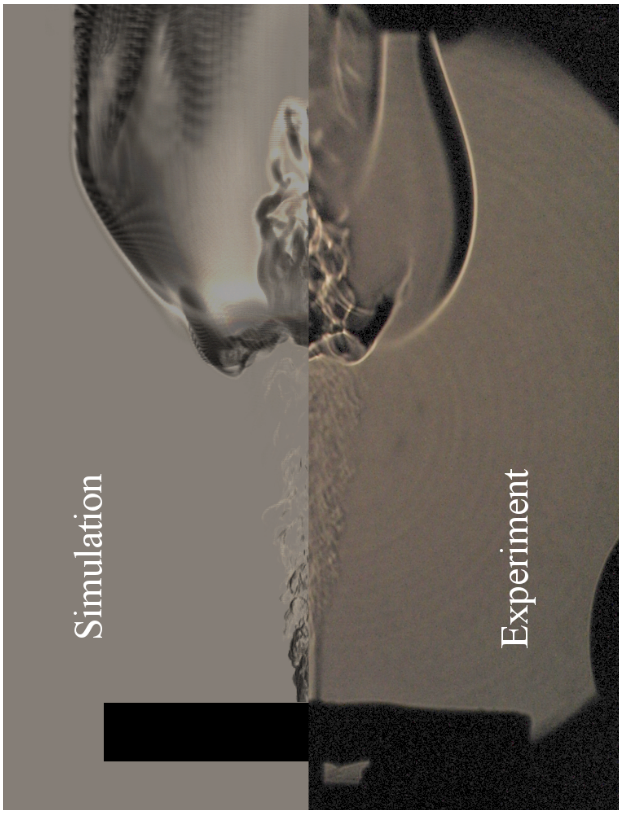

Figure 6.28: Comparison of computational and experimental (Köberl *et al.* 2010, Heimel 2010) schlieren visualizations.

Upstream effects

Eventual upstream effects which are caused by the presence of a flame are frequently not commented, or, sometimes even ruled out in literature. In contrast, small upstream effects could already be observed in the spreading and the axial decay behaviour of the non-reacting near field of the jet shown in Fig. 6.13. Even more pronounced upstream effects were identified in the preceding discussion of the streamlines in Fig. 6.26, especially in the outer lateral regions. Therefore, upstream effects shall be addressed here in some more detail.

At the beginning of the analysis, a precise definition of the region termed "upstream of the flame base" has to be given. In the present case, this zone is defined as the region extending in the streamwise direction from the nozzle to the nearest axial position, where the sum of the temperature mean and fluctuation exceeds the threshold $\overline{T} + \left(\overline{T'^2}\right)^{1/2} = 1.2$. For the case of a double-Dirac-delta shaped probability distribution of the temperature, this definition would denote the zone, where the instantaneous temperature never exceeds $T = 1.2$. For the case of a Gaussian distribution, this would still apply to 84% of the considered sample. As seen from the contours of $\overline{T} + \left(\overline{T'^2}\right)^{1/2}$ plotted in Fig. 6.29, the present definition implies a region "upstream of the flame base" which extends in the streamwise direction between $0 \leqslant x/D \leqslant 15.5$.

The evolutions of the instantaneous streamwise velocity component u at $x/D = 15.5$ are exemplarily shown for two lateral positions $y/D = 4.2$, and $y/D = 0.2$, in Fig. 6.30 a and b, respectively. At the lateral position $y/D = 4.2$, which is located upstream of the lowest mean position of the reactive layer[‖], relatively pronounced buoyancy-induced fluctuations with the typical period of Δt_{bf} can be seen. At this position, the relative contribution of the buoyancy-induced fluctuations can be quantified by the ratio of the buoyancy-corrected to the unfiltered fluctuation, which yields a value of

$$\frac{\left.\sqrt{\overline{u'^2}}\right|_{\text{corrected}}}{\left.\sqrt{\overline{u'^2}}\right|_{\text{unfiltered}}} = 0.47\ . \tag{6.10}$$

This indicates, that more than half of the fluctuating motion at this lateral position is caused by the transient buoyancy effects. The amplitude of these fluctuations, reaching only one percent of the bulk jet exit velocity U_{orif}, is certainly very small.

Notably larger fluctuation amplitudes are observed for the position very close to the jet-axis at $y/D = 0.2$ shown in Fig. 6.30 b. At first sight, buoyant fluctuations can hardly be recognized from the unfiltered signal. However, looking at the dashed line, buoyancy-induced fluctuations appear. They are in phase with the buoyancy-induced fluctuations observed at the other, radially outer, position in Fig. 6.30 a. While their amplitudes are

---

[‖] ... in a geometrical sense, i.e. approximately at the same coordinate y/D. The expected position of the reactive layer corresponds to the darkest region in Fig. 6.29, compare also Fig. 6.12.

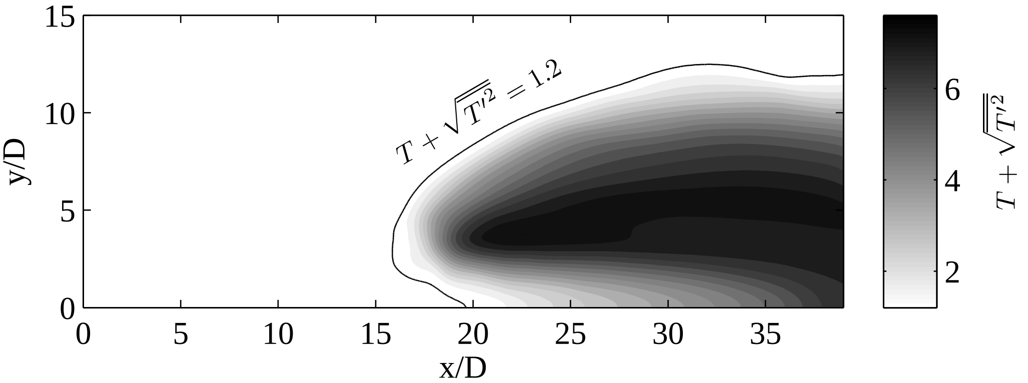

Figure 6.29: Boundary of the flow domain which is directly influenced by thermal effects, illustrated in terms of the sum of temperature mean and fluctuation.

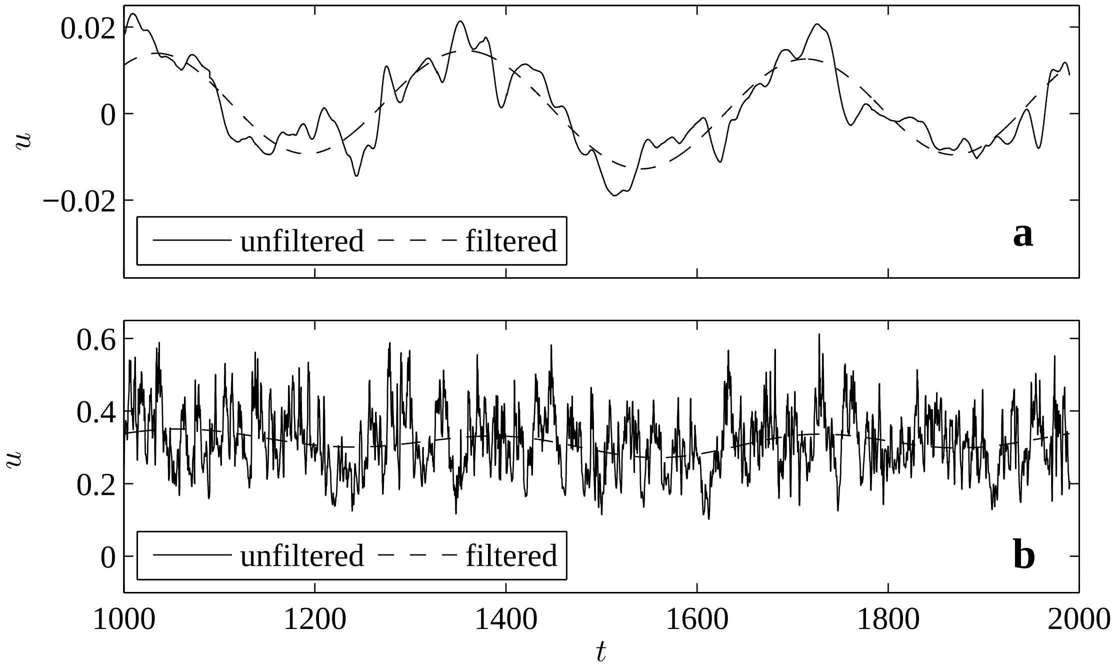

Figure 6.30: Temporal evolution of the streamwise velocity u upstream of the flame base at $x/D = 15.5$, **a** at a lateral position $y/D = 4.2$, **b** at a position close to the centerline $y/D = 0.2$. The dashed lines denotes the buoyancy-induced contribution.

roughly of the same magnitude, the relative contribution to the total fluctuations appears to be negligibly small at $y/D = 0.2$. This also becomes evident in the ratio of buoyancy-corrected and unfiltered fluctuations according to Eq. (6.10), which yields a value of 0.97. This implies that the buoyancy-induced contribution at this position is only three percent, which indicates that the fluctuations in the core flow are mainly due to turbulence.

Summing up, the observed effects on the region upstream of the flame lead to the following conclusions: Pronounced upstream effects of the flame are visible in the radially outer region, as seen from the velocity fluctuations at a selected point (Fig. 6.30 a) as well as the global view of the streamlines in Fig. 6.26. The absolute magnitude of these essentially buoyancy-induced oscillations is however small in comparison to the turbulent fluctuations in the core of the jet. The presence of the flame still leads to a somewhat faster decay and spreading of the jet, as seen from Fig. 6.13.

6.3.4 Flame stabilization

The mechanisms of flame stabilization have already been investigated in various previous experimental and numerical studies as reviewed in Sec. 1.3. The main parameters of

Study	Fuel	D_{orif}	Re	U_{orif}	U_{cofl}
present DNS	CH_4 / N_2	4.0	2750	11.3	0.0
Muñiz & Mungal (1997)	CH_4	4.8	3900 - 10500	14 - 38	0.27 - 0.58
Watson *et al.* (1999)	CH_4	5.0	6600	21.8	0.1
Mansour (2003)	CH_4	8.0	2446 - 5036	4.74 - 11.3	0.2
Upatnieks *et al.* (2004)	CH_4 / N_2	5.0	4300 - 8500	14.0 - 33.2	0.26 - 0.47
Su *et al.* (2006)	CH_4	4.6	4400 - 10700	10.8 - 26.4	0.36

Table 6.3: Parameter setting of experimentally measured laboratory jet flames.

selected experimental studies presented in literature on the stabilization of turbulent laboratory jet flames, which are fairly close to the conditions of the presently computed jet flame, are listed in Tab 6.3. As such, these studies represent well comparable reference cases for the present simulation results.

Especially for the low Reynolds number cases, which are typically associated with low Froude numbers, the buoyancy plays an important role. Buoyancy mostly affects the large-scale structures of the reacting flow field, as it was shown by the large-scale oscillations in Sec. 6.3.3. Similar buoyancy-induced oscillations were observed by Won *et al.* (2002). However, they considered a laminar jet flame at a very low Reynolds and Froude number, so that the impact of buoyancy on the stabilization of their flame is hardly comparable to the presently considered turbulent case. The low Reynolds number experiments of Won *et al.* (2002) are therefore not considered here as an appropriate reference case.

The salient features of the global flow and mixing conditions in the region upstream of the flame, the methods for the localization of the flame base, the statistical analysis of the conditions met there, as well as the role of three-dimensional effects shall be presented in detail in the following.

Flow and mixing fields in the vicinity of the flame

A global view on the average position of the flame is given in Fig. 6.31 showing the contours of the mean reaction rate of the fuel breakup reaction $\overline{\dot{\omega}}_I$. Evidently, the approximately cylindrical layer associated with non-zero reaction rate matches considerably well with the region with minimum density, minimum oxygen concentration, maximum cross-stream velocity, and maximum diffusivity shown in Fig. 6.12. Markedly increased reaction rates are seen at the partially premixed base of the flame, which agrees well with the findings of Ruetsch *et al.* (1995).

To evaluate the main hypotheses on the relevant mixing and flow parameters for flame stabilization (Vanquickenborne & van Tiggelen 1966, Peters & Williams 1983), iso-contours for the mean stoichiometric mixture fraction, flame speed, and scalar dissipation have been

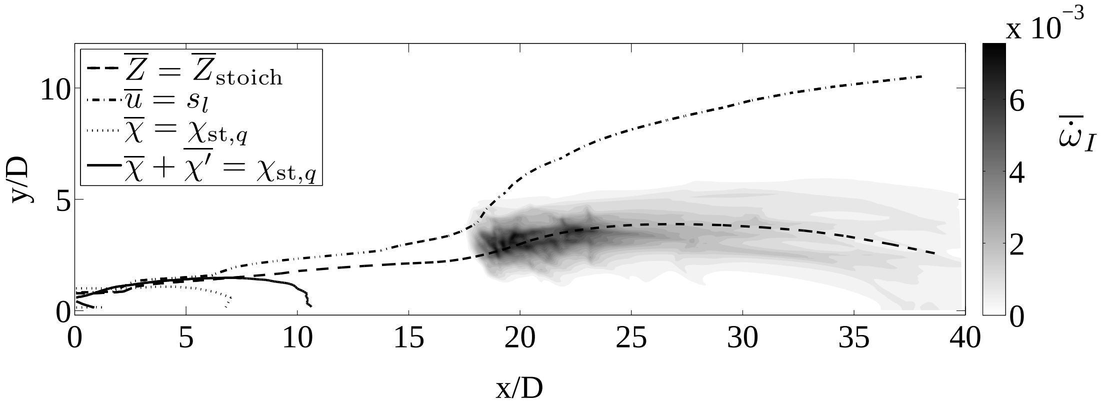

Figure 6.31: Contours of the mean fuel breakup reaction rate $\overline{\dot{\omega}}_I$. Lines denote individual iso-contours of the mean of the mixture fraction, streamwise velocity, and scalar dissipation rate, $\overline{u}$, $\overline{Z}$, and $\overline{\chi}$, respectively.

added to the Fig. 6.31. As commonly stated by all theories, it can be clearly seen that the flame is located at the surface of stoichiometric mixture $\overline{Z} = Z_{\mathrm{st}}$. For the present case of a strongly diluted nitrogen-methane flame, the stoichiometric mixture fraction ($Z_{\mathrm{st}} = 0.104$) is roughly twice as high as that of an undiluted, pure methane feed ($Z_{\mathrm{st}} = 0.055$). This implies that a higher portion of fuel is required for a stoichiometric mixture, so that the iso-contour associated with Z_{st} is located closer to the jet centerline as compared to the undiluted case. As a consequence, the flame base faces a higher local streamwise velocity, which exceeds the laminar flame speed s_L along the whole surface associated with a stoichiometric composition. Accordingly, the contour line for $\overline{Z} = Z_{\mathrm{st}}$ is always closer to the centerline than the contour line for $\overline{u} = s_L$ in Fig. 6.31). The observed excess of the flame propagation speed over the laminar flame speed is consistent with all measurements listed in Tab. 6.3.

The contour, where the mean scalar dissipation rate $\overline{\chi}$ equals the quenching value $\chi_{\mathrm{st},q}$, does not extend far into the flow field. It evidently remains at a considerable distance from the flame base. This supports the conclusion drawn in many previous studies (see, e.g., Mansour 2003), that flame quenching associated with a high scalar dissipation rate is not a determining mechanism for the flame stabilization process. This conclusion still holds, even if the mean fluctuations are increased by including the positive standard deviation. As seen from the solid line associated with $\overline{\chi} + \overline{\chi'} = \chi_{\mathrm{st},q}$ in Fig. 6.31, the extended region, where the fluctuation-augmented scalar dissipation rate exceeds the quenching limit ends fairly distant from the flame. However, neglecting completely the influence of χ only based on first- and second-order statistical moments would be a premature assumption. Fig. 6.32 shows instantaneous contours of the scalar dissipation rate χ. It becomes evident that long slender structures, associated with increased scalar dissipation rates, eventually come very close to the flame base. As a result, the instantaneous local levels of the scalar dissipation rate immediately ahead of the flame base may reach the order of magnitude of the quenching value $\chi_{\mathrm{st},q} = 14.7$. Concerning the influence of the scalar dissipation rate it has further to be noted, that χ_{st} values even well below the critical limit of extinction can significantly influence the flame propagation speed in stratified mixtures (Ruetsch *et al.*, 1995). Therefore, the possible effect of the scalar dissipation will still be considered in the further analysis of the conditions at the flame base.

A validation of the computed average reaction rate $\overline{\dot{\omega}}_I$ (Fig. 6.31) against experiments can be seen from Fig. 6.33. In general, the local values for the instantaneous rates of the elementary reactions cannot be measured directly to date, at least not with satisfactory precision. Therefore, comparisons have to be performed against appropriate quantities which are representative for to the reaction rate. In the studies of Köberl *et al.* (2010) and Heimel (2010), the flame emission was recorded. A filter was used to capture the emission in the blue part of the spectrum only, which corresponds to the luminescence of the CH* (430 nm) and the C_2^* (519 nm) radicals. Since the recorded raw data represent line-of-sight integral measurements, a tomographic reconstruction was applied to recompute the local averages. As the measurements were not calibrated, the experimental values in Fig. 6.33 appear in arbitrary units, whose scaling was adapted to the magnitude of the computed average reaction rate $\overline{\dot{\omega}}_I$. Due to the nonlinear relation between the flame emission and the reaction rate, a comparison between both quantities can only be of qualitative nature. From Fig. 6.33, it can be seen that the contours of the experiments are somewhat smeared. This observation can be attributed partly to imperfections in the tomographic reconstruction. Nevertheless, the average reaction rate obtained from DNS agrees very well with the reconstructed, experimentally recorded flame luminosity. It is also seen, that the lift-off height of the computed flame is in good agreement with the experiment (Fig. 6.33 a).

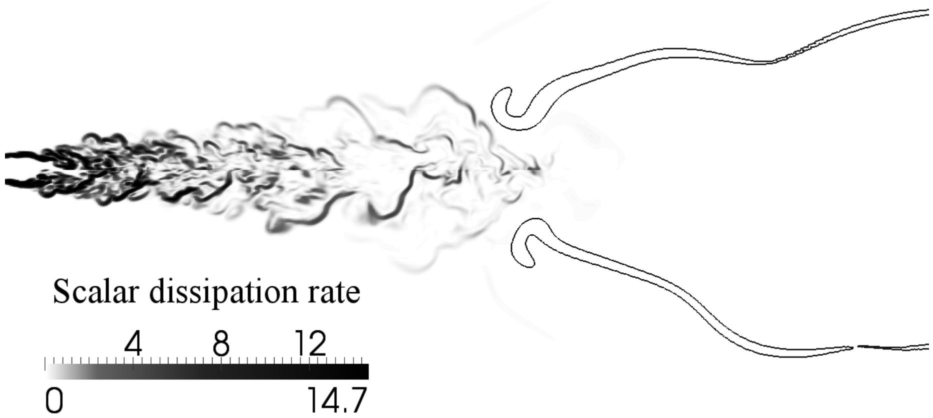

Figure 6.32: Instantaneous contours of the scalar dissipation rate χ at the non-dimensional $t = 1320$. The colorbar is clipped at the value $\chi_{\mathrm{st},q} = 14.7$. A reaction rate contour line at $\overline{\dot{\omega}}_I = 0.004$ denotes the position of the reactive layer.

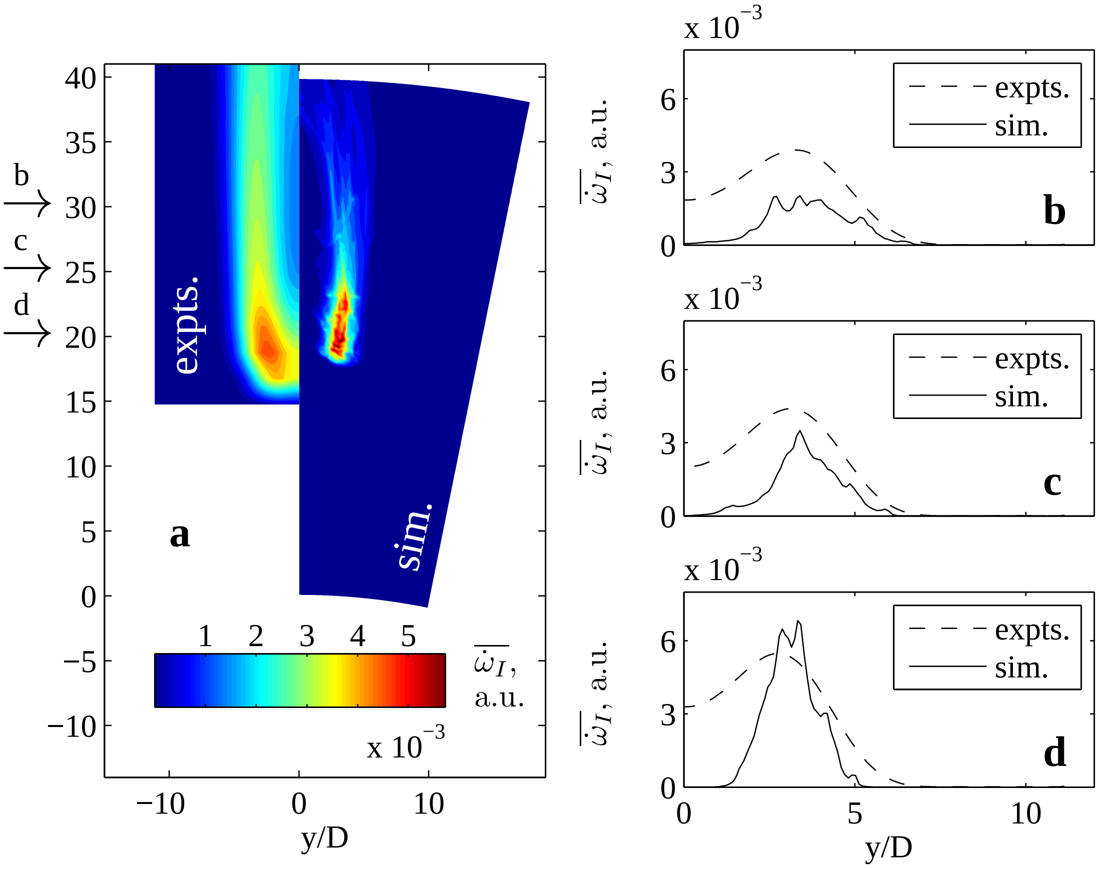

Figure 6.33: Comparison of the reaction rate $\overline{\dot{\omega}}_I$ computed in the present work against the flame emission measured by Köberl *et al.* (2010) and Heimel (2010). Note that the flame emission is measured in arbitrary units. **a** Contours for the experimental (left) and computational data (right). **b**, **c** and **d** illustrate density profiles at selected downstream positions $x/D = 20, 25, 30$, respectively.

The increased reaction rates, which are seen at the base of the flame, are also clearly reflected by the increased flame luminosity which is measured at this position. The shape of the trailing diffusion flame, which exhibits a slender cylindrical structure, is also captured very well by the DNS. The same applies to the predictions for the lateral position of the maximum reaction rates compared against the experimental flame emission data, shown in Fig. 6.33 b, c, d.

Localization of the flame base

In the analysis of the numerical results, where all flow and reaction related quantities are known, the flame base can be identified straightforwardly based on the value of a characteristic elementary reaction rate. The reaction associated with the fuel breakup step serves here as a convenient candidate. In contrast, the local values of elementary reaction rates are generally not available in experimental investigations. Therefore, they have to localize the flame base in an indirect way, mostly based on measurements of the temperature, or the concentrations of radicals generated in the fuel breakup step.

The radical based method provides basically a very accurate tracking of the reaction zone at the flame base, but it requires an additional effort for the Laser Induced Fluorescence (LIF) measurements of the radical concentration (Watson *et al.*, 1999). The calibration of the measured concentrations obtained from the LIF signals is also a non-trivial task. The alternative approach based on the temperature measurements is basically less expensive. Many flame experiments measure the velocity field using PIV (see Tab. 6.3), so that the temperature can be basically retrieved from the presence of the local density of the seeding of particles. Basically, a highest possible temperature contour should be used in this method to come as close as possible to the real position of the reactive layers. However, this cannot be practically realized due to the limited evaporation temperature of the generally used liquid seeding, and the fact that the volumetric dilatation effectively prevents ceramic seeding from entering the reaction zone. Accordingly, Muñiz & Mungal (1997) and Su *et al.* (2006), e.g., locate the flame base, where the glycerol-water seeding evaporates ($T = 100\ [^\circ C]$-contour), while Upatnieks *et al.* (2004) identifies it by the leading edge of the 600 $[K]$ contour, where the ceramic seeding is half as dense as in the reference state at 300 $[K]$. Despite the relatively low temperature used for flame base identification, Su *et al.* (2006) argue, that the leading edge of the temperature contour at $T = 100\ [^\circ C]$ serves well as a proxy for the leading edge of the reaction contour, yielding both equivalent qualitative results.

The simpler temperature based concept faces the problem, that the data are not acquired directly at the reactive layer, but at a certain distance associated with the position of the measured temperature contour. Therefore, the analysis of the data may not reflect the actual flow and mixing conditions in the reactive layer. It rather describes the conditions upstream, i.e. outside, of the reactive layer, where key parameters like the local flow velocity, the mixture fraction, or the scalar dissipation rate may be considerably different. The strong spatial variation of the flow velocity across the flame was already shown in the one-dimensional generic cases in Chp. 4. Due to the different definitions of the flame base used in the experiments listed in Tab. 6.3, the measured data for the flame propagation speed exhibit much scatter, and they are therefore hardly comparable. In addition, particular mixing phenomena, such as the occurrence of non-flammable mixtures (Su *et al.*, 2006), which were experimentally observed at the flame base being identified by a certain temperature contour line, need not be representative for the reactive layer, as it is located further downstream. Moreover, as stated by Upatnieks *et al.* (2004), oncoming eddies may be impeded from penetrating into the reactive layer due to dilatational effects. Thus, the turbulence level detected at the flame base identified at a certain temperature contour may not apply to the reactive layer.

In the present analysis of the DNS data, the flame base is identified by the leading edge of the contour line associated with the reaction rate $\overline{\dot{\omega}}_I = 0.004$. This concept for the localization of the flame base circumvents the aforementioned deficits of the temperature based concepts. It also comes very close to the comparatively accurate experimental approach based on the measurements of CH* radicals (Watson *et al.*, 1999).

The effect of the two different concepts of flame base identification in the analysis of the present simulation results is illustrated in Fig. 6.34. The contours of the reaction rate $\overline{\dot{\omega}}_I$ are plotted in a greyscale colour code together with the $T = 1.1$ iso-contour[**] and streamlines. It can be clearly seen, that the region, where $T > 1.1$ extends further upstream, and is notably broader than the reaction zone. Accordingly, the leading edge of the temperature iso-contour is considerably shifted outwards, so that it intersects with radially outer streamlines associated with the advection of comparatively lean mixtures. This observation can explain the occurrence of non-flammable mixtures at the flame base seen in the

---

[**] T=1.1 corresponds approximately to the 100 [°C] contour utilized by Muñiz & Mungal (1997) and Su *et al.* (2006).

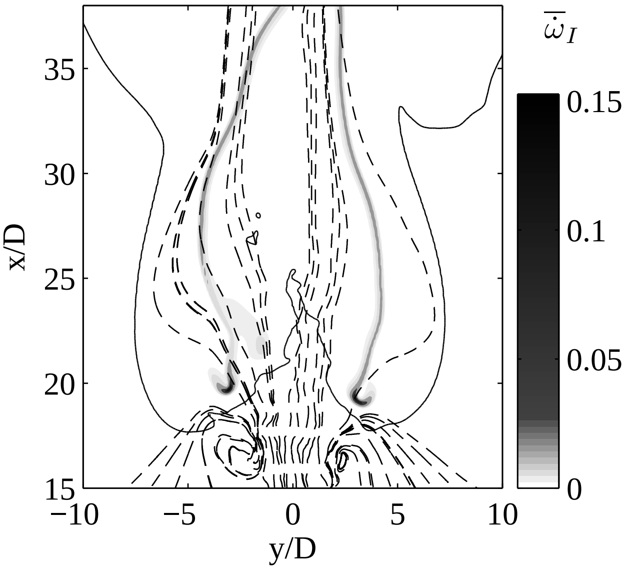

Figure 6.34: Instantaneous contours of the reaction rate $\overline{\dot{\omega}}_I$ plotted in greyscale colour code. The solid line denotes the temperature contour $T = 1.1$. The dashed lines are streamlines.

experiments of Su *et al.* (2006).

The trace of the flame base on a certain meridional plane (fixed azimuthal angle φ) identified with the two different concepts is shown in Fig. 6.35 for the time interval $1000 < t < 1950$. Subfigure a shows the pathline of the position of the leading edge of the temperature contour associated with $T = 1.1$, $(x_{\mathrm{fb,temp}}, y_{\mathrm{fb,temp}})$, while subfigure b shows the pathline of the position of the leading edge of the reaction rate associated with $\overline{\dot{\omega}}_I = 0.004$, $(x_{\mathrm{fb,react}}, y_{\mathrm{fb,react}})$. The mean flame base position obtained with the temperature based concept is evidently shifted by $\Delta x/D = -1.79$ and $\Delta y/D = 0.62$. The observed shift is consistent with the observations of non-flammable mixtures at the flame base by Su *et al.* (2006). On first sight, the streamwise position obtained with the reaction based method $x_{\mathrm{fb,react}}$ seems to fluctuate more amply in Fig. 6.35 b than $x_{\mathrm{fb,temp}}$ in Fig. 6.35 a. Accordingly, the corresponding RMS values are $\left(\overline{x'^{2}_{\mathrm{fb,react}}}\right)^{1/2}/D = 1.54$ and $\left(\overline{x'^{2}_{\mathrm{fb,temp}}}\right)^{1/2}/D = 1.40$. However, it has to be considered that these RMS values are produced by fluctuations acting on very different time scales. As can be seen from Fig. 6.36, a major part of the fluctuations appearing in both signals can be attributed to the buoyancy-induced large-scale oscillations with a period $\Delta t_{\mathrm{bf}} = 350$. Notable differences are seen here only in the small scale structures, as the curve for the leading reaction rate edge $x_{\mathrm{fb,react}}$ is evidently more wrinkled. This higher content of small scale fluctuations indicates a higher sensitivity of $x_{\mathrm{fb,react}}$ to incoming flow disturbances as compared to $x_{\mathrm{fb,temp}}$. This higher sensitivity suggests the reaction based position $(x_{\mathrm{fb,react}}, y_{\mathrm{fb,react}})$ as a reliable variable for conditioning the flow and mixing state at the flame base in the statistical analysis.

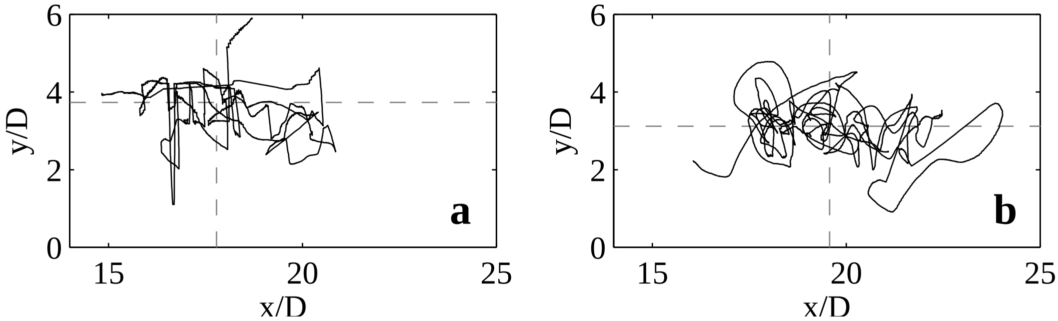

Figure 6.35: Trace of the leading flame edge at a fixed azimuthal angle φ, for the timespan $1000 < t < 1950$. **a** The leading edge $x_{\mathrm{fb,temp}}$ defined by the temperature iso-contour $T = 1.1$, and **b** the edge $x_{\mathrm{fb,react}}$ defined by the reaction rate iso-contour $\overline{\dot{\omega}}_I = 0.004$. Dashed lines denote the mean $(x_{\mathrm{fb}}, y_{\mathrm{fb}})$-positions of the leading edge.

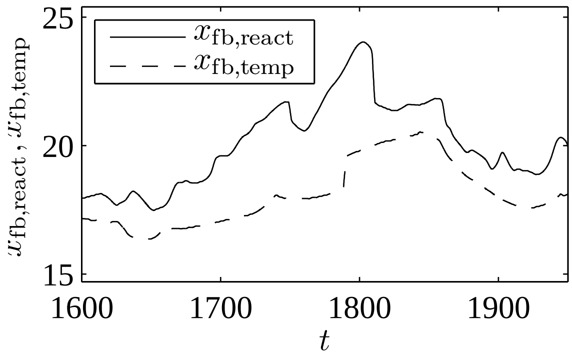

Figure 6.36: Temporal evolution of the streamwise positions $x_{\mathrm{fb,temp}}$ and $x_{\mathrm{fb,react}}$.

Statistical analysis at the flame base

As already noted, the mixture fraction, the oncoming streamwise velocity, and the scalar dissipation rate are regarded as key parameters in most theories on the stabilization of non-premixed lifted flames. The present analysis follows the reaction rate based method for flame localization: the position of the flame base $x_{\mathrm{fb,react}}$ is always identified by the instantaneous leading position of the contour line associated with $\dot{\omega}_I = 0.004$. Figs. 6.37 and 6.38 show the statistical distribution of the key quantities obtained directly at the flame base $x_{\mathrm{fb,react}}$. Fig. 6.37 a depicts the probability density of the mixture fraction at the flame base $Z|_{x_{\mathrm{fb,react}}}$ in terms of a normalized histogram. The shown histogram is associated with a mean value of $\langle Z\rangle_{x_{\mathrm{fb,react}}} = 0.095$, and a RMS value of $\langle Z'^2\rangle^{1/2}_{x_{\mathrm{fb,react}}} = 0.008$. Regarding the stoichiometric mixture fraction $Z_{\mathrm{st}} = 0.104$ this indicates that the flame is basically stabilized close to the surface of the stoichiometric mixture, predominantly on the lean side.

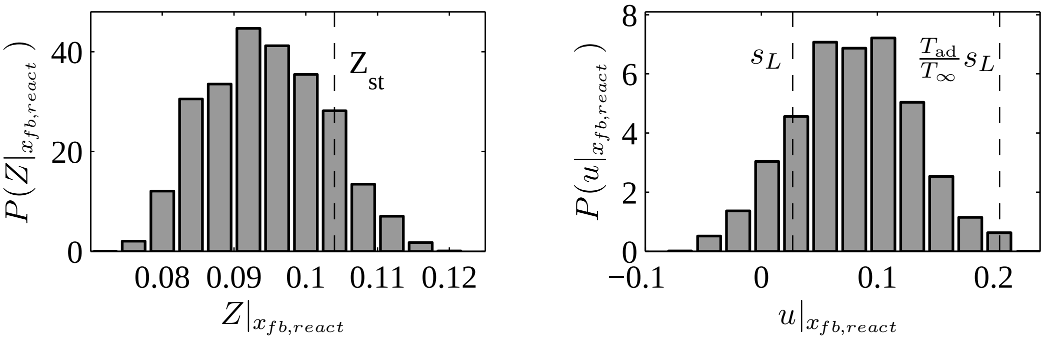

Figure 6.37: Normalized histograms obtained at the flame base located at the position $x_{\mathrm{fb,react}}$. **a** Mixture fraction $Z|_{x_{\mathrm{fb,react}}}$, **b** streamwise velocity component $u|_{x_{\mathrm{fb,react}}}$.

The histogram of the local streamwise velocity at the flame base $u|_{x_{\mathrm{fb,react}}}$ is given in Fig. 6.37 b. The corresponding mean and RMS values of the streamwise velocities are $\langle u\rangle_{x_{\mathrm{fb,react}}} = 0.080$ and $\langle u'^2\rangle^{1/2}_{x_{\mathrm{fb,react}}} = 0.052$, respectively. The observed mean velocity evidently exceeds the laminar flame speed $s_L = 0.027$ considerably (denoted by left dashed line). The apparent difference is conceivable, as the histograms are evaluated at a position with strongly increased temperatures, where the volumetric dilatation already affects the local velocities significantly. The possible magnitude of the dilatational increase of the velocity is shown in Fig. 6.37 b by the right dashed line representing the theoretically highest possible value which can be reached in the burnt-gas region of a corresponding premixed planar flame, $T_{\mathrm{ad}}\,/\,T_\infty\, s_L = 0.206$ (for reference see also Fig. 4.4). It can be seen, that velocities remain for the most part sufficiently below this maximum. The presently observed behaviour for the velocity is well consistent with the findings of Ruetsch *et al.* (1995), who show that the local streamwise velocities in the high temperature burnt-gas region of triple flames assume approximately half the value of their planar counterparts. The here observed mean value $\langle u\rangle_{x_{\mathrm{fb,react}}} = 0.080$, being evidently somewhat smaller than half the value of $T_{\mathrm{ad}}\,/\,T_\infty\, s_L = 0.206$, corresponds to $\langle u\rangle_{x_{\mathrm{fb,react}}} = 2.9\, s_L$, which is in very good agreement with the experimentally observed value $\langle u\rangle_{x_{\mathrm{fb,CH^*}}} = 2.7\, s_L$ by Watson *et al.* (1999).

The histogram of the scalar dissipation rate at the flame base $\chi|_{x_{\mathrm{fb,react}}}$ is shown in Fig. 6.38. As observed in previous studies the distribution resembles a log-normal distribution (Su *et al.*, 2006). The presently shown distribution is associated with mean and RMS values of $\langle\chi\rangle_{x_{\mathrm{fb,react}}} = 0.056$, and $\langle\chi'^2\rangle^{1/2}_{x_{\mathrm{fb,react}}} = 0.056$, respectively. The scalar dissipation rate for flamelet extinction in the corresponding thickened one-dimensional flame, $\chi^t_{\mathrm{st},q} = 3.42$, is significantly higher. Observing mean and RMS values significantly smaller than the quenching limits, previous studies strongly doubted, or even denied any effect of the scalar dissipation rate. Certainly, the effect of scalar dissipation rate may not be as strong as that of the velocity. Nonetheless, some effects of the scalar dissipation rate can still be detected as seen from Fig. 6.39, which shows a scatter plot of the Lagrangian flame propagation

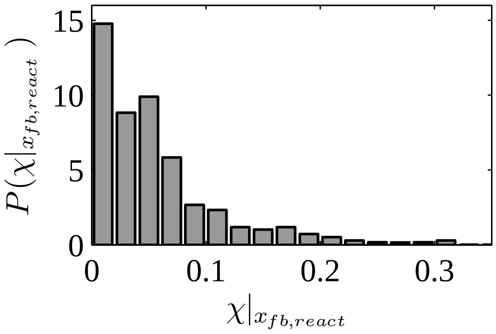

Figure 6.38: Normalized histogram of the scalar dissipation rate obtained at the flame base associated with the position $x_{\mathrm{fb,react}}$, $\chi|_{x_{\mathrm{fb,react}}}$.

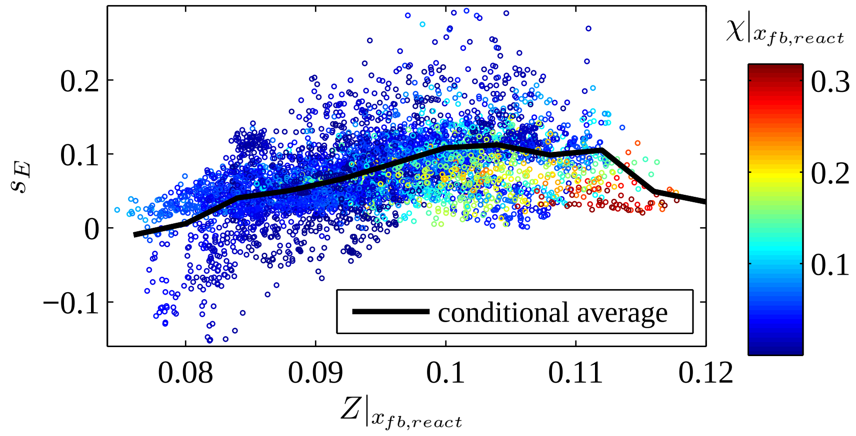

Figure 6.39: Scatter plot of Lagrangian edge flame speed s_E (Eq. 6.11) vs. mixture fraction Z at the flame base $x_{\mathrm{fb,react}}$. Colour code denotes scalar dissipation rate χ, bold line denotes conditional average $\langle s_E | Z_{x_{\mathrm{fb,react}}} \rangle$.

velocity

$$s_E = u|_{x_{\mathrm{fb,react}}} - \frac{dx_{\mathrm{fb,react}}}{dt}\,, \tag{6.11}$$

plotted vs. the mixture fraction, coloured by the scalar dissipation rate. The black bold line denotes the conditional average $\langle s_E | Z_{x_{\mathrm{fb,react}}} \rangle$. According to its definition, the Lagrangian flame propagation velocity s_E represents the speed of the edge of the flame relative to the oncoming fluid. Averaging over all realizations shown in Fig. 6.39 gives a mean Lagrangian edge flame propagation velocity $\langle s_E \rangle = 0.075$, which is somewhat smaller than the mean streamwise velocity $\langle u \rangle_{x_{\mathrm{fb,react}}} = 0.08$ obtained from the histogram in Fig. 6.37 b. This indicates, that the flame receded slightly during the timespan, where the statistical sample was taken. A dependence of the edge flame propagation speed s_E on the mixture fraction Z becomes evident. This can be particularly seen from the conditional average $\langle s_E | Z_{x_{\mathrm{fb,react}}} \rangle$ denoted by the bold line. A distinct maximum for $\langle s_E | Z_{x_{\mathrm{fb,react}}} \rangle$ occurs on the fuel-rich side very close to the stoichiometric mixture fraction $Z_{\mathrm{st}} = 0.104$, which is expected, as the flame propagates fastest into slightly rich mixtures. Nevertheless, the flame is preferably located on the fuel-lean side, as it has been shown in various experimental studies (see e.g. Su *et al.* 2006), as well as in the present work. The influence of the scalar dissipation rate on the Lagrangian speed of the edge flame s_E is seen from the colour code. Although the scalar dissipation rate does evidently not reach the quenching limit, it can be observed that the higher $\chi|_{x_{\mathrm{fb,react}}}$ values are associated with lower flame speeds s_E. Furthermore, it can be seen that high scalar dissipation rates must be expected especially for the higher mixture fractions met on the fuel-rich side. This finding helps also to explain one particular feature of the present flame stabilization process, i.e., the observed tendency to burn predominantly on the lean side of the stoichiometric surface: the closer to the centerline, the more fuel-rich patches occurring in the mixture would basically provide

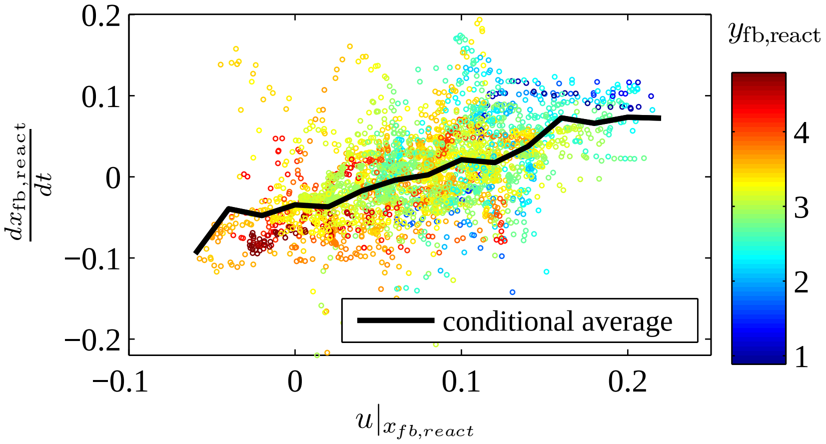

Figure 6.40: Scatter plot of the axial flame base velocity $dx_{\text{fb,react}}/dt$ vs. the streamwise velocity at the flame base $u|_{x_{\text{fb,react}}}$. Colour code denotes the lateral flame base position $y_{\text{fb,react}}$, the bold line denotes the conditional average $\langle dx_{\text{fb,react}}/dt \,|\, u_{x_{\text{fb,react}}} \rangle$.

favourable burning conditions, as the flame propagates fastest into fuel-rich mixtures with an equivalence ratio being somewhat higher than unity. On the other hand, the flame base faces the adverse effects of the higher scalar dissipation rates observed in Fig. 6.39, and the comparatively high streamwise velocity near the center. Therefore, the flame tends to stabilize in a radially further outwards region, where the mixture is somewhat leaner.

The explanation given above for this tendency to stabilize towards the fuel-lean region is also supported by the analysis of the motion of the flame base illustrated in Fig. 6.40, where the instantaneous axial velocities of the flame base $dx_{\text{fb,react}}/dt$ are scatter-plotted vs. the local streamwise velocity $u|_{x_{\text{fb,react}}}$. The colour code denotes the lateral position of the flame base $y_{\text{fb,react}}$. Negative values for the flame base velocity $dx_{\text{fb,react}}/dt$ indicate that the leading edge of the reactive layer $x_{\text{fb,react}}$ propagates upstream. It becomes particularly evident from the conditional average $\langle dx_{\text{fb,react}}/dt \,|\, u_{x_{\text{fb,react}}} \rangle$, that this is primarily the case for the radially farther outward positions with $y_{\text{fb,react}} \gtrsim 3$, where the flame faces comparatively low local axial velocities $u|_{x_{\text{fb,react}}}$. In contrast, for the near-axis positions with $y_{\text{fb,react}} \lesssim 3$, high local flow velocities u lead to receding flames, despite the fuel-rich mixing conditions associated with higher propagation speeds of the edge flame s_E seen in Fig. 6.39.

The distinct effect of the scalar dissipation rate on the flame stabilization point is highlighted in some more detail in the scatter plot Fig. 6.41, which illustrates the statistical correlation between scalar dissipation rate $\chi|_{x_{\text{fb,react}}}$, and the axial and lateral velocities of the flame base, $dx_{\text{fb,react}}/dt$, and $dy_{\text{fb,react}}/dt$, respectively. It can be clearly seen, that the flame base recedes ($dx_{\text{fb,react}}/dt > 0$) and moves radially outwards ($dy_{\text{fb,react}}/dt > 0$), if high scalar dissipation rates $\chi|_{x_{\text{fb,react}}} > 0.1$ are present. For low scalar dissipation rates

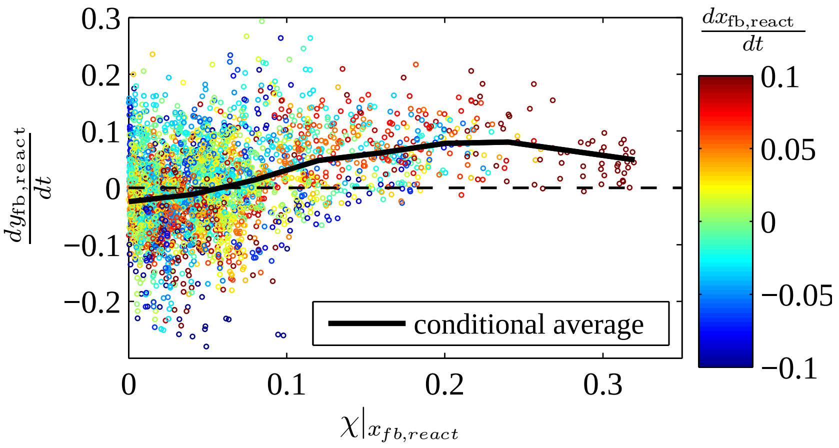

Figure 6.41: Scatter plot of the lateral flame base velocity $dy_{\mathrm{fb,react}}/dt$ vs. the scalar dissipation rate $\chi|_{x_{\mathrm{fb,react}}}$ at the flame base. Colour code denotes the axial flame base velocity $dx_{\mathrm{fb,react}}/dt$, the bold line denotes the conditional average $\langle dy_{\mathrm{fb,react}}/dt \,|\, \chi_{x_{\mathrm{fb,react}}} \rangle$.

($\chi|_{x_{\mathrm{fb,react}}} < 0.1$), the correlation between $\chi|_{x_{\mathrm{fb,react}}}$ and the axial motion $dx_{\mathrm{fb,react}}/dt$ seems to be very weak, as indicated by the amplified scatter around a very weakly inclined conditioned mean $\langle dy_{\mathrm{fb,react}}/dt \,|\, \chi_{x_{\mathrm{fb,react}}} \rangle$.

The mutual statistical dependence of the individual quantities shown in the scatter plots in Figs. 6.39 to 6.41 can be quantified in terms of correlation factors. For two fluctuating, arbitrary quantities $\mathrm{qty_a}$ and $\mathrm{qty_b}$ the correlation factor is usually defined as

$$\mathrm{corr}_{a,b} = \frac{\overline{\mathrm{qty_a}(t)'\,\mathrm{qty_b}(t+\Delta t_{\mathrm{lag},a,b})'}}{\sqrt{\overline{\mathrm{qty_a}(t)'^2}\;\overline{\mathrm{qty_b}(t+\Delta t_{\mathrm{lag},a,b})'^2}}}\,. \tag{6.12}$$

This definition involves a time shift $\Delta t_{\mathrm{lag},a,b}$, which is determined as the time lag, where the correlation factor $\mathrm{corr}_{a,b}$ becomes a maximum. This time lag has to be introduced, if changes in one quantity are reflected by the other after a certain response time[††]. According to the definition Eq. (6.12), two perfectly correlated quantities should yield a correlation factor $\mathrm{corr}_{a,b} = \pm 1$. Such a perfect correlation becomes impossible, if more than two of the involved quantities statistically depend on each other. The correlation factors between the quantities in Figs. 6.39 to 6.41 are listed in Tab. 6.4. The correlation between the scalar dissipation $\chi|_{x_{\mathrm{fb,react}}}$ and the relative edge flame velocity s_E appears to be the weakest. The edge flame velocity s_E is apparently more influenced by the mixture fraction $Z|_{x_{\mathrm{fb,react}}}$, interacting with negligible response time ($\Delta t_{\mathrm{lag},Z,s_E} = 0$). In contrast, the correlation of $\chi|_{x_{\mathrm{fb,react}}}$ and s_E exhibits a much larger response time $\Delta t_{\mathrm{lag},\chi,s_E} = 3.2$, indicating

---

[††] E.g., for a simple linear spring and mass system, velocity and position are clearly correlated. Nevertheless, there is a lag of $\pi/2$ in phase. If this lag were not accounted for, the correlation factor Eq. (6.12) would yield zero.

qty_a	qty_b	$\mathrm{corr}_{a,b}$	$\Delta t_{\mathrm{lag},a,b}$
$Z\|_{x_{\mathrm{fb,react}}}$	s_E	0.47	0.0
$\chi\|_{x_{\mathrm{fb,react}}}$	s_E	-0.12	3.2
$\chi\|_{x_{\mathrm{fb,react}}}$	$Z\|_{x_{\mathrm{fb,react}}}$	0.48	0.0
$u\|_{x_{\mathrm{fb,react}}}$	$\frac{dx_{\mathrm{fb,react}}}{dt}$	0.64	-3.6
$y_{\mathrm{fb,react}}$	$\frac{dx_{\mathrm{fb,react}}}{dt}$	-0.31	1.9
$y_{\mathrm{fb,react}}$	$u\|_{x_{\mathrm{fb,react}}}$	-0.43	3.8
$\chi\|_{x_{\mathrm{fb,react}}}$	$\frac{dy_{\mathrm{fb,react}}}{dt}$	0.36	-1.7
$\chi\|_{x_{\mathrm{fb,react}}}$	$\frac{dx_{\mathrm{fb,react}}}{dt}$	0.3	-7.0
$\frac{dx_{\mathrm{fb,react}}}{dt}$	$\frac{dy_{\mathrm{fb,react}}}{dt}$	0.19	-0.2

Table 6.4: Correlation factors according to Eq. (6.12) for the quantities illustrated in the scatter plots Figs. 6.39 to 6.41 covering the timespan $1000 < t < 1800$.

that an enhanced cooling of the flame does not immediately translate into an altered speed of the edge flame. Additionally, although it becomes evident from Fig. 6.39 that only the higher values of χ (red coloured) significantly alter the flame speed, the correlation $\mathrm{corr}_{\chi,s_E} = -0.12$ is still relatively low. This can be explained with the relatively large time lag $\Delta t_{\mathrm{lag},\chi,s_E}$ associated with this correlation, as well as the scarce occurrence of high χ-values as seen from Fig. 6.38. This scarcity and the relatively long response time basically limit the number of significant events showing a statistical correlation between χ and s_E, which leads to the unduly small correlation factors.

Three-dimensional effects

Experimental studies presented in literature generally give no comment on the possible relevance of three-dimensional ("out-of-the-plane") effects in the flame stabilization process. This is mainly due to the commonly applied laser-optical techniques, where the experimental data are acquired on measurement planes produced by laser sheets crossing the axis of the reacting flow field. As such, these two-dimensional measurements are not supposed to capture three-dimensional out-of-the-plane effects in a reliable way. To some extent the irrelevance of these effects can be certainly justified by the cylindrical symmetry of the considered flow configuration, where the measurement planes are geometrically orthogonal to the statistically homogeneous azimuthal direction. Therefore, instantaneous out-of-the-plane effects should statistically cancel, as also pointed out by Upatnieks *et al.* (2004). Nonetheless, despite the statistically two-dimensional nature of the flow, transient large-scale phenomena may temporally produce highly three-dimensional structures. As shown in the previous section, such large-scale flow phenomena periodically appear in the present jet flame driven by buoyancy. The temporally considerable impact of this buoyancy-induced large-scale motion is demonstrated in Fig. 6.42 showing instantaneous iso-surfaces of temperature at $T = 1.2$. The shown snapshots illustrate a sequence of three periodically occurring events, where the low-density bulb-shaped structure has clearly separated from the flame base to move further downstream towards the exit of the domain. As such, each event belongs to one periodic cycle of the buoyancy-induced large-scale motion with a period $\Delta t_{\mathrm{bf}} = 350$ (see Sec. 6.3.3). Distinct notches are evidently opening the bottom of the iso-surface, every time when a low-density bulb has separated from the flame base. It has to be noted, that the observed notches in general cross the flame base with a different azimuthal orientation, so that the shown snapshots are not taken from equal azimuthal view angles φ.

The notches indicate a strong temporal perturbation of the otherwise mostly annular-shaped flame base. Along two relatively large circumferential portions the leading edge of the flame has evidently receded considerably. The marked local receding may even lead to stronger deformations of the flame base geometry as seen from Fig. 6.43 showing the respective state occurring in a later cycle. At the shown instant of time $t = 2140$, one half of the leading edge has been practically blown-off.

The observed receding of a considerable part of the flame obviously represents a highly critical phase in the flame stabilization process, where the probability of a complete blow-out is certainly the greatest. The fact that a complete blow-out does still not occur and the flame keeps burning at a certain lift-off height can be attributed to the non-axisymmetric nature of the perturbation. Accordingly, only some circumferential portion of the leading edge of the flame recedes, but never the base as a whole. Thus, the flame remains basically

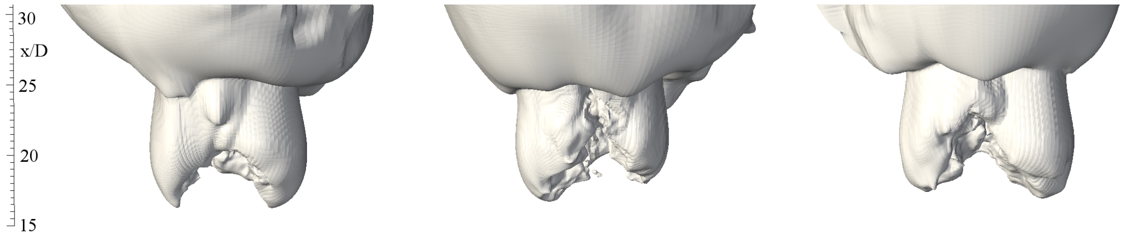

t=1090 t=1440 t=1790

Figure 6.42: Iso-surfaces of temperature at $T = 1.2$ for three different events equally spaced in time by one buoyancy-induced oscillation period $\Delta t_{\mathrm{bf}} = 350$, respectively.

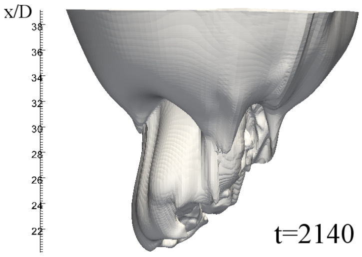

Figure 6.43: Iso-surface of temperature at $T = 1.2$ for the time instance $t = 2140$.

anchored at the non-receding, most upstream parts of the base. The continuous delivery of reactive heat from these anchoring sites helps to laterally close the deeply opened sections in the flame surface, so that the flame can recover its stable cylindrical base structure.

In order to find out the actual reason for the observed partial blow-off of the leading edge flame, a closer look was taken again on the possible influence of the flow and mixing conditions occurring at the flame base during this critical phase. The impact of the three key quantities Z, χ, and u on the reactive layer during one partial blow-off event ($1390 < t < 1470$) is exemplarily shown in Fig. 6.44, where their local values are used as colour-codes on the iso-surfaces of the reaction rate $\dot{\omega}_I$ at $\dot{\omega}_I = 0.004$. For reference, the last column on the right side illustrates the situation during an uncritical, stable phase $t = 1650$, where the bulb-shaped structure has not yet separated from the flame base (referring to Figs. 6.25, 6.26).

The iso-surfaces coloured by the mixture fraction Z in Fig. 6.44 a give no evidence that unfavourable mixing conditions near the flame base would lead to the observed notches. Well premixed regions with flammable mixtures are present along the whole leading edge of the reactive layer, for all time instances during the partial blow-off event. Additionally, the mixing state at the flame base, including the vertices of the notches, seems to be almost identical with the mixing state at the flame base under the uncritical reference conditions.

The comparison against the uncritical reference conditions unveils clear differences for the scalar dissipation rates χ as seen in Fig. 6.44 b. Evidently, the entrainment induced by the separation and the commencing upwards motion of the bulb-shaped structure leads to a contraction of mixture fraction iso-contours resulting in notably increased scalar dissipation rates as compared to the uncritical reference condition ($t = 1650$). At the early stages of the notch formation ($t = 1390$), the higher scalar dissipation rates appear especially near the vertices of the notches. The enhanced heat losses associated with the local maxima in χ basically promote a deepening of the notches, so that the flame locally recedes further downstream with increasing time. In contrast to the conditions at the vertices, the lateral sides of the notches seen at the time instant $t = 1450$ exhibit relatively low levels of χ. Therefore, the flame front favourably propagates into the azimuthal direction, where it faces fresh, burnable mixture, which has been created in the opened flame surface due to the direct contact between the inner fuel-rich core region and the oxidizer-rich ambient medium. It can be seen from the time instant at $t = 1470$, that this mainly lateral flame propagation finally closes the notched surface so that the flame recovers its original state.

It has to be noted, that absolute values of the observed scalar dissipation rate $\chi \lessapprox 0.15$ in Fig. 6.44 b certainly appear to be relatively small when compared to the scalar dissipation rate at quenching $\chi^t_{\mathrm{st},q} = 3.42$. Nevertheless, the here attained levels still belong to the higher range of statistically occurring values (see Fig. 6.38), which are expected to be able to alter the edge-flame propagation speed s_E considerably (see the discussion of Fig. 6.39) leading to the observed local receding of the flame base.

The observation, that the appearance of partially blown-off regions is associated with locally increased scalar dissipation rates, is well consistent with the observed velocity at the reactive layer shown in Fig. 6.44 c. At the beginning of the formation of the notch ($t = 1390$), there are some differences in axial velocity along the leading annular contour. However, these differences are not significant enough to explain a local receding of the flame, because the same levels of axial velocity (light-blue/green) may appear during stably burning periods, as seen from the time instant at $t = 1650$. Nevertheless, at the later stages, where the notch has deeply opened the flame surface ($t = 1450$), the more downstream vertex of the notch is subject to higher axial velocities, which increase downstream due to the acceleration of the buoyancy forces. Since the higher velocities near the vertices of the notches rather promote a further receding of the flame, the open sections of the flame surface are preferentially closed from the lateral sides facing smaller velocities and scalar dissipation rates as already mentioned above.

The presently described scenario occurring in the stabilization process of the considered jet flame has so far not been explicitly investigated and discussed in experimental studies. For some part, this is due to the decreasing influence of the buoyancy with increasing Reynolds number, so that the here observed buoyancy-induced large-scale effects, which destabilize a considerable part of the flame base, may not occur in the mostly higher Reynolds numbers experiments. For the other part, the aforementioned limitation to two-dimensional measurements makes it difficult to describe instantaneous out-of-the-plane effects relevant in the present scenario. Thus, it can be stated, that the present DNS certainly provides a valuable further insight into the complex process of flame stabilization of strongly buoyant lifted jet flames.

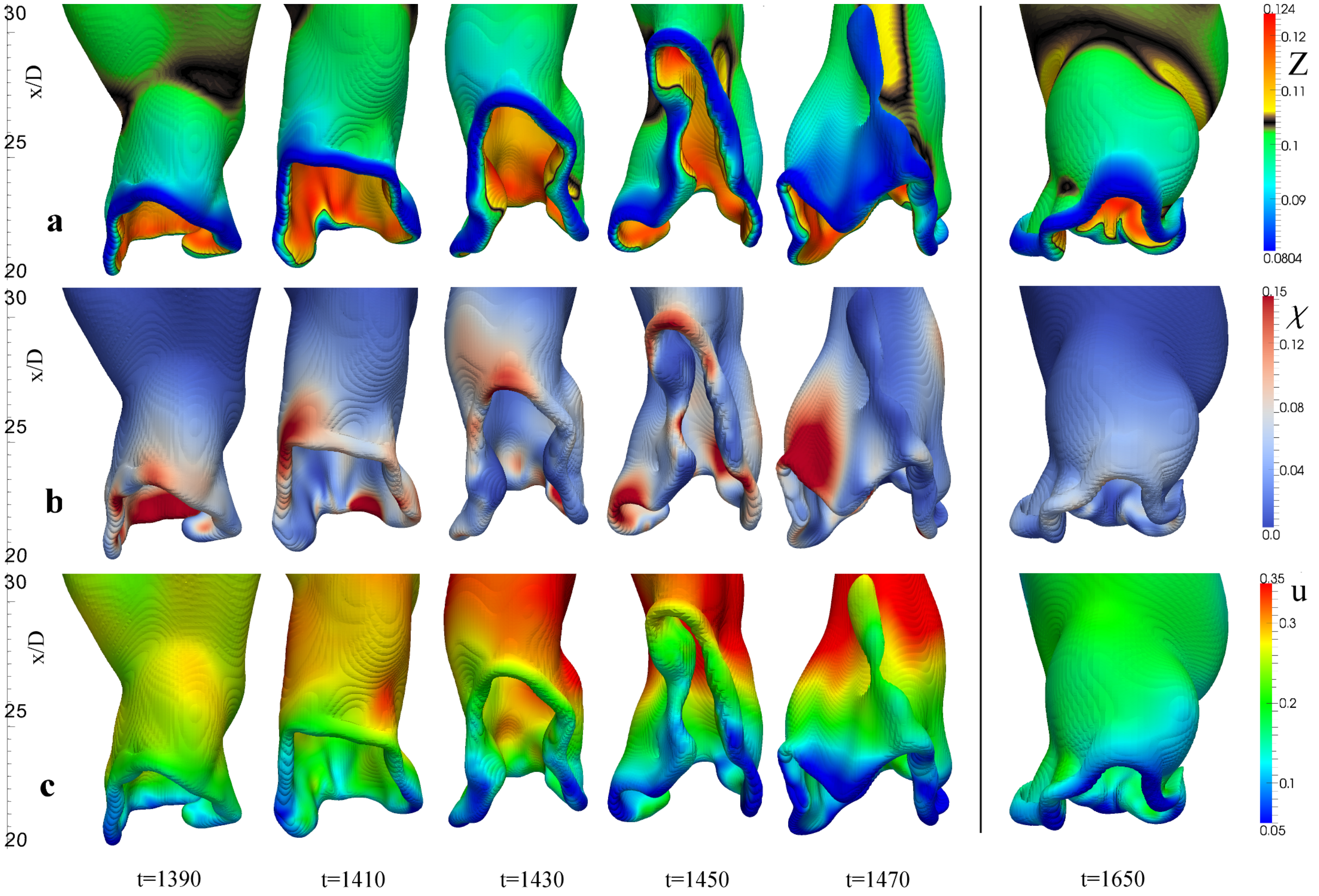

Figure 6.44: Instantaneous iso-surfaces of the reaction rate $\dot{\omega}_I$ at $\dot{\omega}_I = 0.004$ during one partial flame blow-off event. The right column shows conditions during an uncritical later phase for comparison. Colour codes: **a** Mixture fraction Z, **b** scalar dissipation rate χ, **c** streamwise velocity u.

7 CONCLUSIONS

In the present work the dynamics at the base of a lifted, turbulent, strongly buoyant, methane-air jet flame was investigated by means of a three-dimensional Direct Numerical Simulation (DNS). A nitrogen-diluted fuel feed was assumed in order to provide highly sensitive burning conditions, which are convenient to clearly identify the most relevant mechanisms for the stabilization of the considered flame. A non-reacting free jet was simulated as well for use as a reference case to single out the dynamic effects of the flame on the flow field. Results of the lifted jet DNS were compared against experimental reference data obtained by Köberl *et al.* (2010) and Heimel (2010), where generally a good agreement was observed.

For a reliable setup of the DNS, precursor studies were conducted carrying out one-dimensional simulations of premixed laminar planar flames, as well as non-premixed laminar counterflow flames. A numerical code was written to compute the structure of these generic flames embedded in a predefined one-dimensional flow field. The results obtained from these computations were analyzed with a special focus on the applied reduced two-step chemical reaction mechanism. It was shown, that the essential features of both the premixed and the non-premixed flames, i.e., the laminar flame speed, and the scalar dissipation rate at extinction, could be reproduced fairly well. Additionally, estimates for the spatial resolution requirements of the three-dimensional computations were derived, and flame data for the initialization of the reacting flow field were extracted.

For the DNS of the reacting jet, a code originally developed for non-reacting jet flow by Boersma *et al.* (1998) was extended to account for the transport of multiple species and temperature (including the reactive source terms), buoyancy, as well as mixture- and temperature-dependent transfer coefficients. The Dynamically Thickened Flame (DTF) approach, which basically relies on a local thickening of the reactive layers, was applied to resolve the extremely thin reaction zones. First simulations of reacting jet flow revealed large vortical structures, which led to partial flow reversal and numerical instability at the outflow boundary when using standard outflow boundary conditions. To ensure stable simulations without significant losses in accuracy, a robust outflow boundary treatment for strongly buoyant, turbulent jet flames was developed in the course of the present work (Walchshofer *et al.*, 2011).

Comparing the results of the reacting against the non-reacting simulation, the most striking differences in the flame region appeared in the notably increased velocity and scalar half-widths, which are caused by the volumetric dilatation, and the notably attenuated decay of the centerline velocity and mixture fraction, which is caused by the buoyancy forces, as expected. The volumetric dilatation, together with the increased viscosity in the hot product gases, also leads to a significant dissipation of the small scale vortical structures of turbulence. The high turbulence levels of the cold, non-reacting reference jet are retained only in the non-burning core region around the lifted flame base. Upstream effects of the flame on the non-burning near field of the jet, which have been mostly discarded, or considered as insignificant in previous studies, could be unveiled by a close comparison of the results obtained in the near fields of the considered reacting/non-reacting jets. It was shown that the flame evidently impedes the oncoming jet flow, so that the half-widths of the velocity and the mixture fraction in the non-reacting upstream region, and consistently the inverses of the respective centerline values, increase somewhat faster in the region ahead of a lifted flame. Notably increased velocity fluctuations were also observed in the radially outer region due to the action of buoyancy. The absolute magnitude of the velocity differences is however small in comparison to the turbulent fluctuations in the core of the jet.

Marked effects of buoyancy are observed in the large-scale motion especially in the far field embedding the flame. The reactive heat release and the volumetric dilatation periodically generate large bulb-shaped structures with low-density. They keep growing until buoyancy forces their lift-off from the flame base and their further convection upwards towards the exit of the computational domain. These periodically generated large-scale perturbations of the flow, which are also experimentally observed in high-speed schlieren visualizations, translate into strong oscillations of the total mass, momentum, and reaction rate in the computational domain. The lift-off of the bulb-shaped structures with low-density always leads to a strong temporal acceleration of the flow, which results in an oscillating motion of the leading edge of the flame surface.

The analysis of the DNS results on the most relevant mechanisms for the flame stabilization essentially confirms the well established consensus that the stabilization is mainly determined by the premixed flame propagation. Additionally, due to the buoyancy-induced large-scale motion the stabilization process of the present flame also features a highly critical scenario associated with a physically more complex background than only premixed flame propagation. Thus, the strong temporal acceleration caused by the lift-off of the low-density bulbs repeatedly introduces strong large-scale perturbations of the flame, where considerable sections of the flame base are receding deeply downstream. The observed partial receding was shown to be mainly due to an enhanced cooling of the respective flame regions, indicated by a marked local increase of the scalar dissipation rates. Although the increased scalar dissipation rates never reach the extinction limit, it is shown that they still significantly reduce the propagation speed of the leading flame edge into the oncoming mixture. This underlines the high relevance of the scalar dissipation rate for the stabilization process of the presently considered strongly buoyant jet flame. The non-axisymmetric nature of the buoyancy-induced large-scale perturbations is shown to prevent the flame from a total blow-out. It keeps the flame essentially anchored at the non-receding parts, from where the deep notches in the flame surface are laterally closed, which is promoted by the relatively low dissipation rates seen on the lateral rims of the notches and the continuous supply of heat from the burning sections. As a whole, the observed scenario demonstrates that buoyancy can produce a very particular mechanism of flame stabilization characterized by large three-dimensional perturbations of the flame base, and a strong dependence on the scalar dissipation rate in contrast to the generally accepted theory, which mostly discards this influence.

A COMPUTER HARDWARE

In the course of this thesis work several workstations and servers were laid out, assembled, installed and maintained to provide for the required computational resources. The design criteria for the created systems are briefly outlined in the following. Two computer clusters of Graz University of Technology (TUG) were used for the simulations as well. Hardware data is given also for these machines, and generic benchmark results are shown.

Layout

The layout of the computer systems had essentially to meet the objective of delivering maximum performance at acceptable costs. The fulfilment of this objective is not straightforward. The performance of a machine can be measured by running benchmark programs. However, if a system is proven as optimal for running a program “foo”, it is not necessarily optimal for the program “bar”. The quality of a system therefore depends strongly on the used applications.

In the present case, the systems were tailored to the needs of the parallel DNS code described in Chp. 5. The numerical algorithms carried out in this code are characterized by the following: a main loop is implemented for the integration in time, which consumes wall time of the order of seconds per computational time step. Each iteration contains a large number of simple, uncoupled, vectorizeable, double precision floating point operations. Additionally, one (coupled) linear system is solved per time step using fast Fourier transforms (FACR, see Sec. 5.1.2). Three communication processes are needed per iteration: a comparatively small amount of data is exchanged with the “ghost” or “halo” cells (MPI_SENDRCV), and two somewhat bigger blocks of gridpoints have to be communicated when solving the linear system (MPI_ALLTOALL). Furthermore, it was already known from previous runs that the program has a comparably small memory footprint for CFD*, and that the parallel efficiency on already existing systems was quite acceptable for several dozens of processes.

Considering these facts, the following criteria could be derived: The network latency might matter, but the network bandwidth is a quantity of minor importance. When computing e.g. the inert jet in Sec. 6.2 (23 million cells) using 64 processes, only 2.8 MB have to be sent

---

*For the non-reacting jet code that accounts for transport of a passive scalar and variable gas properties e.g. $\approx$ 300 MB per million cells.

and received per MPI_ALLTOALL and process[†]. The amount of memory is also of minor importance. For the above mentioned test case e.g. only 6.8 GB are required, which can be accommodated even on desktop machines. Also the memory speed was found to be only of minor importance for the speed of computation. Therefore, the acquisition of new hardware gave priority to the highest available raw CPU performance per monetary unit, without respect to the total number of CPUs[‡].

The results of two benchmarks which were considered to come comparably close to the present application were used for a first assessment: The high performance linpack (HPL), and the SPEC CPU2006 benchmark. Relating the published results to CPU prices, a certain advantage was found for AMD systems for the present case. AMD processors were therefore used in all assembled systems.

Expecting a strong emission of heat due to the intensive permanent load of the systems special care was also taken for the layout of the cooling. This included appropriately dimensioned heat sinks, appropriate casings with increased ventilation and the proper placement in air-conditioned server rooms.

Different variants of Linux were tested as Operating System (OS). These include Debian, Ubuntu, CentOS and Gentoo, where Gentoo showed to deliver slightly superior performance when running the DNS code. This slight superiority might be attributed to the source code based release which can be compiled specifically for the used hardware, but also to the frequent updates for kernels and compilers in this distribution[§]. For reasons of costs, but also with special regard to code portability, GNU compilers were used in all cases, and OpenMPI was used for the message passing.

Desktop and server systems

For running first test simulations and for the less demanding precursor computations within this thesis, two desktop systems were built from scratch. The main technical data for these systems are given in Tab. A.1. Subsequently, two larger server systems were built for the three-dimensional DNS, see Tab. A.2.

The HPL performance was measured on two of the systems, where the AMD Core Math Library (ACML) was chosen as platform for the BLAS (Basic Linear Algebra Subprograms) component. The computational speeds in Gflops obtained for the benchmark

---

[†] On a "slow" gigabit ethernet, the net transfer time for 2.8 MB would be 22.4 ms. In contrast, one time step for that case takes approximately 3 seconds (I-cluster).

[‡] When dealing with parallel systems and efficient parallel codes, the absolute number of CPUs is unimportant up to a certain threshold. Only the cumulative power (e.g. in terms of "flops") is important.

[§] When new hardware is used, performance is generally better with newer compilers supporting a higher level of optimization.

Name	CPU	Cores / CPU	GHz	Memory	Gflops base/peak
pc13	AMD Phenom 9850 BE	4	2.5	8GB DDR2 (800 MHz)	– / 40.0
qx05	AMD Phenom II 965 BE	4	3.4	12GB DDR3 (1333 MHz)	41.7 / 54.4

Table A.1: Desktop computers built within the framework of this thesis.

Name	CPU	# of CPUs	Cores / CPU	GHz	Memory	Gflops base/peak
qx03	AMD Opteron 2352	2	4	2.1	16GB DDR2 (667 MHz)	55.2 / 67.2
qx04	AMD Opteron 8350	8	4	2.0	32GB DDR2 (667 MHz)	– / 256.0

Table A.2: Server systems built within the framework of this thesis.

(base), together with the theoretically achievable values (peak) are shown in the last column of Tab. A.1 and A.2. Good agreement was found when comparing the results with corresponding values published for similar systems. The velocity ratio base to peak flops which can be achieved with a certain combination of software is often referred to as the numerical performance of a system. The numerical performance achieved in the present benchmark test proves the actually applied combination of software as an appropriate choice. This approval applies especially to the GNU compilers and OpenMPI used, which are often doubted to yield “acceptable” performance.

Computer clusters

Two computer clusters of the Graz University of Technology were employed as well for the jet simulations. The main technical data of the two systems are given in Tab. A.3. It should be noted that the G-cluster was used only for benchmark testing (see the next section), while the I-cluster was used for the production runs.

Name	# of nodes	CPU type	CPUs / node	Cores / CPU	GHz	Memory / node	Network	Tflops base/peak
G-cluster	55	Intel Xeon (32bit)	2	1	2.66	2GB	Gb ethernet	-
I-cluster	$7+2$	AMD Opteron	8	4	2.7/2.3	128GB	Infiniband	1.6/3.0

Table A.3: Employed computer clusters.

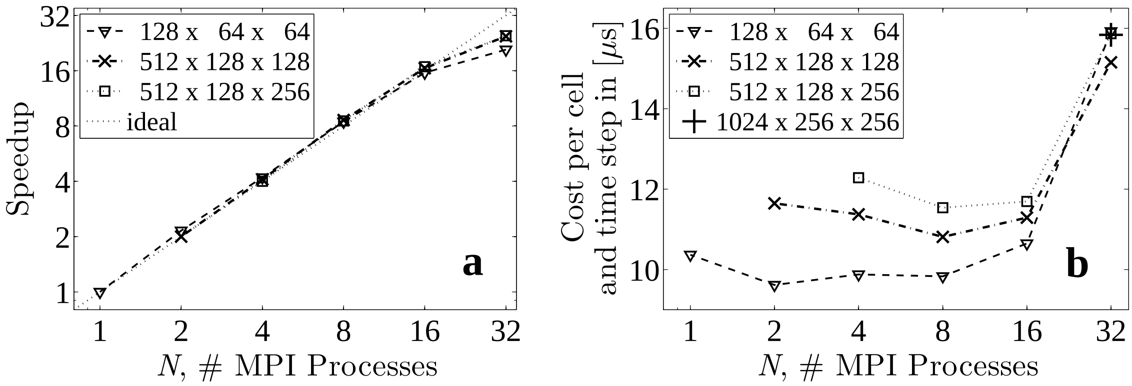

Figure A.1: **a** Speedup and **b** numerical efficiency of the non-reacting jet code on qx04.

Benchmark results

Several test computations were carried out to investigate the performance of the employed DNS code executed on the available hardware. At first, a non-reacting jet flow was computed on the server qx04 (32 cores). The speedup, which is defined as the ratio of wall time per (time-) iteration on one processor, divided by the wall time per iteration using *N* processors, is shown in Fig. A.1 a. Different meshes, ranging from 524.000 (128x64x64) to 16.7 Mio. (512x128x256) cells were used. For the two bigger meshes, data could not be generated for the 1 processor case due to code intrinsics¶. It can be observed, that the code scales reasonably well for all three meshes. Up to eight processes, the speedup even slightly exceeds the ideal linear scaling. It is not fully clear, how this behaviour can be explained, but it is assumed that smaller domains per processor might yield effects similar to those obtained by cache line optimization (techniques that aim at better data management within the caches). Furthermore, for higher numbers of processes associated with the smaller subdomain sizes per process, some of the distributed data arrays might fit entirely into the cache. For 32 processes the speedup falls notably below the ideal scaling. At first sight, this behaviour may be attributed to a communication overhead, especially for the smallest mesh. This reason appears, however, improbable, as the very fast internal HyperTransport (HT) communication of the machine is used. Additionally, this argument cannot explain the losses also seen for the large mesh sizes. Considering the fact that the code maintained a linear speedup to higher numbers of processors on other systems (shown later), the phenomenon is rather attributed to specific hardware issues.

The data in Fig. A.1 a give information about the possible speedup provided by the parallel processing of the code, but no information can be derived about the underlying operational efficiency. Similar to Sankaran *et al.* (2006), efficiency can be evaluated, e.g., by relating the computational time needed for one iteration to the number of cells which are computed

---

¶i.e. too big arrays need to be statically allocated. When using the GNU, but also other compilers, statically allocated data must fit into a 32bit address space, which was not the case.

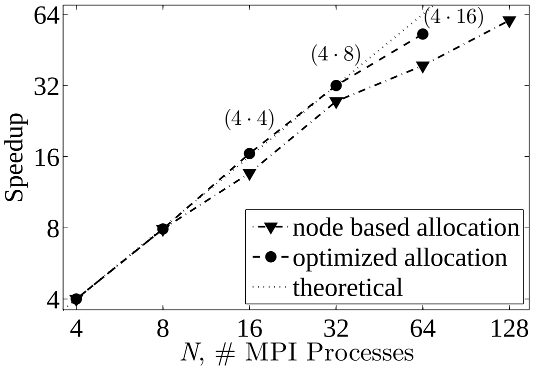

Figure A.2: Speedup for the non-reacting jet code on the I-cluster. Two different process allocation strategies were tested. The numbers in brackets denote the node / processor partitioning used.

by each process. The so obtained costs in terms of the wall time per cell are shown in Fig. A.1 b. For the smaller meshes, better efficiencies can be observed. This behaviour can be explained by the fact, that the operation count N_{op} of the FACR based pressure solver is proportional to

$$N_{\text{op}} \propto \alpha\, i_{\max} j_{\max} k_{\max} \left[\log_2 \log_2 (k_{\max}) - 1\right] + \beta\, \frac{i_{\max} j_{\max} k_{\max}}{2^{\log_2 \log_2 (k_{\max}) - 2}} \log_2 (k_{\max}) \ , \tag{A.1}$$

(where α and β are constants) , so that more operations per cell are needed for the bigger meshes. Furthermore, up to the case with eight processes, it can be seen that the efficiency increases. This is consistent with the hyper-linear speedup already discussed above. For 32 processes a comparatively bad efficiency is observed for all mesh sizes. To investigate this particular issue in more detail, an additional benchmark with an extended mesh of 67 Mio. cells (1024x256x256) was performed. Thereby, the same loss in efficiency is observed for 32 processes. The observed independence of the mesh size gives rise to an explanation based on hardware issues. In the present case, it is believed that cache coherency checks done by the CPUs are the reason for the observed loss in performance.

To investigate on the speedup behaviour up to higher numbers of processes, a mesh of 22.6 Mio. cells (768x230x128) was used in benchmark simulations on the I-cluster. The I-cluster consists of single nodes (Sun Fire X4600), whose architecture is very similar to the server qx04, therefore comparable results are expected. Two different strategies for the allocation of the processes on the given hardware were tested. The results are depicted in Fig. A.2. In the first case, which is termed “node based allocation” in Fig. A.2, up to the maximum of 32 processes are allocated first on each single node before a further node is added for the allocation of processes exceeding the maximum capacity of the already employed nodes. In the second case, termed “optimized allocation”, various distinct allocation strategies were tested for the considered numbers of processes[‖], and the best result is displayed for each case. The comparison of the achieved speedups shows a generally better scalability of the “optimized allocation” strategy.

Summing up the results for the non-reacting code, it can be concluded that the code scales acceptably well using up to 100 processes. However, results also indicate that the used hardware is not optimal when loaded to its maximal capacity.

For the reacting jet the computational costs per time step are significantly higher than in the non-reacting case. Additional transport equations have to be solved for the four transported reacting species. All transport equations have to be solved twice due to the applied predictor-corrector scheme (Sec. 5.1.1). Additionally, the reaction rate terms $\dot{\omega}_j$ have to be evaluated involving computationally costly exponential terms.

In contrast to the non-reacting jet code, the wall time needed per time step strongly depends on the solution for the chemistry: Firstly, the time integration of the reactive source terms (ODEPACK) uses different algorithms depending on the encountered stiffness of the system. Secondly, for reasons of efficiency, the integration of the reactive source terms is skipped in all regions with non-flammable mixtures, to avoid physically meaningless but numerically costly source term evaluations.

The performance results given in the further refer to the DNS of the reacting jet presented in Sec. 6.3. The mesh consists 9.8 Mio. cells (512x150x128), and the whole simulation was run on I-cluster using 64 processes. The wall time needed per time step is approximately 3.7 seconds, which corresponds to a cost in wall time per cell and time step of 24 [μs] (compare Fig. A.1 b). Roughly one fifth of the wall time (0.75 seconds) per time step is spent only for the evaluation and time integration of the reactive source terms. Since the processors working on the non-burning regions compute no chemistry and stand practically idle, the computation of the reaction terms in the non-burning region leads to a disbalanced load. To some extent the problem of unequally distributed load could be alleviated using special load balancing algorithms. For the present case shown in Fig. A.3, e.g., the load could be balanced in a way such that the mean of 0.35 seconds is reached on all 64 processes, hence 0.4 seconds could be theoretically saved for each time step. In practice however, the implementation of load balancing will need additional communication of large arrays[**] which would cost considerable additional time. Therefore, this option has not been pursued further in the present work.

[‖] e.g. 32 processes can be allocated on one node using 32 processes $(1\cdot 32)$, but also like $(2\cdot 16)$ or $(4\cdot 8)$.

[**] For balanced (outsourced) cells, temperature and all species mass fractions would have to be communicated at each time step.

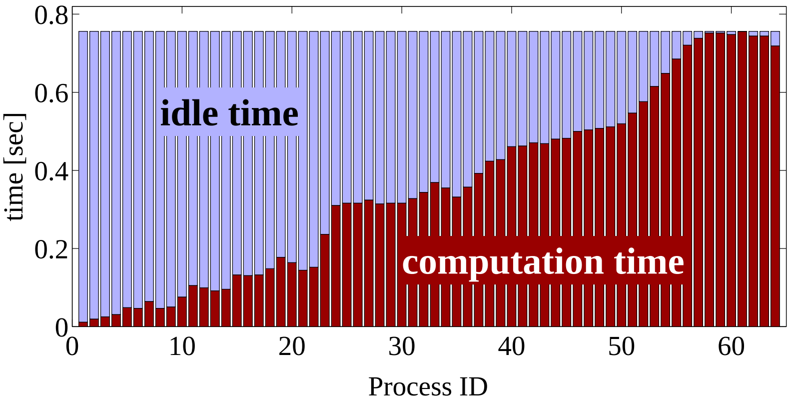

Figure A.3: Fraction of idle/computation time in the wall time consumed for temporal integration of the reactive source terms within one timestep on each process.

REFERENCES

AL-KHATEEB, A. N., POWERS, J. M. & PAOLUCCI, S. 2010 On the necessary grid resolution for verified calculation of premixed laminar flames. *Communications in Computational Physics* **8** (2), 304–326.

AMANTINI, G., FRANK, J. H., SMOOKE, M. D. & GOMEZ, A. 2006 Computational and experimental study of standing methane edge flames in the two-dimensional axisymmetric counterflow geometry. *Combustion and Flame* **147** (1-2), 133 – 149.

AMIELH, M., DJERIDANE, T., ANSELMET, F. & FULACHIER, L. 1996 Velocity near-field of variable density turbulent jets. *International Journal of Heat and Mass Transfer* **39** (10), 2149–2164.

BARLOW, R., FRANK, J., KARPETIS, A. & CHEN, J.-Y. 2005 Piloted methane/air jet flames: Transport effects and aspects of scalar structure. *Combustion and Flame* **143** (4), 433 – 449. Special Issue to Honor Professor Robert W. Bilger on the Occasion of His Seventieth Birthday.

BILGER, R. 1993 Conditional moment closure for turbulent reacting flow. *Physics of Fluids* **5** (2), 436–444.

BOERSMA, B. J. 1998 Direct simulation of a jet diffusion flame. *Center for Turbulence Research Annual Research Briefs* pp. 47–56.

BOERSMA, B. J. 1999 Direct numerical simulation of a turbulent reacting jet. *Center for Turbulence Research Annual Research Briefs* pp. 59–72.

BOERSMA, B. J., BRETHOUWER, G. & NIEUWSTADT, F. T. M. 1998 A numerical investigation on the effect of the inflow conditions on the self-similar region of a round jet. *Physics of Fluids* **10** (4), 899–909.

BURCAT, A. 1984 Thermochemical data for combustion calculations. In *Combustion Chemistry* (ed. J. William Cecil Gardiner), chap. 8, pp. 455–473. Springer-Verlag.

BUTLER, T. D. & O'ROURKE, P. J. 1977 A numerical method for two dimensional unsteady reacting flows. *Symposium (International) on Combustion* **16**, 1503–1515.

CHARLETTE, F., MENEVEAU, C. & VEYNANTE, D. 2002 A power-law flame wrinkling model for LES of premixed turbulent combustion. Part I: non-dynamic formulation and initial tests. *Combustion and Flame* **131** (1-2), 159–180.

CHASE, M. W. (ed.) 1998 *NIST-JANAF thermochemical tables*, 4th edn. American Chemical Society.

CHELLIAH, H., SESHADRI, K. & LAW, C. 1993 Reduced kinetic mechanisms for counterflow methane-air diffusion flames. In *Reduced Kinetic Mechanisms for Applications in Combustion Systems* (ed. N. Peters & B. Rogg), *Lecture Notes in Physics monographs*, vol. 15, pp. 224–240. Springer Berlin / Heidelberg.

CHEN, C. J. & RODI, W. 1980 *Vertical turbulent buoyant jets - a review of experimental data*. Pergamon Press, Oxford, New York.

CHUNG, S. 2007 Stabilization, propagation and instability of tribrachial triple flames. *Proceedings of the Combustion Institute* **31** (1), 877–892.

COLIN, O., DUCROS, F., VEYNANTE, D. & POINSOT, T. 2000 A thickened flame model for large eddy simulations of turbulent premixed combustion. *Physics of Fluids* **12** (7), 1843–1863.

DOMINGO, P. & VERVISCH, L. 1996 Triple flames and partially premixed combustion in autoignition of nonpremixed mixtures. *Symposium (International) on Combustion* **26**.

DU, J. & AXELBAUM, R. 1996 The effects of flame structure on extinction of CH_4-O_2-N_2 diffusion flames. *Symposium (International) on Combustion* **26** (1), 1137–1142.

FOURNIER, G., GOLANSKI, F. & POLLARD, A. 2008 A novel outflow boundary condition for incompressible laminar wall-bounded flows. *Journal of Computational Physics* **227** (15), 7077 – 7082.

FROLOV, S., BASEVICH, V., BELYAEV, A., POSVIANSKII, V. & RADVOGIN, Y. 2001 *Modeling of confined flame stabilization by bluff bodies. In: Roy, G. D. (ed) Advances in Chemical Propulsion: Science to Technology*, chap. 12, pp. 191–214. CRC Press, Washington, D.C.

GANDER, W. & GOLUB, G. 1997 Cyclic reduction - history and applications. In *Proceedings of the Workshop on Scientific Computing, Springer Verlag, New York.*

GEAR, C. 1969 *The automatic integration of stiff ordinary differential equations. Information Processing 68*, pp. 187–193. North-Holland, Amsterdam.

GIVI, P. 1989 Model-free simulations of turbulent reactive flows. *Progress in Energy and Combustion Science* **15** (1), 1–107.

GRINSTEIN, F. F. 1994 Open boundary conditions in the simulation of subsonic turbulent shear flows. *Journal of Computational Physics* **115** (1), 43–55.

GU, X. J., HAQ, M. Z., LAWES, M. & WOOLLEY, R. 2000 Laminar burning velocity and markstein lengths of methane-air mixtures. *Combustion and Flame* **121** (1-2), 41–58.

HEIMEL, M. 2010 *Investigations on flames and flame - instabilities using optical metrology*. Master's Thesis, Graz University of Technology.

HINDMARSH, A. C. 1983 Odepack, a systematized collection of ode solvers. *Scientific Computing, R. S. Stepleman et al. (eds.), North-Holland, Amsterdam* pp. 55 – 64.

JOHNSON, N. L. 1996 The legacy and future of cfd at los alamos. In *Canadian CFD Conference, Ottawa, Canada*.

KALGHATGI, G. T. 1981 Blow-out stability of gaseous jet diffusion flames. Part I: In still air. *Combustion Science and Technology* **26** (5), 233–239.

KAWANABE, H., KAWASAKI, K. & SHIOJI, M. 2000 Gas-flow measurements in a jet flame using cross-correlation of high-speed-particle images. *Measurement Science and Technology* **11**, 627–632.

KLIMENKO, A. Y. 1990 Multicomponent diffusion of various admixtures in turbulent flow. *Fluid Dynamics* **25**, 327–334.

KUO, K. K.-Y. 1986 *Principles of Combustion*, 1st edn. John Wiley & Sons.

KÖBERL, S., FONTANETO, F., GIULIANI, F. & WOISETSCHLÄGER, J. 2010 Frequency-resolved interferometric measurement of local density fluctuations for turbulent combustion analysis. *Measurement Science and Technology* **21** (3), 035302.

LAM, S. H. & GOUSSIS, D. A. 1994 The CSP method for simplifying kinetics. *International Journal of Chemical Kinetics* **26** (4), 461–486.

LAW, C. K., SUNG, C.-J., WANG, H. & LU, T. 2003 Development of comprehensive detailed and reduced reaction mechanisms for combustion modeling. *AIAA Journal* **41** (9), 1629–1646.

LEE, U. D., SHIN, H. D., OH, K. C., LEE, K. H. & LEE, E. J. 2006 Extinction limit extension of unsteady counterflow diffusion flames affected by velocity change. *Combustion and Flame* **144** (4), 792–808.

LEGIER, J. P., POINSOT, T. & VEYNANTE, D. 2000 Dynamically thickened flame LES model for premixed and non-premixed turbulent combustion. *Center for Turbulence Research Summer Program* pp. 157–168.

LEMMON, E., MCLINDEN, M. & FRIEND, D. Thermophysical properties of fluid systems. in NIST Chemistry WebBook, NIST Standard Reference Database Number 69.

LI, J., ZHAO, Z., KAZAKOV, A. & DRYER, F. L. 2004 An updated comprehensive kinetic model of hydrogen combustion. *Int. J. Chem. Kinet.* **36** (10), 566–575.

LIU, Z. & LIU, C. 1994 Fourth order finite difference and multigrid methods for modeling instabilities in flat plate boundary layers - 2-d and 3-d approaches. *Computers & Fluids* **23** (7), 955–982.

LIÑÁN, A. 1974 The asymptotic structure of counterflow diffusion flames for large activation energies. *Acta Astronautica* **1** (7-8), 1007 – 1039.

LU, T. F., YOO, C. S., CHEN, J. H. & LAW, C. K. 2010 Three-dimensional direct numerical simulation of a turbulent lifted hydrogen jet flame in heated coflow: a chemical explosive mode analysis. *Journal of Fluid Mechanics* **652**, 45–64.

LYONS, K., WATSON, K., CARTER, C. & DONBAR, J. 2005 On flame holes and local extinction in lifted-jet diffusion flames. *Combustion and Flame* **142** (3), 308–313.

MANSOUR, M. S. 2003 Stability characteristics of lifted turbulent partially premixed jet flames. *Combustion and Flame* **133** (3), 263–274.

MIZOBUCHI, Y., SHINJO, J., OGAWA, S. & TAKENO, T. 2004 Understanding of combustion phenomena in a hydrogen jet lifted flame by use of DNS with hundred millions of grid points. In *6th World Congress on Computational Mechanics, Beijing*.

MIZOBUCHI, Y., TACHIBANA, S., SHINIO, J., OGAWA, S. & TAKENO, T. 2002 A numerical analysis of the structure of a turbulent hydrogen jet lifted flame. *Proceedings of the Combustion Institute* **29** (2), 2009 – 2015.

MOIN, P. & APTE, S. V. 2006 Large-eddy simulation of realistic gas turbine combustors. *AIAA Journal* **44** (4), 698–708.

MOIN, P. & MAHESH, K. 1998 Direct numerical simulation: A tool in turbulence research. *Annual Review of Fluid Mechanics* **30** (1), 539–578.

MUÑIZ, L. & MUNGAL, M. G. 1997 Instantaneous flame-stabilization velocities in lifted-jet diffusion flames. *Combustion and Flame* **111** (1-2), 16–30.

MUÑIZ, L. & MUNGAL, M. G. 2001 Effects of heat release and buoyancy on flow structure and entrainment in turbulent nonpremixed flames. *Combustion and Flame* **126** (1-2), 1402–1420.

NAJM, H. N. & WYCKOFF, P. S. 1997 Premixed flame response to unsteady strain rate and curvature. *Combustion and Flame* **110** (1-2), 92–94.

NAJM, H. N., WYCKOFF, P. S. & KNIO, O. M. 1998 A semi-implicit numerical scheme for reacting flow: I. Stiff chemistry. *Journal of Computational Physics* **143** (2), 381 – 402.

NICHOLS, J. W. 2005 *Simulation and stability analysis of jet diffusion flames*. PhD Thesis, University of Washington.

NICHOLS, J. W. & SCHMID, P. J. 2008 The effect of a lifted flame on the stability of round fuel jets. *Journal of Fluid Mechanics* **609**, 275–284.

NICHOLS, J. W., SCHMID, P. J. & RILEY, J. J. 2007 Self-sustained oscillations in variable-density round jets. *Journal of Fluid Mechanics* **582**, 341–376.

ORSZAG, S. A. & PATTERSON, G. S. 1972 *Lecture Notes in Physics*, , vol. 12, chap. Statistical Models and Turbulence, p. 127. Springer, 1972.

PANCHAPAKESAN, N. R. & LUMLEY, J. L. 1993 Turbulence measurements in axisymmetric jets of air and helium. Part 1. Air jet. *Journal of Fluid Mechanics* **246**, 197–223.

PAPANICOLAOU, P. N. & LIST, E. J. 1988 Investigations of round vertical turbulent buoyant jets. *Journal of Fluid Mechanics* **195**, 341–391.

PETERS, N. 1997 Four lectures on turbulent combustion. ERCOFTAC Summer School, Aachen.

PETERS, N. 2000 *Turbulent Combustion*. Cambridge University Press.

PETERS, N. & WILLIAMS, F. A. 1983 Liftoff characteristics of turbulent jet diffusion flames. *AIAA Journal* **21** (3), 423–429.

PHILLIPS, H. 1965 Flame in a buoyant methane layer. *Proceedings of the Combustion Institute* **10**, 1277–1283.

POINSOT, T. & VEYNANTE, D. 2005 *Theoretical and Numerical Combustion*, 2nd edn. R.T. Edwards.

POINSOT, T., VEYNANTE, D., TROUVE, A. & RUETSCH, G. 1996 Turbulent flame propagation in partially premixed flames. *Center for Turbulence Research Proceedings of the Summer Program* pp. 111–141.

POLING, B. E., PRAUSNITZ, J. M. & O'CONNELL, J. 2001 *The properties of gases and liquids*, 5th edn. McGraw-Hill.

POPE, S. B. 1985 PDF methods for turbulent reactive flows. *Progress in Energy and Combustion Science* **11** (2), 119–192.

PRIDDLE, R. (ed.) 2008 *World Energy Outlook*. International Energy Agency.

PURI, I. & SESHADRI, K. 1986 Extinction of diffusion flames burning diluted methane and diluted propane in diluted air. *Combustion and Flame* **65** (2), 137–150.

RICHARDS, C. D. & PITTS, W. M. 1993 Global density effects on the self-preservation behaviour of turbulent free jets. *Journal of Fluid Mechanics* **254**, 417–435.

RICHARDSON, L. F. 1922 *Weather prediction by numerical process*.

RICOU, F. P. & SPALDING, D. B. 1961 Measurements of entrainment by axisymmetrical turbulent jets. *Journal of Fluid Mechanics* **11** (01), 21–32.

ROHSENOW, W. M., HARTNETT, J. P. & CHO, Y. I. 1998 *Handbook of Heat Transfer*. McGraw-Hill.

RUETSCH, G. R. & FERZIGER, J. 1996 Lewis number effects on partially premixed flames. *Center for Turbulence Research Annual Research Briefs* pp. 67–84.

RUETSCH, G. R., VERVISCH, L. & LIÑÁN, A. 1995 Effects of heat release on triple flames. *Physics of Fluids* **7** (6), 1447–1454.

SANKARAN, R., HAWKES, E. R., CHEN, J. H., LU, T. & LAW, C. K. 2006 Direct numerical simulations of turbulent lean premixed combustion. *Journal of Physics: Conference Series* **46** (1), 38.

SESHADRI, K. & PETERS, N. 1988 Asymptotic structure and extinction of methane-air diffusion flames. *Combustion and Flame* **73** (1), 23 – 44.

SESHADRI, K. & WILLIAMS, F. 1978 Laminar flow between parallel plates with injection of a reactant at high reynolds number. *International Journal of Heat and Mass Transfer* **21** (2), 251 – 253.

SMAGORINSKY, J. 1963 General circulation experiments with the primitive equations, I. The basic experiment. *Monthly Weather Review* **91** (3), 99–164.

SMITH, G. P., GOLDEN, D. M., FRENKLACH, M., MORIARTY, N. W., EITENEER, B., GOLDENBERG, M., BOWMAN, C. T., HANSON, R. K., SONG, S., WILLIAM C. GARDINER, J., LISSIANSKI, V. V. & QIN, Z. Gri-mech 3.0.

SMOOKE, M. D. & GIOVANGIGLI, V. 1991*a* Formulation of the premixed and nonpremixed test problems. In *Reduced Kinetic Mechanisms and Asymptotitic Approximations for Methane-Air Flames* (ed. M. D. Smooke), chap. 1, pp. 1–28. Springer, New York.

SMOOKE, M. D. & GIOVANGIGLI, V. 1991*b* Premixed and nonpremixed test problem results. In *Reduced Kinetic Mechanisms and Asymptotitic Approximations for Methane-Air Flames* (ed. M. D. Smooke), chap. 2, pp. 29–47. Springer, New York.

SPALDING, D. 1971 Mixing and chemical reaction in steady confined turbulent flames. *Symposium (International) on Combustion* **13** (1), 649–657.

STANDARD PERFORMANCE EVALUATION CORPORATION SPEC CPU 2006.

STEINER, H. & BUSHE, K. 2001 Large eddy simulation of a turbulent reacting jet with conditional source-term estimation. *Physics of Fluids* **13** (3), 754–769.

SU, L., SUN, O. & MUNGAL, M. 2006 Experimental investigation of stabilization mechanisms in turbulent, lifted jet diffusion flames. *Combustion and Flame* **144** (3), 494–512.

SWAMINATHAN, N., MAHALINGAM, S. & KERR, R. M. 1996 Structure of nonpremixed reaction zones in numerical isotropic turbulence. *Theoretical and Computational Fluid Dynamics* **8**, 201–218.

SWARZTRAUBER, P. N. & SWEET, R. A. 1996 Fourier and cyclic reduction methods for solving poisson's equation. In *Handbook of Fluid Dynamics and Fluid Machinery* (ed. J. A. Schetz & A. E. Fuhs). John Wiley & Sons, New York.

TENNEKES, H. & LUMLEY, J. L. 1972 *A first course in turbulence*. The MIT Press.

TSUJI, H. & YAMAOKA, I. 1969 The structure of counterlow diffusion flames in the forward stagnation region of a porous cylinder. *Proceedings of the Combustion Institute* **12**, 997–1005.

UPATNIEKS, A., DRISCOLL, J. F., RASMUSSEN, C. C. & CECCIO, S. L. 2004 Liftoff of turbulent jet flames–assessment of edge flame and other concepts using cinema-piv. *Combustion and Flame* **138** (3), 259–272.

VANQUICKENBORNE, L. & VAN TIGGELEN, A. 1966 The stabilization mechanism of lifted diffusion flames. *Combustion and Flame* **10** (1), 59–69.

VERVISCH, L. & POINSOT, T. 1998 Direct numerical simulation of non-premixed turbulent flames. *Annual Review of Fluid Mechanics* **30** (1), 655–691.

WALCHSHOFER, C., STEINER, H. & BRENN, G. 2011 Robust outflow boundary conditions for strongly buoyant turbulent jet flames. *Flow, Turbulence and Combustion* **86**, 713–734.

WARNATZ, J. 1984 Rate coefficients for the C/H/O system. In *Combustion Chemistry* (ed. J. William Cecil Gardiner), chap. 5, pp. 197–360. Springer-Verlag.

WARNATZ, J., MAAS, U. & DIBBLE, R. W. 2001 *Combustion: Physical and Chemical Fundamentals, Modeling and Simulation, Experiments, Pollutant Formation*, 3rd edn. Springer Berlin Heidelberg.

WATSON, K., LYONS, K., DONBAR, J. & CARTER, C. 1999 Scalar and velocity field measurements in a lifted CH_4-air diffusion flame. *Combustion and Flame* **117** (1-2), 257–271.

WESTBROOK, C. K. 1982 Hydrogen oxidation kinetics in gaseous detonations. *Combustion Science and Technology* **29** (1), 67–81.

WESTBROOK, C. K., MIZOBUCHI, Y., POINSOT, T. J., SMITH, P. J. & WARNATZ, J. 2005 Computational combustion. *Proceedings of the Combustion Institute* **30** (1), 125 – 157.

WESTERWEEL, J., FUKUSHIMA, C. & AANEN, L. 2002 *Investigation of the mixing process in an axisymmetric turbulent jet using PIV and LIF. In: Adrian, R. J. et al. (eds) Selected papers from the 10th International Symposium on Applications of Laser Techniques to Fluid Mechanics*, chap. 15, pp. 339–357. Springer.

WILLIAMS, F. A. 1991 Overview of asymptotics for methane flames. In *Reduced Kinetic Mechanisms and Asymptotic Approximations for Methane-Air Flames* (ed. M. D. Smooke), chap. 4, pp. 68–85. Springer, New York.

WON, S., KIM, J., SHIN, M., CHUNG, S., FUJITA, O., MORI, T., CHOI, J. & ITO, K. 2002 Normal and microgravity experiment of oscillating lifted flames in coflow. *Proceedings of the Combustion Institute* **29** (1), 37–44.

WYGNANSKI, I. & FIEDLER, H. 1969 Some measurements in the self-preserving jet. *Journal of Fluid Mechanics* **38** (03), 577–612.

XU, G. & ANTONIA, R. A. 2002 Effect of different initial conditions on a turbulent round free jet. *Experiments in Fluids* **33**, 677–683.

YARIN, A. L. 2007 Self-similarity. In *Springer handbook of experimental fluid mechanics* (ed. C. Tropea, A. L. Yarin & J. F. Foss), pp. 57–81. Springer.

YOO, C. S., SANKARAN, R. & CHEN, J. H. 2009 Three-dimensional direct numerical simulation of a turbulent lifted hydrogen jet flame in heated coflow: flame stabilization and structure. *Journal of Fluid Mechanics* **640**, 453–481.

ZEUCH, T. 2003 *Reaktionskinetik von Verbrennungsprozessen in der Gasphase: Spektroskopische Untersuchungen der Geschwindigkeit, Reaktionsprodukte und Mechanismen von Elementarreaktionen und die Modellierung der Oxidation von Kohlenwasserstoffen mit detaillierten Reaktionsmechanismen*. PhD Thesis, Georg-August-Universität Göttingen.

Monographic Series TU Graz

Computation in Engineering and Science

Vol. 1 Steffen Alvermann
Effective Viscoelastic Behaviour of Cellular Auxetic Materials
2008
ISBN 978-3-902465-92-4

Vol. 2 Sendy Fransiscus Tantono
The Mechanical Behaviour of a Soilbag under Vertical Compression
2008
ISBN 978-3-902465-97-9

Vol. 3 Thomas Rüberg
Non-conforming FEM/BEM Coupling in Time Domain
2008
ISBN 978-3-902465-98-6

Vol. 4 Dimitrios E. Kiousis
Biomechanical and Computational Modeling of Atherosclerotic Arteries
2008
ISBN 978-3-85125-023-7

Vol. 5 Lars Kielhorn
A Time-Domain Symmetric Galerkin BEM for Viscoelastodynamics
2009
ISBN 978-3-85125-042-8

Vol. 6 Gerhard Unger
Analysis of Boundary Element Methods for Laplacian Eigenvalue Problems
2009
ISBN 978-3-85125-081-7

Monographic Series TU Graz

Computation in Engineering and Science

Vol. 7 Gerhard Sommer
Mechanical Properties of Healthy and Diseased Human Arteries
2010
ISBN 978-3-85125-111-1

Vol. 8 Mathias Nenning
Infinite Elements for Elasto- and Poroelastodynamics
2010
ISBN 978-3-85125-130-2

Vol. 9 Thanh Xuan Phan
Boundary Element Methods for Boundary Control Problems
2011
ISBN 978-3-85125-149-4

Vol. 10 Loris Nagler
Simulation of Sound Transmission through Poroelastic Plate-like Structures
2011
ISBN 978-3-85125-153-1

Vol. 11 Markus Windisch
Boundary Element Tearing and Interconnecting Methods for Acoustic and Electromagnetic Scattering
2011
ISBN: 978-3-85125-152-4